Multiscale, multidimensional renewable energy generation and storage management system

by

Simon Eje Ocheme

Submitted in accordance with the requirements for the degree of

PhD

The University of Leeds
School of Chemical and Process Engineering

February, 2017

The candidate confirms that the work submitted is his/her own and that appropriate credit has been given where reference has been made to the work of others.

Acknowledgements

My profound gratitude to my God Eternal Father for creating me, in his untiring love for me despite my unworthiness. You inspired the Psalmist to say "when I look at the night sky and see the work of your fingers the moon and the stars you set in place what are mere mortals that you should think about them, human being that you should care for" (Psalm 8:3-4). My blessed Saviour our Lord Jesus Christ for redemption of mankind and constant protection, the Most Holy Spirit for unfathomable inspiration that brought this challenging and daunting research work to a logical conclusion. I cannot thank the Most Blessed Virgin Mary for her constant intersection before her son and our Eternal Father. Also, many thanks to nine choirs of angels, my guardian angel and the entire celestial court.

My most beloved wife, a virtuous woman who stood by me through thick and thin, I say thank you "Eneolom" my sweet daughter, who has been used to Matlab and Simulink, thanks for your understanding the sleepless nights.

My gratitude to my prolific, wise, humane and humble supervisor, Dr Joseph Antony. Thank you for your financial and moral support and encouragement in forging a research direction that brought the research to it logical conclusion. I am indebted to him for constant advice. His interpersonal skills and approach to detail is unparalleled. Also, Dr. Antonia Borissova has been helpful in driving the research work to an end, I say thank you for making time to correct my work out of your busy schedule.

I would like to thank my technician, Roberts Harris, Abass in mechanical and Mr Tarsem in Electronic workshop for helping the manufacture of the parabolic trough system using the Laser cutter. Many thanks to Prof. Bill Gale for approving the funds for putting the rig together.

Abstract

Hydrogen combined cooling heating and power system provides an efficient and holistic means of meeting multiscale and multidimensional energy demands through short, medium and long term storage. The energy generation consist of solar thermal heat, photovoltaic electricity and wind power. The energy storage consists of short term battery storage, medium term heat storage and long term hydrogen storage. The general focus is on the system level integration and simulation of the entire system and a particular focus on the parabolic trough receiver shape and the control at the low level, high level supervisory logic control that manages the entire system. Furthermore, the fabrication of an experimental rig is performed originally for the validation purposes of the thermal system, in which the heat transfer characteristics of different nanoliquids under different natural light conditions is assessed. The results show a good performance for control reference tracking and disturbance rejection of the solar radiation. Research on the shape optimisation of the receivers of the parabolic trough reveals that the triangular shape provides a superior performance compared to the classical semi-circular shape in absorbing solar radiation. Also, a system level control oriented model, supervisory energy management system and experimental measurement system to study hydrogen combined cooling power system has been developed. The computational and experimental models developed in this research programme provide a strong basis for further studies, including the analysis and operation of hybrid hydrogen combined cooling energy system in the real tracking space and its overall system control and optimisation.

Table of Contents

Acknowledgements ..... **ii**

Abstract ..... **iii**

Table of figures ..... **xv**

Chapter 1 Introduction **1**

1.1 Background 1

1.2 Hydrogen combined cooling heating and power and energy system 3

1.3 Island energy system in perspective and case studies 4

1.4 Research motivation 4

1.5 Research objectives 5

1.6 Research methodologies 6

1.6.1 Model based design 6

1.6.2 Controller design 6

1.6.3 Design Optimisation and enhanced deterministic algorithm 6

1.6.4 Inverse design optimisation for selecting the parabolic trough shape 7

1.6.5 Frugal engineering and system integration of low cost solar simulator and spectrophotometer 7

1.6.6 Experimental synthesis of graphene based Nano fluid 7

1.6.7 Infrared thermography measurement-based Investigation on an integrated subsystem design of photovoltaic solar parabolic trough 7

1.7 Research problem statement 7

1.8 Research process and thesis thematic structure 10

Chapter 2 Literature review and critical analysis **12**

2.1 Chapter overview 12

2.2 Island energy system 12

2.2.1 Past, current state and case studies 13

2.2.2 Challenges and gaps in the past and current island energy systems 16

2.2.3 Solutions and how to bridge the perceived gaps in island energy systems ... 16
2.3 Standalone hydrogen energy system ... 17
2.3.1 Past, current state and case studies ... 17
2.3.2 Challenges and gaps in the past, current standalone hydrogen energy systems 18
2.3.3 Solutions and how to bridge the perceived gaps in standalone hydrogen energy systems ... 19
2.4 Combined cooling heating and power hydrogen energy system ... 19
2.4.1 Past, current state and case studies ... 19
2.4.2 Adsorption chillers ... 25
2.4.3 Challenges and gaps in the past, current state of combined cooling heating and power hydrogen energy systems ... 25
2.4.4 Solutions and how to bridge the perceived gaps in combined cooling heating and power hydrogen energy systems ... 25
2.5 Sizing of combined cooling heating and power hydrogen energy system ... 26
2.5.1 Past, current state of HCCHP sizing and case studies ... 26
2.5.2 Challenges and gaps in the past, current state of combined cooling heating and power hydrogen energy systems sizing ... 27
2.5.3 Solutions and how to bridge the perceived gaps in combined cooling heating and power hydrogen energy systems sizing ... 27
2.6 Parabolic trough solar thermal system ... 27
2.6.1 Parabolic trough PVT system ... 28
2.6.2 Tracking of parabolic trough ... 28
2.6.3 Shapes of parabolic trough receiver ... 28
2.6.4 Shape selection ... 29
2.6.5 Design optimisation ... 29
2.7 Dynamics of combined cooling heating and power hydrogen energy system ... 30
2.7.1 Past, current state and case studies ... 30

2.7.2 Challenges and gaps in the past, current state of dynamics of combined cooling heat and power hydrogen energy systems 32

2.7.3 Solutions and how to bridge the perceived gaps in dynamics of combined cooling heat and power hydrogen energy systems 32

2.8 Control of combined cooling heating and power hydrogen energy system 33

2.8.1 Primary (low level) layer control 33

2.8.2 Main (master level) layer control 33

2.8.3 Past, current state and case studies 33

2.8.4 Challenges and gaps in the past, current state of control of combined cooling heat and power hydrogen energy systems 35

2.8.5 Solutions and how to bridge the perceived gaps in control of combined cooling heating and power hydrogen energy systems 38

2.8.6 Automation and supervisory control of combined cooling heat and power hydrogen energy system 38

2.8.7 Hardware-in-the Loop in combined cooling heat and power hydrogen energy system 44

2.8.8 Investigation and thermal management of solar thermal PVT parabolic trough system using non-contact infrared computer thermography 46

2.8.9 Historical development of infrared thermography 46

2.8.10 Historical development of sun simulator 49

2.9 Carbon based functional materials for energy applications 52

2.9.1 Graphene synthesis methods 52

2.10 Summary 54

Chapter 3 Design optimisation and enhanced deterministic algorithm approach to sizing hydrogen HCCHP subsystems 55

3.1 Introduction 55

3.1.1 Hypothesis from literature 55

3.2 Methods for sizing hybrid energy system 56

3.2.1 Rule-of-thumb method 56

3.2.2 Paper based method 56
3.2.3 Software based methods 56
3.2.4 Calculus based optimisation techniques 56
3.2.5 Enumerative schemes 56
3.2.6 Random search techniques 57
3.2.7 Hybrid energy system optimisation software 57
3.3 The enhanced deterministic design optimization genetic algorithm solution approach 57
3.3.1 The design optimisation work flow 59
3.4 System input renewable resources and polyload profile data 60
3.5 Hydrogen combined cooling and heating hybrid energy system model development 60
3.5.1 Consumer (user) requirements 60
3.5.2 The design parameters 60
3.5.3 Concentrating solar photovoltaic parabolic trough sizing model 60
3.5.4 Wind turbine average power model 63
3.5.5 Fuel cell power sizing model 64
3.5.6 Alkaline water electrolysis power sizing model 64
3.6 Hybrid energy storage sizing models 65
3.6.1 Long-term storage model 65
3.6.2 Medium-term storage model 66
3.6.3 Short-term storage model 67
3.6.4 Battery secondary storage power model 67
3.6.5 Cooling or refrigeration model 68
3.6.6 Heating model 68
3.6.7 Design optimisation procedure 68
3.6.8 Formulation of optimization problem 68

3.6.9 Modelling income from generation 70
3.6.10 Modelling cost of the renewable energy components 70
3.6.11 Constraints 72
3.7 Research approach and methodology 72
3.7.1 HCCHP subsystem sizing methodology and solution approach 72
3.7.2 Importance and limitation of the research 72
3.7.3 Analysis of result obtained 73
3.8 Design optimisation validation results 81
3.8.1 Sizing result obtained from the MOGA NSGA II optimisation 86
3.8.2 Validation of results obtained 88
3.9 Summary and concluding remark 89
3.10 What next 90
Chapter 4 Shape selection of parabolic trough PVT receiver by inverse Design Optimisation 91
4.1 Introduction 91
4.1.1 Hypothesis from literature 91
4.2 Proposed shapes of the solar non-conventional radiation heat transfer receiver/PVT exchanger. 92
4.3 Mathematical Foundation: The continuity, heat transfer and momentum equations 92
4.3.1 Assumptions 93
4.3.2 Continuity equation 93
4.3.3 Heat transfer equation 93
4.3.4 Momentum equation 94
4.3.5 Thermophysical properties of heat transfer fluid and the solids in the receiver PVT assembly 94
4.4 Research approach and methodology 95
4.4.1 Direct shape optimisation method 95

4.4.2 Indirect or Inverse shape optimisation method 96
4.4.3 Inverse design optimisation methodology 96
4.5 Numerical solution approach of analysis problem 98
4.5.1 Generation of structure mesh of the proposed geometry 99
4.5.2 Boundary conditions 100
4.5.3 Solution of the governing coupled equations for the flow variable and the energy on the mesh generated 101
4.5.4 Verification and validation of numerical SIMPLE solution to the flow fields 101
4.5.5 Grid independence study 102
4.6 Design optimisation problem numerical solution approach 103
4.6.1 Parameter correlation 103
4.6.2 Spearman's rank Correlation 103
4.6.3 Pearson's linear correlation 104
4.6.4 Design of experiment 104
4.6.5 Response surface 105
4.6.6 Goal driven optimisation 105
4.6.7 Six Sigma robust design 106
4.7 Formulation of design optimisation Receiver PVT Problem 106
4.7.1 Boundary conditions 106
4.7.2 Objectives 106
4.7.3 Output dependent parameters 106
4.7.4 Constraints in the design space 108
4.7.5 Design variables or Input independent parameters 108
4.8 Importance and limitation of the research 110
4.9 Analysis and findings of result obtained 110
4.9.1 Analysis problem results 111

4.9.2 Inverse-Design optimisation result 115
4.10 Verification and validation of results obtained 125
4.11 Summary and concluding remark 126
4.12 What next 127
Chapter 5 Dynamical system modelling & Analysis of HCCHPS 128
5.1 Introduction 128
5.2 Hypothesis from literature 129
5.3 Research Approach 129
5.3.1 Model based design 129
5.3.2 MATLAB and SIMULINK 130
5.4 The hydrogen Energy Hub Concept system modelling of HCCHP 130
5.5 The parabolic trough PVT Subsystem 131
5.5.1 Solar thermal parabolic trough PVT system 134
Modelling the solar multiple (Hot water tank, cold water tank and the heat sink) 135
5.5.2 Wind turbine generation system 136
Generation bus system 138
5.5.3 Electrolyser model 138
5.5.4 Fuel cell model 140
Mass balance of oxygen, water and nitrogen about the cathode 141
Mass balance of hydrogen gas about the anode 141
Energy balance about the cathode 141
5.5.5 Hydrogen metal hydride storage model 141
5.5.6 The battery model 142
5.5.7 Solar space heating and airconditioning modeling 143
5.5.8 Space heating and cooling models 145
5.5.9 System Analysis tools of HCCHP 147

5.5.10 Singular value decomposition (SVD) 147
5.5.11 Index of controllability 148
5.5.12 Analysis of level of coupling or interaction 148
5.5.13 Relative Gain Array (RGA) 148
5.5.14 Stability 149
5.5.15 Controllability 149
5.5.16 Analysis and findings of result obtained 150
5.6 Summary and concluding remark 167
5.7 What next 167
Chapter 6 Control structure, architecture and strategies of hydrogen combined cooling heating and power system 168
6.1 Introduction 168
6.2 Research approach and methodology 168
6.2.1 Model based design 168
6.2.2 Programming software tools 169
6.2.3 SIMULINK 169
6.2.4 SIMSCAPE 169
6.2.5 SIMULINK design optimisation 169
6.2.6 Control system toolbox 170
6.3 Control architecture and strategies 170
6.4 Subsystem control structure and architecture 171
6.4.1 Parabolic trough PVT system 171
6.4.2 Mechanical tracking system 171
6.4.3 Process thermal system 177
6.4.4 Full state feedback multivariable LQR control architecture of subsystems 179
6.4.5 Wind turbine system 184
6.5 Hydrogen storage system 187

6.6 Hydrogen metal hydride tank system 188
6.6.1 PEM fuel cell system 188
6.7 Battery storage control system 190
6.8 Cooling and heating system 191
6.9 Analysis of result obtained 193
Subsystems MATLAB/SIMULINK implementation of LQR full feedback controller design 198
6.10 Subsystems Linear Quadratic Regulator controller design 202
Subsystem controller tuning 206
6.10.1 Electrolyser controller tuning with pre-compensator 208
6.10.2 Fuel cell controller LQR tuning with pre-compensator 210
6.10.3 Wind turbine mechanical system LQR controller tuning with pre-compensator 211
6.10.4 Battery LQR controller tuning with pre-compensator 212
6.11 Summary and conclusions 215
Chapter 7 Fabrication of experimental rig and synthesis of Nanofluids 217
7.1 Introduction 217
7.2 Research approach and methodology 217
7.3 Frugal engineering methodology approach 217
7.3.1 The solar simulator subsystem 218
7.3.2 Solar simulator theory 224
7.3.3 Calibration of the solar simulator irradiance 226
7.4 The spectrophotometer subsystem 227
7.4.1 Spectrometer slit unit 227
7.4.2 Spectrometer diffraction grating unit 228
7.4.3 Spectrometer enclosure 228
7.4.4 CMOS mobile camera 228

7.4.5 Learnlight acquisition and analysis software 228
7.5 The flowmeter piping subsystem 229
7.6 Parabolic trough receiver subsystems 230
7.6.1 Trough mirror subsystem 230
7.6.2 Receiver PVT subsystem 230
7.6.3 4 bar Link mechanism subsystem 231
7.6.4 Complete trough PVT system 232
7.7 Preparation of graphene Nanofluids 232
7.7.1 Preparation of graphene oxide 232
Materials 232
7.7.2 Experimental procedure 232
7.7.3 Reduction of graphene oxide 233
7.7.4 Sonication of graphene in solvent 233
7.7.5 Stabilisation of Nanofluid with gum Arabic 234
7.8 Summary and concluding remark 235
Chapter 8 Experimental measurement and validation 236
8.1 Introduction 236
8.2 Research approach and methodology 236
8.2.1 Experimental infrared thermometry 236
8.2.2 Experimental optical spectrometry 236
8.3 Experimental setup 238
8.4 Infrared camera setup, calibration and focusing 238
8.5 Measurement of temperature and acquisition of thermal signature of IR image 239
8.6 Measurement, calibration, and acquisition of LED simulator spectrum 240
8.7 Importance and limitation of the research 241
8.8 Analysis and findings of experimental result obtained 241

8.8.1 Thermal signature measurement & axial and radial profiles 241
8.8.2 Comparison plots of the 3 Nanofluids 242
8.8.3 Sun and simulator spectrum matching 245
8.9 Validation of results obtained 245
8.10 Summary and concluding remark 246
Chapter 9 Conclusions and scope for future research 248
9.1 Conclusions 248
9.2 Contributions of the Research 249
9.2.1 Primary Contributions 249
9.2.2 Derived Contributions 250
9.3 Future outlook 250
List of References 253
List of Abbreviations 269
Appendix A 274
Appendix B 285

Table of figures

Figure 1.1 The hydrogen combined cooling heat and power energy system architecture; solar radiation, ambient temperature wind speed and dew-point temperature are source of energy to drive thermal and electrical load……9

Figure 1.2 Thematic structure of thesis at a glance……10

Figure 2.1 Bonaire Island power system with 14 MW diesel generators, 11 MW wind turbines, 3 MW battery storage and 3 MW containerised back-up generators…….14

Figure 2.2 Work flow for the design optimisation problem……30

Figure 2.3 Agent from an individual point of view: an agent is an entity that senses, thinks and acts in some environment in order to realize its goal……36

Figure 2.4 A hierarchical organized MAS……...37

Figure 2.5 Block diagram of a decentralised three input (u1, u2, u3)-there output (y1, y2, y3) system architecture; The arrows in-between the subsystems S1, S2 and S3 account for interactions between systems for strong interactions that cannot be decoupled…….39

Figure 2.6 Block diagram of a distributed three input (u1, u2, u3)-three output (y1, y2, y3) system architecture; The solid arrows in-between the subsystems S1, S2 and S3 account for interactions between systems for strong interactions that cannot be decoupled; the broken arrows feedback communication between controllers C1, C2 and C3……41

Figure 2.7 Block diagram of a Hierarchical control for coordination of three input (u1, u2, u3)-three output (y1, y2, y3) system architecture; The solid arrows in-between the subsystems S1, S2 and S3 account for interactions between systems for strong interactions that cannot be decoupled; the broken arrows feedback communication between controllers C1, C2 and C3; the coordinator or supervisor the local control action and price or the cost function of the controllers…….42

Figure 2.8 A block diagram of a system with slow and fast dynamics, the slow process is outer loop while the fast dynamics system is placed in the inner loop. The input to the high frequency control coming from the output of the low frequency controller are the control output of the slow loop and input of the fast loop respectively……..43

Figure 2.9 Graphene single sheet and the electronic structure with the 3 covalent sp2 π orbital and one p orbital electron…….52

Figure 2.10 Top-down and bottom-up approach for synthesis of graphene…….54

Figure 3.1 Enhanced deterministic algorithm in detail; the primary energy source is sized from the hourly resources-wind speed, solar radiation from weather station, cooling, heating and electric demand and technical specification of components from manufacturers.....58

Figure 3.2 Flow chart of the design optimisation used to obtain the optimal sizes of the components of the HCCHP hybrid energy system.....59

Figure 3.3 Inputs data obtained from weather stations in Zhouhan Island and National Renewable Energy Laboratory. The Direct Normal Radiation and Diffuse Horizontal Radiation are measurement data while total and beam radiation were calculated.....73

Figure 3.4 The wind speed input data are measurement data. (f)Electric, (g) Heating and (h) cooling load are also measured values for 30 days.....74

Figure 3.5 Power produced or generated and computed using enhanced deterministic algorithm of the HCCHP model with script written in MATLAB; (i) The parabolic trough thermal to electric power; (j) solar PV power; (k) power from the wind turbine; (l) Power produced from the excess power produced from electrolyser after meeting demand 74

Figure 3.6 The long term storage hydrogen storage (m); medium term heat storage (n); short term battery storage (o); Electrolyser power obtained from excess power diverted (p).....75

Figure 3.7 Coefficient of performance for heating (q); Coefficient of performance cooling thermal comfort performance index(s); cooling rate (r) and heating rate (t).....76

Figure 3.8 The state of charge for hydrogen long term storage (u); state of charge of short term battery storage (w); Electrolyser current (v); battery charging current (x).....77

Figure 3.9 Feed-in-tariff present value investment income (a1); present value income obtained from storing excess power generated (a2); Initial investment cost (a3); cost of storing excess power generated (a4).....78

Figure 3.10 Power generated, delivered or supplied to meet electrical load, electrical load demanded, hydrogen long term storage and battery short term storage. A pictorial dispatch schedule.....79

Figure 3.11 Pareto front of bi-objective optimisation of Return of Investment as a function of total power generated (Thermal-to-electric, Photovoltaic and Wind turbine).....80

Figure 3.12 Multi-objective optimisation using NSGA II genetic algorithm; Scoring range histogram for individuals, selection function of the individual's number of children; Pareto

front for the annualised capital cost as objective 2 and the Loss of power supply probability as objective 1; the distance between each individuals; The rank histogram of the individuals in the selection; the average spread of all the generations 81
Figure 3.13 Parameter Kendall correlation of Cost of short, medium and long term 81
Figure 3.14 Parameter Kendall correlation of combine generation with the area of solar parabolic trough collector, PV module and the wind turbine swept area 82
Figure 3.15 Size Kendall parameter correlation of solar parabolic trough collector, PV module and Wind turbine swept area 83
Figure 3.16 Coefficient of determination of cost of storage, long term hydrogen storage, medium term heat storage and short term battery storage 84
Figure 3.17 Response surface of cost of storage, long term hydrogen storage and short term battery storage capacities 85
Figure 3.18 Response surface of cost of storage, long term hydrogen storage and medium term heat storage 85
Figure 3.19 Genealogy plot of the NSGA II multi-objective optimisation of the individual design space variables and the generations 86
Figure 3. 20 A trend test validation of power curve from Proven 15 wind turbine and the predicted power from simulation model 89
Figure 4.1 Proposed geometry of the PVT receiver……..92
Figure 4.2 Workflow of the analysis phase and the inverse design optimisation shape selection algorithm……..98
Figure 4.3 Structure mesh of both geometry……...100
Figure 4.4 Temperature and pressure contour flow field of triangular and semi-circular shape…….111
Figure 4.5 Analysis temperature plots of the heat transfer fluid……...113
Figure 4.6 Pressure drop along the length of the receiver in laminar and turbulence flow……114
Figure 4.7 Histogram with a normal distribution fit of Nusselt Number and fanning Friction Factor……...115
Figure 4.8 Full quadratic response surface prediction plots of parameters of five design variables.....116
Figure 4.9 Full quadratic response surface coefficient of determination of triangular and Semi-circular Nusselt number…….117

Figure 4.10 Box-Behnken design cube for design of experiments of the design variables on the Nusselt response……...118

Figure 4.11 3D response surface plot of Nusselt number Vs receiver length and inlet velocity of the heat transfer fluid……....119

Figure 4.12 Triangular shape multi-objective optimisation plots……121

Figure 4.13 Semi-circular shape multi-objective optimisation plots……122

Figure 4.14 Six-sigma Monte Carlo simulation of 10000 samples of design variables of triangular shape……..123

Figure 4.15 Six-sigma Monte Carlo simulation of 10000 samples of design variables of Semi-circular shape…….123

Figure 4.16 Capability probability of manufacturing the triangular shape……124

Figure 4.17 Capability probability of manufacturing the Semi-circular shape……...124

Figure 4.18 Nusselt number versus Reynolds number comparison of the semi-circular shape receiver with parabolic trough receiver of Ebrahim and Petukhov empirical correlation at constant heat flux along the length of the receiver…….....125

Figure 4.19 Heat transfer coefficient versus Reynolds number comparison of the semi-circular shape receiver with parabolic trough receiver of Ebrahim et al. (2013) and Reddy et al. (2008) empirical correlation at constant heat flux along the length of the receiver..126

Figure 5.1 Model based design "V" work flow, starting with requirement analysis to system design through model in the loop, software in the loop to hardware in the loop simulation……..130

Figure 5.2 Energy hub unified concept combining hydrogen gas, heat and electric current transportation between all the subsystems…….131

Figure 5.3 solar fields consisting of solar thermal parabolic trough with solar module place at the focal
line……134

Figure 5.4 Tank in series modelling of solar multiple thermal energy storage of hot and cold tank with a boiler as the heat
sink…….135

Figure 5.5 A boiler heat exchanger as the heat sink…….....136

Figure 5.6 A 3-mass representation of the VAWT mechanical system……137

Figure 5.7 Electro-mechanical and power electronics description of the wind turbine system…….....138

Figure 5.8 Proton Exchange Membrane electrolyser system components and subsystems…….139

Figure 5.9 Fuel cell material and energy flow with hydrogen and oxygen gas in counter-current flow into the anode and cathode respectively…….141

Figure 5.10 A simple equivalent circuits of a Lead acid battery with a voltage source internal resistance and capacitance……..143

Figure 5.11 An integrated room space heating and air-conditioning system, with heater, room space, supervisory controller, 3-way control valve and air ducts…….....145

Figure 5.12 Phase portrait trajectory of copper metal temperature (Tm) versus heat transfer fluid (Tf) module temperature……...150

Figure 5.13 Phase portrait trajectory of copper metal temperature (Tm) versus PV module temperature (Tp)……151

Figure 5.14 Phase portrait of temperature against height of the tank trajectory with the equilibrium point at the zero point on the height axis…….152

Figure 5.15 Phase portrait of a linearization hot storage tank……..152

Figure 5.16 Phase portrait and Phase portraits linearization of height of hot and boiler storage tank…….....153

Figure 5.17 Phase portrait of linearized boiler heat exchanger…….....153

Figure 5.18 Phase portrait of the wind turbine generator rotational speed and the turbine rotational
speed……..154

Figure 5.19 Phase portrait of the wind turbine generator rotational speed and the turbine rotational
speed……154

Figure 5.20 Phase portrait of converter DC current (IDC) versus voltage (UDC)……155

Figure 5.21 Phase portrait between battery state of charge (SOC) and the voltage with the gradient and the direction vectors arrow diagram……..157

Figure 5.22 Phase portrait between electrolyser moles of hydrogen produce and the temperature with the gradient and the direction vectors arrow diagram…….159

Figure 5.23 (a) Pole Zero map of trough with 6 poles along the zero real axis;(b) a zoom view of five crowded poles about the zero of the real axis;(c) The Nyquist plot of the 4 input total and beam radiation, flow rate and ambient inlet temperature by 2 output temperature of the heat transfer fluid and the PV module temperature……..164

Figure 5.24 (a) Bode plots of the trough PVT of 4 input by 2 output total and beam radiation, flow rate and ambient inlet temperature by 2 output temperature of the heat transfer fluid and the PV module temperature multivariable system;(b) Bode plot of beam radiation effect on PV module output temperature with gain and phase margin and their corresponding crossover frequencies…….....165

Figure 5.25 (a) Nyquist plot of beam radiation input and PV module temperature;(b) Nyquist stability plot of frequency response dynamics of flow rate input and heat transfer fluid temperature output…….166

Figure 6.1 A 3D native CAD model of the parabolic trough mirror PVT and the four-bar link mechanism, realised in solidworks……..173

Figure 6.2 High fidelity SIMMECHANICS model of the parabolic trough mirror receiver PVT system and the four bar link mechanism……174

Figure 6.3 two-degree of freedom PID Controller……..175

Figure 6.4 A more detailed implementation of the 2 degree of freedom architecture…...176

Figure 6.5 physical components high fidelity model of a DC motor……....177

Figure 6.6 Parabolic trough plant process flow diagram (PFD)……...178

Figure 6.7 Block diagram decomposition of the process flow diagram in figure 6.6……178

Figure 6.8 Control structure and architecture of the thermal and mechanical one-axis tracking of the parabolic trough PVT system……..179

Figure 6.9 Overall control strategies and architecture for the trough tracking and thermal system.....180

Figure 6.10 tracking subsystem block feedback feedforward control architecture detail..181

Figure 6.11 Multivariable State Feedback Linear quadratic regulator (LQR) control strategy and architecture……..182

Figure 6.12 Multi-loop control strategies and architecture for the full parabolic trough tracking, thermal temperature, hot tank storage, Heat exchanger-boiler and the cold storage tank…….....…..183

Figure 6.13 Control structure and architecture of wind turbine system with rotor speed control as inner loop and generator speed control as outer loop and rotor, generator angular velocity and electromagnetic torque (Electrical DC/AC power) as outputs……184

Figure 6.14 Full multivariable centralised Linear Quadratic Regulator (LQR) implementation of the wind turbine mechanical subsystem control……185

Figure 6.15 Control architecture of the electrolyser with and inner pressure loop and outer electrolyser controlled direct current……...187

Figure 6.16 Full multivariable centralised Linear Quadratic Regulator (LQR) implementation of the wind turbine mechanical subsystem control……188

Figure 6.17 Control architecture of the fuel cell with a hydrogen fuel utilisation and outer master loop hydrogen gas flow rate……189

Figure 6.18 The H2 tank inner loop is a decoupled PID control architecture……..190

Figure 6.19 A two loop inner battery PI and outer battery controller……191

Figure 6.20 A multivariable Multiple Input Multiple Output (MIMO) LQR control architecture of Full multivariable centralised Linear Quadratic Regulator (LQR) implementation of the Heating and cooling subsystem control……..….192

Figure 6.21 Trough PVT mechanical tracking PID control strategies and architecture...193

Figure 6.22 A root locus plot of the trough mechanical tracking subsystem with poles at the zero and left hand plane of the complex plane…….194

Figure 6.23 (a) Time domain step response of tuned 2DOF PID controller with antialiasing filter compensator; (b) 2DOF PID controller effort in frequency domain(c) Bode plot of output disturbance rejection in frequency domain (d) Bode frequency response of tuned 2DOF PID controller; (e) Input disturbance rejection of 2 DOF controller in time domain……....195

Figure 6.24 (a) Trough PVT position in pace relative to the tracking angle position of the sun;(b) Trough velocity response to motor speed actuation to position the trough;(c) Trough rate of change of velocity during actuation;(d) Motor current requirement for actuating positioning the trough;(e) motor displacement relative to the trough and sun position;(f) motor velocity for positioning the trough…….197

Figure 6.25 Full feedback centralised multiple-input multiple output multivariable optimal Linear quadratic regulator (LQR) controller with 6 step inputs, multiplexed and the gain K_t subtracted and fed as error signal to the State space block implemented the state vector x and output y…….....198

Figure 6.26 (a) Step response of step input obtained from LQR controller design in figure 16 of the Heat transfer fluid temperature in the trough PVT thermal subsystem; (b) Step response of step input obtained from LQR controller design in figure 16 of the PV temperature in the trough PVT thermal subsystem……...199

Figure 6.27 Cooling/Heating subsystem full feedback Linear Quadratic Regulator Controller with state space state equation and output block……....200

Figure 6.28 Fuel cell subsystem full feedback Linear Quadratic Regulator Controller with state space state equation and output block……...…200

Figure 6.29 Electrolyser subsystem full feedback Linear Quadratic Regulator Controller with state space state equation and output block……....200

Figure 6.30 Wind turbine mechanical subsystem full feedback Linear Quadratic Regulator Controller with state space state equation and output block……...201

Figure 6.31 Wind turbine electrical subsystem full feedback Linear Quadratic Regulator Controller with state space state equation and output block……...201

Figure 6.32 Battery subsystem full feedback Linear Quadratic Regulator Controller with state space state equation and output block……...….201

Figure 6.33 Multi-loop mixed architecture and control strategies implementation of block diagram in fig. 6.6 in MATLAB/SIMULINK…….202

Figure 6.34 A step response plot for the heating and cooling subsystem…….207

Figure 6.35 A typical step plot with performance position and locations……208

Figure 6.36 Electrolyser step response to step input of an LQR controller with a pre-compensator.....209

Figure 6.37 Fuel cell step response LQR controller tuning with pre-compensator……210

Figure 6.38 Wind turbine subsystem LQR controller tuning with pre-compensator step response to a unit step input……212

Figure 6.39 Battery LQR controller response to a unit step input tuned with a pre-compensator…….213

Figure 6.40 Hydrogen gas storage tank step response to unit step function of the transfer function with a PID controller……214

Figure 6.41 (a) Pade approximation of order 3: step response comparison; (b) the Bode plot of the frequency domain behaviour of the hydrogen storage tank temperature……215

Figure 7.1 (a) Back view of CREE LED boards with holes for the thermal paste; (b) Front view of the CREE LED boards with connecting wires between boards……..218

Figure 7.2 (a) up-turn view of Maker driver up pro with the blue connectors for connecting each LED printed circuits board, green connector for connecting each power supply unit to the driver and Molex female connector for the cooling fan; (b) top view of Maker driver up pro with the dial for increasing and decreasing the contrast of the LED's……219

Figure 7.3 (a) The 4 12 V cooling fan for each CREE LED boards for removing heat at intensity values ≥ 10%; (b) Heat sink for mounting and installing LED's, fans, drivers and for dissipating heats……...219

Figure 7.4 (a) Controller mounted on the heat sink with the audio data cable; (b) details of the controller with knob, LCD character display with sunrise, day, sunset night and storm features……..220

Figure 7.5 Connections schematics of drivers to drivers with audio data cable to controller, LED's to LED's and the output……....221

Figure 7.6 (a) the 48 V power supply unit (PSU); (b)the wiring connection of battery 1 and 2 to the 24 V flow meter and the 24 V battery charger in the control panel box enclosure; (c) Interior of the control panel enclosure box with the control panel buttons to the right……...222

Figure 7.7 (a) Solar sun simulator with reflector under a lambertian target test calibration; (b) dimension of triangular part of the reflector…….223

Figure 7.8 (a) Simulator hanging kits with all the accessories for installing the hanger; (b) 4 nylon washers, 4 stainless steel hex cap screws, and 4 stainless hex lock nuts to mount to MakersLED fixture and 2 2.5 inch screws for top stud installation ; (c) installation of the

hanger eylette, and the lock nut. Using a 7/16" open face wrench to tighten down the lock nut; (d) y-hanger cable for suspending the heat sink from the top……...224

Figure 7.9 The sun solar irradiance on the earth surface with the atmosphere covering for illustrating the concepts of 1 sun, Air mass (AM) 0, 1 and 1.5 at different locations on the earth surface…….....225

Figure 7.10 Sun simulator solar power versus intensity curve, obtained by measuring the light corresponding to an intensity value on the solar controller……227

Figure 7.11 Ambient Weather TM-206 Solar Power Meter (Pyranometer)…….227

Figure 7.12 A linear diffraction grating with 1000 lines/mm and a measurement range of between 300 and 700 nm……228

Figure 7.13 Flowmeter and piping subsystem components installation……...229

Figure 7.14 (a) An exploded view of the parabolic trough mirror and (b) the assembly view of the subsystem…….230

Figure 7.15 (a) An exploded view of the receiver PVT and the (b) the assembly view of the receiver PVT
subsystem……...231

Figure 7.16 Four bar link mechanism with 2 fixed frame, a crank, rocker and a connector…231

Figure 7.17 A 3D native CAD model of the parabolic trough mirror PVT and the four bar link mechanism, realised in solidworks……...232

Figure 7.18 (a) A Fisher scientific bath sonicator with Nanofluids with 3/4 water level; (b) Probe sonicaor with control panel and graphene-MEG Nanofluid; (c) A Thermo scientific centrifuge with LCD display of rpm (8000), time (2 h) and operating temperature (250 C); (d) Centrifuge Vals tubes with sediment of graphene oxide on the walls; (e) Centrifuge bucket with Val and Counter-Val during loading of sample……....234

Figure 7.19 Graphene Nanofluids prepare using Tours Modified Hummers method and stabiliseb by 0.01mg/mL……235

Figure 8.1 Working principle of infrared thermography from object infrared radiation emission sensing or detection to display of the image with the colour temperature map……....237

Figure 8.2 Part of the electromagnetic spectrum measured by infrared camera……...237

Figure 8.3 Working principle of visible light spectroscope……..…238

Figure 8.4 (a) Pictorial installation of the IR thermometry setup; (b) a schematic view of the experimental apparatus and
instrumentation…….....238

Figure 8.5 FLIR 325sc infrared camera used for acquiring the thermogram, x-y plots and csv data exports……..239

Figure 8.6 Software post-processing interface for analysing the spectrogram obtained from the spectrophotometer and a cell phone CMOS detector……....240

Figure 8.7 (a) Thermogram of 0.1 mg/mL graphene-MEG (250 mL Monoethylene glycol + 28mg graphene) of after 10 min of introducing Nanofluid into the receiver; (b)Thermogram of 0.1 mg/mL graphene-MPG (250 mL 28g of mono-propylene glycol); (c)Thermogram of 0.1 mg/mL graphene- DH2O (50g of graphene + 500 mL mono-ethylene glycol after 10 mins of heating in the receiver; (d) 0.1 mg/mL graphene-MEG temperature profiles; (e) 0.1 mg/mL graphene-MPG temperature profiles;(f) 0.1 mg/mL graphene- DH2O temperature profiles…….....241

Figure 8.8 Infrared temperature thermal signature measurement along the axial length of the trough PVT receiver of 3 Nanofluids heat transfer fluids……..242

Figure 8.9 Infrared temperature thermal signature measurement along the diameter of the trough PVT receiver of 3 Nanofluids heat transfer fluids…….....243

Figure 8.10 Infrared temperature thermal signature measurement of area average of the trough PVT receiver of 3 Nanofluids heat transfer fluids……....244

Figure 8.11 Spectral matching of the Sun direct normal radiation at 1.5 Air Mass in blue (1.5 AM ASTMG 173) and the spectrum of the CREE LED simulator radiation in green measured in the laboratory with fabricated Spectrum…….…….245

Figure 8.12 Validation of conjugate heat transfer computation against the infrared measurement obtained using FLIR IR 625 AC camera……...246

Chapter 1 Introduction

1.1 Background

The sun a huge solar ball rotating from the earliest strict of dawn to the radiant glow of sunset, moving steadily from east to west, the sun majestic daystar of the Cosmos, catalyst of life, and source of light, heat and energy. The apt and poetic description of the sun captures the increasing importance of solar energy as a renewable source that is capable of making the world's power generation drive realisable. The light from the sun drives the photo-electric effect of solar electricity, the heat extracted by cooling water or heat transfer fluid through a point or line focus underpins solar thermal energy system and the kinetic energy from the pressure differential created by the sun provide the base for wind energy conversion systems. To put this in perspective, the following fact was provided by two independent reports.

Firstly, a report from Department of Energy and Office of Science (SC) (2014) (Basic, Tools, & Planning, 2014) presented an obvious fact that the world demand for energy is projected to more than double by 2050 and to more than triple by the end of the century. Incremental improvements in existing energy networks will not be adequate to supply this demand in a sustainable way. Finding sufficient supplies of clean energy for the future is one of the society's most daunting challenges. Sunlight provides by far the largest of all carbon-neutral energy sources. More energy from sunlight strikes the Earth in one hour 4.3×10^{20} J than all the energy consumed on the planet in a year 4.1×10^{20} J. It is interesting to know that we currently exploit this solar resource through solar electricity, a 7.5 billion industry growing at a rate of 35-40 percent per annum and solar-derived fuel from biomass, which provides the primary energy source for over a billion people. Yet, in 2001, solar electricity provided less than 0.1 percent of the world's electricity, and solar fuel from modern (sustainable) biomass provided less than 1.5 percent of the world's energy. The huge gap between our present use of solar energy and its enormous undeveloped potential defines a grand challenge in energy research and for a fact, sunlight is a compelling solution to our need for clean, abundant sources of energy in the future.

Secondly, in a more recent study by Elliston, MacGill, & Diesendorf, (2013), a cost optimisation model found the least cost option for energy generation mix including wind turbine, photovoltaic, and concentrated solar thermal as the cheapest in a replacement fleet

between 2029 and 2043. A generation mix for this research is underpinned by this research outcome, with a system approach to a poly-generation and poly-load hydrogen standalone combined cooling heat and power system. In co-generation or poly-generation, the total energy consumption can be decreased and the demand for electric power can be reduced. This is achieved by allowing dispatchable heat storage rather than electricity to provide the desired energy service to thermally activated technology. One practical example is air conditioning that can be shifted from electricity powered as in vapour compression chillers to adsorption chillers that run on waste or heat absorbed from the sun.

Currently, the concept of combined cooling heating and power is growing dramatically around the world and has become a research hotspot. In the US the grand challenge set by department of energy (DOE) in collaboration with environmental protection agency (EPA) and the combined cooling heating and power (CCHP) for building 2020 Vision, which also provide a timetable for the development of CCHP. The outcome of the grand challenge was a document that by 2020, 50% of new buildings and 25% of existing commercial institutional buildings in the USA will be provided with CCHP (Wu & Wang, 2006). In Europe, 11% of energy generated comes from cogeneration systems and Denmark distributed energy generation currently have a market share of 60%. There are indications that renewable energy market share in Germany will have increased from its current 12.55% to 25% by 2020 (Gu et al., 2014). The steady growth in renewable energy penetration is supported by the plummeting price of some of these technologies, especially wind and solar, have seen recent dramatic price decreases, for instance onshore wind turbines can produce electricity at a levelised cost of 3p to 10.43p/ kWh at a discount rate of 5%, while photovoltaic (PV) systems are at about 14.34p/kWh and dropping at a 5% discount rate and 25% capacity factor, according Michael & Brett, (2010).

In the context of CCHP, the performance depends largely on the energy management. Energy management of this system is daunting as a result of energy coupling of heat, cold and electricity; multi-operational objectives in terms of running costs, energy efficiency and emission; multiple time scales in the short term and long term regime. The aforementioned underpins the primary focus of this research as a multi-scale, multi-dimensional renewable energy generation management system. The focus of this research or main objective of this thesis is to establish the best shape of the trough receiver that will extract heat maximally at low pumping effort from solar simulator designed in-house from scratch. Also, to develop a supervisory control system to manage and coordinate the multidimensional hydrogen

combine heat and power system to capture wind turbine dynamics, PV dynamics and fuel cell oxidation-reduction reaction. Also, micro-scale reactions, electrolyser dynamics and battery electrochemical reactions and response to charging variations during changes with wind, solar PV and solar thermal heat / cold storage system. In this study, a model-based model of the various subsystems is developed and implemented using MATLAB /SIMULINK tools. A thermographic measurement of the trough receiver for system identification and estimation of controller parameter tuning is investigated. A heat transfer fluid was synthesize for effective solar heat transfer. Data for complete analysis are based on the case study of a remote island located in Zhoushan, China longitude $29^0$56' 44.7"N latitude 122^0 05'05" E and Los Angeles, Longitude 34^0.05'22" Latitude 118.24'37"W. The section that follows provides a brief of the content of the thesis.

1.2 Hydrogen combined cooling heating and power and energy system

Hydrogen standalone energy system is a better alternative to battery based standalone energy or power system owing to the short battery life of lead acid, lithium ion and other battery technologies. The hydrogen can be stored and discharged to Fuel cell system to produce power for un-met load during sun down and when the wind is not blowing while the battery supplies the short transient power for 5-10 minutes before the fuel cell come on, which is a consequence of system inertia response. However, for long term storage, a hydrogen storage system is a more robust alternative. There are hydrogen standalone systems already deployed around the world. However, such system fails because of balance of plant failure which is a consequence of little or complete absence of system or model based modelling and automatic control. Apart from this problems, in the event that load cannot be fulfilled by the hydrogen storage system, a heat storage system based on heat extraction or cooling of the solar cell from a concentrated parabolic trough will provide dispatch able energy in form of heat from a heat transfer fluid to produce saturated steam to drive a conventional Rankine or Stirling engine cycle. The heat can also drive an adsorption chiller and take away the load from the electric power side for energy efficiency and utilisation. An agent based control and supervision system should manage and coordinate the system. Locations such as Zhoushan Island is poly-load based as it has electric, space heating and cooling load, the electricity demand and the space heating in winter is to be driven by electricity from the solar photovoltaic and wind power, while the heat from the parabolic trough supplies the thermal power for the space cooling or air-conditioning and domestic hot water supply. The energy system for remote Islands can be

deployed once the system components sizes are determined and the loads, wind and solar resources are obtained. The chapter that follows will explore the current state of the hydrogen standalone system.

1.3 Island energy system in perspective and case studies

In a study conducted by intergovernmental Panel on Climate Change on renewable energy sources and climate mitigation revealed that approximately half of new generation capacity added globally between 2008 and 2009 were obtained from renewable energy (Mitigation, 2011). The implication of the study is that the future of renewable energy as the base or major source of power for Island and remote communities is promising and looks bright.

There is however the challenge of fluctuations of the renewable energy and must be addressed to ensure continuous availability and efficient use of the energy produced. There must be ways of managing demand side and appropriate storage solutions including better forecasting tools. Traditionally, large scale electricity storage systems were based on pumped hydropower systems. The modern trends are emerging, including affordable and long lasting batteries. This technology field is developing rapidly and prices are falling. The current direction of island is on modelling and testing of energy systems before deploying on site as stated in the work of Komor & Glassmaire, (2012). In the report presented by these authors, it was strongly recommended that a close attention must be paid to system from the perspective modelling and ensuring that the components constituting the energy systems are sized correctly and the components can work together. Testing and debugging system components before sending them out to rural/isolated locations was also recommended. Also, System monitoring and operation and maintenance are critical to ensure system reliability and longevity. There are case studies of Apolima Island, Bella Coola, Bonaire, King Island, Kiribati, Metlakatla, Osmussaare, Padre Cocha, Ramea Island, San Juanico and Eigg. The details of the power generation and storage systems will be elucidated in chapter 2.

1.4 Research motivation

The motivation for the research was underpinned by the superabundance of solar energy and system approach to optimal energy system realisation which is supported by the fact as follows;

- All of mankind energy generation in one year is 4.1×10^{20}J of sunlight hitting the earth every hour (Basic, Tools, & Planning, 2014)

- The amount of energy generated since the dawn of human civilisation is 17 TW and the amount of sunlight reaching the earth is 100,000 TW (PBS, 2011)
- Wind turbine, photovoltaic, and concentrated solar thermal as the cheapest in a replacement fleet between 2029 and 2043 (Elliston, MacGill, & Diesendorf, 2013)
- Distributed CSP CCHP is cost competitive with coal at 1.33p/kW_th, 4p/kW_eh (Glöckner, et al, 2004)
- Hydrogen standalone power system can bridge the power divide in distributed or embedded generation
- Solar energy provides both cooling and heating energy
- Solar energy is generated and consumed on site directly
- Solar energy enables dispatchable power on demand with thermal energy storage
- 2/3 of population in sub-Sharan Africa is still without electricity and energy is very precious

1.5 Research objectives

The main aims of the thesis are as follows:

- To size and optimise system components (wind solar photovoltaic, solar thermal trough area, wind turbine, fuel cell, battery, electrolyser etc.)
- To establish the best shape for the parabolic trough receiver that will absorb the maximum solar radiation at lowest pumping number
- To study the dynamic behaviour of the renewable energy sub-systems and their system level response when they are combined.
- To develop a system of system low level control strategies on subsystems level
- To developed a decentralised hierarchical supervisory logic to coordinate and manage the hydrogen combined cooling heat and power system
- To develop a hardware-in-the loop model of parts of the HCCHP for verification and validation of part of the low level and supervisory control
- To develop a sun simulator and calibrate it for laboratory study of solar energy systems

- To synthesize a graphene based Nano fluid for effective absorption of solar radiation and thermal energy storage and comparison of thermal signatures and profile with the conjugate heat transfer simulation of the trough receiver

1.6 Research methodologies

1.6.1 Model based design

The model based techniques are used for a comprehensive study of the dynamics of the system, to understand the open-loop response of the system to disturbances or perturbations. The control algorithm and the strategies for the control of the system are investigated. The control systems respond to set-point values. Sometimes, the processes may deviate from the control objective, which means an appropriate tuning will have to be performed to determine the control parameters. A control optimisation study is also necessary to identify the system and tune the controller for optimal performance.

1.6.2 Controller design

The control system design is a follow-up of the decision on the control objective and it involves three main steps:

- Selection of the controlled, manipulated and measured variables
- Choosing the control strategy and control structure
- Specifying the controller settings

The control variable is the physical quantity to be controlled, such as the temperature for solar PV, wind turbine rotational speed, electrolyser current, charging current to the battery, etc. The manipulated variables are the cooling water flow rate from the heat exchanger, pulse width angle and maximum power point tracking for the wind turbine and the PV. The measured variables, includes: multi-physics goals, such as wind speed, PV close circuit current, current output from the busbar, electrolyser electrolyte flow rate, solar radiation from the solarimeter, electron transfer charge, etc., measurement data from sensor arrays and output port of a multi-physics simulation.

1.6.3 Design Optimisation and enhanced deterministic algorithm

Design optimisation is for selection of the best shape for the trough receiver. Also, a design optimisation is performed for sizing subsystems that constitute the hydrogen combined cooling heat and power system.

1.6.4 Inverse design optimisation for selecting the parabolic trough shape

An inverse-design optimisation approach was used to select the parabolic trough shape that delivers the maximum heat transfer rate at minimum fanning friction factor. In this approach, the temperature and the pressure flow field of the receiver is obtained from the solution of conjugate heat transfer and results is used to obtained the best shape using design optimisation.

1.6.5 Frugal engineering and system integration of low cost solar simulator and spectrophotometer

Frugal engineering is an emerging economic cost concept of producing a device optimum cost yet, meeting product design specification and requirement analysis. A sun simulator is fabricated from scratch to enabled the measurement of solar radiation in the laboratory, thereby eliminating the problem of un predictability of the sun. The spectrophotometer was realised using the frugal engineering concept for measuring and calibrating spectrum the LED light.

1.6.6 Experimental synthesis of graphene based Nano fluid

A graphene oxide exfoliation based on improved Hummer method was used in the production of few layer graphene oxide. The graphene oxide was dispersed in deionised water, propylene glycol, ethylene glycol, castor oil and perm kernel oil to ascertain the best heat transfer fluid for solar thermal application. The Nanofluid was synthesized to because of it high solar radiation absorption characteristics.

1.6.7 Infrared thermography measurement-based Investigation on an integrated subsystem design of photovoltaic solar parabolic trough

Investigations are performed on of the heat transfer distribution in a semi-circular and a triangular shape of a solar parabolic trough receiver, using the thermal signatures produced by the Infrared camera. The study provides results that can be a benchmark for the multi-physics model to quantitatively determine the best shape for the receiver-collector duo.

1.7 Research problem statement

A conceptual hydrogen combined cooling heat and power system is depicted in Figure 1. Hydrogen standalone renewable system have been investigated by (Vanhanen, 1996); (Voss et al., 1996); (Schucan, 2001) and some of the systems function as expected and others failed as results of absent or complete absence of system study. In the energy hub of multiple

energy source with Combined heat and power approach investigated by Geidl (2004); Geidl and Anderson (2007), it is assumed that the solution of the energy hub algorithm, meet requirement of a hybrid energy system.

This thesis extends the energy hub approach to cover hydrogen and seeks to address the following key research questions;

1. Can an optimum parabolic trough shape be obtained that will capture the maximum heat from the sun and transfers it to the heat transfer fluid at minimum pumping requirement?
2. Can an optimum size of subsystems be obtained from the electric, cooling and heating load using design optimisation to meet short-term, medium-term and long term storage?
3. Can a system level model be obtained to establish interactions, stability, controllability, coupling and decoupling of dependent and independent subsystems?
4. Can a control oriented model be obtained from the dynamics of the subsystems?
5. Can a low level and supervisory control system coordinate and manage all the subsystems in the HCCHP?
6. Can all the subsystems work together?
7. Can an experimental model of the trough PVT receiver with a laboratory based solar simulator be realised?
8. Is it possible to develop a spectrophotometer to measure the simulator LED light and benchmark the spectrogram provided by the manufacturers of the lamp?
9. Is the carbon based heat transfer fluid better in heat transfer and thermal storage performance compared to non-carbon based heat transfer fluid?

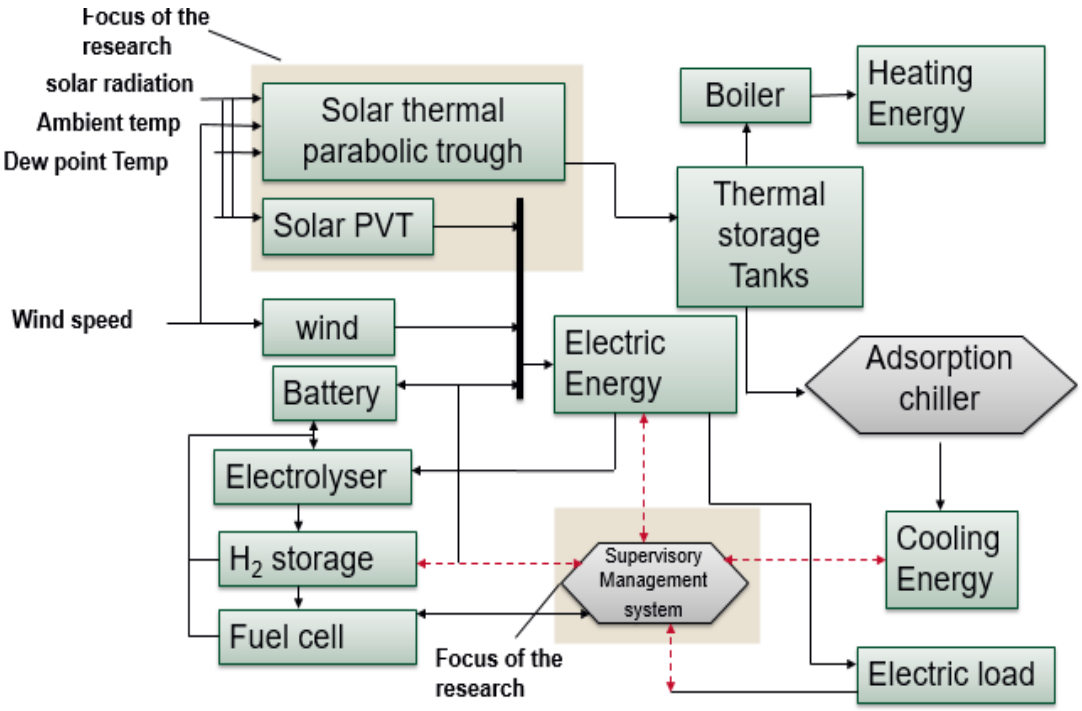

Figure 1.1 The hydrogen combined cooling heat and power energy system architecture; solar radiation, ambient temperature wind speed and dew-point temperature are source of energy to drive thermal and electrical load

1.8 Research process and thesis thematic structure

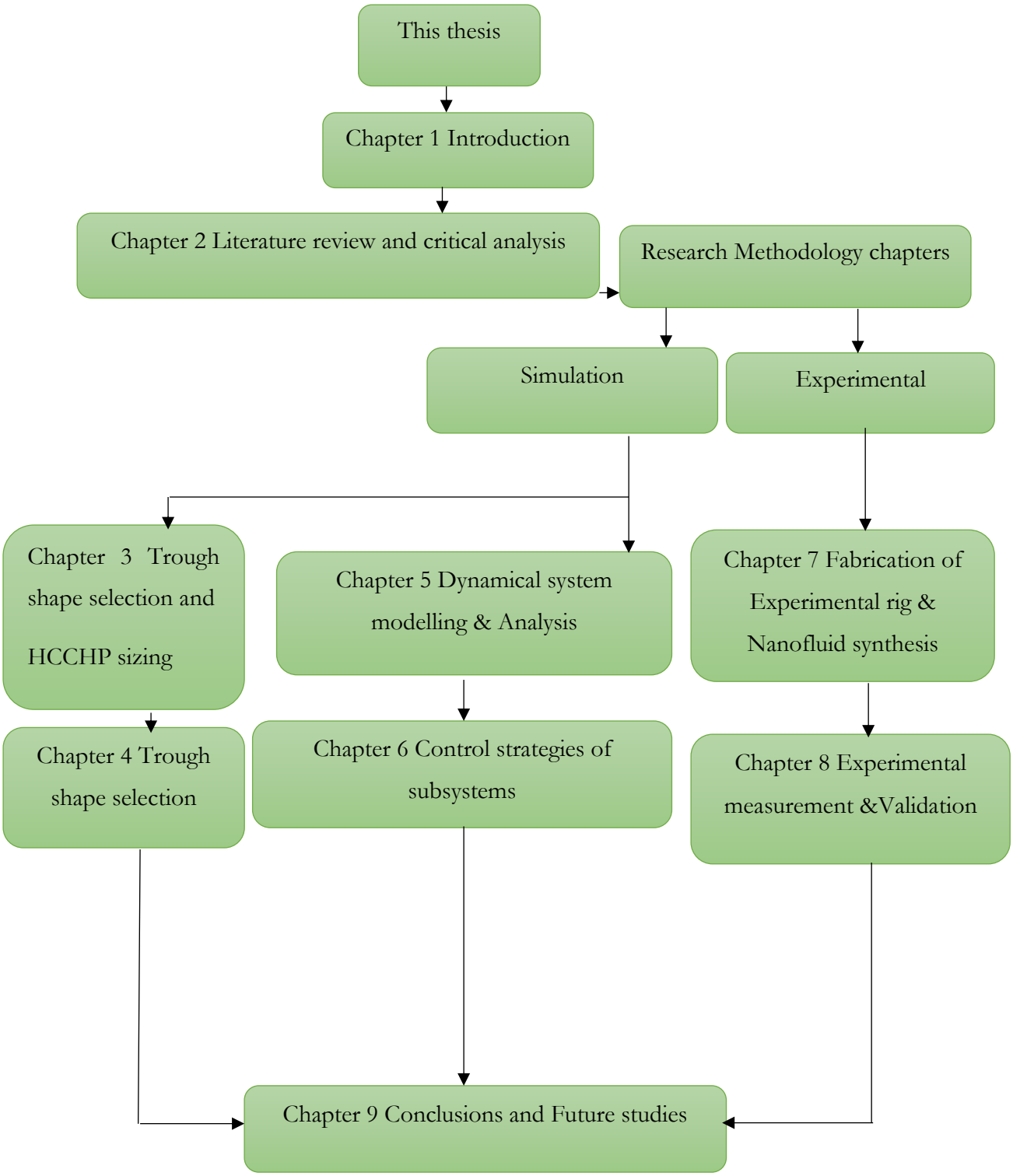

Figure 1.2 Thematic structure of thesis at a glance

This thesis is arranged as follows:

Chapter 2 Present the survey of the literature, and in parallel discusses system thinking which serves as a spring board or the motivation for the study of the hydrogen Combined cooling heat and power (HCCHP), Sizing and optimisation of HCCHP system and shape selection of the trough PVT, HCCHP system dynamics, control schemes and control strategies of HCCHP system, Automation and supervisory management of HCCHP system and Model in the loop, hardware in the loop simulation, experimental investigation of infrared thermography of the parabolic trough PVT system, solar simulators and carbon based Nano fluid thermal characteristics under laboratory sun simulator.

Chapter 3 is on hybrid enhanced deterministic algorithm and design optimisation for sizing the subsystems in the HCCHP

Chapter 4 presents a novel shape of the parabolic trough receiver selection, based on analysis problem and inverse-design optimisation approach.

Chapter 5 will present dynamical system analysis of the HCCHP for stability response, fast and slow subsystem behaviour, control loop coupling and decoupling, controllability, reachability and other system dynamics studies

Chapter 6 presents control strategies of combined cooling heat and power system, using model based design control techniques with MATLAB SIMULINK

Chapter 7 is on fabrication and integration of experimental and synthesis a carbon based Nano fluid and compared the thermal performance with non-carbon based heat transfer fluid.

Chapter 8 is focused on the investigation of the integrated subsystem design of the photovoltaic solar parabolic trough, using computed Infrared tomography. Investigation of the heat transfer distribution in a semi-circular and a triangular shape of a solar parabolic trough receiver, using the thermal signatures produced by the Infrared camera. The study should provide results that can be benchmark by multi-physics model to quantitatively determine the best shape for the receiver-collector duo.

Chapter 9 Summarises the main conclusions, significance of research to practical applications, limitations of the research and future research outlook.

Chapter 2 Literature review and critical analysis

2.1 Chapter overview

The chapter dwell on system thinking from the perspective of combined cooling heating and power system, standalone hydrogen energy system, island power, sizing of the combined cooling heating energy system, dynamic 1 dimensional, 2 dimensional and 3D model of a parabolic trough PVT system. A low-level control strategy, supervisory high level control strategies, automation of system and a hardware-in-the loop testing and verification of the low level and high level control specifications is expounded in details. Finally, literature review pertaining to an experimental investigation of infrared thermography, design, implementation of solar sun simulator and graphene as a carbon-based material for energy storage. The related literatures are critically reviewed on the themes highlighted above.

System based thinking in energy system

A top-down approach was adopted in reviewing the related literature, the elements in the hydrogen combined cooling and heating power system (HCCHP) and the interconnectedness between these subsystems constituting the energy system.

Systems thinking involves a consideration of the notion that the element, component parts of a system can best be fathomed in the context of relationships with each other and with other subsystems or systems, rather than their separate parts. A system thinking approach is founded on the basis that the only way to fully comprehend a complex or complicated problem is to understand the parts in relation to the whole.

In a more universal and qualitative definition, combining the three requirements for defining system thinking- purpose, element and interconnections- underpinning causality (cause and effect) and how both connect and feed into each other was proposed by Arnold & Wade, (2015). Their research was focused on definition of system science that captures the essence of the three requirements. A more detailed definition is detailed in Arnold & Wade, (2015). The system is a HCCHP to provide heat and electricity to meets heating, cooling and electricity load demand of an island. Consequently, a review of related literature for island energy system is sought in the section that follows.

2.2 Island energy system

Island energy systems are mainly standalone either because of their remote location or interconnections to national grid infrastructures difficulty, as a result of challenging terrain (Komor & Glassmire, 2012). Some island may have steady energy sources like hydro and geothermal energy, which are continuous and not intermittent and often not require storage. It is common in most islands that the resource available are intermittent (solar and wind)

and may require storage. To form the motivation, case studies based on 8 islands will be reviewed and critically discussed with focus on success and failures and the gaps that will have to be understood in this research.

2.2.1 Past, current state and case studies

Apolima island with a population of 100 residents is among the 4 islands that constitutes the nation of Samoa, which can only be accessed by boat. The source of electricity to the island was a 15 kVA diesel generator that provided power for only 5 hours per day and was characterised with noise and emissions from the generator exhaust. These problems provided an opportunity for the island to transition to 100% renewable energy, consisting of 13.5 kW photovoltaic array, lead-acid storage batteries, inverters and other balance of plant. The system was able to meet and provide 24 hours power to the 100 residents of the island, with consumer discipline and power management of not using inductive load appliances such as electric kettles and cookers. A system analysis after a period of use revealed that the system operated with minor technical issues because the inverters were stacked instead of using large inverters (Clay , 2005). The only challenge with the system was that recouping the initial capital outlay was difficult as the resident of the island were not engaged in any meaningful work to pay for the electricity consumed.

The island of Bella Coola, British Colombia, Canada deployed 100 kW fuel cell, 125 kW flow battery storage with generation from run-of-river hydro facility and supported by diesel generator when demand exceeds hydro output. A combined capacity of 8 MW for both hydro and diesel generator was sized for population of 1,900 inhabitants in the island. The system is the most technologically advanced energy system for remote location. The challenge was the high diesel consumption and the excess hydropower wasted, which was overcome by short-term and medium-term flow battery storage and long-term hydrogen storage fuel cell and a 60 Nm^3/hr electrolyser (Miles and Gillie, 2012). Control and optimisation at the system level was identified as a major challenge with the system and fine-tuning and research is ongoing to improve the system.

The two island energy described above were developed based on the need for power, this was however different for the Bonaire island located near the coast of Venezuela. Bonaire Island have a base population of 14,000 with a peak electricity demand of about 12 MW, transformed the challenge of destruction of island only power supply by fire into full scale renewable energy power. The installed capacity of the island consists of 14 MW of diesel generator, 11 MW of wind and 3 MW of Nickel-based battery, producing 845 kWh 640 V with a nominal capacity of 1320 Ah. The battery was able to fit into a three standard transport containers (Johnston, 2010). The system is not a 100% renewable energy as diesel generators were still in the loop, an electrolyser fuel cell duo for long-term storage could

easily have addressed the storage problem. The installation of mesh or cascades of Stirling engines could have enhanced the system efficiency, peak shaving and mini-grid frequency stabilisation. Figure 1 shows the implementation of Bonaire Island power.

King Island, an Island of the Australian state of Tasmania, with population of 1,700 inhabitants, migrated from the fossil fuel based diesel to renewable energy. The renewable energy system consists of three 250 kW wind turbines in 1998, another 850 kW wind turbine in 2003, a 200 kW 6 Sumitomo cell stacks, a 400 kW Hydro power from the government of Tasmania and 100 kW solar Photovoltaic system in 2010. The challenge with the overheating of the electrolytes of the Vanadium flow batteries could have easily been eliminated with a good system thinking modelling of the elements constituting the system. A battery management and overall management system, with event and time modelling is required to understudy the system level behaviour before actual deployment is highly recommended for such system.

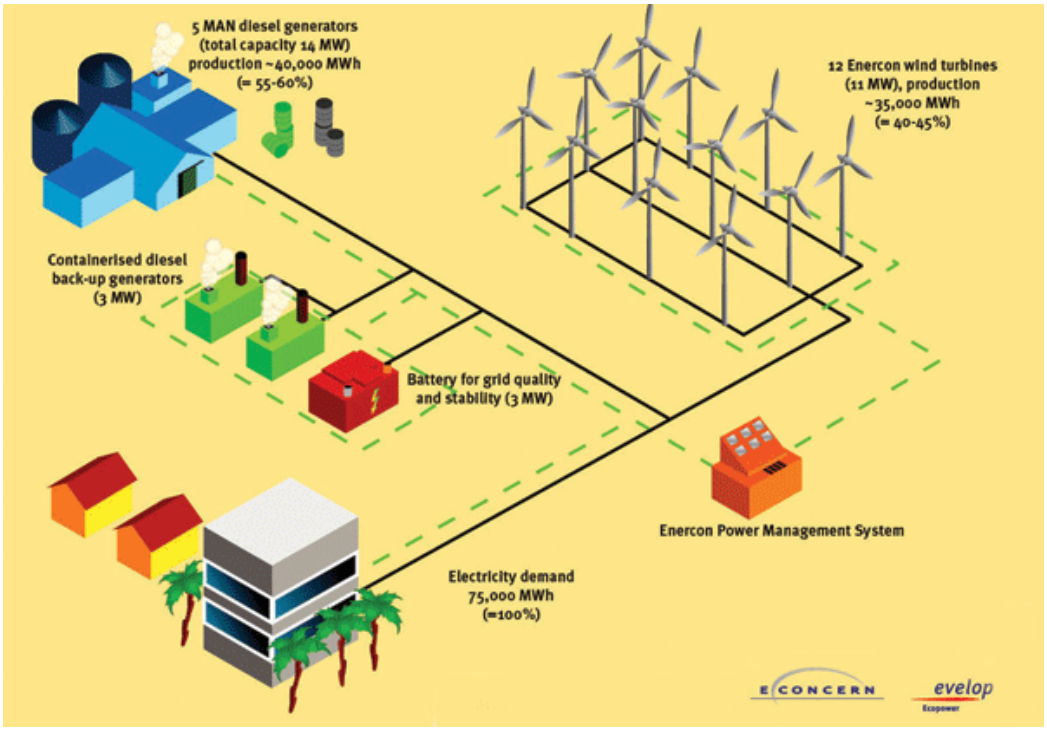

Figure 2.1 Bonaire Island power system with 14 MW diesel generators, 11 MW wind turbines, 3 MW battery storage and 3 MW containerised back-up generators (Johnstone, 2010)

The energy system in Outer islands of Kiribati, Republic of Kiribati, central tropical Pacific Ocean is an interesting one, as the system is fully distributed. A fully distributed energy system is one with all its users or consumer generating and using it energy its location (rooftops in residential home, rooftops in commercial properties). The systems consist of 100 W PV panels connected to 140 Ah lead-acid batteries with other balance of plant such as charge controllers. The system was investigated and was discovered to be far better and

cost effective than diesel for 1,700 residences (because of high cost of diesel, carbon dioxide pollution and logistics of transporting it to the island). Systems managed by individuals are always a challenge as maintenance, operational and replacement is also a challenge.

Metlakatla Island, Alaska is a small and isolated native coastal community located in the rural Alaskan panhandle with population of 1,400 inhabitants. The Island consists of a 4.9 MW hydroelectric system, supplemented with a 3.3 MW diesel generator and a 1 MW battery storage system. The storage system has been in operation since 1997 and well maintained with sufficient data for system evaluation for both technical and economic performance. The challenged with the system was the high diesel maintenance cost and logistic challenge of providing diesel to the Island (Alaska state government 2008; Hunt, and Szymborski, 2009; Murphy et al.,2009; Szymborski et al.,2001). The batteries were so well maintained that after 12 years of replacement, they were discovered to they were in excellent condition and may have been able to operate even longer with intelligent battery charging.

A remote island Osmusssaare, off the Estonian coast, provided power to a radar facility with a diesel generator. However, the high cost of diesel provided an opportunity for the island to deploy a 30 kW wind turbine, connected to two 32 kW diesel generators. A 408 V (nominal), 250 Ah (~102 kWh) lead-acid battery bank storage was installed to provide back-up power for the radar station. Operational evaluation of the system showed that 85% of the electricity generation was from wind, with in a sharp reduction in diesel consumption. The back-up battery system was replaced after seven years.

In another study of a predominantly handcrafts and ceramics producing Island for tourists, located in Padre Cocha village a small Peruvian village on the Nanay River, accessible only by boat is powered by PV and diesel. The installed capacity consists of Two sets of 120 2-volt lead-acid batteries with a total storage capacity of 312 kWh; 378 80-watt PV panels, with a total rated peak power output of 30.2 kW, 128 kW diesel generator, an inverter, electronic control units and other balance-of-plant.

The Island of with 631 inhabitant Ramea, located off the southwest coast of Newfoundland and accessible only by boat, migrated to renewable energy as the main power for the island, after the huge consumption of 1 million litres of diesel per year. An installed electricity capacity of 1.1 MW, consisting of three 100 kW Northwind wind turbines, a Hydrogen electrolyser, with a rated power input of 162 kW, three tanks for Hydrogen storage, with a total capacity of 1,000 m^3 at 235 psi Hydrogen-fuelled generators (total rated power of 250 kW) and Energy management system to provide automated monitoring and control.

Finally, the Island of San Juanico as a small fishing village on Baja California Sur in Mexico migrated to renewable energy providing 24 hours power. The Island electricity consisted of 17 kW PV array, A flooded lead-acid battery bank, ten wind turbines, with a total rated

capacity of 70 kW and 80 kW diesel generator. The system worked for 2.5 years and the inverters, a prominent point of failure, was replaced. The system worked sustaining the inductive load from refrigerators and fans and the inhabitant of the Island were very pleased with the energy system.

2.2.2 Challenges and gaps in the past and current island energy systems

The major challenges with these energy systems are overall system control and operation challenge, and getting the various components to integrate into whole and optimize their operation is time consuming some time a herculean task. The systems are often not fully automated. In addition, there has been shortage of highly trained operations personnel, which are not readily available in rural area.

Also, the importance of testing and fine-tuning innovative technologies before sending them out into the field, particularly for remote applications, the availability of trained personnel, spare parts and technical support is limited, it is essential that attention and time must be spent ensuring that all the subsystems of the energy systems are working properly before it is sent out for installation in remote locations.

The problem of overcharging event leading to overheating of the electrolyte, which in turn damaged the cell stack membrane can be avoided if intelligent charging algorithm is deployed for charging batteries. Installations should be located away from salt water and dust as several of the wind turbines suffered from failed alternator bearings. Remote monitory system and proactive maintenance of the inverter that suffered from several minor issues, which is often responsible for extended downtimes must be installed. This will help the onsite maintenance staff without the technical expertise to fix the inverter, trouble-shoot with remote instruction from the expert.

2.2.3 Solutions and how to bridge the perceived gaps in island energy systems

The simplest way forward is to understand the nature of the remote location from the perspective of logistics and support. These provides foundation for driving a focus on robust technical solutions that are tried and tested. It is important that the right balance between islands being excellent test beds for emerging technologies and the risk of an asset failure and the impact this can have on system performance, is established.

The system must be understood on the basis of whole system operations and not just individual or part of the system. The implication of this is that there should be emphasis on the full delivery system, including power and, of course, a fully scenario-tested control system with adequate interlocks rather than just focusing on the storage technology. There will invariably be a single point of failure that cannot be avoided. In such a situation, redundancy should be created with several small inverters.

The components or element constituting the power system are always equipment from original equipment manufacturers. These manufactures suppliers these elements directly or indirectly, working with experienced suppliers is also necessary as they provide a rule of thumb that guides installers and system integrators. Delays are uncommon in supplying components, for instance, wind developers will always like to see 1,000 units in the group before they make a wind turbine order because of economic-of-scale. This is not possible with island systems, and particularly storage. It cannot be emphasised enough that working with supplier who has worked in this space before and solved remote area location issues are as important as the technician. Also, remote monitoring and telemetry of system was found to be critical for identifying operational problems before they led to a system shutdown. An overall new hybrid power system must be designed and optimized with consideration for wind speed, average load power, load power profile, diesel generator output and battery bank capacity to evaluate the system behaviour and interactions.

2.3 Standalone hydrogen energy system

2.3.1 Past, current state and case studies

NEMO- Finland (Vanhanen, 1996) is a photovoltaic array with 1.3 kW peak, 0.8 kW alkaline electrolyser, a pressurised steel vessel at 25 bars with hydrogen capacity of 200 Nm^3, a 0.5 kW phosphoric acid fuel cell and a 12kWh lead-acid batteries. System degraded after 2000 hours as a result of crude ON/OFF bang-bang control. Robust control and optimisation studies were later recommended to minimise power consumption by auxiliaries.

Self-sufficient House in Freiburg-Germany (Voss et al., 1996), a photovoltaic array with 4.2 kW peak, 2 kW PEM electrolyser, a pressurised steel vessel at 28 bars with hydrogen capacity of 400 Nm^3, a 3.5 kW PEM fuel cell and a 20 kWh Lead-acid batteries. Loss of system battery capacity after 3 years as a result of crude ON/OFF bang-bang control. An advanced control and optimisation studies was later recommended for the battery state-of-charge (SOC).

SAPHYS- Italy, Norway and Germany (Galli et al., 1997), a photovoltaic array with 5.6 kW peak, 5 kW PEM electrolyser, a pressurised steel vessel at 200 bars with hydrogen capacity of 120 Nm^3, a 3 kW PEM fuel cell and a 51 kWh Lead-acid batteries. Both electrolyser and plant efficiencies were encouraging and compare well with other experimental studies. However, faults were in auxiliary equipment required for system operation such as compressor air treatment and inert gas were responsible for plant shutdowns.

Trois Rivieres- Canada (Agbossou et al., 2004), a 10 kW peak wind turbine, a photovoltaic array with 1 kW peak, 5 kW Alkaline electrolyser, a pressurised steel vessel at 10 bars with hydrogen capacity of 40 Nm^3, a 5 kW PEM fuel cell and a 42 kWh Lead-acid batteries. An

autonomous renewable energy system operated on a DC bus. The most successful because of good automatic control, and standard for this research work, though the control architecture not mentioned.

INTA-Spain (Schucan, 2001), a photovoltaic array with 8.5 kW peak, 5.2 kW Alkaline electrolyser, a pressurised steel vessel at 200 bars with hydrogen capacity of 9 Nm^3, A metal hydride with hydrogen capacity of 24 Nm^3 (maximum of 10 bars) and a 10 kW phosphoric acid fuel cell. System component were integrated on a DC mini-grid, electrolyser was powered by either direct connection to PV array or through MPPT or a power supply. The pneumatic water feed pump was the only component that was responsible for periodic malfunctioning of system.

SCHATZ-USA (Schucan, 2001), a photovoltaic array with 9.2 kW peak, 6 kW Alkaline electrolyser, a pressurised steel vessel at 8 bars with hydrogen capacity of 60 Nm^3, a 1.5 kW PEM fuel cell and some Lead acid batteries with capacity of 5.3 kWh. Electrolyser was connected directly to PV array. Frequent shutdowns were caused by a hood error cause by a defective switch. The electrolyser required extensive inspections and maintenance.

2.3.2 Challenges and gaps in the past, current standalone hydrogen energy systems

The standalone hydrogen energy systems discussed above were prone to failure because the systems were not operated on the firm foundation of system thinking, that is as a whole with interactions, interdependency and feedback. Also, control at the system level was missing in all of the installation except the Trois Rivieres (Agbossou, et. Al, 2001) - Canada system, which was a fully automation based system. In the final analysis, attention to balance of system components such as, switches, valves, compressors and pumps were missing and these often becomes potential failure points.

The standalone hydrogen energy system is also prone to fluctuating or intermittent power generation from wind, solar radiation and unpredictable consumer load profile. In small scale hydrogen standalone energy system are characterised by small buffers and prone to instability and reduction in system efficiency due to low system inertia. The following challenges emerges, power quality due to frequency or voltage control, response time of elements in the integrated system requires careful control, fluctuation in generation and load profile, long-term energy storage, secured supply and progressive load growth due to an increasing demand.

2.3.3 Solutions and how to bridge the perceived gaps in standalone hydrogen energy systems

The solution to the challenges highlighted in section 1.4.2, are intelligent load control and energy storage viable solutions. The intelligent load control can be implemented at the supervisory control level, through specification of priority load, essential load, and non-essential load. The priority load can come on during excess generation and turn-off when demand far exceeds supply. The other solution is to enable hydrogen long-term storage when supply is far in excess of demand and have the necessary buffer for the system inertia to balance the mini-grid when supply falls far below demand.

2.4 Combined cooling heating and power hydrogen energy system

Combined cooling, heating and power (CCHP), is a cogeneration system derived from combined heat and power (CHP). It is a proven and reliable technology with more than 100 years history, which was utilized mainly in large-scale centralized power plants and industrial applications. In some literatures, CCHP is also trigeneration system. The innovation here is the inclusion of hydrogen storage and the electrolyser, hence the term hydrogen combined cooling heat and power system. The past, present and future development in CCHP forms the themes in the next section.

2.4.1 Past, current state and case studies

The development of combined cooling heating and power system is based on a continent from North America, Europe, Asia and the Pacific and the other countries. The historical development of CCHP in America can be traced back to 1978, when the Public Utility Regulatory Act was enacted (PURPA). Soon after the PURPA was enacted, the installed capacity stood at 12 GW in 1980 with an annual average growth rate of 2.2 GW, as stated in the work by Chenzhang (2003); Laiter et al., (2000); Lemar & Honton (2004). The installed capacity reached 45 GW and increased to 46 GW in 1998. In 1999, the Department of Energy, the Environmental Protection Agency and the Combined Heat & Power Association proposed a CHP challenge to boost its installed capacity. The collaboration produced the combined cooling heating and power building vision 2020 initiative, which increased the installed capacity from 46 GW in 1998 to 92 GW in 2010. The overall objective is for a 25% application of CCHP in existing building and 50% in new constructions. In the United States, CCHP has been proven to minimise or even eliminate major black-out as a result of outages and terrorist attack on power system infrastructures (WADE, 2003; WADE, 2004; Reicher 2004).

In Europe, the development of CCHP is rather diverse because of the complex government and political structure. Consequently, different member states had to develop their CCHP

market independently. The market share of CCHP in Europe is only 9% which is rather poor compared to their American counterpart. To overcome the low market share, a strategic plan was proposed with a target of 18% by 2010 (ESD COGEN Europe et al., 2001; Minett, 2003; Chenzhang, 2003). The Netherlands and Denmark outshines the other countries with a 55% of their total electricity installed capacity coming from CCHP. Finland is next with 40%, Austria with 30%, Italy with 25%, Germany, Spain and Portugal at 20%, the UK at 15%, Sweden at 12% Belgium and Ireland at 10%, France at 8% and Greece at 5%. The studies were conducted between 1999 and 2010 (COGEN Europe, 2001; COGEN guide Europe, 2001; COGEN Europe, 2002; WADE,2003; Loffler, 2002; Taylor, 2004; Fazekas, 2004; DEFRA, 2004). There is a huge potential for CCHP in member countries in the European Union with low percentages installed capacity, though a lot of effort is being deployed to address seemingly small penetration of CCHP.

In Asian and the Pacific, China CCHP commenced in 1980 with an installed capacity of 3.1 GW which is expected to grow annually with 620 MW for industries, 2000 MW for cities in the North and 500 MW for new industrial areas in the south of China (COGEN China, 2001). In Japan, 2915 CCHP units with combined capacity of 1429 MW for commercial application and 5074 MW for industrial use (Japan Cogeneration, 2003). India CCHP cogeneration market is driven by the huge industrial sugar cane production, specifically the by-product bagasse-based cogeneration. The large scale production of bagasse from sugarcane has led to 87 new spin-off distributed generation (Smouse et al., 1998; Casten, 2004). A total of 710 MW came from sugarcane waste and is projected grow to 15 GW with 2 GW already installed. Russia dominate the CCHP space for the rest of the world, with a 30% of its total electricity installed capacity reaching a whopping 65 GW annually (WADE, 2004). In the Middle East, the impetus to develop CCHP is lacking because of the abundance of crude oil. However, pollution and environmental concerns will eventually drive CCHP application into mainstream electricity generation (Jaber and Probert, 1999). Brazil is considering CCHP with Fuel cell connection to an absorption refrigeration system for buildings in the energy market. The Brazilian gas companies have proposed and targeted a new entry into the CCHP market (WADE, 2004). In Africa, CCHP penetration still remain elusive because of poor electricity infrastructure. However, small scale distributed CCHP provides power to remote areas, rather than large centralised power plant (Joseph and Roy-Aikins, 1995). The current West African Pipeline gas line will be the enabler for CCHP penetration in no distant future in sub-Saharan Africa. South Africa power is predominantly driven by 93% coal and the capacity of distributed Energy Resource is only 0.5 GW, which is 1.4% of total installed capacity, put the development of CCHP in its infancy. The potential for CCHP in Africa is huge, despite the current challenges.

2.4.1.1 Types and scales of CCHP

In a reports by Shipley and Neal (2000); WADE (2002) decentralised energy resource (DER) can be divided into two; the classical large-scale CCHP applications (mainly CHP systems without cooling) which is common in centralized power plants or large industries; and the somewhat small throughput distributed CCHP units with advanced prime mover and thermally activated technologies to meet multiple energy demands in commercial, institutional, residential and small industrial.

The scale or sizes of a CCHP systems can cover a broad range from 1 kW to 500MW. In centralized power plants and industries making use of cogeneration, the size can exceed 1MW. The scale of distributed CCHP systems ranges from as small as 1 kW in domestic dwellings to more than 10MW in hospitals or university campuses, and as much as 300MW to supply energy to a district of a city (Ackermann and Anderson, 2001; RDC, 2001). In another classification size of CCHP under 1MW is regarded as small-scale, Mini-scale is under 500kW and micro-scale is under 20 kW (COGEN guide Europe, 2001).

2.4.1.2 Prime movers in CCHP

In every CCHP system, prime movers clearly play the most important components; they are the heart of CCHP systems and, to some extent, they drive the system possibilities and availability of other dependent technologies. Prime movers are classified based on fuel used, technical maturity, market shares or capacity range. They are either conventional prime movers such as reciprocating internal combustion engines, steam turbines and combustion turbines; gas driven such as fuel cells, Stirling engines and micro-turbines (COGEN guide Europe, 2001; IEA, 2002; Navarro and Diaz, 2004). The prime movers considered in details in the section that follows.

2.4.1.2.1 Steam turbines

Steam turbines have come a long way in power generation, a ubiquitous Rankine cycle device used in converting steam power to mechanical energy in combustion and nuclear power plant. This mature device can be classified into two; backpressure turbines and condensing turbines (Gu, Ren, Gao, & Ren, 2012). The backpressure turbines work with an outlet pressure at least equal to atmospheric pressure, and are suitable for locations with steam demand of intermediate pressure. Condensing turbines have the advantage of changing electrical and thermal power independently and they work with an outlet pressure below atmospheric pressure. Steam turbines designed with a suitable boiler can operate as a multi-fuel system. They are reliable and can work for a long time before maintenance. They are however, prone to low electrical efficiency, slow start-up time, and poor partial load performance.

2.4.1.2.2 Reciprocating internal combustion engines

These engines are established technology which outshines the other prime movers in terms of lowest initial capital outlay and spans a range of sizes. Reciprocating internal combustion engine are classified based on their ignition engines, which could be spark or combustion. The spark are driven by natural gas, biogas and landfill gas while the combustion ignition are driven by diesel, biodiesel and heavy oil. They are the most widely used prime movers for power below 1 MW, as they have fast start-up. They are however, characterised with high vibrations.

2.4.1.2.3 Combustion turbines

These turbines are only applicable for large scale cogenerations as they have high reliability at high power range. They are not suitable at power below 1 MW as a result of their low electrical efficiency and high cost per kW of electrical power output. They are much easier to install in comparison to steam turbines, occupy less area, maintenance cost less than reciprocating engines, lower emissions compared to reciprocating engines. They are also used as intermediary in supplementary firing technology to increase the steam temperature from typically around 540 ^{0}C to 1000 ^{0}C. This often called Combined-Cycle gas turbine (CCGT), characterised with high electrical efficiency of 35-55%. They are however, most suitable for high-end fuel like natural gas. The high temperature operating range makes them expensive as they require special material for their construction.

2.4.1.2.4 Micro-turbines

Micro-turbines are scale-down version of combustion turbine, driven by natural gas, diesel, gasoline and biogas (Wu & Wang, 2006). The technology is interesting as they are characterised with only one moving part, use air bearing and have very high rotational speed of 120,000 rpm. They can be combine or cascaded to large scale. It is a new technology and still being developed. They are used in distributed generation to produce power for residential, industrial, institutional and commercial use. The temperature is tolerable as result low pressure steam and domestic hot water can be obtained on-site.

2.4.1.2.5 Stirling engines

Stirling engines are external combustion engines, which have been proven to driven by almost any fuel. One of the major advantage of this technology is that the emission and noise can be controlled because of its external combustion nature. They also have less moving parts which result in less wear and reduced vibration of the parts. The technology is still evolving with a lot of research and development. It is a promising technology for combined cooling heat and power for portable and residential trigeneration owing to their

small footprints. They have been used successfully in solar thermal dish for converting the mechanical power form the turbine in the power block to electrical power.

There are currently, Stirling engine reverse cycle for refrigeration with a linear actuator in the sol call cryocooler. The gap that this thesis wishes to address is to operate the engine both in the forward cycle for electric power and reverse cycle for cooling in a trigeneration hydrogen combined cooling heat and power system. There are three major types of Stirling engines, defined by their kinematics; the traditional; alpha, beta, gamma; Non-traditional; Rotary, Fluidyne, Ringbom, Franchot, Free piston, Flat and Thermoacustic Stirling engines. According to Wikipedia, (2016) the alpha configuration has two power pistons, one in a hot cylinder, one in a cold cylinder, and the gas is driven between the two by the pistons; usually in a V-shape with pistons connected at the common point on a crankshaft. In the beta configuration a single cylinder with a hot end and a cold end, containing a power piston and a displacer drives the gas between the hot and cold ends. The gamma configuration has two cylinders one containing a displacer, with a hot and a cold end, and one for the power piston. The two cylinders are connected to form a single space with the same pressure in both cylinders. The pistons are usually in parallel and connected 90 degrees out of phase on a crankshaft. The Free Piston is without a piston but rather contain a diaghrams with energy increasing and decreasing by an electrical actuator such as linear actuator, dc motors or pumps.

2.4.1.2.6 Fuel cells

Fuel cell are electrochemical devices which take hydrogen and oxygen and convert them into water, heat and direct electrical current using membrane redox reaction/separation in the gas diffusion layer. They are silent, small foot-print device without moving parts. They are currently deployed in portable and stationary applications. There are five types of fuel cell; Proton Exchange Membrane Fuel cell (PEMFC), Alkaline Fuel Cell (AFC), Phosphoric Acid Fuel Cell (PAFC), Molten Carbonate Fuel Cell (MCFC) and Solid Oxide Fuel Cell (SOFC). The PEMFC are small and can adjust variable power, limited by low temperature and expensive platinum catalyst and requires high purity hydrogen and oxygen. They are suitable for small-scale CCHP because of their low quality waste heat by products. The AFC have been deployed in space mission which require strict and stringent design requirements and have the characteristics of low temperature, rapid start-up and high system efficiency of about 70%. They are however, prone to high purity hydrogen fuel and conversion of carbon dioxide into carbonate electrolytes that are less conductive. PAFC is the most robust of the fuel cell technologies as it can take various fuel sources such as natural gas, LPG and methanol. The catalyst is less expensive compared to the other Fuel cell technologies. They have less system efficiency and a corrosive acid electrolyte. The PAFC are ideal for small

and medium scale CCHP in hospitals, hotels and airports. The MCFC utilise a mixture of molten salts of lithium carbonate and potassium carbonate, a chemically aggressive mixture that introduces strain and wear on the cell materials making it more expensive than SOFC and PEMFC. They withstand high temperatures which make them suitable for baseload in national grid networks and heavy industries. In SOFC, all materials are solid states ceramics stable, robust, multi-fuel based and high operating temperatures that eliminate the use of catalyst. The SOFC can be deployed for continuous and stationary application for CCHP of up to 5 MW with system efficiency of 60%. SOFC are however expensive compare to the other Fuel cell technologies.

2.4.1.3 Thermally activated technologies

Apart from the prime movers, in every CCHP systems thermally activated components provides heating, cooling and sometimes dehumidification for space air-conditioning. They are a major subsystem in the CCHP system and contribute in no small measure to the overall system efficiency of a CCHP. The thermally activated technologies can be absorption chillers, adsorption chillers and desiccant dehumidifiers.

2.4.1.3.1 Absorption chillers

Absorption chillers according to Kim & Ferreira, (2008) are proven thermally activated technologies with evaporator, absorber, generator, condenser, pumps and expansion valves. It is similar to vapour compression heat pump except that the temperature of the working fluid is raised by heat from prime movers, solar flat plate and parabolic trough as against rotating device in vapour compression refrigerators. In the absorption refrigeration cycle, the working fluid vapour from the evaporator is absorbed in the absorber into a liquid absorbent. A pump transfers the weak absorbent working fluid to the generator where the heat from the prime mover or solar parabolic trough release the refrigerant from solution by stripping. The refrigerant vapour is condensed in a condenser and enters the expansion valve and back to the evaporator and the cycle continues. The absorption chiller can be single effect, double-effect or tipple-effect. There are 40 refrigerant compounds and 200 absorbent compounds as reported by Srikhirin et al., (2001). The most commonly used working fluids are water/NH_3 and LiBr/water. The working fluids in both water/NH_3 and LiBr/water absorption refrigeration are both corrosive and toxic at high temperatures for double and triple effect absorption chillers, sealing problems for high vacuum pressures operation. The high toxicity/inflamability, corrosion of copper and brass and the high capital outlay affect the high penetration of ammonia refrigeration.

2.4.2 Adsorption chillers

Adsorption refrigeration technology was first conceived by Faraday in 1848 (Critoph and Zhong, 2005) and the first refrigerator based on Silica gel-SO_2 working pair with evaporation temperature from 0^0C to -60^0C was credited to Hulse, (1929). Adsorption is the adherence of an ion to the surface of a solid absorbent. In adsorption cooling, a thermally driven or enabled bed of solid absorbent is used to compress a working fluid or refrigerant to the surface of an absorbents. It can be single effect, double or triple effect. There are two broad types of absorption refrigeration working pairs; physical adsorption pairs and chemical working pairs. The physical adsorption pairs are zeolite-water, activated carbon-methanol, activated carbon-ammonia and silica gel-water. The chemical working pairs are metal hydride-hydrogen and metal chloride-ammonia. There currently challenges with existing adsorption chillers, such as low thermal conductivity of absorbent, low cycle mass of working pair and vacuum condition. The vacuum condition often poses a serious maintenance problem with water and methanol as working fluids. The overall thermal performance with respect to the coefficient of performance can improve with control strategies and optimisation. They are used with to provide cooling power in small range of 10-200 kW for small scale CCHP systems. An extensive treatment of thermal activated technologies is well documented in the work of Deng, Wang and Han, (2010).

2.4.3 Challenges and gaps in the past, current state of combined cooling heating and power hydrogen energy systems

From the foregoing, there are gaps in the current CCHP systems in terms of the size of the prime movers, initial capital outlay, fuel input to the prime movers, and working fluids/absorbent in the absorption and adsorption refrigeration cycle. Also, a control and optimisation framework for coefficient of thermal performance improvement requires addressing as a research problem.

2.4.4 Solutions and how to bridge the perceived gaps in combined cooling heating and power hydrogen energy systems

In mitigating the perceived gaps, new materials such as carbon nanotube, and graphene could fill in the gaps for high absorption and adsorption surface. The low thermal conductivity of the current absorbent can be substituted with graphene, an emerging material with incredibly high thermal conductivity. The glycols blended with carbon based material could act as a complex matrix for compound absorbent. In addition, an optimisation driven model based control strategies with a supervisory logic higher level control can improve overall system level performance of the CCHP. Finally, Stirling engine as prime mover, especially the free piston and the thermoacoustic type can be design for

cooling, power and heating with hydrogen from renewable energy. The adsorption refrigeration and interesting and attractive technology that can be in the loop to augment the Stirling engine cryocoolers.

2.5 Sizing of combined cooling heating and power hydrogen energy system

The importance of sizing in any energy or power system cannot be overemphasised. It is the starting point as this will ensure that the parts, components, subsystems are not undersized or oversized. In energy systems, oversizing has cost penalty and undersizing has system reliability and failure consequences.

2.5.1 Past, current state of HCCHP sizing and case studies

Sizing a power or energy system sought to obtain the optimum parts, components and subsystems in the overall system, which would eventually operate as a whole. In a HCCHP, the parts, components and subsystem in the overall mix, such as prime mover, thermally activated subsystem, hydrogen electrolyser, hydrogen storage, heat storage tank and other auxiliaries must determine for expandable load or fixed load. Currently there are literature on sizing CCHP, adopting a wide variety of methodology. In a study conducted by Li et al, (2006) a comparison was done to compare CCHP with a view of obtaining energy savings in heating and cooling modes in a variety of prime movers. A more residential-centric investigation, Fumo and Chamra (2010) focused on the overall efficiency of the CCHP. A parametric and techno-economic investigation of internal combustion prime mover by Onoviona et al. (2007), to establish the effect of size of internal combustion engine on the selection of electric and thermal storage for a variety of scenarios. A network flow approach of an existing micro-CCHP was used to minimise the cost of 3 base case in a 24 hours temporal resolutions by Cho et al., (2009). A benchmarking criteria for evaluating the performance of CCHP system, based on primary energy consumption (PEC), operation cost (OP) and carbon dioxide emission (CDE) was investigated by Ren and Gao, (2010); Jin, Bai and Wang, (2012). A following hybrid electric-thermal load and following electric load strategies for micro-CHP was proposed by Mago and Chamra, (2009); Mago et al., (2010). In their findings, the micro-CCHP-FHL has low sites energy consumption, primary energy consumption, operating cost and carbon dioxide emission compared to micro-CCHP-FEL and micro-CCHP-FTL.

In their 2007 study, Yang, Lu, & Zhou, used a Hybrid Solar-Wind System Optimization Sizing (HSWSO) model, to optimize the capacity sizes of different components of hybrid solar-wind power generation systems employing a battery bank. Their model was based on the Loss of Power Supply Probability (LPSP) and the Levelised Cost of Energy (LCE) model. The model considered the ability of the model to handle the power supplied to the

load and a minimal cost of investment in the wind, solar photovoltaic and battery bank. However, their models fail to account for the optimal mix of the components of the power system. A rather simple hybrid system sizing algorithm, based on the life cycle cost of system minimisation, while load power demand was satisfied without any load rejection was proposed by Li, Wei, & Xiang (2012). The study was elaborate but did account for the loss of power probability in the event of shortage of power and short fall from wind and solar and was based on battery storage. Renewable energy based on battery storage only will affect the overall system life cycle as the life of the battery drops substantially in the event of depth-of-discharge below about 50%. Another study was carried out by Koutroulis, Kolokotsa, Potirakis, & Kalaitzakis (2006) with a genetic algorithm for a wind, photovoltaic and battery system to provide power to a residential apartment. A 20-year system life cycle was proposed and round total system cost was minimized subject to the constraint that the load energy requirements are absolutely covered, resulting in zero load rejection. Again the studies considered only battery short term storage which is fragile and reduces the overall system life. An investigation by Yang, Wei, & Chengzhi, (2009) on the optimal design model for designing hybrid solar–wind systems employing battery banks for calculating the system optimum configurations and ensuring that the annualized cost of the systems is minimized while satisfying the custom required Loss of Power Supply Probability (LPSP). The system was deployed for a telecommunication remote base station. The system is still prone to system design life depreciation, since it is strictly based on short-term battery power storage.

2.5.2 Challenges and gaps in the past, current state of combined cooling heating and power hydrogen energy systems sizing

The gaps identified from the literatures cited are that individual parts, components and subsystems were not sized to ascertain if they match the load for expandable growth of the load or for a fixed system.

2.5.3 Solutions and how to bridge the perceived gaps in combined cooling heating and power hydrogen energy systems sizing

The research objective is to size the components and subsystems to meet load for short, medium and long term storage. A cost penalty and temporal constraints will be imposed on the system with a multi-criteria or multi-objective optimisation, respecting system bounds such as maximum battery strings, maximum and minimum system voltage etc.

2.6 Parabolic trough solar thermal system

Parabolic trough is a special kind of heat exchanger that convert Solar beam radiation into heat by focusing it to a line receiver or absorber. Hence, the name focal line collectors or concentrators. There are two types of solar collectors; Stationary or non-concentrating and

concentrating. The parabolic trough is a type of concentrating collector and share the same classification with parabolic dish, linear Fresnel reflector and Heliostat Central receiver. A parabolic trough collector produce heat effectively at temperature of 50^0C up to 400^0C. The trough is formed by folding a reflective material into a parabolic shape. A metal black tube covered with a selectively coated glass tube with the aim of reducing heat losses at the focal line of the folded reflective material. This is called the heat collecting element or absorber.

2.6.1 Parabolic trough PVT system

The parabolic trough is a system with subsystem such as collector (concentrator) for concentrating the parallel total radiation and focusing it as a beam, receiver (absorber or heat collecting elements) for receiving or absorbing the beam solar radiation and converting it into heat as a black body. The system also has supporting components and parts such as piping, pumps and flow meters. The collector handles the optical characteristics while the receiver responsible for the thermal characteristics of the system. Tracking is used to enhance the efficiency of the heat collecting elements and the optics of the collector. The collector shape is usually the same while that of the receiver can change as elucidated in the next section. A single axis tracking is often sufficient but controllers can be design with the supervisory logic to alternate between the tracking modes to harvest more solar energy. A gap that the thesis needs to fill.

2.6.2 Tracking of parabolic trough

The movement of the sun is followed by the collector/ receiver duo azimuthally or along the elevation. In the azimuthal mode the trough/ receiver is oriented in the east-west direction and the tracking of the sun is followed from north to south. In this mode, there is very little adjustment of the concentrator during the day as it is constantly focused to the sun but adjustment is done at the early hours of the morning at sunrise and evening at sunset. This due to the high incident angles or cosine loss. The elevation mode is achieved by positioning or aligned north-south and tracking is done east-west. The converse applies to the elevation tracking mode. The azimuthal harvest more solar radiation than the elevation. The azimuthal is more suitable during the summer as it collects more radiation than in the winter whereas, the vertical tracking mode is better in winter than in summer (Kalogirou, 1991).

2.6.3 Shapes of parabolic trough receiver

A study on the quantitative and analytical analysis of the optimum heat collecting element or parabolic trough receiver, Bennett (2008), smashed the nearly over a century and half idea that, the cross section of the heat collection tubes used at the focus of parabolic trough solar concentrators has to be circular. Although, the shape of the tube is clearly simple and easily

fabricated, it is however not optimal. The study was based on Gaussian intensity distribution, which is the fraction of solar insolation reflected from a given position on the mirror that strikes the central heat collection element. The Gaussian distribution was expressed in term of angular width, which in turns depends on the size and the shape of the receiver heat collecting elements. The focal length to diameter of the trough aperture was used to establish that 2 intersecting parabola shape with height twice the width of the intersecting parabola. The investigation is however deficient as it was based on light distribution and excludes flow distribution, thermal enhancement and the manufacturability. Energy flux distribution is a major variable in computing the optical efficiency. There are 3 approaches for computing flux distribution; the semi finite integration techniques proposed by Jeter, (1986); Zhao et al., (1994), the ray tracing formulation by Daly, (1979); Jiang et al., (2010) and the cone optics formulation of Bendt and Rabl, (1981). A detailed analytical procedure for computing the overall optical efficiency is elucidated in Huang et al., (2011).

2.6.4 Shape selection

The shape selection is based on a design optimisation approach, a more robust and detailed procedure taking into consideration the velocity and temperature flow fields, the statistical and random or uncertainty in manufacturing the shape. The shapes of the heat collecting element or receivers are obtained from a circle of 26 mm diameters and the two forms; semi-circular and triangular profile are derived from the circle.

2.6.5 Design optimisation

According to the Mathworks Inc. (2016), design optimisation represents a procedure or technique for determination of the best design parameters that meet product driven project conditions or requirement. It is also a way of looking at multiple design point spurn-off by a what-if analysis and design of experiments sampling, using a parameters correlation to screen variables that matters and affect the design space and use response surface to connect or interpolate the design point sample by the design of experiment. The optimisation iterates and select the best candidate meeting a set of multiple objectives. A robust design optimisation ensures that what is predicted by virtual CAD driven product development process works in the real world. The section that follows considers the various part of the design optimisation process and a work flow is provided in fig. 2.2.

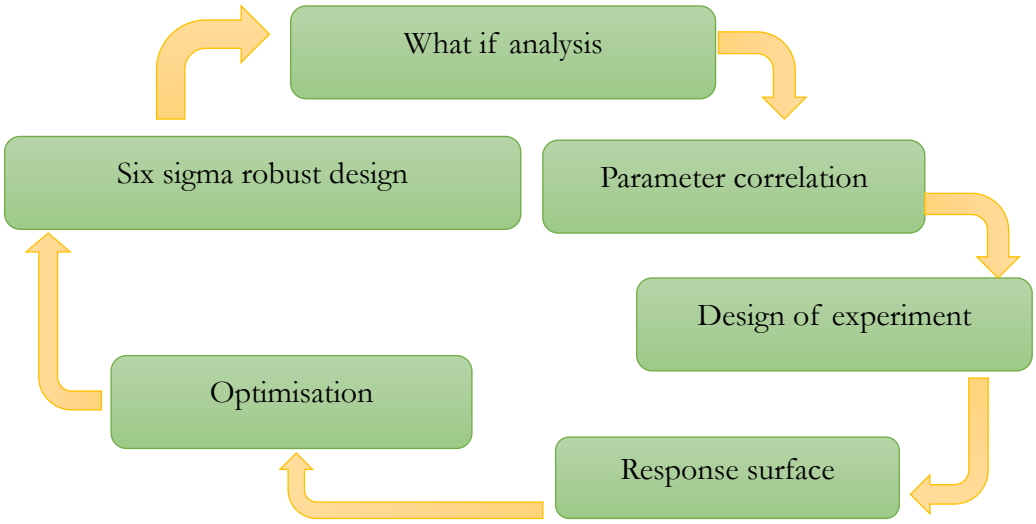

Figure 2.2 Work flow for the design optimisation problem

2.7 Dynamics of combined cooling heating and power hydrogen energy system

The time or transient change of the combined cooling heat and power hydrogen system, provides an understanding of the underlying behaviour of the subsystem. The dynamic or transient behaviour enable the insight and remove the many extraneous misconception and exposed the core of the subsystems. It makes the cause-and-effect relationship between the variables more obvious. The dynamics model of the system is the linchpin and the enabler of the control system. To sum the discussion, system dynamics is a technique of understanding the non-linear behaviour of a complex system like the CCHP over a time evolution using stocks, flows, internal feedback loops and time delays.

2.7.1 Past, current state and case studies

In a study to determine the optimal system configuration and control strategy for the HRES using multi-objective design for an isolated island, Bernal-Agustin and Dufo-Lopez (2009a) proposed Genetic algorithm to minimise cost and unmet load simultaneously. A Pareto evolutionary algorithm was applied as the main algorithm and a genetic algorithm as the secondary algorithm.

In another study Nema et al. (2009) critic the current state of design, operation and control requirements of the stand-alone PV– wind hybrid energy systems with diesel generator or grid as backup sources. The study was based on modelling of PV system, wind energy system and diesel generator with a prefeasibility analysis of hybrid system. In the pre-feasibility analysis attention was focussed on the assessment of the wind speed and solar insolation to ensure proper sizing of the equipment as well as optimisation of the sizing. Also Ender et al. (2010) put forth an interactive decision making tool for HRES portfolio planning using the system-of-systems approach.

In addition, a Multi-attribute decision making process, quality function deployment and dynamic analysis underpin by neural network surrogate modelling were also utilised. In an integrated approach Demiroren and Yilmaz (2010), using HOMER software to analyse how model from several small isolated power systems was developed by island Go¨kc¸eada in Turkey can be served with renewable energy. An interesting study was conducted by Lund (2007a) to evaluate possibility of Denmark migrating to 100% renewable energy. A number of resolutions became evident from the study based on technological changes and suitable implementation strategies: (i) replacing oil with electricity for transportation, (ii) inclusion of small CHP plants and heat pumps and (iii) inclusion of wind power in electricity supply. The three scenarios were simulated using the EnergyPLAN (Lund et al. 2007b) energy system analysis models.

In a more detailed and encompassing study Trinkl et al. 2009, investigated and optimised a heating system comprising of solar thermal collectors, heat pump, stratified thermal storage and water/ice latent heat storage systems. A system control strategy based on control model-ready model developed particularly for this project with two storage tanks, the influence of the parameter on the proposed system in terms of seasonal performance factor and maximum degree of solidification was identified by simulation. The optimal system configuration was then derived. An agent based capacity planning tool of solar energy resources using hybrid simulation was realised by Mazhari et al. (2009). The planning tool included generation and storage segments and agent based models for demand. A meta-heuristic optimisation technique was used to obtain the most economical configuration of the solar generators and storage units.

In a rather out of the box thinking, de Durana and Barambones (2009) proposed an object oriented HRES model using Any Logic for the purpose of micro-grid design and control strategies (for instance supervisory control, local decentralised control and centralised/decentralised load dispatching) analysis. Specifically, the seven object elements, the DC Bus object, aggregating all the others such as wind turbines, diesel generator, battery, PV was constructed using system dynamics approach. An interesting modelling work was investigated by Kaikko and Backman (2007) in which a component-specific models was applied to analyse the performance of a single-shaft micro-turbine in CHP. The load level of the micro-turbine is controlled by the heat demand of the system. The effect of recuperation and non-recuperated configurations and different load control methods on the technical and economic performance of the operation and the optimal sizing of the micro-turbine was investigated. A daily simulation model to analyse natural gas micro-turbine applications for a residential complex was investigated by Aguiar et al. (2007). It is also a related work as the electric and the thermal load curve of the building were investigated. The study was based on the micro-turbine configurations analysed to satisfy the entire thermal

demand and part of the electrical demand by purchasing the rest of the required electricity from the grid and to meet the electricity demand and have an excess of thermal energy.

In another related work, Takagi et al. (1999) developed a simulation model of an absorption chiller for its dynamic characteristics in order to evaluate energy consumption for the heating, ventilation, and air conditioning (HVAC) systems and the control strategies. The authors were resolute in applying FORTRAN language to simulate the model consisting of equations which describes heat transfer among the evaporator, the absorber, the generator and the condenser.

In a more fascinating work Hatziargyriou et al. (2007) used a distributed energy resources customer-adoption model (DRE-CAM) approach to select the optimal; equipment combination which includes CHP equipment and renewable sources; the corresponding operational schedules for each installed technology, to minimise the annual energy cost while meeting energy balance, and operational, regulatory, investment and storage constraints. DRE-CAM was formulated as a mixed-integer linear program and was enhanced by the incorporation of electrical and thermal storage capacities. The model was applied to a hypothetical hotel in San Francisco, to size components in the CHP.

2.7.2 Challenges and gaps in the past, current state of dynamics of combined cooling heat and power hydrogen energy systems

The challenges and gaps are still lacking except for the DRE-CAM by Hatziargyriou et al. (2007), Kaikko and Backman (2007), Aguiar et al. (2007) and Takagi et al. (1999) that included CHP, most of the surveyed research works have limited scope in terms of types of energy systems they modelled. There are still needs for modelling the detailed dynamics of the energy system with combined heat and power.

2.7.3 Solutions and how to bridge the perceived gaps in dynamics of combined cooling heat and power hydrogen energy systems

The approach identified by the literature's cited above on the dynamics of hybrid energy systems, with very few work on the combined cooling heat and power, lacked detailed analysis of the dynamic behaviour, stability, inter-subsystem interactions, fast and slow dynamics characteristics of dynamical systems and system level interaction for loop pairing and decoupling for distributed and decentralised control to be discussed in the control section. The current research main objective is to develop dynamical system models to capture these perceived gaps.

2.8 Control of combined cooling heating and power hydrogen energy system

Integration of varieties of energy sources or carriers present a daunting challenge in terms of generation, distribution and end-use application or demand-side. The coordination or management of the system resulting from the union is obligatory for the resulting system to function as a single system, irrespective of the individual subsystem. In a hydrogen combined cooling heat and power energy system (HCCHP), there are 3 transports (distribution or pipeline) system- electricity, heat and hydrogen gas- which are consequence of the cooperation of the different entities making the HCCHP system. According to Geidl et al., (2007) an energy hub interface emerges from integration of the multiple energy producers, demand and transmission infrastructure. The energy hub can be managed or coordinated either centrally or distributedly. In control system engineering parlance, the system is controlled centrally or through a distributed control architecture. The control architecture either centralised or distributed is made up of primary or low level control layer and the main or master control layer, coordinated through a hierarchical control structure.

2.8.1 Primary (low level) layer control

The primary level control algorithm resides in the parts, components and subsystem level and ensures that the generation, distribution and demand or user subsystem keep the control variables closed to the prescribed set points. The control algorithm could be the classical PID, robust, fuzzy logic, Neural Network, adaptive control, LQR, H-infinity, sliding mode control.

2.8.2 Main (master level) layer control

The main control is responsible for managing the entire system. It brings the system frequency, hydrogen volume and heating hot line temperature to its nominal value. It monitors the distributed generation system and it commands the dispatch of the desired energy output of each controllable DGS component. The algorithm could be Model predictive control and all it variant, programmable logic controller, computer area network, ZigBee communication protocol, X10 communication protocol, FPGA or Agent based control. A more detail review of the main level control will be discussed in the automation section.

2.8.3 Past, current state and case studies

Control started out as an automatic feedback system with more 2 millennium history and could be trace to the time of the earliest water clocks described by Vitruvius and attributed to Ktesibios (circa 270 B.C.). Three hundred years later, Heron of Alexandria described a range of automata which employed a variety of feedback mechanisms for the control of the complex mechanism of gigantic town clock. Feedback as control term was introduced in the

1920s by radio engineers to describe parasitic, positive feeding back of the signal from the output of an amplifier to the input circuit. Automatic control and it application to feedback fundamentally enabled automation. Feedback control was used in the ancient world for level control, water clock control and pneumatic/ hydraulic control.

The progress in control in 17th century, saw a mark improvement with system design for temperature control, mechanical control of mills and control of steam engines. The 19th century witness yet another with a significant finding that feedbacks are inherently prone to instability. A solution to the feedback instability of feedback was resolved by the brilliant independent work of Routh in England and Hurwitz in Switzerland. The technique was jointly referred to as the Routh-Hurwitz stability criteria. In the same century, the servomechanism was invented for ship steering, stabilization and autopilot. The evolution of communication as engineering tool in 1930s, provided the impetus for the 3 term control problem, with ready application in process control and gun control. This pave the way for a coherent body of classical control theory during and after the second world war in the US, UK and the rest of the world. This was followed by the concept of cybernetics, dynamic modelling, the Poincare approach and the Lyapunov stability criteria in the USSR.

The period of the cold war saw another major development in control system design with the compact state space modern control technique. The invention of state space opens up a new frontier in the development of missile technology. The post war period marked a new beginning with the discovery of digital computer, opening up new opportunities for automatic control. The first major application was in the supervisory control of the refinery in Louisiana. In the mid 60's Programmable Logic Control was developed to replace individual relays used in sequential programming. Control algorithm like adaptive control, optimal control, robust control, much celebrated Linear Quadratic Gaussian and the H_{inf} control was developed from 1960 onwards. The development of digital computer a paradigm shifts from mathematical based control system design to a rule based human language type control called Fuzzy logic control. The discovery of Fuzzy led to a new area of control called artificial intelligence. The late 1970s witness the application of Model Predictive Control in the industry. As an industrial control technique, varieties of MPC such as Model Predictive Heuristic Control or Model Algorithmic Control (MAC) (Richalet et al. 1978), the Dynamic Matrix Control (Cutler and Ramaker 1980) and the Quadratic Dynamic Matrix Control (Garcia and Morshedi, 1986).

2.8.4 Challenges and gaps in the past, current state of control of combined cooling heat and power hydrogen energy systems

The current state of control methods for distributed Energy resource as espoused by Xinhua et al., (2007) are plug-and-play technology, power electronics device and Multi-Agent based technology.

2.8.4.1 Plug and play control technology

It is a control architecture that enable the addition of signals, subsystems to existing control system running and having the system automatically utilise the new device online. It is a network control technology for medium to large-scale automation such as power plant, refineries, chemical process plant. Plug-and play is premised on semi-autonomous agent with emphasis on fault tolerance (Hangstrup et al., 1999; Rotkowitz and Lall, 2005; Khambhampati et al., 2006; Patton et al., 2006; Rantzer, 2007; Lee et al., 1995; Anderson, 2001). One of the strength of the plug-and-play control architecture is that decommissioning and system identification form scratch is not required when a new device is added to an existing control system. There are two approaches for incorporating a new device to an existing control scheme are; the sensor fusion and the Youla-Kucera parametrization of all stabilizing controllers (Dasarathy, 1994; Brooks and Iyenger, 1998; Abdelrahman and P. Kandasamy, 2003).

2.8.4.2 Multi-Agent based control technology

Agents and multi-agent systems has evolved as a new way of analysing, design and implementation of complex software system according to Jennings et al., (1998). An agent is a class of entity and not necessarily a specific object or thing as explain by Nwana, (1996). The entity notion of an agent makes it goal accomplishing and rational for it behaviour to be predicted, given a clear description of their goal. An agent is an entity that senses, think and act on its environment to realized its goal (Russel & Norvig, 1995). An agent is schematically represented in figure 3 below.

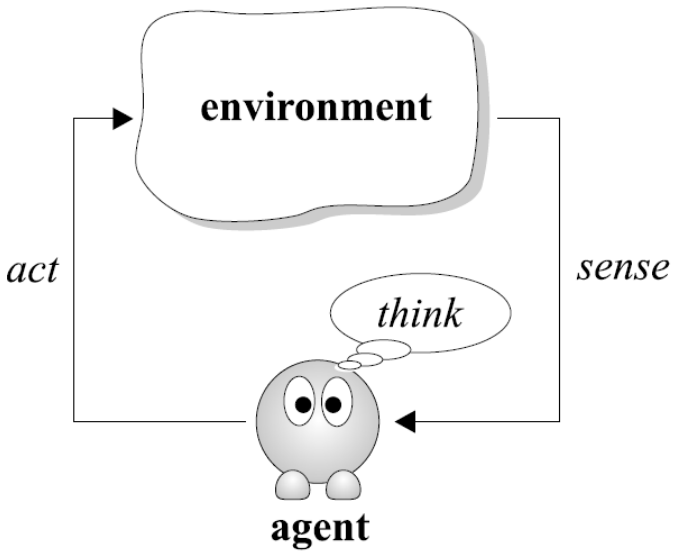

Figure 2.3 Agent from an individual point of view: an agent is an entity that senses, thinks and acts in some environment in order to realize its goal

There are 3 examples of agent that comes to mind; the ant as a biological agent, several goals of building net, sorting brood, finding food and protecting the nest. The ant communicate with other ant in a colony by means of pheromones in addition to being able to sense and act in its physical environment (Van Dyke Parunak, 1997). The second instance of an agent is Herbert a robotic agent, capable of collecting empty soda can in an office space. Herbert have sensors and actuator to detect and grab cans in its environment (Brooks, 1990). The last example is a computational agent called Sumpy, who resides in a software Unix file system with the goal of maintaining the file system (Song, Franklin & Negatu, 1996). The computational agent example is very interesting for realising a software for controllers. The ant biological agent provides a means of leaping to another level of agent because of the communication among the ants in the colony. This is a society of agent called Multi-agent system. In a more technical treatise, Durfee and Lesser (1989) see a Multi-Agent System(MAS) as a loosely connected network of problem solvers that work together to solve problems that are beyond the individual capabilities or knowledge of each problem solver. A MAS is an attractive concept for modelling a distributed system such as medium and even large scale control system. In terms of design MAS involves the distribution of tasks, information, resources and coordination. In a study Lesser (1998) postulated that agent coordination is choosing of agent activities, the ordering, and communication of the results obtained, so that an agent function effectively in a group setting. The choice the coordination mechanism given the interdependencies between agents in a MAS is of major importance, as the coordination mechanism may have a considerable impact upon the performance of the system. This provides coordination mechanism of Multi-agent system which could be; centralised, decentralised or hybrid. In a centralised coordination, a single

locus of aggregating related data/knowledge and decision-making/authority is sought. Decentralised coordination, data, knowledge and decision are separated. The hybrid coordination is in-between the centralised and distributed form of coordination. Apart from the coordination classification, MAS can be classified based on organisational structure according to Ferber, (1999). A special type of organizational structure is a hierarchical structure, which is focused on here. A hierarchical organization consists of multiple levels of organization. This means that several agents are placed into a group and interdependencies between them are handled by a local coordination mechanism. Figure 4 shows a hierarchical organized MAS. At the "bottom" of the hierarchy so called elementary agents are located.

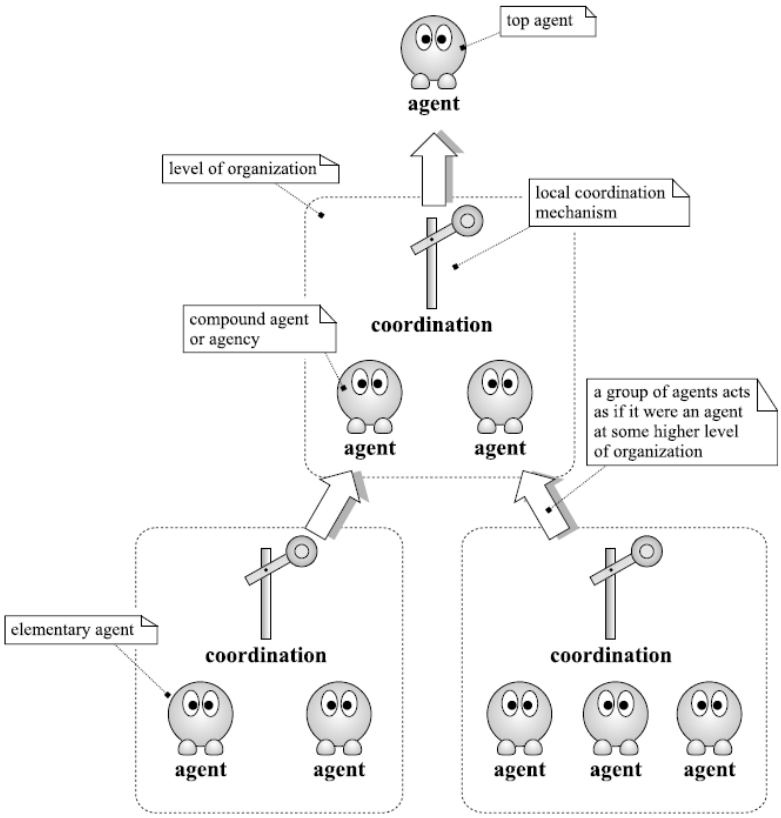

Figure 2.4 A hierarchical organized MAS (Ferber, 1999)

In terms of control, the fusion of MAS and control result in a Multi-Agent based control system, although the marriage is not as smooth as expected in terms of how both evolve. MAS focus mainly on abstract description of systems whereas control theory has a strong foundation in mathematical foundation. A variety of knowledge representations and manipulation techniques can be combined into one system (such as PID control, symbolic planning and fuzzy logic). Also, multiple communication paradigms can be used

(negotiating, poke and request messages; communicating complete data structures at the planning level and single data values at the control loop levels).

From the foregoing, control and communication and provides an avenue for mixed control. A Distributed Model Predictive Control multi-agent based control system is a growing area in distributed energy system (Alejandro, 2011). The control system was a demonstration of unique and versatile application capability of Model predictive control to even fast response electrical and electrochemical system. Model predictive control evolved as a slow response industrial control technique for thermal system with low time constant but great in handling constraint, disturbance rejection and for prediction of horizon of a process over a time evolution. In the section that follows, a review of the different flavour of distributed MPC is sought to put the thesis in perspective for a system of system discuss in chapter 5. Generally central control can be follow a centralised or decentralised control paradigm. The centralised control scheme is difficult to realise as the volume of information is large, making it unfavourable because of expensive communication and limited bandwidth. Also, conflicting design objectives of local controllers makes the design process complicated. The decision making process requires high computational power and the scheme is very sensitive to changes making it prone to instability. A decentralised approach would be preferable but there is no formal control theory, hence a multi-level hierarchy consisting of semi-autonomous agents.

2.8.5 Solutions and how to bridge the perceived gaps in control of combined cooling heating and power hydrogen energy systems

The solution to the perceived gaps is to develop a control system at the lower level for each subsystem. The control system will be realised at the subsystem level with their connections to the overall hydrogen combined cooling heat and power.

2.8.6 Automation and supervisory control of combined cooling heat and power hydrogen energy system

Coordination and organisational structure are at the heart of automation of the HCCHP. Automation is a set of technologies that results in operation of systems without significant human intervention and achieves performance superior to manual operation. It is the aggregation of various local, higher level control, coordination and organisation of the aggregate subsystems into a functional, robust and stable system. There are several studies of the organisation and coordination of the aggregate subsystems.

2.8.6.1 Past, current state and case studies

Generally speaking, large scale systems are often composed by many interacting subsystems and can be difficult to control with a centralized control structure due to the required inherent computational complexity, due to robustness and reliability problems and due to communication bandwidth limitations. Consequently, a variety of distributed control structures have been developed and applied in a period spanning four decades. Among these techniques are completely decentralized structures, distributed control systems with exchange of information among local regulators and hierarchical structures.

2.8.6.2 Decentralized control

In decentralised coordination architectures, the control (input u) and the controlled (output y) variables are grouped into disjoint sets. These sets are then coupled to produce non-overlapping pairs for which low/local controllers are designed to operate in a completely independent manner. The local controllers can be single-input single-output or Multi-input-multiple output (locally centralized) depending on the cardinality of the selected input and output groups. Figure 5 illustrate a decentralised three input (u_1, u_2, u_3)-two output (y_1, y_2, y_3) system

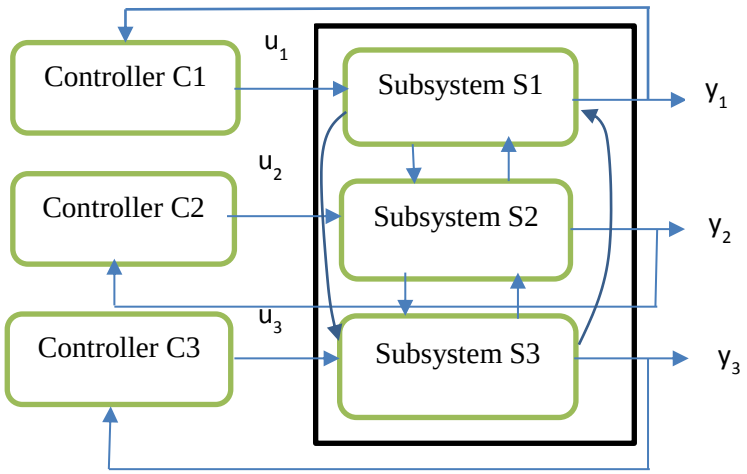

Figure 2.5 Block diagram of a decentralised three input (u_1, u_2, u_3)-there output (y_1, y_2, y_3) system architecture; The arrows in-between the subsystems S1, S2 and S3 account for interactions between systems for strong interactions that cannot be decoupled

There has been research work on decentralised control since the early sixties, such as the vector based Lyapunov functions (Siljak, 1991), sequential design approach by Hovd and Skogestad (1994), the optimization based techniques by Davison and Ferguson (1981); Scattolini and Schiavoni (1985), and the overlapping decompositions of Iftar (1993); Ikeda et al., (1984) and Ikeda et al., (1981). There are classical text dealing with decentralized

control such as Lunze (1992); Siljak (1991) and research work serving as a milestone of the time by Sandell et al (1978). Also, more recent discuss on decentralized control detailing the state of the art has been considered by the following authors Siljak (1996); Siljak, and Zecevic (2005); Bakule (2008).

2.8.6.3 Distributed control

The distributed control architecture is illustrated in the block diagram in Figure 6, show the intercommunication feedback between controllers C1, C2 and C3 in the systems consisting of subsystems S1, S2 and S3. The local/low level controllers are designed with MPC, the information transmitted typically consists of the future predicted control or state variables computed locally, so that any local controller can predict the interaction effects over the specified prediction horizon. The MPC controllers C1, C2 and C3 are designed to control the subsystems S1, S2 and S3, respectively. The communication protocol specified for the inter-control backbone bus, have a major impact of the overall system performance. The distributed architecture is classified based on the topology of the communication network and can be fully connected algorithm for information transmitted or received from any local controller. The second classification is based on information transmitted or received from any local controller as a subset of others called partially connected algorithms. Rawlings and Stewart (2008) investigated a partially connected information structure and concluded that it is convenient in the case of large scale systems as a result of a great number of loosely connected subsystems. This architecture, restrict the information exchange among directly interacting subsystems and produces a negligible performance deterioration. The transmission of data over a controller is classified into 2 protocol; noniterative algorithm protocol in which information is transmitted and received by controllers only once within each sampling time; iterative algorithm protocol involves information transmission and reception by controllers many times within a sample time. The iterative algorithmic protocol is further subdivide into; independent algorithm in which the controllers in the subsystems minimises a local performance index; the cooperating algorithm in which the controllers in the subsystems minimises a global cost function.

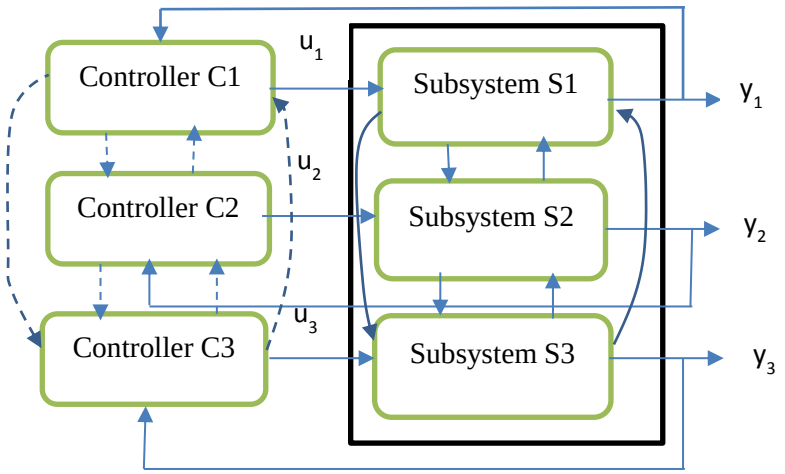

Figure 2.6 Block diagram of a distributed three input (u1, u2, u3)-three output (y1, y2, y3) system architecture; The solid arrows in-between the subsystems S1, S2 and S3 account for interactions between systems for strong interactions that cannot be decoupled; the broken arrows feedback communication between controllers C1, C2 and C3

2.8.6.4 Hierarchical control for coordination

The hierarchical control is an alternative to the distributed control schemes described in the previous section. It consists of a two level hierarchical control structure shown in Fig 2.7. In this two level control structure, an algorithm at the higher level supervises the actions of local controllers placed at a lower level, which can be classical control schemes or possibly an MPC. The design of the coordinator has been the preoccupation of control engineers for more than four decades and well documented in in the text of Findeisen et al., (1980) and Mesarovic et al., (1970). The overall system is made up of a number of subsystems connected through some interconnection in which the inputs of a subsystem are the outputs or the states of another subsystem. A system optimization problem is computed with MPC by minimizing a local cost function under local state, satisfying an input and output constraints. The procedure is concluded once the computed local solutions satisfy the constraints imposed by the interconnecting variables that is if there is coherence among the values of the interconnecting by the local controllers. Otherwise, an iterative Lagrange multipliers of the coherence constraints in the global optimization problem called price coordination method is invoked.

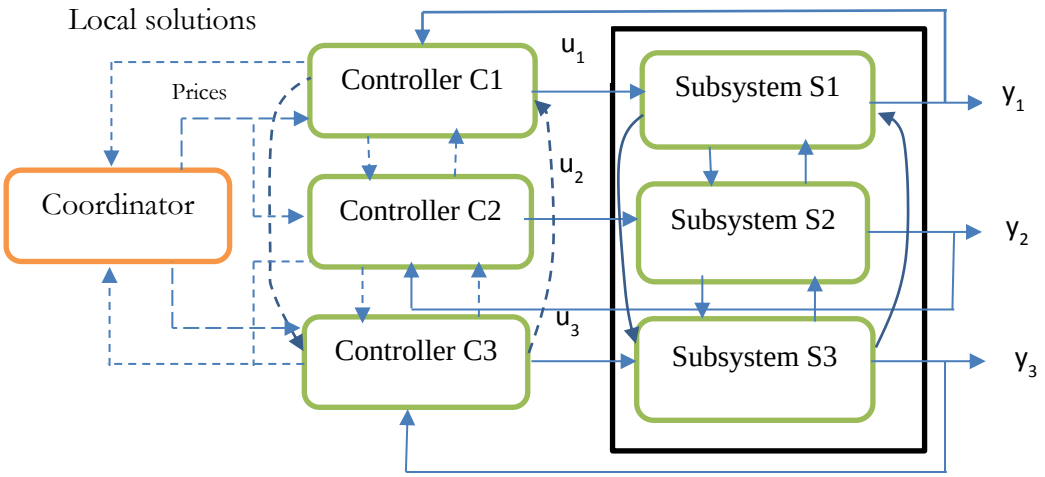

Figure 2.7 Block diagram of a Hierarchical control for coordination of three input (u1, u2, u3)-three output (y1, y2, y3) system architecture; The solid arrows in-between the subsystems S1, S2 and S3 account for interactions between systems for strong interactions that cannot be decoupled; the broken arrows feedback communication between controllers C1, C2 and C3; the coordinator or supervisor the local control action and price or the cost function of the controllers

2.8.6.5 Hierarchical control of multilayer systems

In hierarchical multilayer supervisory architecture in fig. 2.8, the control action is performed by a number of controllers working at different time scales. The approach is important from the overall process under control which is characterized by different dynamic behaviour as slow and fast dynamics, or in the case of optimization and control algorithms working at a different rates and compute the optimal targets and the effective control actions. The architecture has been applied successfully in waste water treatment plant by Brdys et al., (2008) and greenhouse control problem of Henten and Bontsema (2009). This coordination and organisational structure is well suited for distributed generation with variety of energy sources operating at different time scales.

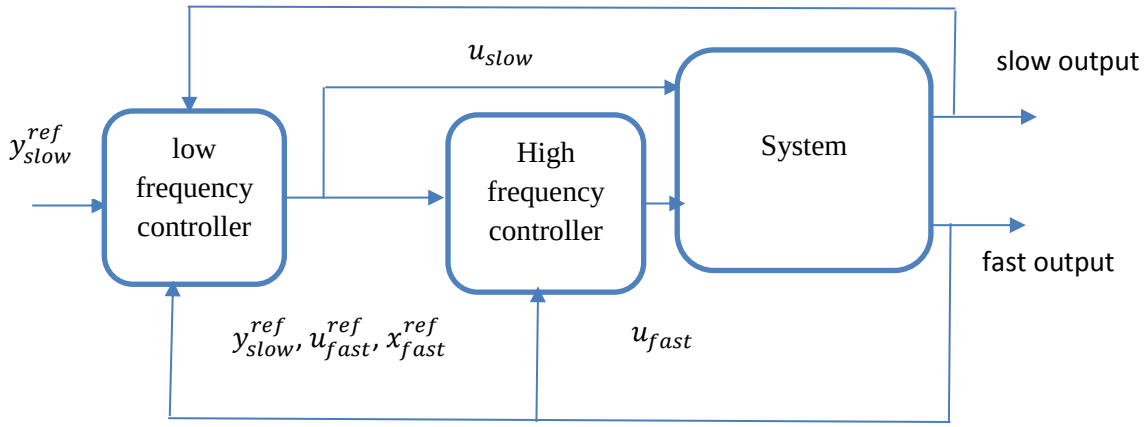

Figure 2.8 A block diagram of a system with slow and fast dynamics, the slow process is outer loop while the fast dynamics system is placed in the inner loop. The input to the high frequency control coming from the output of the low frequency controller y_{slow}^{ref}, u_{fast}^{ref}, x_{fast}^{ref} are the control output of the slow loop and input of the fast loop respectively.

2.8.6.6 Coordinated control of independent systems

The coordinated control of independent systems architecture is decoupled based dynamic subsystems, operating independently. It involves, coordinating a number of decoupled systems or agents which must cooperate to achieve a specific objective to globally minimize a cost function subject to joint constraints. Also in these cases, instead of solving a unique centralized control problem, in principle it is possible to solve a number of local optimization problems and to coordinate the local actions of the agents by means of a suitable communication bus. From the perspective of MPC, Franco (2008) investigated the coordination of independent nonlinear discrete-time systems with delayed intercommunication which also provides stability results obtained by resorting to Input to State Stability (ISS) concepts. In another study, Keviczky et al., (2005; 2006) applied an any agent node of a graph to describe a discrete time nonlinear system which knows the state of its neighbourhoods without delay. The weight of the local performance indices of the neighbourhoods and the local future control values were calculated over the specified horizon to predict the transient of the local state.

2.8.6.7 Challenges and gaps in the past, current state of automation and supervisory control of combined cooling heat and power hydrogen energy systems

Having reviewed related work on the supervisory control of large scale, in which the current work of supervisory management of HCCHP reside, some of the challenges are that new algorithms with guaranteed properties are in need in many theoretical decentralised MPC. Also, criteria for selection of control structure is required. Reconfigurable control structures

and hybrid systems are required, especially a mix of the plug-and-play control with distributed and hierarchical architecture. Optimization methods for distributed and hierarchical MPC are still lacking and required attention both at the academic and industrial level. System partitioning method such as relative gain array, state space gramians, temporal and model reduction are not sufficient and new approach tailored specifically for distributed and hierarchical control systems with MPC are required. Finally, Synchronization and communication protocols also require attention (Negenborn, 2007).

2.8.6.8 Solutions and how to bridge the perceived gaps in automation and supervisory control of combined cooling heat and power hydrogen energy systems

In this research the hypothesis would be that a supervisory logic controller would be able to manage the subsystems in the HCCHP energy system. The work will contribute to this using finite state machine control theory, model-based design and discrete event to address some of the challenges identified in the previous section.

2.8.6.9 Finite state machine

According to the free online Wikipedia (2016) a Finite-state machine (FSM) or finite-state automaton (FSA) is an abstract machine that can be in one of a finite number of states. The machine exists in only one state at a time and the state it is in at any given time is called the current state. It can change from one state to another when initiated by a triggering event or condition called a transition. A FSM is defined by a list of its states, and the triggering condition for each transition. The coordination or supervision can be implemented using other methodology and this will be discussed further in chapter 6.

2.8.7 Hardware-in-the Loop in combined cooling heat and power hydrogen energy system

In control system design especially rapid prototyping, the model of control system as an executable specification must be tested on a real hardware to ascertain system level performance in rea-time or true-time corresponding to the actual time. Hardware-in-the-loop (HIL) simulation is a methodology used in the development and testing of complex process systems. HIL simulator is a setup that prototypes parts of a given system in hardware and virtually emulates the rest while maintaining bidirectional information flow between these physical and virtual subsystems. The more traditional application of the HIL concept is controller design and testing, in which a control unit in hardware is integrated with virtual models of the devices and systems being controlled.

HIL simulation provides an effective platform by adding the complexity of the plant under control to the test platform. The complexity of the plant under control is included in test

and development by adding a mathematical representation of all related dynamic systems. These mathematical representations are referred to as the plant simulation. Hardware-In-the-Loop is a form of real-time simulation but differs from real-time simulation by the addition of a real component in the loop. This component may be an Electronic Control Unit (ECU) such as microcontrollers, processors with a real time kernel. The purpose of a Hardware-In-the-Loop system is to provide all of the electrical stimuli needed to fully extend the functionality of the ECU. In this way you the ECU fool into thinking that it is indeed connected to a real plant. The main purpose with the HIL Simulation is to test the hardware device on a simulator before we implement it on the real world.

2.8.7.1 Past, current state and case studies

HIL evolved from a testing procedure developed by the aviation, though it becoming prevalent in other industries. The technology has a 2-decade history and provides a quick time to market and deploy systems with complex algorithms. As a testing, validation and verification tool, it plays a unique role in the development of automotive safety systems, powertrain controllers, unmanned underwater vehicles and defence system. It is has received global acceptance industry as attested by the following authors Anakwa et al., (2002); Boot et al., (1999) and in the academia as reported by Anakwa et al., (2001); Grega (1991); Temeltas et al., (2002).

2.8.7.2 Challenges and gaps in the past, current state of HIL in combined cooling heat and power hydrogen energy systems

The application of HIL in the testing and validation of a microCHP was reported by Wessam, et al., (2016), which is the most recent in the field of combined heat and power system. In this system, a Stirling engine based micro CHP, Whispergen 1 kWe-14.5kWth, is used along with an 800 litre heat buffer storage in a simulation loop for a single family house, room temperature controller, and the micro CHP controller. The hardware data acquisition system is based on LabVIEW, while the single family house, temperature controller, and micro CHP controller have been modelled in SimulationX, a Modelica based software. A Matlab was developed to act as a communication manager between the two programs, LabVIEW and SimulationX. The effect of the thermal comfort on the occupant was evaluated. The challenge with the current system LABVIEW in the loop, the cost of the hardware is astronomically high and the system response under the software can be high and may not capture the overall system dynamics.

2.8.7.3 Solutions and how to bridge the perceived gaps in HIL in combined cooling heat and power hydrogen energy systems

The solution to the challenge identified with the system deploy for the microCHP is to implement the system in a single platform that support C code for code generation. In this thesis, MATALB and all it supports blockset is proposed for the testing of the HCCHP system.

2.8.8 Investigation and thermal management of solar thermal PVT parabolic trough system using non-contact infrared computer thermography

Infrared measurement of solar thermal system is still a new area and the application is not as ubiquitous as other measuring techniques. The challenge with the conventional measurement techniques is that contact is required and large number of sensors are required to track the temperature signatures of the receiver. Infrared thermography shines in this light as it is a non- contact method.

2.8.8.1 Past, current state and case studies

The importance of infrared thermography as a contactless measurement technique cannot be overemphasized. The technique is attracting attention as friendly means of measuring temperature. The historical, current and applications are addressed as follows;

2.8.9 Historical development of infrared thermography

The development of infrared technology is premised on the accidental discovery of infrared portion of the electromagnetic spectrum by Herchel, while searching for an optical filter material for reducing the brightness of the sun image in telescopes during solar observation. This discovery laid the foundation for infrared thermometry, though thermometers, as radiation detectors, remained unchallenged until 1820, coinciding with the same time the discovery or invention of thermocouple. The thermocouple measurements techniques were extended by Melloni, after connecting a number of thermocouples in series to form the first thermopile, with sensitivity 40 times that of the best thermometer available for detecting heat radiation.

The advances in thermocouple sensitivity was soon followed by the invention of bolometer, a thin blackened strip of platinum connected in one arm of a Wheatstone bridge circuit located at the focal point of the infrared radiation. This arrangement provided the infrared measuring system the capability of detecting heat from a distance as high as 400 meters.

The period spanning the two devastating world wars, precisely between the 1900 and 1945, saw the military taking advantage of this seemingly scientific and peaceful technology to another level of tactical military experimental system for enemy intrusion/detection, remote

temperature sensing, secure communications and flying torpedo guidance systems for submarines underwater monster. This was chronicled by infrared advanced search system capable of detecting an approaching airplane at a distance of 1.5 km and a person more than 300 meters away.

The invention of the bolometer as an electronic long distance measurement system, was also exploited between the end first world war and the beginning of the Second World War, saw the development of yet another piece of Military war artefact called the image converter and the photon detectors. These two gizmos revolutionize the infrared measurement and sensing systems, as the image converter attracted tremendous attention, providing a means of clear visibility in the dark but was discontinue because it gave the military observer away too in trying to have a visual of an enemy. The historical development of the infrared thermography will provide the necessary basis for exploring the current state of development of this versatile method in solar thermal application as an emerging non-invasive method of measuring and tracking temperature trajectories in solar receiver. These in highlighted in the next section.

2.8.9.1 Current state of infrared thermography in solar thermal energy system

The grand challenge is on how to establish the most appropriate, experimental device, and computational method to absorb or capture sunlight and heat from the sun and convert it into energy in form of thermal heat storage and electricity to drive human satiable appetites for energy, especially with the growing climate change problem caused by conventional energy production process. It is a known fact that, day in and day out, the sun is shining in the sky. Its rays transmit light and heat to Earth and the total of this energy surpasses global energy consumption many times over.

The measurement techniques for determination of the temperature distributions in the receiver in the solar thermal plant requires a non-contact method that will eliminate the risk of putting the person taking the measurement on exposure to concentrated solar radiation containing high infrared and ultraviolet rays. Infrared thermometry fits into this because of the non-invasive and non-contact nature.

In a study on the investigation of heat loss in absorber tube, Yaghoubi, et al., (2013), used a Testo 881 IR-Thermograph camera to determine the temperature distribution in vacuum jacket tube, lost vacuum tube and broken glass tube. It was concluded from the investigation that glass cover and vacuum was very critical as the loss vacuum tube and the broken glass tube, suffers considerably from heat loss and a significant reduction in thermal efficiency of 40% for the loss vacuum tube and 16% for the glass cover. The challenge encountered by these authors was that measurement through glass tube was difficult as glass cover was opaque and obstruct the measurement of the heat transfer fluid inside the vacuum tube.

A more detailed investigation of solar trough absorber tubes using dual method pyrometric solar-blind measurement, based on a spectral measurement range approach in regions, where the solar spectrum shows gaps due to the discrete absorption of the atmosphere.

The second method is a solar-blind pyrometric temperature measurement, which is a consequence of the optical behaviour, of the distinct angle dependence of the directional reflectance and emittance of a typical selective trough absorber coating. This method were reported by Pfänder, Lüpfert, & Pistor, (2007), for qualifying the thermal thermogram of the Eurotrough Schott PTR-70 receiver and the Solel-UVAC absorber tubes. The result obtained from these investigations was a marked improvement from the contact method.

Operating a solar thermal high temperature collector receiver system present a daunting and challenging measurement requirement, as the concentrated radiation makes it difficult for accurate determination of the temperature of the surface of the receiver. The contact method based on thermocouple and the pyrometer fails when an external light source, such as solar radiation interferes significantly with measurement results. Pfänder et al., (2007) described a solar blind pyrometric temperature measurement on solar thermal high temperature receiver and demonstrated the potential possibilities and limitations of the method in accounting for atmospheric absorption with models based on heat transfer. Solar blinds are gaps in the infrared spectrum covered by carbon dioxide and atmospheric water. These gaps provide a solution to the removal of reflections of the solar radiation that interferes with measurement signals.

The investigations carried out by Hernandez et al., (2004) and Tschudi & Morian (2001) provides an excellent experimental work on solar-blind pyrometers with different spectral measurement and have been validated and compared in a solar furnaces for the measurement on diffusely reflecting measurement species often referred to as targets. These approaches eliminate mounting glass sleeve and the vacuum in between the glass cover and the absorber tube that makes contact thermometric method cumbersome and expensive.

Technology and innovative thinking has brought drones technology side by side with thermography as a former aerial photography methodology found a new love in solar photovoltaic thermogram. Hambsch, (2011) reported the application of drones in field thermography measurement and preventive and proactive maintenance of large scale solar PV installation in Calau Germany. This proves very effective but requires extensive training of the drone operators and IR camera training.

2.8.9.2 Challenges and gaps in the past, current state of thermal management of solar thermal PVT parabolic trough system using non-contact infrared computer thermography in combined cooling heat and power hydrogen energy systems

Currently there are not many infrared experimental measurement applications in the measurement of temperature signature of the indirect steam generation from trough. Though there are few report of application of IR thermometry in measuring temperature for carbon based Nanofluid for investigating boiling heat transfer reported by Moo et al., (2014). There is a need for more research that can capture the temperature of the fluid in the tube with a class cover.

2.8.9.3 Solutions and how to bridge the perceived gaps in thermal management of solar thermal PVT parabolic trough system using non-contact infrared computer thermography in combined cooling heat and power hydrogen energy systems

In this research, an open flow channel flow with a specially design and fabricated shape was realised with thin film PV modules to study the effect of temperature on heat transfer fluid and the PV modules.

2.8.10 Historical development of sun simulator

The historical development of solar simulator will be based on the four class of solar simulators Space solar simulators (SSS); Standard solar simulator for terrestrial photovoltaic (SSTPV); large scale solar simulator collector (LSSC); High-flux solar simulator (HFSS).

2.8.10.1 Space solar simulators (SSS)

The development of sun simulator can be trace back to Indoor solar simulator by National Aeronautics and Space Administration (NASA). The objective was aimed at developing a ground-test facility which can simulate the space environment for earth satellite and other spacecraft testing at the beginning of the 1960s. The facility was called the space environment test chamber (NASA final report,1961; Bartera et al., 1970). The solar simulator was used to simulate solar radiation in space with a light source of mercury xenon lamp. The 3 years that follows, witness a surge in construction vacuum chambers to simulate orbital altitudes for complete spacecraft testing by US government and private companies as reported by Hollingsworth (1963); Uguccini, and Pollack (1962); Cope (1964). A 7.6m diameter space simulation chamber with 1.52m diameter solar simulator was constructed at NASA Jet Propulsion Laboratory (JPL) to meet the increasing testing requirement of space technology. This was meant to replace the existing 3m diameter simulator as reported by Cope (1964); Barnett and Thiele (1963); Barnett and Bartera (1963); JPT Tech Memorandum (1965); Eddy (1968); Bartera et al., (1970); Morgan (1973). The facility in JPL was extended

from 1.52 to 4.72m for simulation of the environment of Venus and Mercury, which makes it one of the largest solar simulator in the world (JPL Caltech Facility, 2001). The European Space Agency (ESA) develop a much larger simulator called the Large space simulator (LSS) to provide testing facility for the agency. The simulator optical space for the simulator was larger than the JPL with a diameter of 6m (Brinkmann, 1984). The development of simulator in the free world and Europe, spurn the Russians, Japanese and the South Koreans developed and constructed large scale simulators for their space missions triggering the space age as elucidate in the works of Galiaev (1997); Chikashi et al., (1997); Lee et al., (2004). In a study by Carek (2004) the largest space simulator is the 400kW solar simulator for investigating fundamental research and testing in a grand scale. The simulators reviewed above come under the classifications of Space solar simulators (SSS) all built with the objective of emulating the conditions of space on earth.

2.8.10.2 Standard solar simulator for terrestrial photovoltaic (SSTPV)

The next class of simulators are the standard solar simulator for terrestrial photovoltaic cell testing (SSTPV). The SSTPV class of simulator evolved out of the need for testing PV cells and modules for terrestrial application that matches the air mass zero standard (AM0) as the large scale simulators were rather more suitable for testing cells for space application and astronaut's conditions in space and other planet conditions. One of the major challenge of with terrestrial simulators are the light source that can emulate conditions similar to that of space. The problem was resolved by Hoffman Electronics Corporation and Optical Coating Laboratory with lamp combinations of xenon arc and tungsten bulb as light sources for their simulator. The second development in this class of simulator was the development by Spectrolab Corporation of optical filter based simulator with a variety of light sources Solar (ASTIA report, 1963). The development of PV industry soon leads to a call for standardising testing procedures to ascertain performance of light source, PV cell sample comparison from varieties of manufacturers, cell performance as a function of time and to provide design data for engineers and marketing experts (Pernisz,1983). The first solar cell testing condition was established in 1975 and updated in 1977 (ERDA/NASA, 1977; Brandhorst et al., 1975). The European commission documents and the American Standard Testing and Measurement (ASTM) standard for testing PV was finally available in 1985 (Hogan, 1986). The attention for the development of PV solar simulator move to reduction in the average power and temperature as a results of extended exposure to light as reported by Mueller (1993); Cannon (1998). The emergence of high powered Light Emitting Diode (LED) at the dawn of the 1990, change the light source for simulators to LED's because of their low cost, compact form factor, high efficiency and extended life (Bliss ,2008). The initial problem with LED light was it low light intensity which was resolved by advances in high power LED technology in the submission of Kolberg et al., (2011). The one interesting development

that attracted the most attention was when researchers at the University of Illinois a fully functional, full fledge LED Simulator design covering the AM1.5G solar spectrum and a class C uniformity over an area of 100mm×50mm (Bazzi et al., 2012).

2.8.10.3 The large scale solar simulator collector (LSSC)

The large scale solar simulator collector (LSSC) testing was next for outdoor testing of flat plate solar collectors. These class of solar collector was developed for new and efficient solar flat plate collector that can offer standard condition at high accuracy and short time. They were designed to test solar collectors under indoor laboratory conditions and the results obtained from these simulators were in agreement with outdoor normal sun conditions as reported in the work of Simon (1975); Vernon (1975); Simon and Buyco (1975); Johnson and Simon (1976); Simon (1976). The LSSC simulators unlike the standard solar simulators for PV with high spectral composition requirements, only need high power output and large testing area. Consequently, cheap tungsten halogen lamps as source of light to reduce the cost of fabricating the valuable equipment (Solanki et al., 2009; Ho and Loveday, 2002). Apart from tungsten lamps, Compact Source Iodide (CSI) and Metal halides lamps can be used to attain closer match to sun spectra composition (Zahler et al., 2005; Zahler et al., 2008; Meng, 2011; Kuhn and Hunt, 1991).

2.8.10.4 High-flux solar simulator (HFSS)

The last class is the High-flux solar simulator for Concentrated Solar Power and Concentrated Photovoltaic research, it can provide spectrum and high flux to match real concentrated solar radiation with the right optical concentrator. A HFSS was first realised at Lawrence Berkeley Laboratory for investigating chemical reactions at high temperature and flux (Kuhn and Hunt, 1991). The simulator was able to deliver 3 kW on a 7×7 cm target at a peak flux of 16MW/m^2. In another application, a thermochemical solar simulator was design in ETH-Zurich with a 200 kW DC high pressure argon arc light source and 2D ellipsoidal concentrator. The simulator was able to deliver up to 75 kW of continuous radiative power at a peak power flux of 4.25 MW/m^2(Hirsch et al., 2003). The Paul Scherrer Institutes developed (HFSS) for thermochemical processing of fuel, with a rating of 50 kW 11,000 suns based on xenon arc lamp and an ellipsoidal source (Petrasch and Steinfeld, 2005). It was design from the ground up for scalability in power capacity and ease of maintenance. The same design concept was followed by Deutsche Luft-Reederei (DLR) (Alxneit and Dibowski, 2011) and the University of Minnesota (Krueger et al., 2011).

2.8.10.5 Challenges and solution with the current HFSS

The current challenges faced with the HFSS is that they are made from light source that consume a lot of power and required longer start-up and warm-up time. The contribution

of the simulator use in this research work try to bridge some of the gaps by using and LED simulator with warm white and blue LED to cover the full spectrum. The design and assembly and calibration is discussed in chapter 9. There are still room for designing a higher flux simulator if the necessary resources are provided and with ample time.

2.9 Carbon based functional materials for energy applications

From the point of view of utilising energy materials, there is a growing revolution with carbon not as a pollution derivative but as an enabler of the technology of the future called graphene. Every new age is defined by the material, graphene will define the new age. A tool for Nano-architecting new functional materials from display, battery and supercapacitors, seawater desalination bed materials, new solar collectors etc. Graphene is a fully 2D material that can be functionalised at the surface. It an excellent conductor of heat and electricity and the strongest material. It has excellent optical properties such that a single layer can absorbed 2.3% light of any wavelength that fall on it which is a strong attraction for solar thermal application, optoelectronics, solar cells and thermal storage. The properties of graphene are attributed to it atomic and electronic sp^2 hybridization with 3 fixed carbon atom with strong covalent sp^2 π orbital bond and one lose p orbital electron that can only move up and down and not sideways. This is shown in figure 9 below.

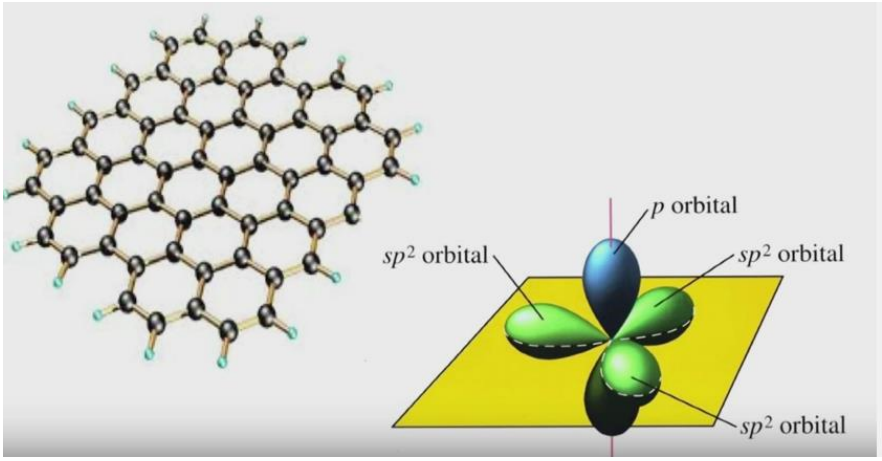

Figure 2.9 Graphene single sheet and the electronic structure with the 3 covalent sp^2 π orbital and one p orbital electron (Löfwander & Fogelström ,2007)

The work will include a chapter on the preparation of graphene based Nano fluid for direct steam generation and for thermal energy storage.

2.9.1 Graphene synthesis methods

Graphene generally can be synthesize either by the bottom-up or top-down approach. In the bottom-up approach, a carbon precursor is grown to form a sheet of graphene by chemical vapour deposition on copper substrate and epitaxial growth on silicon carbide as reported by Edwards and Coleman (2013), though the epitaxial method has a drawback of

highly specialized equipment which increases the cost of the graphene produced and growth is limited to the Silicon Carbide terrace size of 7. The good side is that large-areas of both single crystals and few layers of graphene can be grown over insulating substrates with the epitaxial method (Whitener and Sheehan 2014). The chemical deposition (CVD) method is a pyrolysis reaction in the presence of metal catalyst such as Copper and Nickel (Lavin-Lopez et al., 2014). CVD is a self-limiting process making the graphene produced to be single or few layers with large single crystal areas. The CVD route initially has the disadvantages of contamination during the transfer process and damage to graphene sheets during the transfer process (Whitener and Sheehan 2014). It is pertinent to point out that recently, substrate-free CVD synthesis of graphene was reported by Edwards and Coleman (2013), thus eliminating the use of metal substrates.

The top-down approach of synthesizing graphene include mechanical exfoliation, micromechanical cleavage, exfoliation of graphite intercalation compounds (GICs), arc discharge, unzipping carbon nanotubes (CNTs), graphene oxide exfoliation, and solvent-base exfoliation. The micromechanical cleavage method credited to Novoselov and Geim which won both a Nobel Prize in 2010 (Katsnelson, 2007; Novoselov et al., 2004) involves breaking the graphite sheet with Scotch tape. The rather easy method can be used with several layered materials, it has the drawback of both being inefficient for large-scale production and only limited to few layers or multilayer graphene. The second top-down route is graphite exfoliation through the graphite intercalated compounds (GICs). The method can be either the solvent-assisted exfoliation or the thermal exfoliation of Graphite Intercalated Compounds. Shear exfoliation using impeller mixer is another method of producing large scale graphene in the presence of surfactant. The approach produce very few layers of graphene. The two step route of exfoliation and followed by reduction of graphene oxide have attracted great attention in graphene synthesis. The Tour method which is an improved method of Hummer is the most popular and received the highest hit and citation as reported by Tour et al., (2010). The other graphene oxide methods are Brodie method (Szabó et al., 2006; Botas et al., 2013), Staudenmaier method (Chua et al., 2012; Sheshmani and Fashapoyeh 2013), Hummers method Marcano et al.,2010; Hummers and Offeman 1958) Modified Hummers method and the Improve Hummers methods (Marcano et al., 2010). The modified and the improved Hummers method are by far the one most broadly used because safety of their production process. The drawback of graphene oxide exfoliation is the degradation of the electronic properties of the graphene produced by the method and the dimension of the graphene obtained is constrained to the size of the initial size of graphite used. The modified Tour's method and the mechanical share exfoliation will be used for the production of graphene oxide for dispersion in solvent solar thermal

application. The general approach methodology of synthesizing graphene is shown in fig. 2. 10

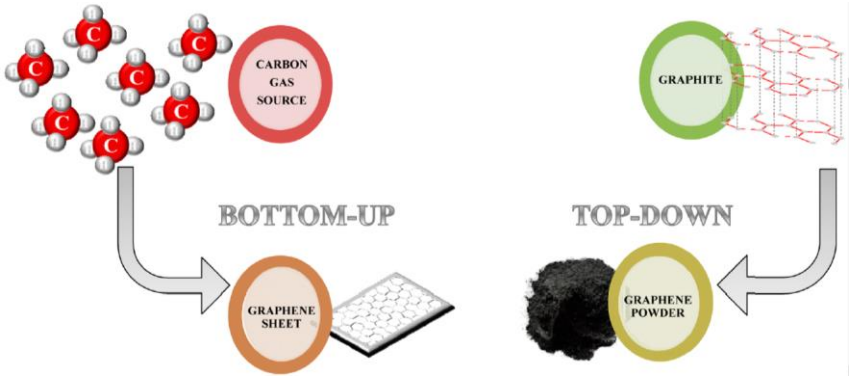

Figure 2.10 Top-down and bottom-up approach for synthesis of graphene (Marcano et. al., 2010)

2.10 Summary

In this chapter, a comprehensive and emerging work pertinent to this research thesis were presented. The work includes system thinking, combined cooling heating and power system with particular emphasis on prime movers, standalone hydrogen energy system dwelling on system level behaviour and root cause of failure in the existing island power system. The receiver shape selection based on design optimisation, sizing of the combined cooling heating energy system, and dynamical system approach to modelling in one dimension and 3D model of a parabolic trough PVT system was also reviewed. A low level control strategy, supervisory high level control strategies and the automation of the system with hardware-in-the loop testing and verification of the low level and high level control specifications. Experimental investigations of infrared thermography, frugal design, implementation of solar sun simulator and graphene as a carbon based material for energy storage is also reviewed. The review has provided background information on the focus of previous work, gaps to be addressed, motivation and boundaries for the research.

Chapter 3 Design optimisation and enhanced deterministic algorithm approach to sizing hydrogen HCCHP subsystems

3.1 Introduction

One of the major challenges with renewable energy is its intermittency or unpredictable availability. Consequently, a single source system for a higher power demand application such as farm, residential, commercial, remote telecommunication or remote island community often leads to high cost as a result of a need for over sizing the single energy source supply to meet specific reliability requirements. In other to reduce the cost and increase the overall system requirement, hybridising the single renewable source with another renewable energy source would reduce the life circle cost of the system, increase reliability and increase system efficiency and energy utilisation. In a study, by Seeling-Hochmuth, (1998), it was observed that a single-source renewable energy system more often constitute an unreliable and maintenance-intensive energy generation source, specifically if training of users and maintenance personnel is required. The experience of the author with women craving for energy demanding appliances such as electric cooker, iron and schools in remote areas, or in school wanting to turn on laboratory tools and run photocopier, simply but a lot of power demand on the single source system.

The size of the 10 subsystems that form the hydrogen combined cooling heating power systems increases efficiency gains and cost savings. The literature cited on energy system sizing are based on optimisation some meta-heuristic, dynamic or static equation with and without combine heat and power. In this research, a hydrogen combined cooling heat and power system is considered. The technique or methodology is based on enhanced deterministic design optimisation, supported by pattern search and genetic algorithm.

3.1.1 Hypothesis from literature

As a sequel to the literature cited and for the islands presented in chapter 2, it could be hypothesised that;

(i) the components obtained from this approach will have sizes that will be able to meet heating, cooling, electrical load at minimum cost of the initial capital outlay

(ii) the components and the subsystems will work together to meet cooling and heating comfort for summer and winter as the case may be

(iii) components and subsystems can interact to accommodate growing load demand of the overall HCCHP system

3.2 Methods for sizing hybrid energy system

Energy system sizing is important in other to achieve and derive the maximum capacity utilisation and energy efficiency. This is also underpinned by control of the energy system which this research is premised on. The techniques or methods for sizing are presented in the session that follows.

3.2.1 Rule-of-thumb method

The rule-of-thumb method provides practical guidelines on how to size and operate a hybrid energy system based on experience with installed system as provided by the national renewable energy laboratory (NERL). The most common rule of thumb was compiled after a workshop by the NERL and detailed in the work of Seeling-Hochmuth, (1998).

3.2.2 Paper based method

The paper-based method is a spread sheet sizing approach for PV/diesel hybrid system and employ rule-of-thumb methods (FSEC, 1987); (SANDIA, 1995). It is a step-by-step approach hybrid system design also called the Ampere hour method. Ampere hour method in general is advantageous in that they largely ignore voltage drops over cables, regulators and variations in the operating voltage.

3.2.3 Software based methods

The software based method are based on mathematical description of components characteristics operation and system energy flow with financial cost of the hybrid system. The software includes HYBRID2 a simulation tool implemented in Visual basic by NEREL (1993), INSEL a block diagram software for logistic simulation of renewable by Schumacher (1993), PHOTO, RAPSIM, RAPSYS and others. An extensive treatment of the software tools is presented by Seeling-Hochmuth, (1998).

3.2.4 Calculus based optimisation techniques

The calculus based methods is a direct or indirect method. In the direct calculus method, the local optima are sought by hopping on the function and progressing to the direction of local gradients while the indirect method seek the local extreme by solving the usually non-linear set of equations setting the gradient of the objective function to zero.

3.2.5 Enumerative schemes

The enumerative schemes are a search algorithm that seeks the objective functions values at every point in the space. It is a simple scheme but lack efficiency.

3.2.6 Random search techniques

The random search techniques evolved from the shortcomings of the enumerative methods and are global optimisation methods of a stochastic nature. The method is driven by random fluctuations introduced into the system to prevent the searching trajectory being trapped in local minima. Genetic algorithm and Simulated annealing are the most applied techniques in sizing hybrid energy systems.

3.2.7 Hybrid energy system optimisation software

The hybrid energy system optimisation techniques are software based on commercial and open source for sizing and overall system optimisation. The software such as HOMER and SOMES are used as sizing and optimisation of hybrid energy systems.

3.3 The enhanced deterministic design optimization genetic algorithm solution approach

The solution methodology is based on deterministic sizing methodology proposed by Gazey (2004). The approach involves sizing a hybrid renewable energy system based on wind as the primary energy source. In this study, the deterministic algorithm was modified with solar thermal and solar PV as the primary energy source in the hydrogen combined cooling heating energy system. The enhanced deterministic algorithm provides the deterministic sizes, capacity factors profiles of the average power as input to the evolutionary algorithm to optimized the sizes of the components based on the cost and time objectives and respecting the operational and limits constraints of the components.

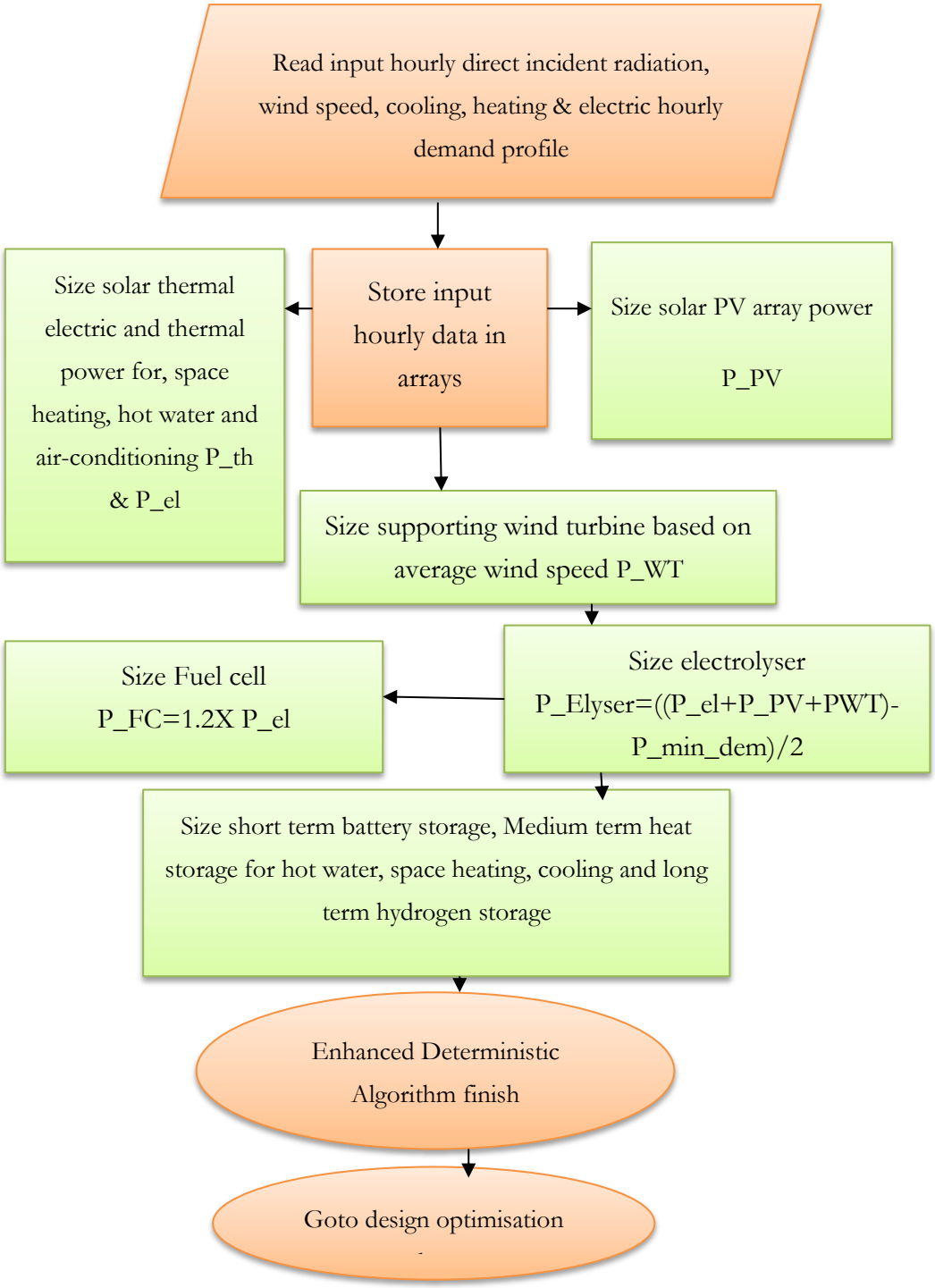

Figure 3.1 Enhanced deterministic algorithm in detail; the primary energy source is sized from the hourly resources-wind speed, solar radiation from weather station, cooling, heating and electric demand and technical specification of components from manufacturers

3.3.1 The design optimisation work flow

The input to the design optimisation block is the deterministic algorithm, and the output of the response surface is optimised using multi-objective genetic algorithm. flow chart of for optimising the output. The iterative procedural workflow is illustrated in figure 4.

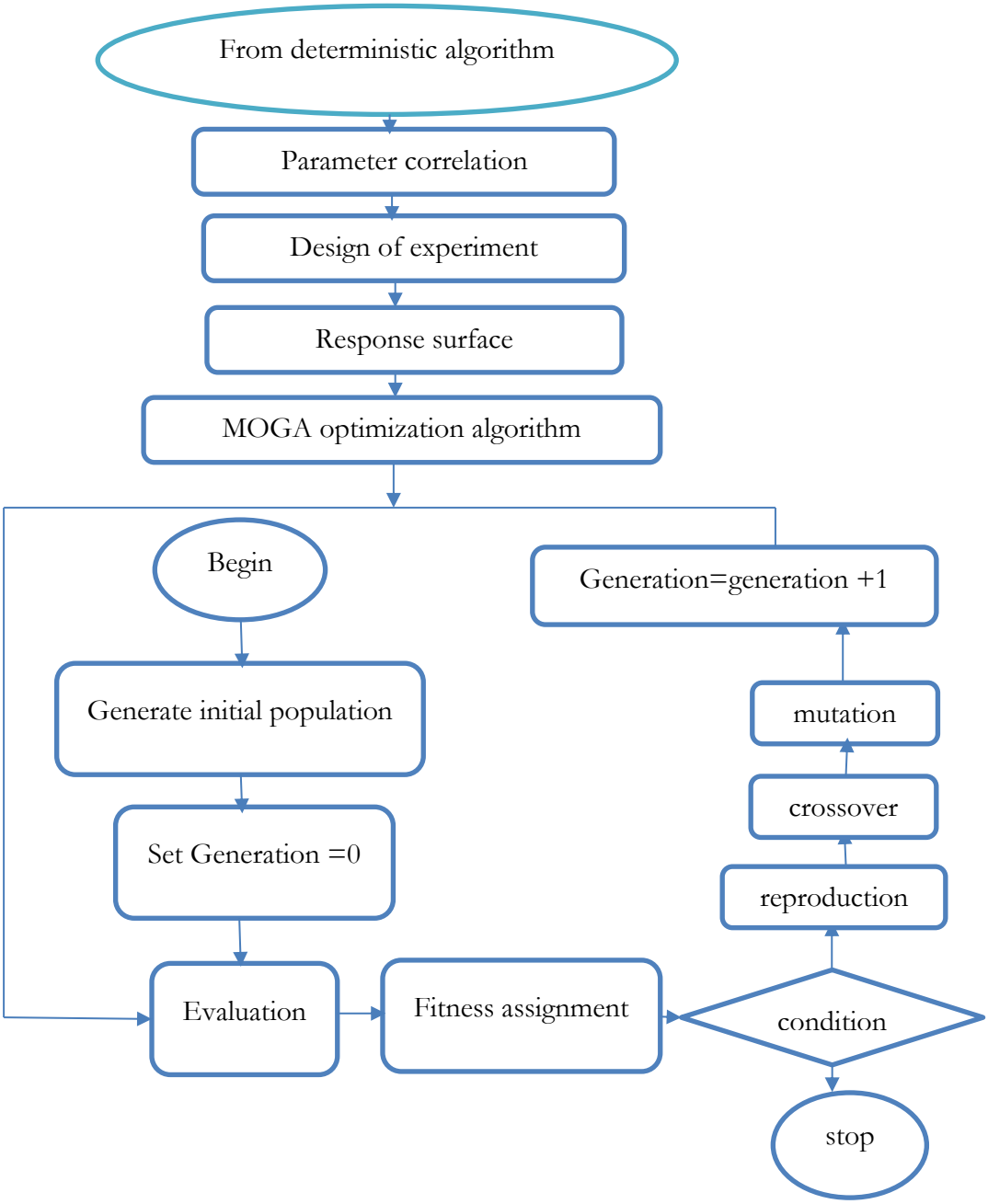

Figure 3.2 Flow chart of the design optimisation used to obtain the optimal sizes of the components of the HCCHP hybrid energy system

3.4 System input renewable resources and polyload profile data

The first point of call for energy system modelling is the input data which could be acquired from weather station or from onsite weather instruments. The accuracy of such data is crucial to the accurate sizing and optimum selection of the energy system components. Table 1 shows the details of the weather location, geographical coordinates, and measuring specifications.

3.5 Hydrogen combined cooling and heating hybrid energy system model development

The input data for sizing of the components that constitute the hydrogen combined cooling heating hybrid energy system are user or consumer requirement and the design parameters.

3.5.1 Consumer (user) requirements

The user requirements are the electric, heating and cooling load, the number of hours for heat storage during the night with energy to power ratio of 10 hours, for medium term storage. The long term storage is for situations with long and extreme weather conditions such as snow fall and long winter, which could last for a maximum of 21 days (504 hours) and short term storage of 15 minutes' maximum.

3.5.2 The design parameters

The design parameters are obtained for the given user or consumer requirements. The parameters include, size of solar collector, photovoltaic modules, wind turbine, electrolyser, fuel cell, battery heat storage tank, hydrogen storage, adsorption chiller and space heating unit.

Thermodynamic equilibrium, steady state, and negligible kinetic and gravitational terms in the energy balances, radiation uniformly concentrated along PV area. In addition, the negligible temperature gradients in the PV film and in the substrate, are assumed due to the small thickness of the PV layer and the high conductivity in the metal substrate. In other words, PV and substrate temperature are assumed uniform.

3.5.3 Concentrating solar photovoltaic parabolic trough sizing model

The concentrating parabolic trough consists of the thermal and electrical part. The thermal part also consists of the collector or concentrator and the receiver. The concentrator is a mirror which focuses the light from the sun to the receiver located at the focal line of the cylindrical paraboloid. A thin film is wrapped around the metal half tube with the tedlar backsheet and the EVA film. A half glass cover is used to cover PV modules, tedlar

backsheet and the EVA. An alligator clip is connected to the wire tab to collect the direct current produced simultaneously as cooling at the inner pipe occurs.

3.5.3.1 Thermal model of the parabolic trough system sizing model

The sizing model of the thermal parabolic trough receiver is aimed to obtain the total area of the collector as a function of the available solar radiation for the island. The total insolation of place is the sum of the beam and the diffuse radiation, which are functions of the longitude, latitude, day of the year, declination angle and the sunrise and sunset hour angle. The total area sizing mathematical relation is given in Eq. 1. The first step is to model the solar insolation or radiation falling on the surface of the collector/concentrator mirror, reflected unto the PV module and the copper inner tube receiver at the focal line of the parabolic trough. The tilt angle of the collector receiver PVT is location based and there are different models for estimating the beam, reflected and diffuse radiation. The models are classified as isotropic or anisotropic; isotropic models were obtained assuming a constant intensity for the diffuse sky radiation over the dome of sky as expounded in the work of Liu and Jordan (1961), Tian et al., (2001) and Koronakis (1986). In the anisotropic model, the brightening around the solar disk and the isotropically distributed diffuse components from the rest of the dome of the sky were accounted for in the model and investigated by Hay and Davis (1980), Temps and Coulson (1977), Klucher (1979) and Perez, Ineichen and Seals (1990). The total parabolic trough collector receiver area required is given in Eq. (3.1)

$$A_{co} = \frac{E_{re}}{\eta_{th} I_{G_{eff}}} \tag{3.1}$$

$I_{G_{eff}}$ is the effective total global radiation on the tilted surface of the trough expressed mathematically in Eq. (3.2);

$$I_{G_{eff}} = I_b IAM_b + I_d IAM_d + I_r IAM_r \tag{3.2}$$

$$I_b = I_{bh} R_b \tag{3.3}$$

$$R_b = \frac{\cos(\theta)}{\cos(\theta_z)} \tag{3.4}$$

$$I_r = \rho I_{Gh} \left(\frac{1 - \cos(\beta)}{2} \right) \tag{3.5}$$

$$I_d = I_{dh} \left(\frac{1 + \cos(\beta)}{2} \right) \left(1 + F_{kl} sin^2 \left(\frac{\beta}{2} \right) \left(1 + F_{kl} cos^2(\theta) sin^3(\theta_z) \right) \right) \tag{3.6}$$

The models are valid if the state of the sky is accounted and the clearness factor F_{kl} , captures the radiation changes due to overcast skies and expressed in (3.7) Klucher (1979).

$$F_{kl} = 1 - \left(\frac{I_{dh}}{I_{Gh}}\right)^2 \quad (3.7)$$

The Incident Angle Modifier (IAM) account for inclination as a result of radiation falling off surface of the collector receiver, especially at angles greater than 65^0 investigated by Soto, Klein and Beckman (2006). The IAM is computed from a model proposed by Armstrong (2006) Eq. 3.8.

$$IAM = b_0 + b_1\theta + b_2\theta^2 + b_3\theta^3 + b_4\theta^4 \quad (3.8)$$

b_0 =1 b_1 =-1.098×10^{-4}, b_2 =-6.276×10^{-6}, b_3=6.583×10^{-7} and b_4 =-1.4272×10^{-8}

The equations for the effective angle of incidences for diffuse, reflective and beam radiation are expressed mathematically in (3.9), (3.10) and (3.11) and this would be required for calculation of incident angle modifiers of the diffuse, reflective and beam IAM_b, IAM_r and IAM_b with (3.2);

$$\theta_d = 59.7 - 0.1388\beta + 0.00149\beta^2 \quad (3.9)$$

$$\theta_r = 90 - 0.5788\beta + 0.00269\beta^2 \quad (3.10)$$

$$\theta_b = \theta \quad (3.11)$$

Equations (3.1) -(3.11) are used to compute the area and the number of collector's receiver's

The energy required is twofold as the load profile for the island is for both cooling during summer time and heating during winter time. The limit will be express as a function of day of the year and expressed as a conditional equation in Eq. (3.12);

$$E_{re} = \begin{cases} P_{lc} & \text{if} \quad \text{March} \leq \text{DOY} \leq \text{October} \\ P_{lh} & \text{otherwise} \quad \text{October} \leq \text{DOY} \leq \text{March} \end{cases} \quad (3.12)$$

Where P_{lc} and P_{lh} are the cooling and heating loads obtained from hourly thermal load profile of the island.

3.5.3.2 Electric model of the CPVT system parabolic trough sizing model

The energy required for the PV module sandwich between the copper tube and the glass cover is a function of the irradiance and the solar cell temperature. The module should be

sized to cover; energy required for running daytime load, energy required for the nighttime load and energy required during no-sunny days or days of autonomy. The equation relating the energy generated by the PV module is expressed in Eqs. 3.13 and 3.14;

$$E_{PV} = G\eta_{PV}\left(1 + \beta_{PV}\left(T_{PV} - T_{ref}\right)\right) \tag{3.13}$$

$$G = A_{PV} I_b C_{PV} \eta_{opt} \tag{3.14}$$

Energy required or provided by the PV is a sum of daytime, night time and days of autonomy, which is expressed in Eq. 3.15;

$$E_{PV_{req}} = E_{day} + \frac{E_{night}}{\eta_{bat}} + \frac{\left(E_{day} + \frac{E_{night}}{\eta_{bat}}\right) D_{no-sun}}{\eta_{bat}} \tag{3.15}$$

The area of PV required in Eq. 3.14 is function of the energy provided or supply by PV in Eq. 3.15 and is expressed in Eq. 3.16;

$$A_{PV} = \frac{E_{PV_{req}}}{I_{G_{eff}} \eta_{PV}} \tag{3.16}$$

The electric power, current, voltage and temperature at the surface of the of the module is given in Eq. 3.17;

$$P_{PV} = N_P N_S V_{OC} I_{SC} FF \tag{3.17}$$

$$I_{SC} = \frac{\left(I_{SC-STC} + K_1(T_C - 25)\right)G}{1000} \tag{3.18}$$

$$V_{OC} = V_{OC-STC} - K_V T_C \tag{3.19}$$

$$T_C = T_A + \frac{(NOCT - 20^0 C)G}{800} \tag{3.20}$$

3.5.4 Wind turbine average power model

The Weibull distribution does a good job of modelling the variance in the wind; therefore, the wind profile can be estimated using the following probability density function. The model was first proposed by Department of energy, which relate the wind at any height to a reference height and expressed mathematically Eq. 3.21 (Esteban, et al., 2010);

$$v_h = v_{ref}\left(\frac{h}{h_{ref}}\right)^{\alpha} \tag{3.21}$$

Eq. 3.21 can be used to define the power of a wind turbine generator with a conditional equation in Eq. 3.22;

$$P_w = 0 \qquad v_h < v_{cut-in}$$

$$P_w = aV_h^3 - bP_r \qquad v_{cut-in} \leq v_h < v_r \tag{3.22}$$

$$P_w = P_r \qquad v_r \leq v_h < v_{cut-out}$$

$$P_w = 0 \qquad v_h \geq v_{cut-out}$$

$$a = \frac{P_r}{(v_r^3 - v_{cut-in}^3)} \tag{3.23}$$

$$b = \frac{v_{cut-in}^3}{(v_r^3 - v_{cut-in}^3)} \tag{3.24}$$

The turbine actual power is expressed mathematically in Eq. (3.24) (Akiki, Eng, & Avenue, 1998);

$$P_{wG} = P_w A_w \eta_w \tag{3.25}$$

3.5.5 Fuel cell power sizing model

The fuel cell is sized to meet the maximum load demand and in a combined heat and power system it is also use as a prime mover. According to Zhang et al., (2006), when the load demand exceeds the energy from renewable generation, the deference is met by the fuel cell. The fuel cell size is selected to meet or exceed the maximum power demanded by the load. A margin of 20% is added to the size of the fuel cell to accommodate any modest increase in peak demands. Fuel cell power output is, therefore, calculated using Eq.3.26;

$$P_{FC} = 1.2\, P_{el-load} \tag{3.26}$$

3.5.6 Alkaline water electrolysis power sizing model

The electrolyser is used to produce hydrogen for long term energy storage when generation is far in excess of the demand. The size of the electrolyser with respect to the deterministic algorithm is computed by subtracting the minimum load demand from the total rated power that can be delivered by the renewable sources. However, Ulleberg, (2003); Ulleberg, (2004) investigated the underutilisation of size of electrolyser emanating from this sizing a reduction by a fraction is required to make it effective. Electrolysers purchase is typically on the high side and hence desirable to operate them with a high level of utilisation. Therefore, the calculated value, as suggested in literature, is to be reduced by around 50% on the average is advisable. Though the value is location dependent could have the effect of increasing the electrolyser level of utilisation. The fraction comes at a cost as there are times when the total

renewable generation exceeds the total power consume by the combined load and storage. The equation for the electrolyser power is expressed mathematically as;

$$P_{ely} = \frac{((P_{el-th} + P_{PV} + P_{WG}) - P_{min-dem})}{2} \tag{3.27}$$

3.6 Hybrid energy storage sizing models

In the hydrogen combined cooling and heating energy system, the storage is for long-term provided by the hydrogen storage tank, medium-term provided by heat storage tank and the short-term storage provided by the battery. The storage must provide energy at least greater than or equal to the difference between generation and demand. The storage combined share is expressed as follows in Eq. (3.28) (Gazey, 2006);

$$P_{store} = \sum P_{bal} \tag{3.28}$$

$$P_{bal} = P_{gen} - P_{dem} \tag{3.29}$$

3.6.1 Long-term storage model

The long-term storage systems are sized to deliver full power for a typical location for up to three weeks. This kind of storage can be used to overcome the so called "dark calm 5" periods, which are considered to be the most challenging in the event adverse weather condition for a power system with high shares of renewables. To bridge or fill-in, the long deficit of power during prolonged high pressure weather systems (reducing wind generation to a minimum) in winter time (high power demand, low solar generation) and in the worst case with widespread fog and/or snow cover (hindering solar generation). Studies have shown that these weather situations typically do not exceed three weeks.

The energy to be store in the hydrogen tank was sized to supply the total energy in the absence of medium-term and short-term storage and is expressed in Eq. (3.30);

$$E_{H_2-Tank} = P_{store} \frac{T_{long}}{\eta_{FC}} \tag{3.30}$$

The size hydrogen storage tank is sized with the average volume of hydrogen that needs to be stored in the hydrogen tank and computed based on the absolute energy content of the hydrogen gas. This is known as the Higher Heating Value (HHV) of the hydrogen gas which is known to be 3.55 kWh/Nm^3 and expressed mathematically in Eq. (3.31) (Gazey, 2014);

$$V_{H_2-Tank} = \frac{E_{H_2-Tank}}{HHV} \tag{3.31}$$

The hydrogen storage tank is usually discharge and charged during operation and the charge and discharge cycles are expressed mathematically in Eq. (3.32) a metal hybrid tank was assumed;

$$SOC_{MH-H_2} = \frac{(N_{MH,start} + \int \dot{V}_{H_{2-Elyser}} dt - \int \dot{V}_{H_{2-FC}} dt)}{N_{MH-Norm\ Cap}} \tag{3.32}$$

$$\dot{V}_{H_{2-Elyser}} = \frac{I_{H_{2-Elyser-Nor}}}{2F} \rho_{H_2} \tag{3.33}$$

$$\dot{V}_{H_{2-FC}} = \frac{CR_{H_2} RT}{3600\ P_{atm} T_{long}} \tag{3.34}$$

3.6.2 Medium-term storage model

Medium storage provides storage typically for 6 hours in form of heat. Heat storage tank stores solar energy in the form of heat by raising the temperature of the fluid. When sunlight is not available, this stored energy is utilized for cooling during summer or heating during winter. The size of the tank depends on the maximum amount of energy that needs to be stored and the physical properties of the fluid used for circulation. The amount of energy to be stored depends strongly on the amount of night cooling or heating load. The total energy required the sum of the night and day energy and expressed in Eq. (33);

$$E_{Heat-store} = \frac{(K_1 E_{re} + K_2 E_{re} D_{no-sun})}{\eta_{Heat}} \tag{3.35}$$

The size of heat storage tank required is expressed in Eq. (34);

$$V_{Heat-Tank} = \frac{E_{Heat-store}}{\rho_{HTF} C_{p-HTF} (T_{max} - T_0)} \tag{3.36}$$

The charge and discharge cycle during the day, night and when is no sun is model and represented in Eq. (3.37), (3.38), (3.39) and (3.40) (Bayón, Rojas, Valenzuela, Zarza, & León, 2010);

Charging:

$$T_{SOC-SM} = T^0_{SOC-SM} + \frac{\dot{m(t)}}{\sum m_i c_i} \dot{Q}_{HTF} \tag{3.37}$$

$$\dot{Q}_{HTF} = E_{Heat-store} + L_{lv} \int_{t_a}^{t_b} \big(1 - x(t)\big) dt \tag{3.38}$$

Discharging:

$$T_{SOC-SM} = T^0_{SOC-SM} + \frac{\dot{m(t)} L_{lv}}{\sum m_i c_i} \dot{Q}_{HTF} \tag{3.39}$$

$$\dot{Q}_{HTF} = \int_{t_a}^{t_b} (x(t))dt \tag{3.40}$$

$$x(t) = \left(\frac{2\pi k_{SM}}{\dot{m(t)} L_{lv}} \frac{T_m - T_{HTF-in}}{In\left(\frac{r_m(t)}{r_i}\right)} \right) L \tag{3.41}$$

3.6.3 Short-term storage model

3.6.4 Battery secondary storage power model

A battery can provide storage for days if sized correctly and it is system dependent. The battery is to provide short term storage of about two hours. The battery model for which the Hydrogen Standalone Combined Cooling Heating and Power or energy system is based on, is a Lead-acid Advanced Glass Mat battery type. The battery key role is to provide the short term storage and for start-up and shut-down discharge and recharging circle of the fuel cell, an electrolyser, and the hydrogen primary storage tank discharge and recharge cycles. The selection of a proper size and type of the battery bank for short term storage and types of applications requires a complete analysis of the battery charge and discharge requirements, including load, output, and pattern of the solar or wind energy sources, the operating temperature, and the efficiency of the charger and other system components. Current state of charge (SOC) is used to determine the charging and discharging of a battery. At any time, *t*, SOC is

defined by the Eq. (3.42) (Yang et al., 2007):

$$SOC(t) = SOC(t-1)\left(1 - \frac{\sigma \Delta t}{24}\right) + \frac{I_{bat}(t)\Delta t \eta_{bat}}{C_{bat}} \tag{3.42}$$

$$C_{bat} = \frac{P_{el-Load}\, T_{short}}{V_{bat}\, DOD_{max} T_{bat} \eta_{bat}} \tag{3.43}$$

The battery current of a hybrid Solar thermal-WG-PV at any time is expressed mathematically in Eq. (41);

$$I_{bat}(t) = \frac{(P_{PV} + P_{el-th} + P_{WG}) - P_{el-Load}}{V_{bat}} \tag{3.44}$$

where σ is the self-discharge rate (0.2% per day), C_{bat}. is the nominal capacity of a battery. As in the battery charge efficiency η_{bat} is set to round-trip efficiency and the discharge efficiency is set to 1(Yang et al., 2007).

3.6.5 Cooling or refrigeration model

The cooling for the island cooling demand is provided by an adsorption heat pump or chiller. The cooling is expressed as a function capacity of the absorption heat pump and the nominal coefficient of performance. The hourly cooling rate is given in Eqs. (3.45) and (3.46) (Sharafi et al.,2015);

$$HP_{cool_{Abs}}(t) = P_{lc}(t)\, COP(t) \tag{3.45}$$

$$COP(t) = COP_{max}(k_0 + k_1 T_{ewt} + k_2 T_{ewt}^2) \tag{3.46}$$

$COP_{max} = 4.5$ for cooling

3.6.6 Heating model

The heating for the island cooling demand is provided by radiator driven heat from the solar thermal parabolic trough. The heating is expressed as a function capacity of the heat pump and the nominal coefficient of performance. The hourly heating rate is given in Eq. (3.47);

$$HP_{Heat}(t) = P_{lh}(t)\, COP(t) \tag{3.47}$$

$COP_{max} = 5.5$ for Heating

The temperature of the inlet hot water or steam entering the heat pump is computed from the Eqs. (3.48), (3.49) and (3.50), (Sharafi et al.,2015) for both cooling and heating;

$$T_{ew}(t) = T_{min} + \left(\frac{T_{ew,max} - T_{ew,min}}{T_{d,cool} - T_{d,heat}}\right)\left(T_a(t) - T_{d,heat}\right) \tag{3.48}$$

$$T_{ew,max} = Min\left(T_g + 20^0F, 110^0F\right) \tag{3.49}$$

$$T_{ew,min} = T_g - 15^0F \tag{3.50}$$

3.6.7 Design optimisation procedure

The design optimisation is a tri-objective optimisation to ascertain the optimum configuration of hydrogen combined cooling heat and power system that will maximise generation and Return on Investment (ROI) at minimum Carbon emission footprint.

3.6.8 Formulation of optimization problem

The size of the subsystems in the HCCHP depend to a large extent on the economics and the profitability of the initial capital outlay. In this study, the return on investment (ROI) of the design space was used as a design candidate to quantify the economic benefit or measure of the HCCHP. The system must also be reliable enough to meet load requirement and this

is captured by the loss of load probability (LOLP). A new factor called the storage reliability is also introduced to ascertain the benefit of storage on the investment (LOLP_store).

3.6.8.1 Objective functions

The tri-objective functions are expressed mathematically in Eqs. (3.51), (3.52) and (3.53);

$$maximise, minimise = f\left(-Gen_{obj}, -ROI_{obj}, CO2_{obj}\right)$$

$$subject\ to\ ; g_i(x) = 0\ , i = 1$$

$$H_j(x) \leq 0\ , j = 1, \dots, 4$$

$$lb \leq I_k(x) \leq ub\ , k = 1, \dots, 13$$

$$Gen_{obj} = \sum_{t=1}^{360} (x1\ P_{el-th} + x2\ P_{PV} + x3\ P_{WG} - \ P_{el-Load}) \tag{3.51}$$

$$ROI_{obj} = \sum_{t=1}^{360} (\frac{I_{Total} - C_{Total}}{C_{Total}}) \tag{3.52}$$

$$CO2_{obj} = \sum_{t=1}^{360} (P_{cool-Load} + P_{heat-Load}) G_{CO2,eqv}^{gas} + P_{el-Load}\ G_{CO2,eqv}^{elec} \tag{3.53}$$

Where;

$g_i(x)$ is the linear equality constraints and i is the number equality equations

$H_j(x)$ is the linear inequality constraints and j is the number inequality equations

$I_k(x)$ is the lower and upper bounds constraints and k is the number bounds equations

lb is the lower bound value

ub is the upper bound value

Gen_{obj} is the generation technical objective function

ROI_{obj} is the return on investment economic objective function

$CO2_{obj}$ is the carbon dioxide emission objective function

$G_{CO2,eqv}^{gas}$ is the unit cost of using gas for heating and cooling

$G_{CO2,eqv}^{elec}$ is the unit cost of using electricity for heating and cooling

Table 3.1 Feed-in-tariff, initial capital cost and levelised cost of energy of subsystems in the HCCHP ((Kamjoo et. al., 2012);(IRENA)

Technology	Feed-in-tariff (p/kWh)
Solar thermal (CHP) 15 March 2013 to 15 January 2016	13.61
Photovoltaic (PV) Solar photovoltaic (other than stand-alone) with total installed capacity greater than 10 kW but not exceeding 50kW	4.53
Wind (Wind with total installed capacity greater than 15kW but not exceeding 100kW) 1 October 2015 to 15 January 2016	13.89
Selling tariff (Export tariff) 1 Apr 2015 - 31 Mar 2016	4.85
Unit Costs, O&M and LCE	**Cost (p/kWh)**
Unit capital cost of solar thermal subsystem $C_{Unit,th-el}$	2.028
Unit capital cost of solar PV subsystem $C_{Unit,PV}$	0.741
Unit capital cost of Wind turbine subsystem $C_{Unit,WG}$	0.525
Solar thermal O & M	0.0267
LCOE solar thermal	0.208
LCOE solar PV	0.039
LOCE Wind turbine	0.067

3.6.9 Modelling income from generation

The model of income is in 2-fold, the income accruing from the electric power from tri-generation form thermal electric power block, the solar PV and the supporting wind turbine. The total investment from the generation is the sum of the Feed-in-tariff for solar thermal, PV and wind multiply by the power generated over the life of the HCCHP. The third investment is the income obtained from the selling the excess power from the 3 source to the grid through the export tariff. This are expressed in (3.54), (3.55) and (3.56) as follows (Kamjoo et. al., 2012);

$$I_{Total} = I_{FIT} + I_{store-sellGrid} \quad (3.54)$$

$$I_{FIT} = L_p\left(FIT_{th-el}P_{th-el} + FIT_{pv}P_{pv} + FIT_{WG}P_{WG}\right) \quad (3.55)$$

$$I_{store-sellGrid} = L_pT_{store-sellGrid}\left(\left(P_{th-el} + P_{pv} + P_{WG}\right) - P_{el-load}\right) \quad (3.56)$$

3.6.10 Modelling cost of the renewable energy components

The cost model consists of the capital cost, installation cost, operation and maintenance cost, replacement cost and the cost of buying electricity for worst case scenario of no wind and solar resources.

$$C_{Total} = C_{IC} + C_{rep} + C_{O\&M} + C_{buy,grid} \quad (3.57)$$

3.6.10.1 Initial Capital Cost

The initial capital cost is the sum of the unit cost multiply by the area of solar parabolic trough, solar PV and the wind turbine. It is also the multiple of the number of unit, capacity and the unit cost of the long term storage, medium term storage and the short term storage. This are expressed in Eqs. (3.58) and (3.59) as follows (Kamjoo et. al., 2012);

$$C_{IC} = A_{th-el}C_{Unit,th-el} + A_{PV}C_{Unit,PV} + A_{WG}C_{Unit,WG} + C_{store} + C_{main} \quad (3.58)$$

$$C_{store} = N_{Heat}C_{unit,Heat}\ C_{Heat} + N_{H2}C_{unit,H2}\ C_{H2} + N_{bat}C_{unit,bat}\ C_{bat} \quad (3.59)$$

3.6.10.2 The present value of replacement cost

The only subsystem that requires replacement during the 20 years' period of operation is the battery, since it design life is between 3 and 10 years. In this study, a 5 years' replacement period was adopted. The battery life is a function of the battery float life and the battery cycle life and must be replaced even if not in use after the design lifetime and is expressed in Eq. (3.60) as follows (Kamjoo et. al., 2012).

$$C_{rep} = N_{bat}C_{unit,bat}\ C_{bat} \sum_{i=1}^{N_{rep}} \left[\frac{1+f}{1+k_d}\right]^{(\frac{N_i}{N_{rep}}+1)} \quad (3.60)$$

3.6.10.3 The present value of operation and maintenance cost

The present value of the operation and maintenance of the hybrid HCCP for maintaining and operation of the subsystems. The subsystem includes wind turbine, solar thermal parabolic trough mirror and solar PV dust cleaning. This is expressed in Eq. (3.61) as follows (Kamjoo et. al., 2012);

$$C_{O\&M} = C_{O\&M,0}\left(\frac{1+f}{1+k_d}\right)\left[1-\left(\frac{1+f}{1+k_d}\right)\right]^{L_p} \quad (3.61)$$

The maintenance and operation cost $C_{O\&M,0}$ at the beginning year of deployment is expressed in Eq. (3.62) as follows (Kamjoo et. al., 2012);

$$C_{O\&M,0} = kC_{IC} \quad (3.62)$$

Where k is assumed 1% for PV panels, 3% for wind turbine and 1% for battery(Kamjoo et. al., 2012).

$$C_{buy,grid} = L_p\left(LCOE_{offpeak,grid}\ P_{shortage,offpeak}\right) \quad (3.63)$$

3.6.11 Constraints

The constraints are the upper and the lower bounds, equality and inequality of the design space variables and are summarized in table 3.2 below.

Table 3.2 Constraint for optimisation of storage, long, medium and short term storage

Constraints	Long term storage	Medium term storage	Short term storage
Bounds(hrs)	$48 \leq T_{long} \leq 504$ (x9)	$1 \leq T_{medium} \leq 48$ (x11)	$1 \leq T_{short} \leq 24$ (x6)
	Number of unit bounds constraints		
PV modules(x2)	$10 \leq N_{PV} \leq 232$	Electrolyser (x7)	$0 \leq N_{Ely} \leq 5$
Receiver (x1)	$5 \leq N_{SR} \leq 116$	Inverter	$2 \leq N_{IN} \leq 5$
Wind turbine (x3)	$3 \leq N_{WG} \leq 57$	Hydrogen tank (x8)	$2 \leq N_{IN} \leq 5$
Fuel cell (x4)	$0 \leq N_{FC} \leq 6$	Heating unit (x12)	$2 \leq N_{IN} \leq 5$
Battery (x5)	$20 \leq N_{bat} \leq 120$	Cooling unit (x13)	$2 \leq N_{IN} \leq 5$

3.7 Research approach and methodology

3.7.1 HCCHP subsystem sizing methodology and solution approach

A hybrid enhanced deterministic algorithm and design optimisation technique was used to obtain the optimum sizes of the subsystems. Evolutionary optimisation algorithm such as NSGA II are often difficult to implement in system sizing, as a results a 5 step approach was implemented to obtain the optimum sizes of each components in the HCCHP systems. In the 1st step, the sizes of the subsystems were obtained using enhanced deterministic algorithm with input, hourly solar radiation, wind speed, cooling load, heating load, electric load and the technical datasheet specifications of the selected nominal rated capacities of subsystems. The sizes obtained from stage one used to establish the dependencies of inputs sizes obtained correlate with response (generated power, investment and emission control) parameter correlation, design of experiment and response surfaces. In the 3rd step, the lower, upper bounds, equality constraints and inequality constraints are evaluated. The 4th stage involves computing the 3 objectives using the NSGA II generated power, investment and emission control). The 2nd – 4th step constitutes the design optimisation methodology. Figure 1 & 2 depict the workflow of the enhanced deterministic and design optimisation algorithm. The 5th step is the validation of the numerical code.

3.7.2 Importance and limitation of the research

A hybrid energy or power system such as the hydrogen combined cooling heat and power system under study provides a means of evaluating the performance of the overall system.

The system provides a basis for determining the sizes of the subsystems that meet economic scares resources at reliable system condition. However, one of the limitation of the current study is availability of energy resource and demand data from a single source. A real or existing system to obtained data for validation on a large scale is often difficult. The point highlighted are serious limitation and can be mitigated if research institutions and private organisation can provide data for validation. A statistical approach is used based on subsystems specification sheets. This is discussed in detail in the validation and verification section.

3.7.3 Analysis of result obtained

The results obtained from the design optimisation simulation using the inputs data is presented in figure 3.3 a, b, c, d, e, f, g and h. The input to the sizing model also include the technical datasheet containing nominal operating values from original equipment manufacturers. The datasheets are presented in the appendix. The results in figures (i), (j), (k), (l), (m), (n), (o), (p), (r), (s), (t), (u), (v), (w) and (x) was obtained from the implementation of the enhanced deterministic algorithm represented in the flowchart in fig.3.1. The algorithm implementation was quite challenging as the weather data was CSV format and had to be imported into MATLAB and transformed as an array. The direct normal and diffuse radiation was used to calculate the total radiation and beam radiation. The clear sky index was obtained from the total radiation and the direct normal radiation.

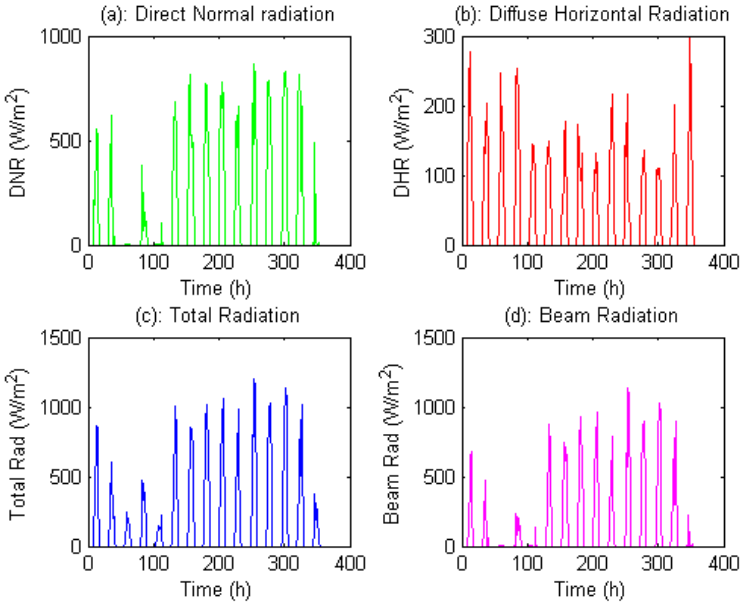

Figure 3.3 Inputs data obtained from weather stations in Zhouhan Island and National Renewable Energy Laboratory. The Direct Normal Radiation and Diffuse Horizontal Radiation are measurement data while total and beam radiation were calculated

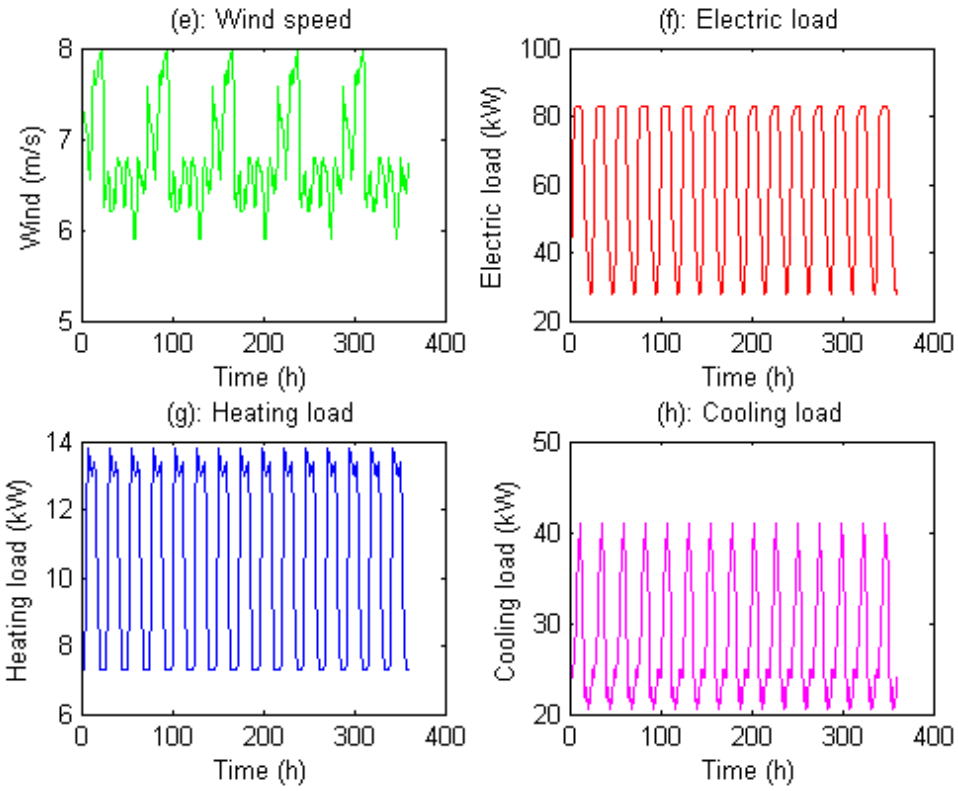

Figure 3.4 The wind speed input data are measurement data. (f)Electric, (g) Heating and (h) cooling load are also measured values for 30 days

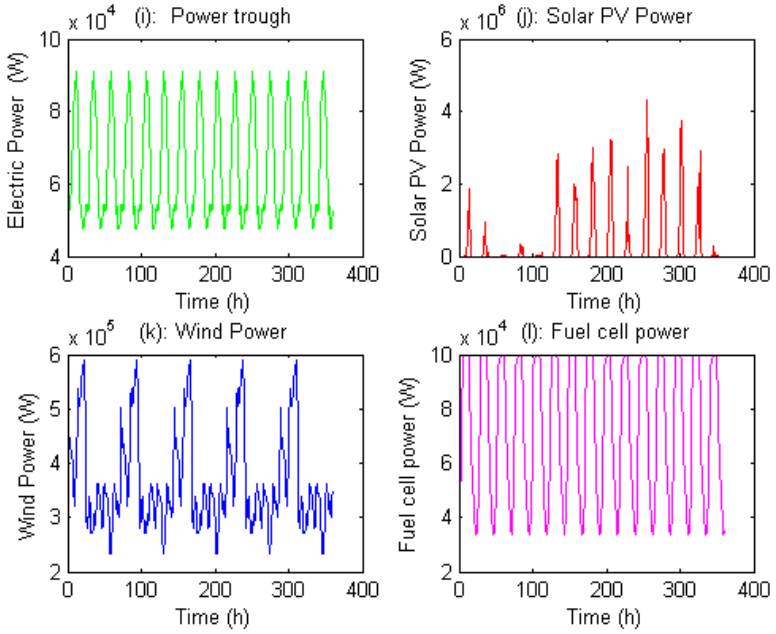

Figure 3.5 Power produced or generated and computed using enhanced deterministic algorithm of the HCCHP model with script written in MATLAB; (i) The parabolic trough thermal to electric power; (j) solar PV power; (k) power from the wind turbine; (l) Power produced from the excess power produced from electrolyser after meeting demand

Fig. 3.5 (i) shows the trend of electric to thermal power over a 360 hour's period with a maximum of 90 kW of electric power. The electric power is obtained from the conversion of the thermal power using a Stirling engine or Rankine thermodynamic cycle. The power produce from the removal of heat from the surface of the solar module attached to the parabolic trough receiver have a maximum value of 400 kW at 200 h represented in Figure 3.5 (j). The PV power trend captures the erratic nature of solar power the power produce during sun down is captured by the gaps between successive peaks. In a mathematical sense, there are discontinuities between peaks. The excess power generated from the PV modules is diverted or stored as hydrogen to meet demand during sun down. The power produced from the wind turbine also captures the stochastic behaviour of the wind and at maximum of 600 kW represented in figure 3.5 (k). In Figure 3.5 (l), the power produce from the excess power will meet the demand when supply fall short demand.

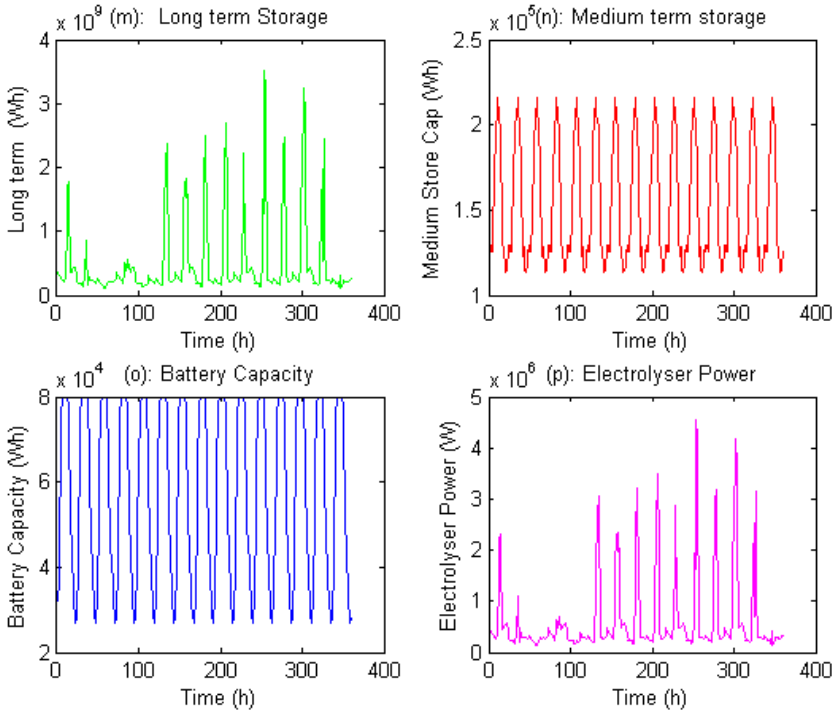

Figure 3.6 The long term storage hydrogen storage (m); medium term heat storage (n); short term battery storage (o); Electrolyser power obtained from excess power diverted (p)

The fig. 3.6 (m), (n), (o) and (p) are storage capacity obtain from the excess energy generated from the solar and wind resource. The long term storage is of the 10^9 order compared to the 10^5 for the medium term and 10^4 for the short term storage. The values represent the time involved in storing the excess energy, long term storage can last up to 3 weeks, 2 days for medium term and a day for short term storage. The electrolyser current in fig. 3.6 (p) shows the trend or variation of the current requirement by the water electrolyser for the

production of hydrogen for long term storage. The values are proportional as the selected electrolyser has a high voltage requirement of 200 VDC.

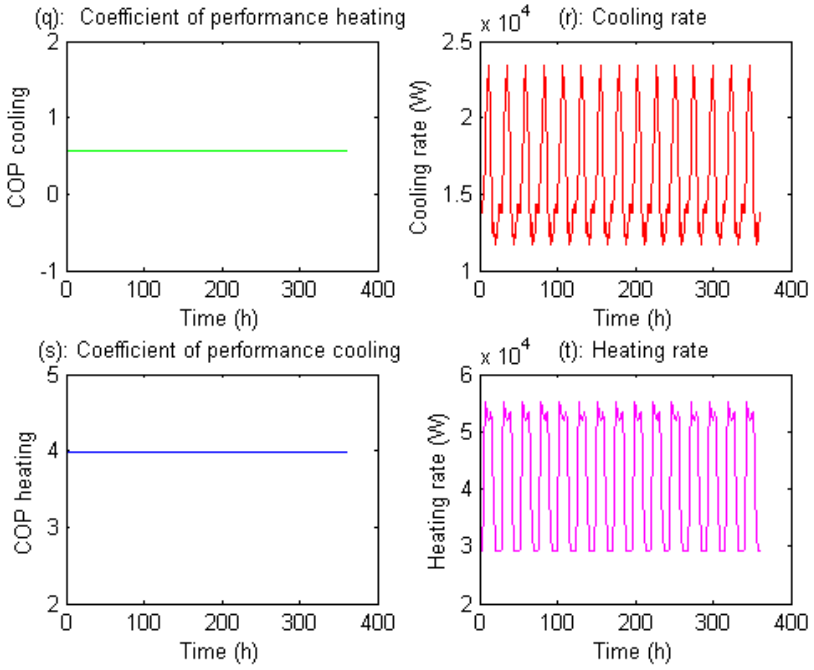

Figure 3.7 Coefficient of performance for heating (q); Coefficient of performance cooling thermal comfort performance index(s); cooling rate (r) and heating rate (t)

The cooling and the heating requirement for the HCCHP system is captured by the result in fig. 3.7 (q), (r), (s) and (t). The coefficient of performance which is an index for quantifying the cooling and heating rate is 0.5 for cooling and 4 for heating. The index is a ratio of the cooling and heating rate to the input energy to the system. The heating rate is more than a factor of 2 compared to the cooling rate.

The state of charge (SOC) for the hydrogen storage metal hydride tank for long storage, the electrolyser current, the battery state of charge and the battery charging current is shown in figure 3.8 (u), (v), (w) and (x). The SOC is dimensionless quantity for indicating the extent of energy in an accumulated or buffer storage system. From (u) the maximum state of charge of 100% occurred 280 hours in the 30 day's monthly cycle and the minimum average of 10% depth of discharge.

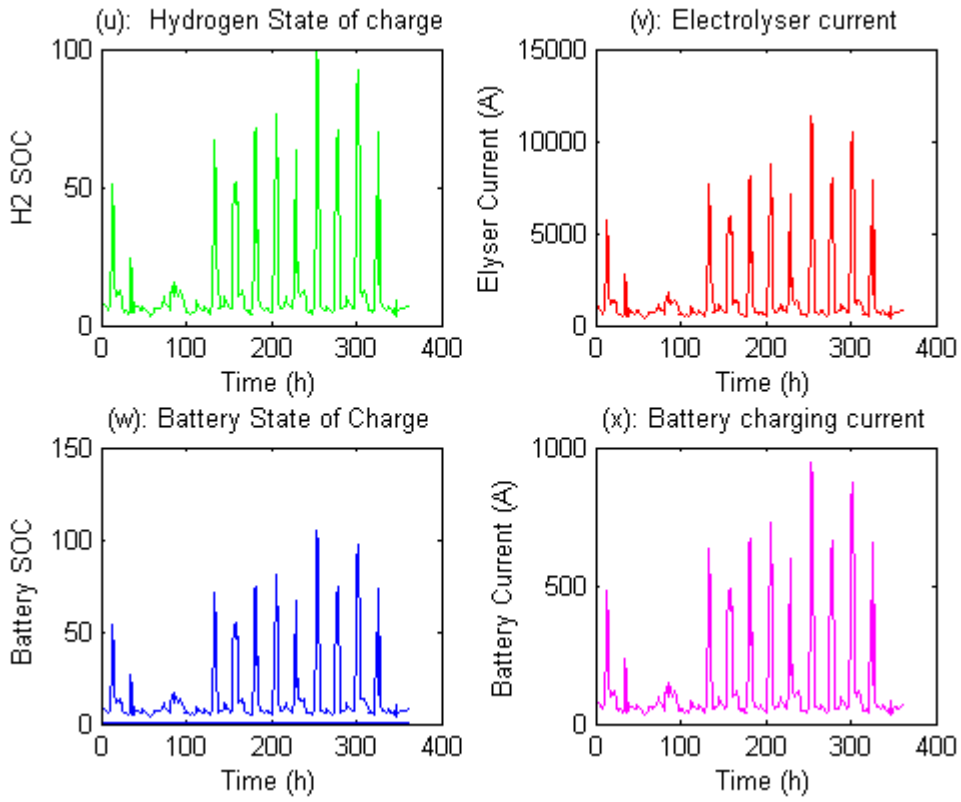

Figure 3.8 The state of charge for hydrogen long term storage (u); state of charge of short term battery storage (w); Electrolyser current (v); battery charging current (x)

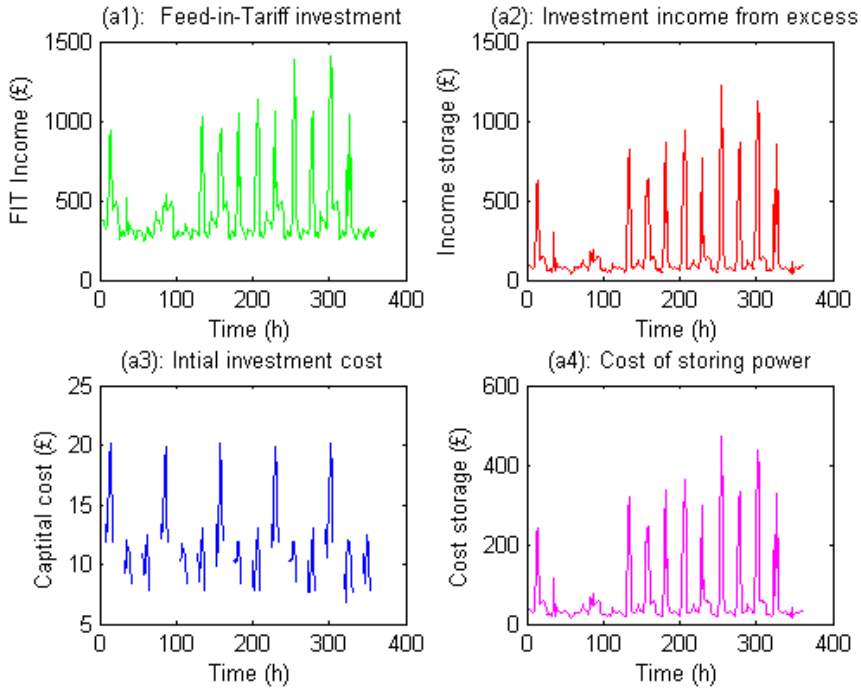

Figure 3.9 Feed-in-tariff present value investment income (a1); present value income obtained from storing excess power generated (a2); Initial investment cost (a3); cost of storing excess power generated (a4)

The economics of the hydrogen combined cooling heat power is shown in fig. 3.9 (a1), (a2), (a3) and (a4). The feed in tariff (a1) is the investment that will accrue if the power generated is to be sold to the grid. A maximum of £1480 occurred 280 hours in the 30 day's monthly cycle spread over a 20-year design life of the HCCHP system. The maximum value corresponds to the time of maximum availability of solar and wind resources. The power diverted to charge battery, electrolyser to produce hydrogen, investment that will accrue if the excess power generated is to be sold to the grid. In fig. 9 (a2) A maximum of £1250 occurred 280 hours in the 30 day's monthly cycle spread over a 20-year design life of the HCCHP system. The initial capital outlay of £20 spread over a 20-year period with discontinuity between peaks in fig.3.9(a3). The discontinuity is as a result of unavailability of solar and wind resources. In fig. 3.9 (a4), the maximum cost of £500 occurs at 289 hours when the solar and wind resource at it maximum. The storage cost is the expenses incurred during storage such as running the compressor during charge and discharge cycles.

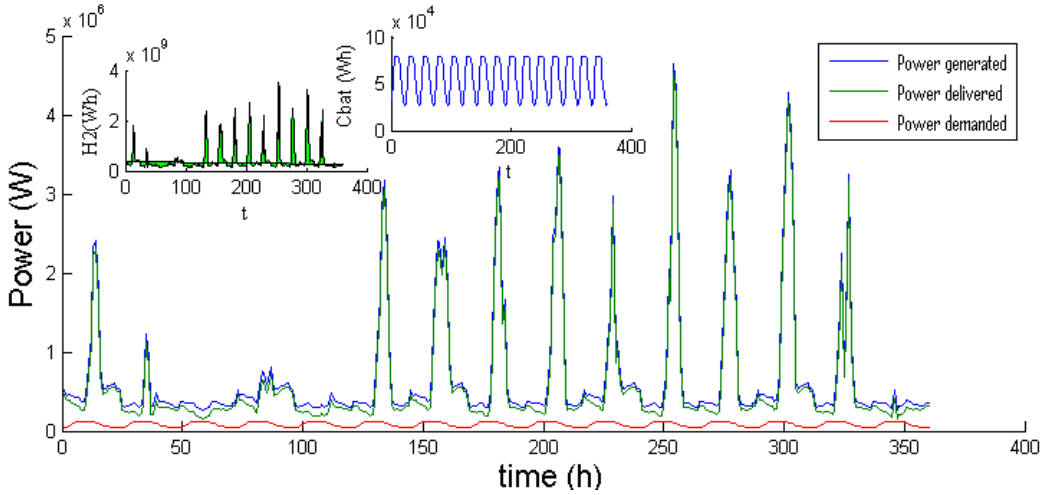

Figure 3.10 Power generated, delivered or supplied to meet electrical load, electrical load demanded, hydrogen long term storage and battery short term storage. A pictorial dispatch schedule

In fig. 3.10, is the comparison trend between the power generated, delivered and demanded. The two smaller plot shows the trend of the hydrogen and battery storage. The demand by from the electric load is met by the total power generated and the generation exceeds the demand. The excess power produce in store as hydrogen for long term storage short term battery storage, as seen in the hydrogen H2 versus time and Cbat versus time plots. The sizing subsystem were optimally sixed to meet demand.

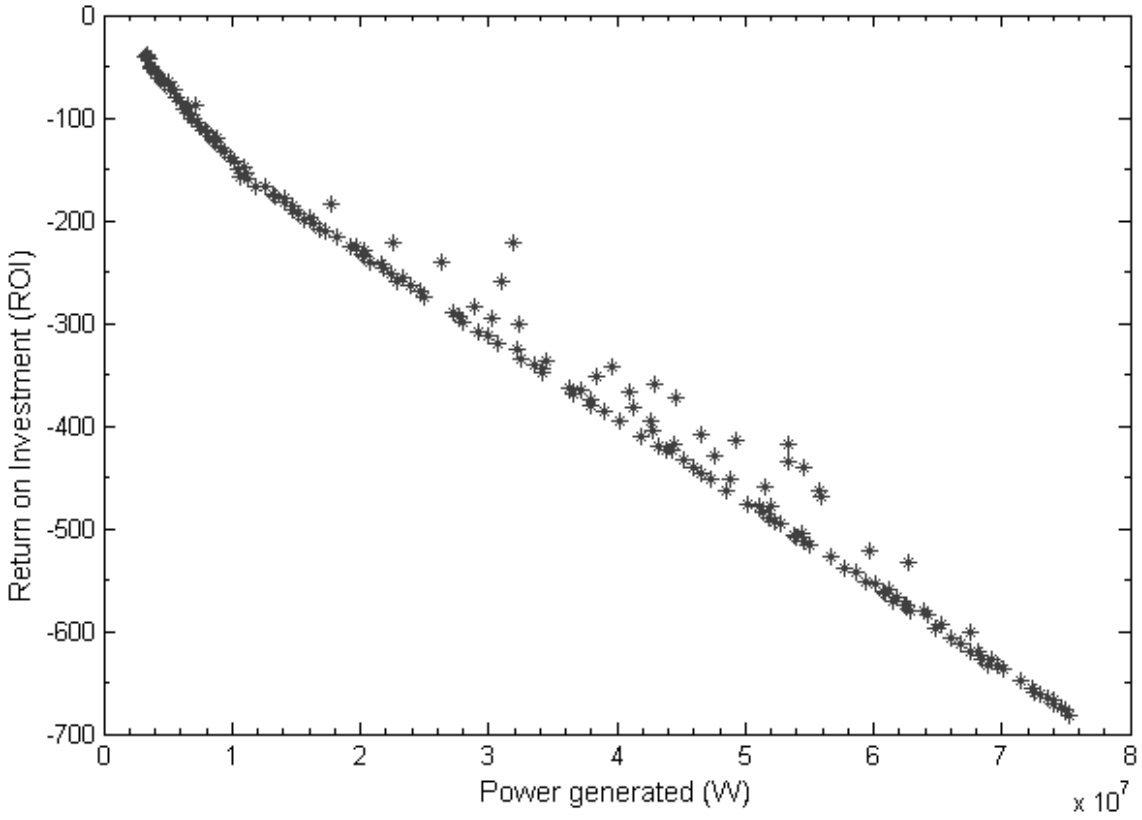

Figure 3.11 Pareto front of bi-objective optimisation of Return of Investment as a function of total power generated (Thermal-to-electric, Photovoltaic and Wind turbine)

The power delivered trailed the produced or generated, the differential is the power stored to meet demand during sunset and absence of wind. The demand is met all of the time in the 30 days simulation period as depicted in fig. 3.11. The dispatch is activated only if the battery is fully charged and the excess is used to activated electrolyser and provide power through the fuel cell.

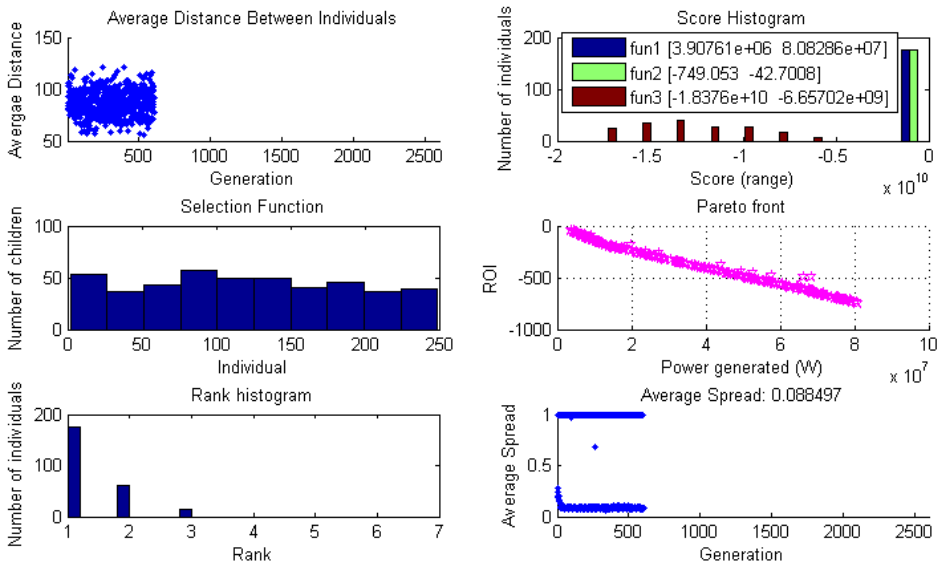

Figure 3.12 Multi-objective optimisation using NSGA II genetic algorithm; Scoring range histogram for individuals, selection function of the individual's number of children; Pareto front for the annualised capital cost as objective 2 and the Loss of power supply probability as objective 1; the distance between each individuals; The rank histogram of the individuals in the selection; the average spread of all the generations

3.8 Design optimisation validation results

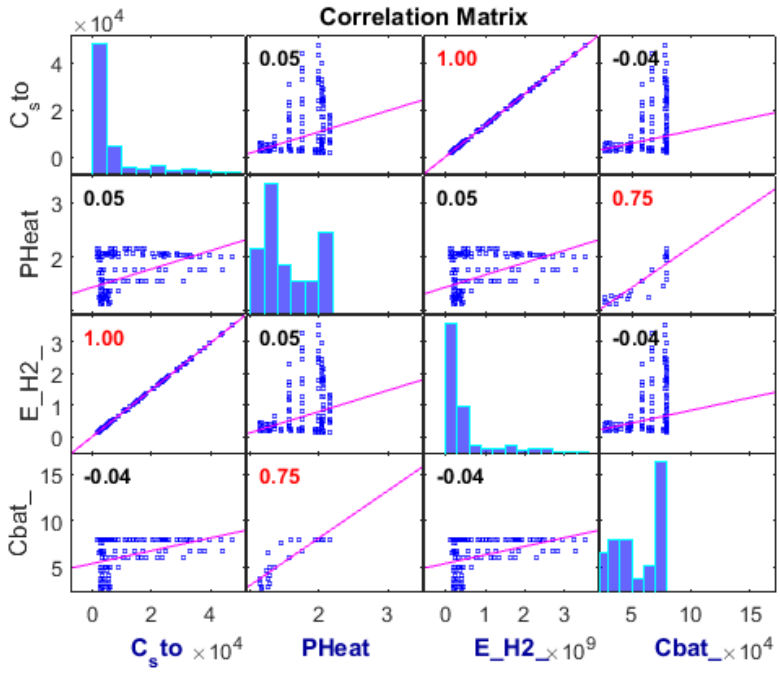

Figure 3.13 Parameter Kendall correlation of Cost of short, medium and long term

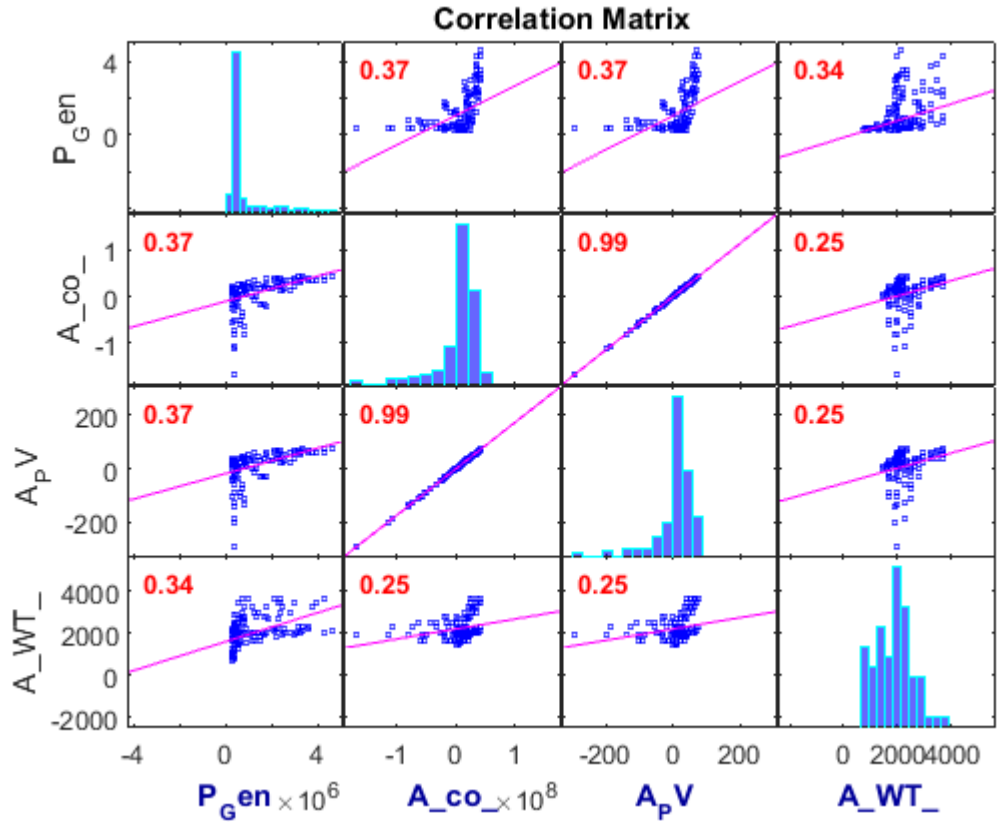

Figure 3.14 Parameter Kendall correlation of combine generation with the area of solar parabolic trough collector, PV module and the wind turbine swept area

In fig. 3.14 the total power generation is correlated to the sizes of the of the solar thermal collector, PV module and the wind turbine all have a positive Kendall correlation coefficient of 0.37, 0.37 and 0.34 respectively. The area or sizes of the increases with the power generated, which is expected.

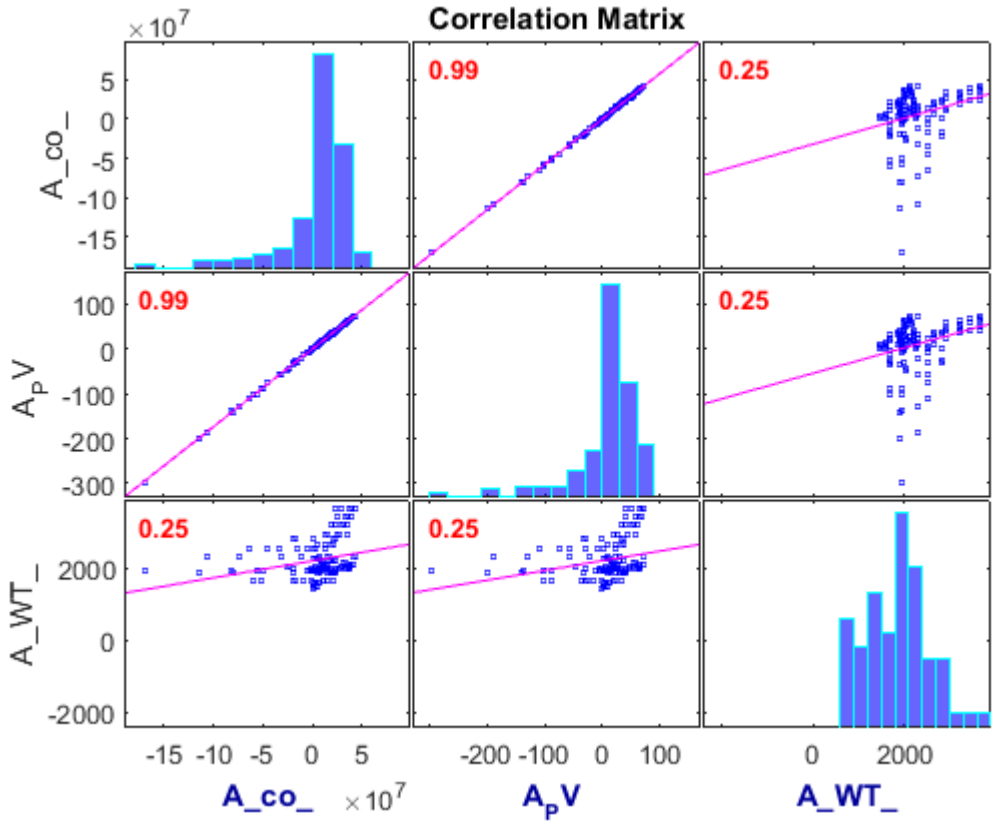

Figure 3.15 Size Kendall parameter correlation of solar parabolic trough collector, PV module and Wind turbine swept area

In fig. 3.15, the correlation scattered plot of the sizes of collector and the PV module is 0.99. This a strong relationship and an indication of the dependency of the size of the solar parabolic receiver and the PV module. The correlation of the wind turbine size on the solar parabolic trough collector and the PV module, though positively correlated is weak. Hence, this is an indication that wind turbine sizes is less significant in determining the sizes of the solar collector and PV module.

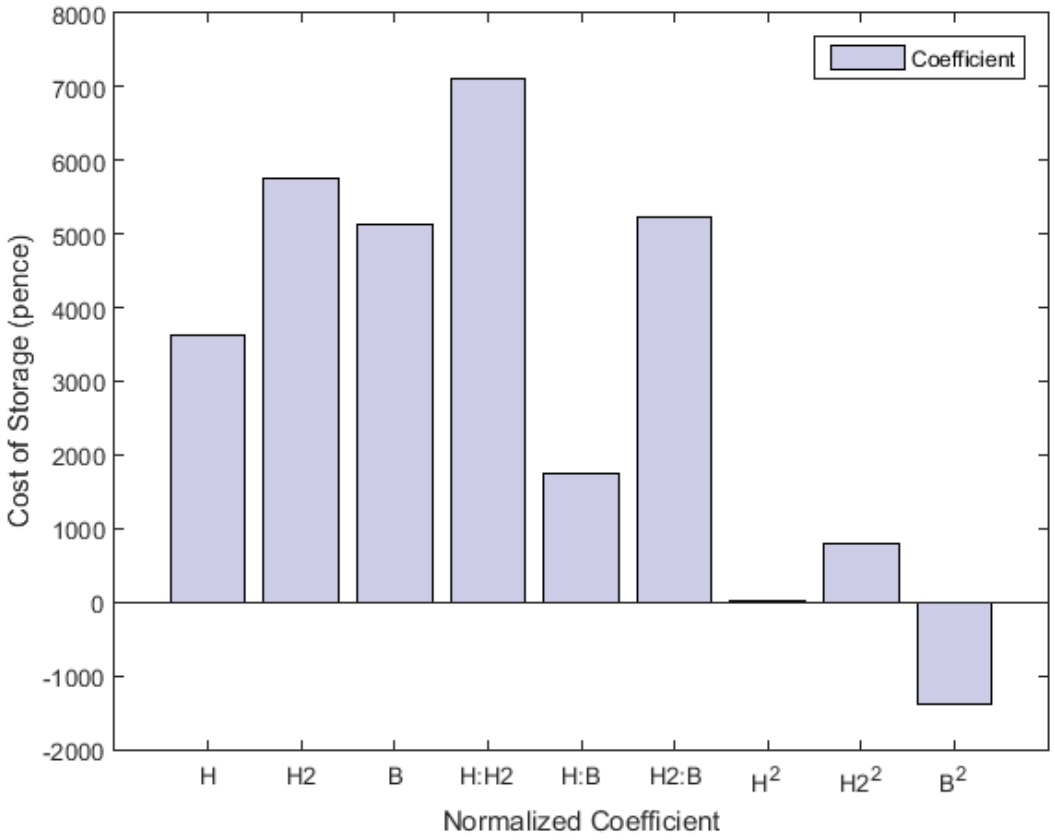

Figure 3.16 Coefficient of determination of cost of storage, long term hydrogen storage, medium term heat storage and short term battery storage

Fig. 3.16, shows the coefficient of determination of cost on the long, medium and short term storage. The effect of heat and hydrogen storage is higher and much more significant than all the other storage combinations. In an island or even grid scale storage, heat and hydrogen combined make the best storage combinations.

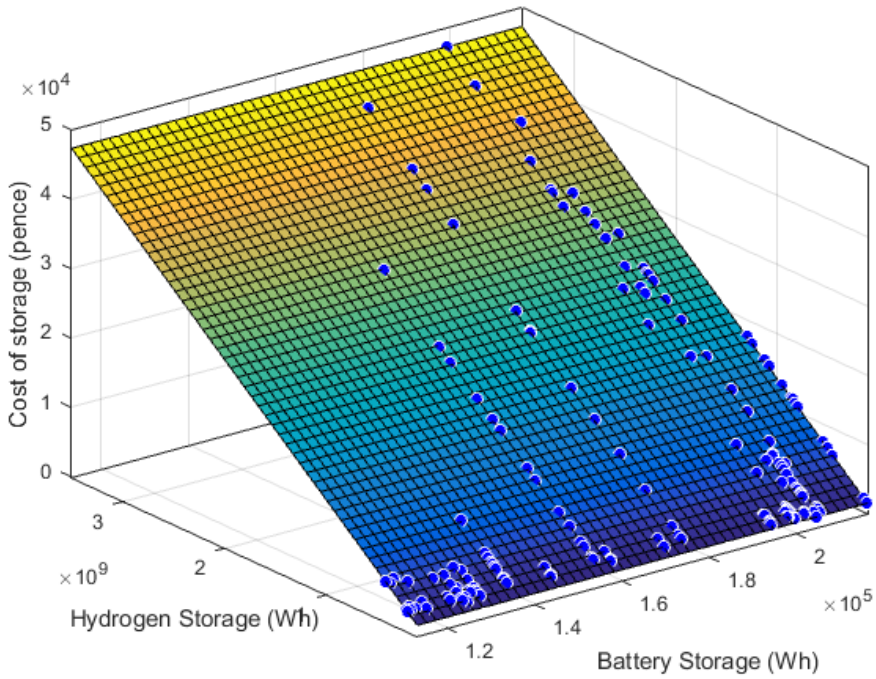

Figure 3.17 Response surface of cost of storage, long term hydrogen storage and short term battery storage capacities

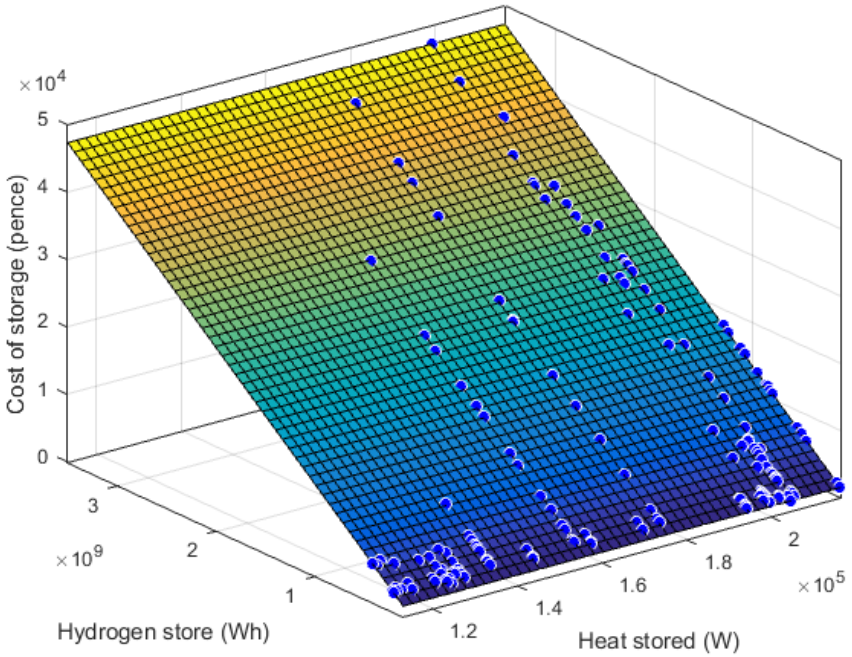

Figure 3.18 Response surface of cost of storage, long term hydrogen storage and medium term heat storage

The response surface plot in fig. 3.17 and 3.18, shows the variation of combined hydrogen storage and battery storage, combined heat and hydrogen storage with cost of storing the excess energy from the excess energy. The cost of both combinations is about £480. The cost is the same because the time of storing the medium and the short term storage is the same.

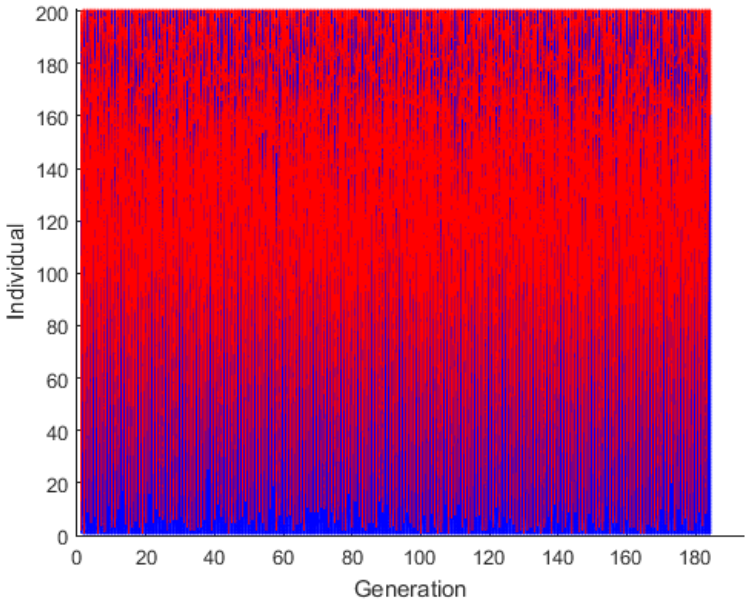

Figure 3.19 Genealogy plot of the NSGA II multi-objective optimisation of the individual design space variables and the generations

3.8.1 Sizing result obtained from the MOGA NSGA II optimisation

The sizes and number of each subsystem that constitutes the HCCHP obtained from enhanced deterministic algorithm and the design optimisation based on MOGA NSGAII algorithm are summarised in table 3.2. The Multi-objective NSGAII parameters use for obtaining the solutions are presented in table 3.

Table 3.3 Sizes, number of subsystems and time of energy-to-power ratio (time of storage) for short term, medium term and long term storage in HCCHP

Design space variables (Number of subsystems)		Sizes of subsystems	
Number of subsystems	**Values**	**Subsystems**	**values**
x (1)	101	P_{th}	64940 W
x (2)	116	P_{pv}	328000 W
x (3)	9	P_{wG}	366000 W
x (4)	2	P_{FC}	72300 W
x (5)	34	P_{Ely}	31500 W
x (7)	2	P_{bat}	57869 W
x (8)	3	P_{H2}	969400 W
x (10)	5	V_{heat}	3.695 m^3
x (12)	14	V_{H2}	1.4×10^8 Nm^3
x (13)	17	C_{bat}	1206 Ah
Design space storage Energy/power (time)			
Time of storage	Value (h)		
x (6)	4		
x (9)	115		
x (11)	6		

The result from table 3.3, present and interesting findings, the HCCHP can only hold or provide battery short term storage for 4 hours during the day, 6 hours of heat between midnight and the early hours of the morning and can provide long term hydrogen storage for 5 days (115 h). The values are very much dependent on the wind and solar resources availability.

Table 3.4 Parameters and values of MOGA NSGA II solver and algorithm settings

Parameters	Value
Population size	250
Creation function	Constraint dependent
Selection	Tournament
Reproduction crossover fraction	0.8
Crossover function	Intermediate
Migration direction	forward
Migration fraction	0.2
Migration interval	20
Pareto front population fraction	0.7

Table 3.4 shows the parameter settings of the solver and the solution converged after 276 iterations. The optimisation routine was automatically terminated after the average change in the spread of Pareto solutions less than options selected at the beginning.

3.8.2 Validation of results obtained

The verification and validation of the numerical code is a 2 phase approach, first the validation for the enhanced deterministic algorithm and the second is the design optimisation.

3.8.2.1 Validation of the enhance deterministic algorithm

A trend test validation approach, which is a time-series behaviour of a certain output. A tests on a single Proven 15 wind turbine selected for the sizing model one by one to compare the trend in 1-year, 30-day and 24-h time span due to seasonal demand and generation difference as well as amplitude of important factors. In this thesis, the power output curve from simulation model and the Proven 15 turbine from the manufacturer specification were compared and presented in figure 12 as follows;

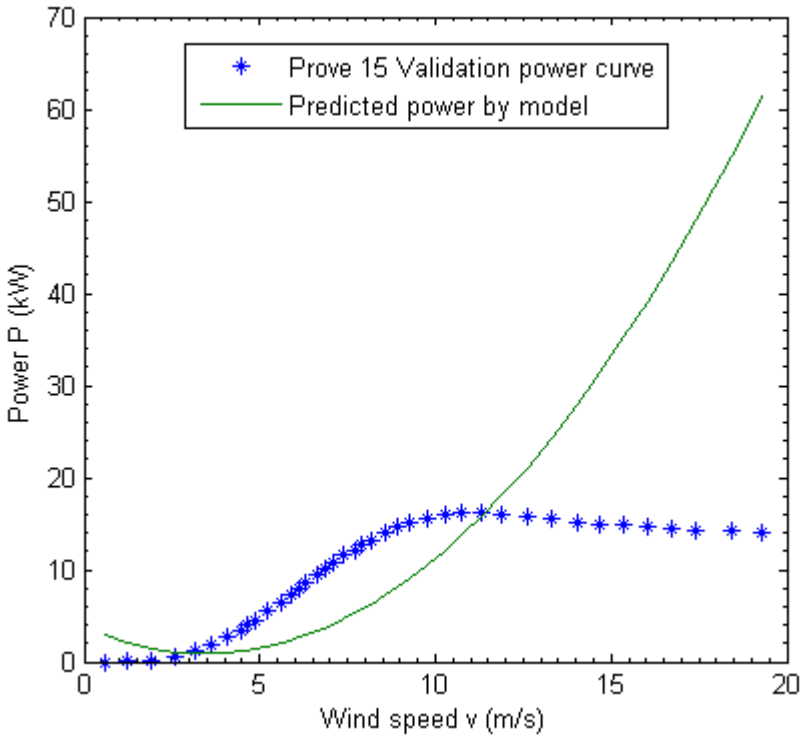

Figure 3. 20 A trend test validation of power curve from Proven 15 wind turbine and the predicted power from simulation model

In Figure 3.20, the deviation of the of the generated power from the power curve specification is due to much more power generated from the power produced by a single Proven 15 wind turbine rated at 15 kW. In the island HCCHP, more than one wind turbine in multiples and the right spacing are installed to meet demand. The number of wind turbine was determined by the NSGA II, genetic algorithm.

3.9 Summary and concluding remark

In this chapter an enhanced deterministic and design optimisation based on Non-dominated Sorting Genetic Algorithm II (NSGA II) duo was applied to obtain optimum size of the HCCHP subsystems. The enhanced deterministic algorithm complemented the NSGA II in obtaining the constraints from datasheets. A solar thermal PV hybrid system supported by wind turbine provided the power and a short term, medium term and long term storage was provided by battery, heat and hydrogen.

The optimum sizes of subsystems obtained, was able to meet short term, medium term and long term demand with least computational resource as the multi-objective optimisation converge at the global optimum with Pareto front for generation, return on investment and emission control. The decision search space variables are the numbers of solar thermal receivers, solar PV modules attached to the solar receivers, number of wind turbines,

number of fuel cells, number of batteries, number of hydrogen storage tanks, number of electrolysers and heat storage tanks.

The proposed sizing method was used to obtained the optimum sizes of the subsystems to provide electric power, heat and hydrogen to meet alternating current, heating and cooling demand for a remote island located in Zhoushan, China. The was used to test the effectiveness of the sizing algorithms since the solar, wind resources, electric, cooling, and heating loads were available. The model can be applied to other site if similar data are available. The data was supported by data from National Renewable Energy Laboratory as the data from the Island lacked data on the direct normal insolation, day of the year, sun azimuth and zenith angle required for computing the total and diffuse radiation.

The size of subsystems obtained from the deterministic algorithm 65 kW solar thermal to electricity, 327 kW solar PV, 366 kW wind power, 72.3 kW fuel cell, 57.9 kW battery storage, 969 kW hydrogen storage and 155 kW heat storage. These values are average values since the model was based on 30 days' simulation, at 1-hour variation. The number of subsystems were computed by the NSGA II algorithm as set of non-dominated solutions. A 70% Pareto efficiency was use as a decision support or judging criteria to imposed a penalty weighing factor to obtained the number of subsystems.

Conclusively, the model was able to predict and capture the stochastic and intermittent behaviour that characterise a renewable energy resource like the sun and wind. This trend is represented in the power generated, storage, investment and cost plots presented in the preceding sections. The island storage short term storage for 4 hours during the day, 6 hours of heat between midnight and the early hours of the morning and can provide long term hydrogen storage for 5 days (115 h). The result validate hypothesis I and II proposed at the beginning of the chapter. The third hypothesis was validated by the chart in figure 10 since the power demanded is far less than that supplied and generated.

3.10 What next

The conclusion on the sizing study provide the basis for system and control study in chapter 5 and 6 to help in understanding the effect of undersizing and oversizing on the HCCHP system.

Chapter 4 Shape selection of parabolic trough PVT receiver by inverse Design Optimisation

4.1 Introduction

Sequel to related work cited in chapter 2, the circular shape of about a century old was found to be suboptimal. Two new shapes, a semi-circular and triangular are proposed and design optimisation approach is applied to establish the shape with the optimum heat transfer area corresponding to the lowest friction factor or lowest resistance to flow of the heat transfer fluid, without discriminating or favouring either of the selection criteria. The approach adopted completely automated starting from a what-if analysis of the initial shape best guess, followed by a correlation studies that provides parameters that matter to the analysis of the shape and its the output. A design of experiment takes the parameters from the correlation studies based on the design space and bind them within the design space. A response surface provides the interpolation algorithms that produce the line for 2D and surface for 3D visualisation of how the input parameters predict the output parameters, based on a mathematical model. A multi-objective GA provides a design set of shape based on a criteria for minimum heat transfer area and pressure drop. Finally, a Six-Sigma or robust design was used to benchmark the shape to ensure that shape works well both in the virtual world and the real world, based on uncertainty such as ease or difficulty of manufacture and operator handling during the manufacturing process. The approach is validated by comparing the analysis conjugate heat transfer numerical study results with experimental result from a solar simulator, the experimental results by Dudley et al., (1984) and empirical correlations.

4.1.1 Hypothesis from literature

Following the citations form previous shape of solar parabolic heat collecting element, it was hypothesised that;

(i) the triangular shape geometry of the parabolic trough PVT is a better shape compared to the semi-circular shape in terms of maximum heating enhancement (Nusselt Number) and minimum pumping number (Fanning friction factor)

(ii) The manufacturability of the semi-circular shape is easier and cheaper than the triangular shape

The intent of the shape selection design optimisation above is to validate the two hypothesis above.

4.2 Proposed shapes of the solar non-conventional radiation heat transfer receiver/PVT exchanger.

The proposed shape of the solar non-conventional radiation heat transfer receiver, popularly referred to as parabolic trough receiver, are the semi-circular cross-section half cylindrical paraboloid sandwiches of glass, EVA film, triple junction PV modules, Tedlar back sheet, half copper tube for the semi-circular profile and a copper angle for the triangular pyramidal geometry and the copper oxide propylene glycol Nano fluid heat transfer fluid. The details of the both proposed geometry is illustrated in figure1 below.

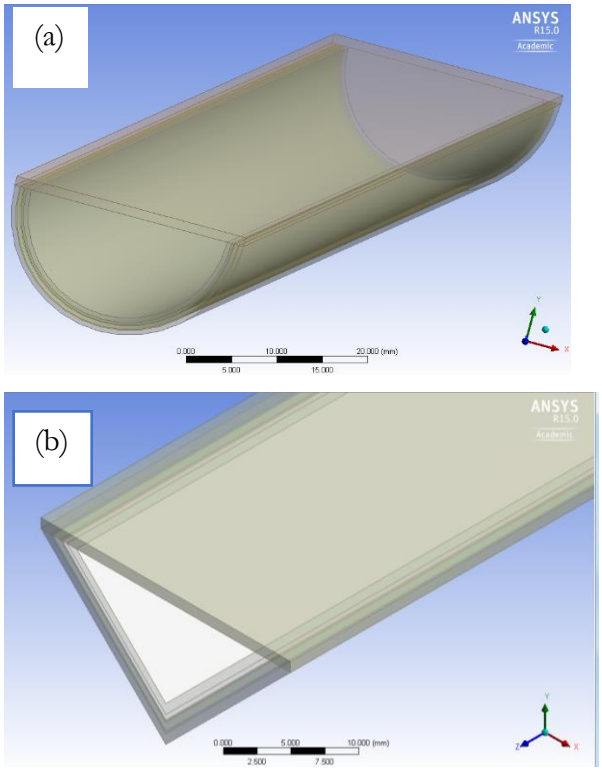

Figure 4.1 Proposed geometry of the PVT receiver (a) semi-circular geometry of a half cylindrical paraboloid arranged layers of glass, EVA film, triple junction PV modules, Tedlar back sheet, half copper tube and copper oxide propylene glycol Nano fluid heat transfer fluid (b) triangular pyramidal geometry arranged in the same way as the semi-circular geometry of glass, EVA film, triple junction PV modules, Tedlar back sheet, copper angle and the copper oxide propylene glycol Nanofluid heat transfer fluid

4.3 Mathematical Foundation: The continuity, heat transfer and momentum equations

The numerical iterations of the proposed geometry flow field velocity, mass balance and the temperature or heat transfer was obtained, through an iterative solution of the momentum

equation, continuity and energy equations, expressed as partial differential equations and presented below. The PDE's predict the flow fields about the heat transfer fluid and the temperature about the solids and HTF. The numerical solutions of the flow fields were obtained using a commercial Multiphysics software package ANSYS FLUENT and ANSYS Design Explorer. The flow through the cylindrical paraboloid and the triangular pyramidal is laminar with Reynold number of 18.69 as this captures realistic behaviour of the momentum and heat transfer in the geometry and incompressible with constant physical properties.

4.3.1 Assumptions

The following assumptions are made in underpinning the mathematical equations of the laminar flow physics;

- Incompressible flow through the cylindrical paraboloid and the triangular pyramidal
- Steady state and laminar forced convection with a neglible viscous dissipation and buoyancy contribution
- A Newtonian behaviour for the Heat transfer fluid
- A constant thermo-physical properties for fluids and solids

4.3.2 Continuity equation

The continuity equation predicts the mass balance, based on the mass conservation law in which the unsteady partial change term in the Naiver Stokes equation is zero, consequence of the incompressible heat transfer fluid. The continuity is given in equation (1);

$$\nabla.(\rho u) = \rho\left(\frac{\partial u}{\partial x} + \frac{\partial v}{\partial y} + \frac{\partial w}{\partial z}\right) = 0 \tag{4.1}$$

4.3.3 Heat transfer equation

The heat transfer equation is a conservation of energy, which can be qualitatively stated as the change in energy equal to the heat source minus the divergence of the diffusive heat flux. The second order 3 dimensional equation solves for the temperature in the fluid and solid domains in the semi-circular paraboloid and triangular pyramidal sandwiches. The PDE for the energy conservation equation is given in equation.

$$\rho C_p\left(\frac{\partial T}{\partial t} + u.\nabla T\right) + \nabla.(-\kappa\nabla T) = Q \tag{4.2}$$

4.3.4 Momentum equation

The basic steady state laminar flow equation momentum equation is the equation of motion relating the velocity of the heat transfer fluid u along the radial direction x, axial velocity v in the y direction and the longitudinal velocity w along the z direction in Cartesian coordinate, to the pressure field, the dynamic viscosity and the stress tensor, accounting for the resistance to flow along the wall. The equation can be written as and presented in (4.3), (4.4) and (4.5).

$$\rho\left(u\frac{\partial u}{\partial x}+v\frac{\partial u}{\partial y}+w\frac{\partial u}{\partial z}\right)=-\frac{\partial P}{\partial x}+(\mu+\mu_t)\left\{\frac{\partial^2 u}{\partial x^2}+\frac{\partial^2 u}{\partial y^2}+\frac{\partial^2 u}{\partial z^2}\right\} \quad (4.3)$$

$$\rho\left(u\frac{\partial v}{\partial x}+v\frac{\partial v}{\partial y}+w\frac{\partial v}{\partial z}\right)=-\frac{\partial P}{\partial y}+(\mu+\mu_t)\left\{\frac{\partial^2 v}{\partial x^2}+\frac{\partial^2 v}{\partial y^2}+\frac{\partial^2 v}{\partial z^2}\right\}-\rho g_y \quad (4.4)$$

$$\rho\left(u\frac{\partial w}{\partial x}+v\frac{\partial w}{\partial y}+w\frac{\partial w}{\partial z}\right)=-\frac{\partial P}{\partial z}+(\mu+\mu_t)\left\{\frac{\partial^2 w}{\partial x^2}+\frac{\partial^2 w}{\partial y^2}+\frac{\partial^2 w}{\partial z^2}\right\} \quad (4.5)$$

The iterative solution of the four Eqs. (4.1), (4.2), (4.3), (4.4) and (4.5) was obtained using the Semi-Implicit Method for Pressure Linked Equation (SIMPLE) algorithm, a brainchild of Patankar and Spalding (Versteeg & Malalasekera 1995). The details of the procedure are in the work of Versteeg & Malalasekera (1995).

4.3.5 Thermophysical properties of heat transfer fluid and the solids in the receiver PVT assembly

The thermo-physical properties of the heat transfer fluid were computed from correlations while that of the solids were obtained from databank and literatures, presented in table 4.5.

Table 4.1 Thermo-physical properties of the heat transfer fluid computed from correlations and solids properties obtained from databank and literatures

	Solids and Fluids					
Properties	Glass	EVA	Triple junction PV	Tedlar backsheet	Copper Plate & tube	Heat transfer fluid
Density (kg/m^3)	2550	960	2000	1530		3156.5
Specific Heat (J/kg.K)	50	1400	840	1760		1709.1
Viscosity (N/s.m^2)						0.0261
Thermal conductivity (W/m.K)	0.8	0.34	93	0.36		0.381

4.4 Research approach and methodology

In the research planning, a critical consideration was given to the methodology applied in obtaining or arriving at the optimum shape of a geometry. Generally speaking, the aerospace industry has had a long history in optimisation and selection of best shape of an airfoil of an aircraft wing. Shape selection methods could be achieved either by direct or inverse optimisation method.

4.4.1 Direct shape optimisation method

In the direct numerical optimisation methods, aerodynamic analysis methods are coupled with numerical optimisation algorithms. It involves minimising (or maximising) a given aerodynamic objective function by iterating over a geometry directly. The geometry parametrised and represented by a general function, such as polynomial and cubic splines, by a linear combination of known airfoils, or by a basic shape plus a combination of typical geometry perturbations. The shapes are selected through search algorithm such as the gradient-based method (GM) and simulated annealing (SA) Press et al., (1992). SA is a heuristic strategy for obtaining near-optimal solutions, and derives its name from an analogy to the annealing of solids. Apart from SA, Genetic Algorithm, one of the evolutionary algorithms design result demonstrates the superiority of GA for aerodynamic optimisation compared to others. However, GAs application to CFD problems, was limited by intense numerical or computing power required by the direct numerical optimisation methods. The

direct approach requires CFD flow field evaluation of each member of the population and at every generation in GAs. Consequently, it requires a huge amount of computational time, making the inverse approach more flexible for engineering shape optimisation applications.

4.4.2 Indirect or Inverse shape optimisation method

The inverse numerical optimisation methods which deals with pressure flow field distributions rather than the geometry, to minimise, maximise a geometrical shape is computationally benign alternative to the direct method. In the approach flow fields are the primary variable for specifying a design space objective target. Once the target pressure distribution is optimised, the corresponding shape can be obtained by the inverse methods. The methods itself form a class of powerful design tools for selecting optimum shape of a geometry. These methods solve the classical inverse problem of determining the CFD shape which produce some given flow field distributions. However, the method is not fool proof as it leaves the designer with the problem of interpreting the design goals into properly defined flow field distributions exhibiting the required CFD or Multiphysics characteristics (Labrujere and Slooff, 1993).

4.4.3 Inverse design optimisation methodology

The method selected for this research work is an inverse method driven by a statistical decision support design optimisation approach. In this method, the temperature and pressure flow fields of the conjugate heat and fluid flow over the semi-circular and triangular geometry. The methodology involves a 2-prone approach;

4.4.3.1 The Analysis phase

In the analysis phase, the geometry of the proposed shapes is created in ANSYS design, the shapes are discretised in ANSYS mesh, the temperature and pressure flow fields are obtained using ANSYS FLUENT Multiphysics solver and the shapes are post processed with ANSYS post processing tool to obtained the output variables (temperature and pressure contours). The whole scheme is managed by ANSYS workbench.

4.4.3.2 Design optimisation-inverse design phase

In the Design optimisation-inverse design phase, multiple design point spurn-off by a what-if analysis and design of experiments sampling, using a parameters correlation to screen variables that matters and affect the design space and use response surface to connect or interpolate the design point sample by the design of experiment. The optimisation iterates and select the best candidate meeting a set of multiple objectives. A robust design optimisation ensures that what is predicted by virtual CAD driven product development

process works in the real world. The section that follows considers the various part of the design optimisation process and a work flow is provided in figure 1.

In fig. 4.1, the results of the flow field distribution enter into the design optimisation, starting with the "what-if analysis" of the design point. The is a non-scientific or trial and error approach to explore the effect of the design space variable on the output Nusselt number and the fanning friction factor. The parameter correlation, design of experiment, response surface, optimisation and finishing with a six-sigma robust design. The decision support design optimisation was driven by a hard hand coded parameter correlation, design of experiment, response surface, NSGA II Multiobjective optimisation and Six-sigma in MATLAB. The procedure is automated as a co-simulation paradigm.

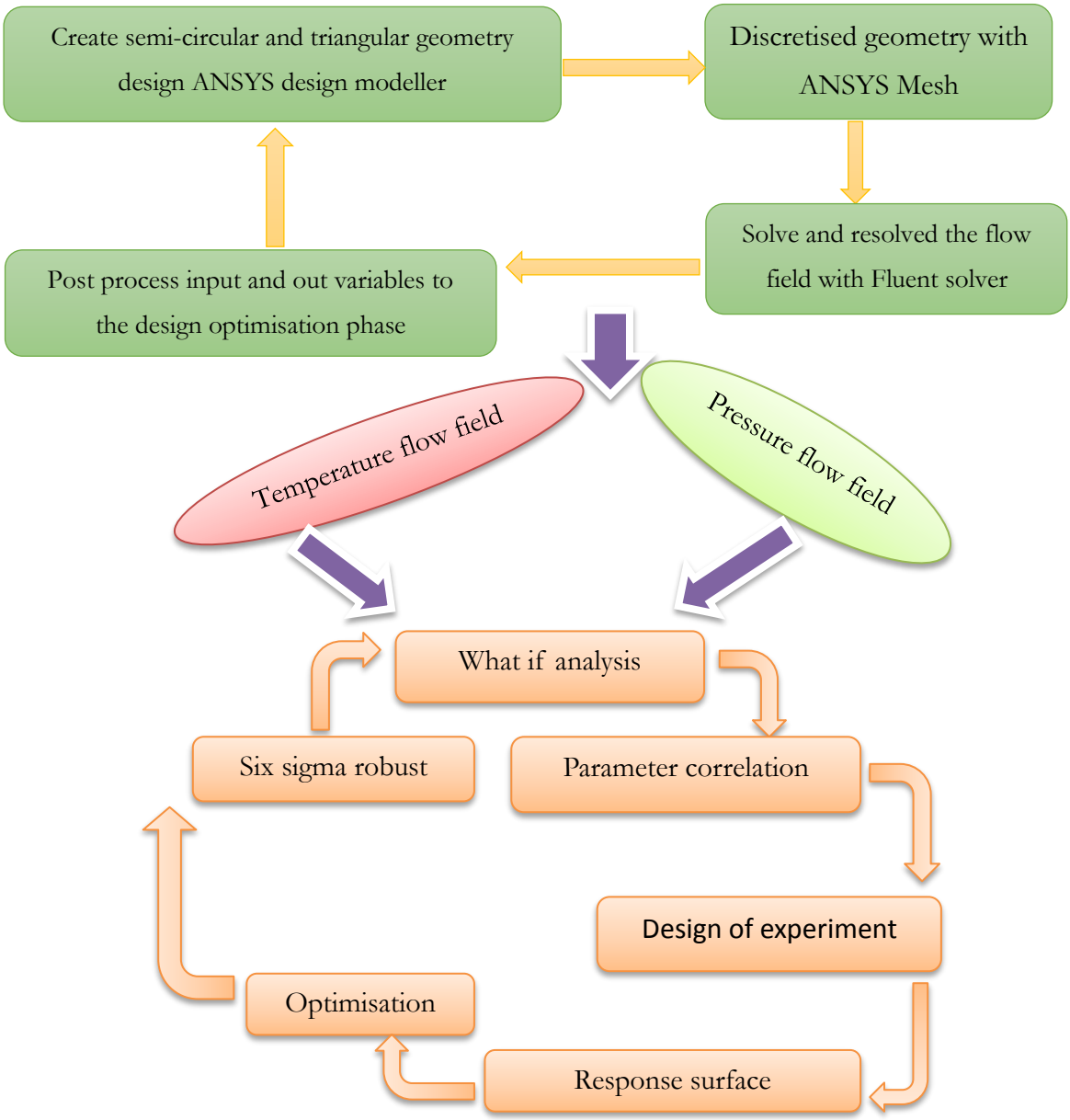

Figure 4.2 Workflow of the analysis phase and the inverse design optimisation shape selection algorithm. The analysis flow field distribution results are fed to the design optimisation decision support phase driven by MATLAB

4.5 Numerical solution approach of analysis problem

The standard operating procedure for solving thermofluids problem, is to prescribe the geometry, generate mesh or discretise the geometry, apply boundary conditions, specify the thermophysical properties and solve the governing partial differential equations to obtain the velocity, pressure and temperature fields. This problem is referred to as analysis problems solution approach.

The numerical iterative solution methodology was based on the pressure velocity coupling, Semi-Implicit Method for Pressure-Linked scheme of Patanker and Spalding. It is a guess-and-correct iterative procedure for computing the pressure on a staggered grid arrangement. The iterative procedure was activated by the SIMPLE algorithm calculation process, where the pressure field was guessed to initiate the calculation.

Evaluation of the objectives of the proposed shape

The main trust of the analysis was to obtain the velocities flow, pressure flow field and the temperature fields to enable the best shape that capture and convert the solar radiation to heat and electricity at optimum heat transfer rate and at least material.

Shape geometry design

The geometry was design with ANSYS design modeller, a geometry creation tool. Creating the geometry was a bit of a challenge after tweaking with solidworks and exported to design modeller and geometric parameters were a nightmare to activate as input in the parameter module in ANSYS. The geometry was design starting with a 2D profile of a circle, circle was trim, and assigned a sketch plane in the XY plane. The EVA, tedlar, triple junction cells, copper tube and heat transfer fluid were all assigned separate plane and the 3d extrude feature was assigned to all eight planes and the extrude features were frozen to separate each solids and fluid domain. The new part was formed from the eight parts to make the sandwich parts, with one part and eight solids communicating with themselves. The fluid was selected from the solids domain in design modeller. The same procedure was followed in making the geometry for the triangular pyramidal sandwiches.

4.5.1 Generation of structure mesh of the proposed geometry

The geometry meshing was obtained using ANSYS meshing module in the ANSYS software suite. The mesh quality to large extent affect the result of a thermofluid study. The mesh was set for CFD. Name selection for the 7 solids domain and the heat transfer fluid domain was created in the meshing tool including the inlet and the outlet flow surfaces. The number of nodes and elements for the semi-circular paraboloid is 3894422 and 3729600 respectively, while that of the triangular pyramidal is 2662709 and 2512800 respectively. The orthogonal mesh metric minimum, maximum and average are 0.5639, 1 and 0.9796 for the semi-circular paraboloid shape, while the orthogonal mesh metric minimum, maximum and average are 0.3659, 1 and 0.8112 for the triangular pyramidal shape.

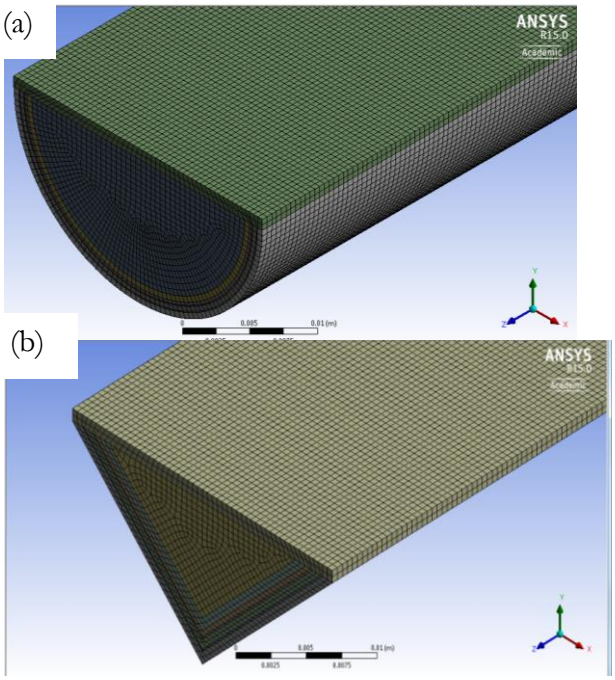

Figure 4.3 Structure mesh of both geometry (a) structure mesh of the semi-circular paraboloid with minimum size of 0.00004, maximum face size of 0.0005 and maximum size of 0.0005 (b) structure mesh of the triangular pyramidal sandwiches with minimum size of 0.00004, maximum face size of 0.0005 and maximum size of 0.0005

4.5.2 Boundary conditions

The boundary conditions for the complicated sandwich geometry were generated by Fluent solver, once the name selections for the solid domains and surface domains were created in the ANSYS meshing module. The 32 boundaries were generated and populated in the boundary condition tab. It is important to state that semi-circular and triangular geometry were modelled numerically as full geometry, since the overall strategy is to perform a design optimisation, with geometry dimension parameter update iteratively. The boundary conditions have been sub-divided into entry-exit, interior, and wall conditions for the sake of better quality of presentation. The inlet velocity edged boundary condition was set as velocity magnitude; the interiors boundary conditions were set zone Names of the body geometry in the zone; The walled thermal conditions for the EVA, Tedlar, half copper tube, were set to convection while that of the Glass cover and the triple junction modules were set to Heat Flux and the value of the heat flux was set to the beam radiation. The wall thermal condition for the top copper plate cover heat flux was set to total radiation. It is important to state that Wall-copper_half_tube- propyleneglycol_nano_fluid boundary condition and the Wall-copper_half_tube- propyleneglycol_nano_fluid-shadow condition, which provide or ensure transfer of heat between the solid domain and the liquid domain

was set to coupled and the shadow zone the wall motion was set to stationary; Shear condition was set to No slip and the convective thermal condition was set to coupled.

4.5.3 Solution of the governing coupled equations for the flow variable and the energy on the mesh generated

The continuity, momentum and energy equations were solved using the Semi-Implicit Method for Pressure Linked equations (SIMPLE). The justification for choosing the SIMPLE solver was because of it robustness compared to the SIMPLEC, which is for problems with simple geometries and the PISO algorithm which is more suitable for unsteady problems. Essentially, in the SIMPLE algorithm the calculation proceeds with a guess of the pressure field and the momentum equations 3, 4 and 5 discretised from the ANSYS meshing are solved iteratively with the initial guessed pressure field to obtain the velocity component u, v and w and temperature$\emptyset$. A correction was made to the initial guessed pressure to obtain the true pressure. The same correction is made to the velocity and temperature fields. A detailed procedure for implementation of the corrections are contained in the work of Versteeg and Malalasekera, (2007). This proceeds until convergence was reached as indicated in the residuals monitor. The modelling was for both laminar and turbulent flow using enhanced wall functions for the favourite k-ε model.

4.5.4 Verification and validation of numerical SIMPLE solution to the flow fields

It is a good numerical practice to check solutions to flow fields before post processing the result to analyse key result quantities. The mass conservation or mass imbalance test ensures that the mass is conserved as dictated by the continuity equation. This was done by calculating the mass flow rate flux between the inlet and the outlet boundary conditions. Another verification check is the discretisation error, which is done by refining the mesh with body and edged sizing with an increase in the size from 30 to 100 and inflation mesh refinement by increasing the maximum layer from 10 to 50. The momentum imbalance check is ensuring that rate of change of linear or axial momentum is conserved. It is the axial momentum control volume enclosing the heat transfer fluid from the inlet to the outlet of the receiver PVT geometry, as this is the part of the geometry where momentum transport occurs. This procedure involved creating a user defined function in the axial momentum balance in the ANSYS result module. Post-processing of the obtained results to extract the values of the objective functions for these specific shapes

The post processing was the final step in the analysis part of the numerical prediction of the laminar and turbulent flow behaviour of the receiver PVT geometries. The overall aim was to visualise the pressure, temperature and velocity contours; the velocity vectors and the streamlines for the entire geometries. The temperature along the length or Z axis, outlet

pressure and the velocity at the centre of the receiver were plotted in 2D, using the chart tool in ANSYS result module. The Skin friction and the Y plus was also plotted. The two most critical output quantities, the friction factor and the Nusselt number were extracted and created as user defined functions, with the aid of the CFX expression language. The Nusselt number was computed from the global radiation heat flux, the heat transfer coefficient was computed from the wall temperature and the mean temperature. The characteristic length is a key parameter that quantifies and characterise the shape of the receiver, as it is the ratio of the hydraulic area of the heat transfer fluid to the wetted perimeter of the heat transfer fluid.

4.5.5 Grid independence study

The mesh independence study involves a series of mesh refinement for both geometries and proceed from coarse mesh, to medium mesh or grid to fine and even finer mesh. This was done for both laminar and turbulent conjugate heat transfer flow predictions. The result for the coarse was divergent as shown in the residual monitors and temperature contours. The medium and fine mesh with sizing gave a better result as indicated in the residual monitors and temperature contours. The medium mesh was 790088 elements, 274980 nodes and orthogonal quality are 0.99917 maximum and 0.10326 minimum. The finer mesh was pretty high to ensure that the solution is totally independent of the grid or mesh sizes. The finer mesh has 5664398 elements, 1518309 nodes and orthogonal quality of 0.99969 maximum and 0.21824 minimum. This was done for the laminar prediction. Turbulence model k-ε with standard wall function, did not converge and there was serious mass imbalance and instability. The concentration ratio was increased to 2 from default 1 by multiplying the beam radiation ($2\times 800\ w/m^2$) @ the Wall-Glass_cover boundary condition and @ the Wall-Triple junction condition.

Turbulence model k-ε with Enhanced wall function, the solution converged and the mass imbalance was eliminated and stability was restored. The concentration ratio was increased to 2 from the default value was doubled by multiplying the beam radiation (2×800 w/m^2) @ the Wall-Glass_cover boundary condition and @ the Wall-Triple junction condition. There was instability in the energy residuals. Perhaps, the hybrid initialisation was also important in attaining the stability and elimination of the mass imbalance. The standard initialisation method produce a very unstable result, as a result it was discontinued. It is also important to state that, a refined mesh by adding 2 Edged sizing at the inlet and the outlet help in convergence. However, there was serious energy imbalance from the residuals monitor. The under relaxation factor was decreased to fixed the imbalance

4.6 Design optimisation problem numerical solution approach

4.6.1 Parameter correlation

The parameter correlation commences from where the manual optimisation fails by identifying and addressing the key driving parameter for the receiver shape that keeps heat transfer optimum yet keeping the friction factor minimal to reduce the cost of pushing the heat transfer fluid through the receiver. The parameters correlation uses the input parameters of input geometry parameters, such as length and the inner radius of the heat transfer fluid, thickness of the top copper plate and the glass cover outer diameter and thickness, to spurn out the output parameters. The parameter correlation determines which input parameter have the most or least effect or impact on the design or selection of the right shape. It also goes further by identifying the degree to which the relationship is linear or nonlinear i.e. quadratic or cubic. This is based on Spearman rank correlation and the Pearson's linear correlation. The correlation studies could be set up for either of the two algorithms.

4.6.2 Spearman's rank Correlation

This is a nonparametric test used to measure the degree of association between the input parameters and the output parameters (Statistics Solutions, 2016). The algorithm is based on ranking of samples from the what-if analysis and the correlation is based on the ranking of the design point samples. The Spearman approach captures the non-linear monotonic relationships between and across variables both independent (geometric parameters) and the dependent variables. A monotonic relationship could be increasing or decreasing. In the monotonic increasing procedure, as one variable increases the other variables increases as well, whereas in the monotonic decreasing relationship one variable increases the other decreases. The Spearman's is as postulated statistically to be the most accurate method for correlating variables. The mathematical relationship used for computing the ρ the Spearman ranking correlation is expressed mathematically in equation (4.6) (Zaiontz, 2016).

$$\rho = 1 - \frac{6\sum_{i=1}^{n} d_i^2}{n(n^2-1)} \tag{4.6}$$

where the ranking difference between all the variables $d_i = rank\ x_i - rank\ y_i, n$ is the number of design points, $x_i$is the independent variables (geometry parameters, length and the inner radius of the heat transfer fluid, thickness of the top copper plate and the glass cover outer diameter and thickness) and the y_i dependent variables (Nusselt number and the friction factor).

4.6.3 Pearson's linear correlation

According to Zaiontz (2017), the Pearson's correlation is statistical measure of the degree of associativity or relationship between linearly dependent variables. From the definition, the Pearson's correlation can handled a linear relationship between variables and tends to fail in predicting nonlinear relationships. It uses the actual design point sample data to evaluate the correlation coefficient. The computation of the coefficient of multiple correlation R as expounded in the free online encyclopaedia Wikipedia, the free encyclopaedia (2017), as transpose of the vectors of the correlations between the predictors independent variables (geometric parameters of the receiver PVT geometries) and the target dependent variables (Nusselt number and the friction factor), multiply by the inverse of correlation matrix R_{xx} and vectors of the correlations between the predictors independent variables. This is expressed mathematically in Eq. (4.7) (Zaiontz, 2017).

$$R^2 = c^T R_{xx}^{-1} c \tag{4.7}$$

where $c = (r_{x1y1}, r_{x2y2}, \dots, r_{xnym})^T$, n is the number of independent variables and m is the number of dependent variables.

$$R_{xx} = \begin{pmatrix} r_{x1y1}, r_{x1x2} & \cdots & r_{x1yn} \\ \vdots & \ddots & \vdots \\ r_{xnx1} & \cdots & r_{xnxn} \end{pmatrix}$$

The expectations from the parameter correlation is that the correlation matrix chart, correlation scatter chart, determination matrix chart, determination histogram chart and the sensitivity chart visually bring to life all relationships between independent and the dependent variables in design space envelope. The strength of parameter correlation is that it compares the weight of each input independent variables against the output independent variables, however, does not necessarily address the bounds of the design envelope. This is where design of experiment fits in the entire design optimisation workflow.

4.6.4 Design of experiment

Design of experiment as expounded by Canonsburg, (2013) is a statistical scientific method used to determine the location of sampling point in the design space envelope. It takes the weighted input from the parameter correlation and distribute sample points optimally within a bounded design space. Also, it runs and generate the discrete unconnected point specified

by the lower and upper bounds of the input independent variables. There is a wide range of DOE algorithms, the most commonly used are the Central Composite Design (CCD), Box-Behnken design, Latin Hypercube design and the Optimal Space-Filling design (OSF) (Canonsburg, 2013).

4.6.5 Response surface

The response surface is an interpolation of discrete design point spurn-out by the design of experiment, to come up with a smooth mathematical formulation. The mathematical formulations can be used to capture the output behaviour at other design point that was not addressed during the design of experiment sampling. It formalises the mathematical relation in which output dependent variables are mapped into the input independent variables in the design space envelope. It provides a sound understanding of how each dependent output parameters is driven by input independent variables parameters and how the design can be modified to improve its performances. There are several meta-modelling algorithms for creating a response surface, there are the standard response surface-full 2^{nd} order polynomial, Kriging, Non-Parametric Regression, Neural Network and the Sparse Grid algorithm (Canonsburg, 2013).

4.6.6 Goal driven optimisation

In the goal driven product development optimisation, the design space from the design of experiment (DOE) is searched to obtain the optimal candidates based on user specified goals and priorities. It is a sort of response surface amplifier and adds requirement for advance optimisation algorithms to efficiently search the design space envelop for the optimum candidate participating in design. It is more like a comparative reporting tool. The advanced optimisation algorithms are the screening, Multi-objective Genetic Algorithm (MOGA) and the Non-linear Programming by Quadratic Lagrangian (NLPQL). The MOGA algorithm is well suited for this research, as a trade-off must be sort between multiple conflicting objectives as specified in the output dependent variable of Nusselt Number and the friction factor (Canonsburg, 2013).

A solution is not possible in this case but a design set emerges from the optimisation. A Pareto optimal set is used to impose a penalty a-priori to ensure that no objective is favoured over the other. In this case the solution is said to be Pareto efficient, since none of the objective functions can be improved in value without degrading the other objective values. A Pareto percentage was specified for convergence control during computation, which is the ratio of number of desired Pareto points to the number of sample per iteration. It has a weakness of not addressing or capturing non-technical factors or uncertainty that affect the performance of the design candidate obtained. A robust design such as six sigma addresses this shortcoming.

4.6.7 Six Sigma robust design

In Six Sigma robust design, the extent to which uncertainties in the model affect the results of an analysis is captured through statistical distribution functions such as Gaussian (Normal), Log normal distributions etc. Uncertainties like manufacturing variables, operator handling and quality of materials are random variables that are impossible to determine at any given time or at a given location in the design space. The Six Sigma quality benchmarking criteria is that a product is six sigma qualify if only 3.4 parts out of every 1 million manufactured fail (Vlahinos, 2008).

4.7 Formulation of design optimisation Receiver PVT Problem

The formulation of the optimisation problem was based on the entry and exit boundary conditions such as inlet and pressure outlet conditions, the objective functions of maximising the heat transfer rate and minimising the pressure drop and the design input variables. The details are provided as follows;

4.7.1 Boundary conditions

The inlet velocity =0.0005m/s

Inlet temperature= 293K

4.7.2 Objectives

The objectives are;

To maximise heat rate, with the sole aim of reducing the volume of the receiver PVT geometry which is expressed in terms of the Nusselt number and to minimise friction losses, proportional to the pumping power number, expressed as fanning friction factor.

$$maximise, minimise = f\left(-Nu_{obj}, f_{p,obj}\right) \quad (4.8)$$

$$subject\ to\ ; g_i(x) = 0\ , i = 0 \quad (4.9)$$

$$H_j(x) \leq 0\ , j = 0 \quad (4.10)$$

$$lb \leq I_k(x) \leq ub\ , k = 1, \dots ,5 \quad (4.11)$$

4.7.3 Output dependent parameters

Heat transfer rate of the shapes expressed as Nusselt number which is a function of the heat transfer rate, the shape factor characteristic length and the thermal conductivity in Eqs. (4.12) and (4.20);

$$Max\left(Nu_{obj}\right) = \frac{q''\frac{Area}{Peri}}{k\left(T_w - T_{ref}\right)} \tag{4.12}$$

4.7.3.1 For the triangular shape

The area and the perimeter is given in Eq. (4.9) and (4.10) as follows;

$$Area = \frac{b_f h_f}{2} \tag{4.13}$$

$$Peri = 2l_s + b_f \tag{4.14}$$

The Nusselt Number of triangular shape is rewritten with the in Eqs. (4.13) , (4.14) and expressed in Eq. (4.15) as follows;

$$Nu_{Tri} = \frac{q'' b_f h_f}{2k(T_w - T_m)(2(\sqrt{(\frac{b_f}{2})^2 + (h_f)^2}) + b_f)} \tag{4.15}$$

4.7.3.2 For the semi-circular shape;

The curved surface area of a half cylinder and the perimeter given in Eqs. (4.16) and (4.17) as follows;

$$Area = \frac{\pi d_{cu} L}{2} \tag{4.16}$$

$$Peri = \frac{\pi d_{cu}}{2} + d_{cu} \tag{4.17}$$

$$Nu_{Semi\_Cir} = \frac{q''\pi d_{cu} L}{2k(T_w - T_m)(\pi d_{cu} + L)} \tag{4.18}$$

The Nusselt Number of semi-circular shape is rewritten with the equation in Eqs. (4.16) and (4.17) and expressed in Eq. (4.18) as follows;

where

$$T_m = \frac{\int_0^R urT\, dr}{\int_0^R ur\, dr} \tag{4.19}$$

$$Min\left(f_{p,obj}\right) = \frac{2\Delta P D_h}{\rho_f L u^2} \tag{4.20}$$

From the numerical post processing result the pressure drop is computed as a constant an average value 2.5×10^5 N/m^2 was used in the optimisation routine calculation.

4.7.4 Constraints in the design space

Table 4.2 Design space constraints for investigating the effect on the objectives for response surface, optimisation and robust six-sigma design

Design space constraints		
Parameters	Semi-circular shape	Triangular shape
Length (L) (m)	$0.8 \leq L \leq 2$	$0.8 \leq L \leq 2$
Internal diameter and height copper tube and triangular angle (d_c, h_{ca}) (m)	$0.0213 \leq d_c \leq 0.0223$	$0.0213 \leq h_{ca} \leq 0.0223$
HTF channel dimension (d_{HTF}, h_{HTF}) (m)	$0.018 \leq d_{HTF} \leq 0.0213$	$0.0213 \leq h_{HTF} \leq 0.0223$
Inlet velocity (u_{in}) (m/s)	$0.005 \leq u_{in} \leq 5$	$0.005 \leq u_{in} \leq 5$
Beam radiation (q_b) (w/m^2)	$300 \leq q_b \leq 1000$	$300 \leq q_b \leq 1000$

4.7.5 Design variables or Input independent parameters

The design variables are defined in table 4.7 for both geometries

Table 4.3 Geometrical parameters of the solids and heat transfer fluids for semi-circular paraboloid and triangular pyramidal sandwiches

	Solids and Fluids													
	Semi-circular paraboloid							Triangular pyramidal						
Geometrical Parameter	Glass	EVA	Triple junction PV	Tedlar back sheet	Copper tube	Copper top plate	Heat transfer fluid	Glass	EVA	**Triple junction PV**	Tedlar backsheet	Copper tube	Copper top plate	**Heat transfer fluid**
Length (mm)	1200	1200	1200	1200	1200	1200	1200	1200	1200	1200	1200	1200	1200	1200
Width (mm)	NA	NA	NA	NA	NA	26	NA	NA	NA	NA	NA	NA	NA	NA
Thickness (mm)	1	0.2	0.8	0.5	1	1	18.6	1	0.2	0.8	0.5	1	1	18.6
diameter (mm)	26	24.8	24	23.3	22.3		21.3	NA	NA	NA	NA	NA	NA	NA

4.8 Importance and limitation of the research

The research is important considering the need for increased capacity in distributed power generation. A determination of the optimum shape configuration that harvest the solar radiation and transfer it to heat and direct current will increase the overall efficiency of solar thermal generation and mitigate the concern for global warming.

Interesting as this study is, there are myriad of challenges that emerge in attempting to obtain the shapes. Computing resource required for Multiphysics and design optimisation decision support system of a 3D realistic simulation is a huge problem. One of the challenge that was contended with was updating the design table during the "what-if analysis" and the other process fails as result of licences unavailability, as each design point requires licence. The problem was resolved with MATLAB statistics and machine learning toolbox. A scripts MATLAB files was created with temperature and pressure flow fields from ANSYS Fluent software packages to automate the design optimisation process.

4.9 Analysis and findings of result obtained

The result obtained are the 3D analysis numerical temperature, pressure flow field, 2D plots axial and radial and inverse-design optimisation such as parameter correlations, response surface plot, design cube for DOE, optimisation plot and the six-sigma plot. The results are presented in fig 4.4;

4.9.1 Analysis problem results

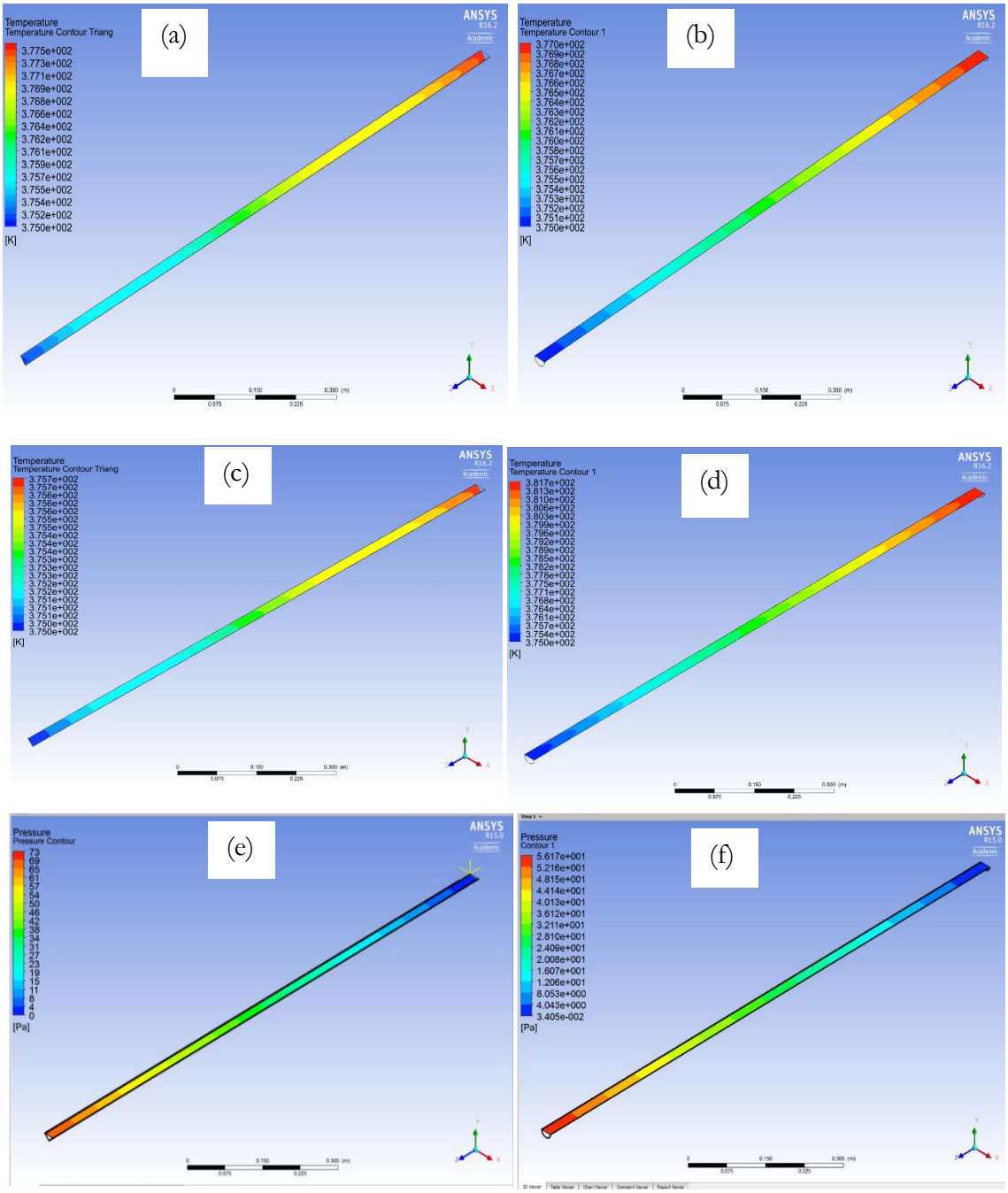

Figure 4.4 Temperature and pressure contour flow field of triangular and semi-circular shape; (a) Temperature contour flow field for triangular shape at 2m/s;(b) Temperature contour flow field for semi-circular shape at 0.005 m/s;(c) Temperature contour flow field for triangular shape at 0.005 m/s;(d) Temperature contour flow field for semi-circular shape at 0.005 m/s;(e) Pressure flow field contour for triangular shape;(f) Pressure flow field contour for semi-circular shape

In fig. 4.4, a, b, c, d, the temperature of the heat transfer fluid changes and increases from the inlet and attains a maximum at the outlet as supported by the 2D line plot in fig. 4.5 overleaf. Fig. 4. 4 e and f shows the variation of the pressure along the length of the receiver decreasing from the maximum at the inlet and zero at the outlet.

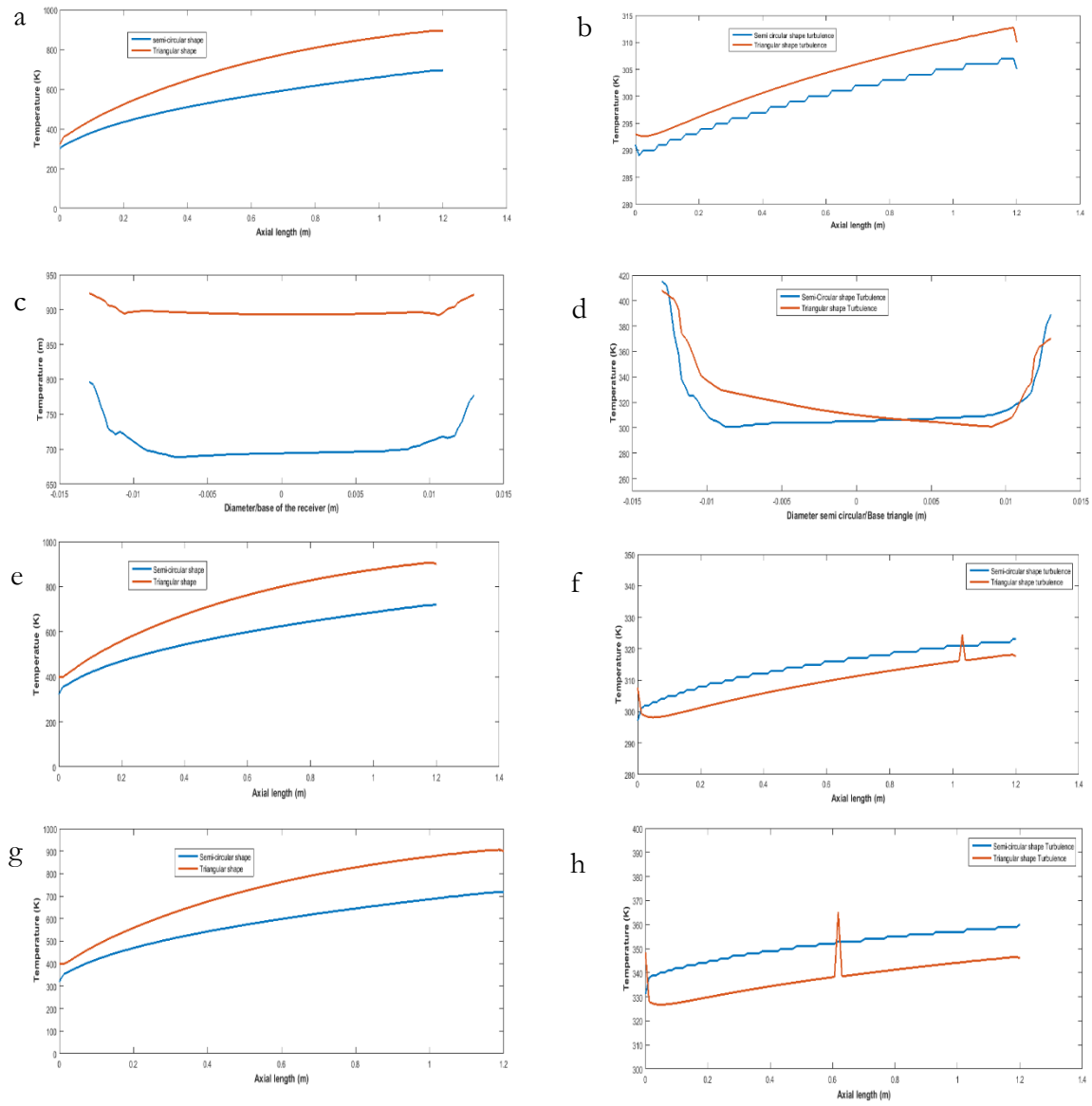

Figure 4.5 Analysis temperature plots of the heat transfer fluid, copper half tube wall and the outer surface of the triple junction solar module; (a) temperature along the axial length of the semi-circular and triangular shape receiver in laminar flow; (b) temperature along the axial length of the semi-circular and triangular shape receiver in turbulent flow; (c) temperature at the outlet of the semi-circular and triangular shape receiver cross-sections in laminar flow; (d) temperature at the outlet of the semi-circular and triangular shape receiver cross-sections in turbulent flow; (e) wall temperature profile along the axial length of half copper tube in laminar flow; (f) wall temperature profile along the axial length of half copper tube in laminar flow; (g) surface temperature profile along the axial length of triple junction solar module in laminar flow; (h) surface temperature profile along the axial length of triple junction solar module in laminar flow

From fig.4.5, the 2D plot of the triangular shape for turbulence and laminar flow along the length and the radial or circumferential direction in Fig. 4.5a, b, c, d, e, f and h shows that

the triangular shape heat transfer rate out stripes that of the semi-circular shape. The laminar flow is characterised by a higher temperature compared to the turbulence flow. This is as a result the higher residence time of heat transfer fluid in laminar flow compared to the low residence time in turbulence flow. The HTF stays longer in laminar flow but a trade-off must be reached to prevent spikes in circumferential temperature along the diameter of the circular shape and the base of the triangular shape. The 2D plots shows that the triangular shape absorbed more solar radiation than its semi-circular counterpart.

a

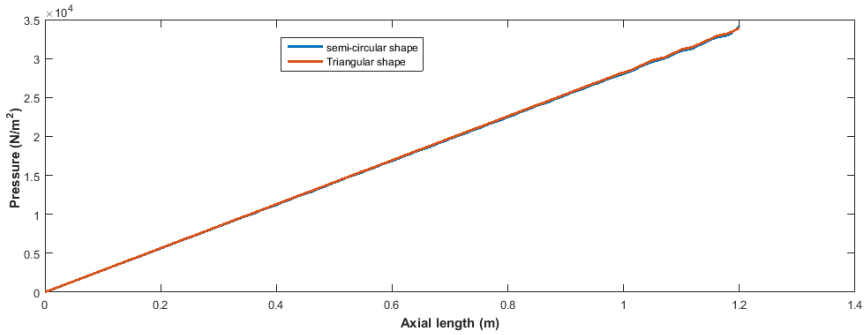

b

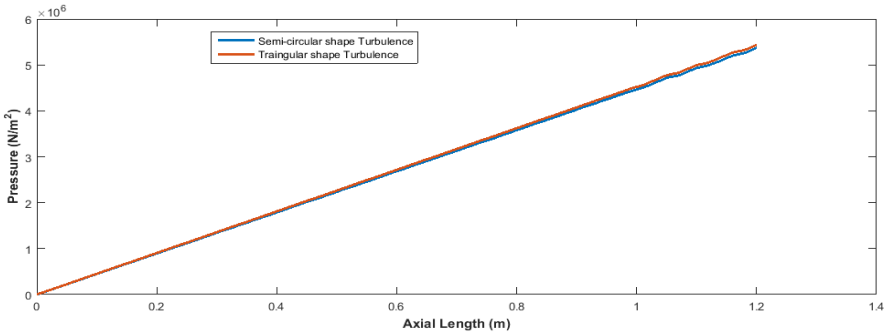

Figure 4.6 Pressure drop along the length of the receiver in laminar and turbulence flow; (a) variation in pressure drop of the semi-circular and triangular shape in laminar flow; (b) variation in pressure drop of the semi-circular and triangular shape in turbulent flow

From fig. 4.6 the pressure drop along the length of the receiver for both shapes is practically the same with no mark difference for laminar flow regime. However, for turbulence flow regime, the semi-circular design slightly outperforms the triangular design by 171 N/m2. The analysis results may not conclusively reveal the shape with a minimum pumping requirements, this will be resolved in the design optimisation phase in the next section.

4.9.2 Inverse-Design optimisation result

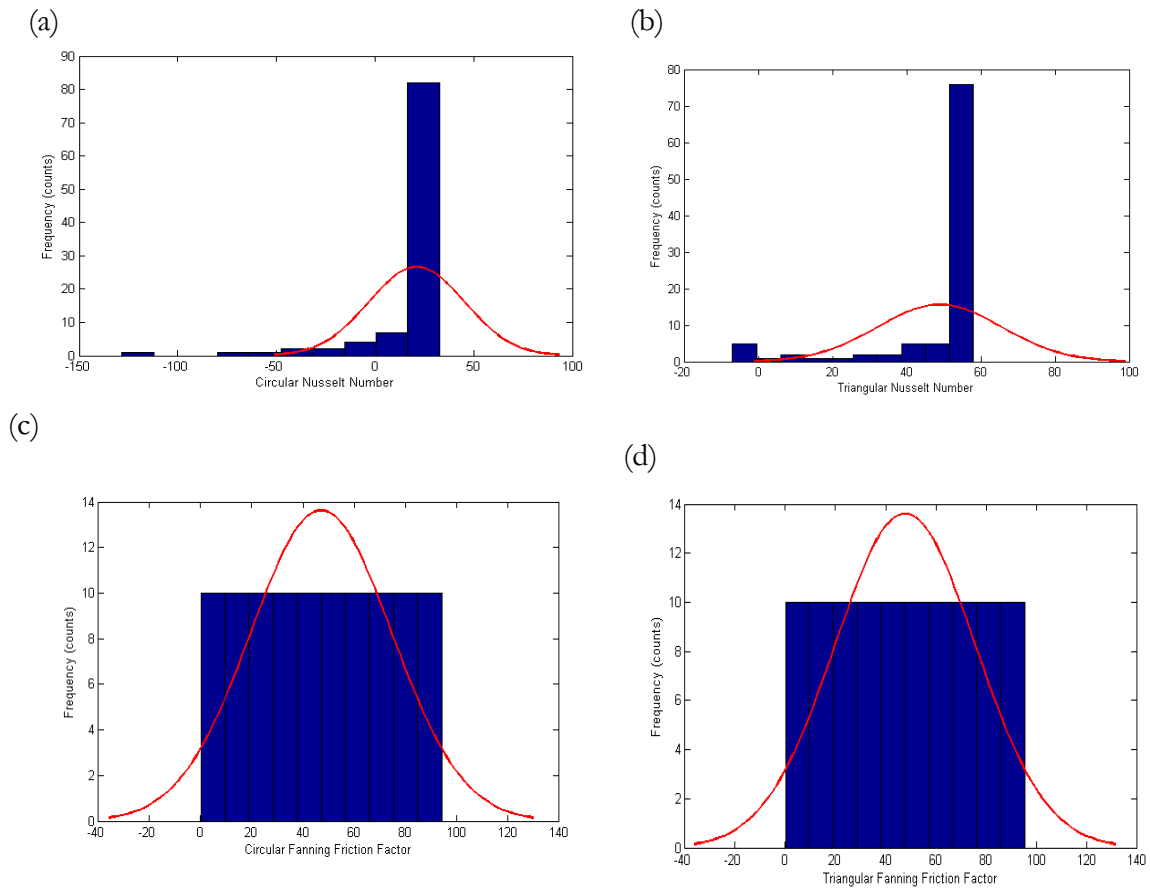

Figure 4.7 Histogram with a normal distribution fit of Nusselt Number and fanning Friction Factor; (a)semi-circular shape Nusselt; (b)Triangular shape Nusselt number; (c) semi-circular Fanning friction factor; (d) semi-circular Fanning friction factor

In fig.4.7, the frequency curve was fitted with a normal distribution for both shapes and the Nusselts number indicated a left skewed non-normal distribution. The triangular distribution is more spread than the semi-circular with Nusselt number 58 far higher than the circular design of 28. From the visualisation the triangular shape captures more radiation

from the visible spectrum than the semi-circular shape. Fig. 4.5(c) and (d) are essentially same and the pumping requirement for both shapes are the same and are all normally distributed about the same mean, mode and median.

In fig. 4.8, all the three design variables indicate a quadratic behaviour response to the Nusselt number in the semi-circular shape design. The dominant or the strongest quadratic behaviour is indicated by inner diameter of the copper tube and the length of the receiver, followed by the heat transfer fluid flow diameter and the flow velocity of the fluid and the solar insolation as with the least quadratic effects. The optimum values of the design variables are not really obvious from the response surface analysis, the goal driven optimisation will establish the optimum values. The local optimum is also a possible solution if non-evolutionary algorithm is applied to the optimisation. The result is valid as flow in pipes and other channels are usually characterised with a quadratic velocity term, hence the non-linear behaviour of flow systems. It is even more revealing that the length of the flow channel has the same dominance as the internal diameter of the flow channel.

4.9.2.1 Response surface result

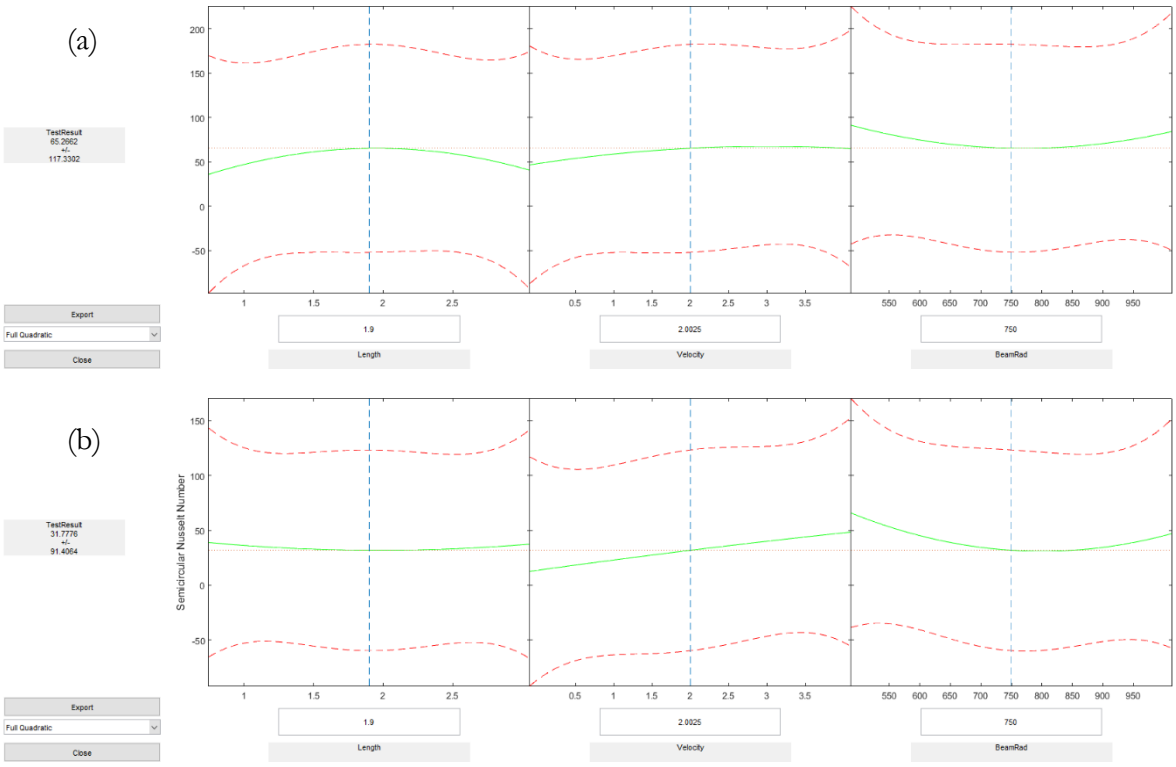

Figure 4.8 Full quadratic response surface prediction plots of parameters of five design variables (length of receiver, diameter of copper pipe, HTF channel, inlet velocity and the beam radiation) on the semi-circular shape Nusselt number

The response surface prediction plot of 3 design variables length, velocity and beam radiation for both shapes shows a quadratic behaviour with beam radiation as the most dominant quadratic behaviour. The length and velocity also, exhibit quadratic behaviour as indicated in fig 4.8 a and b. This is a typical characteristics of fluid problems.

(a)

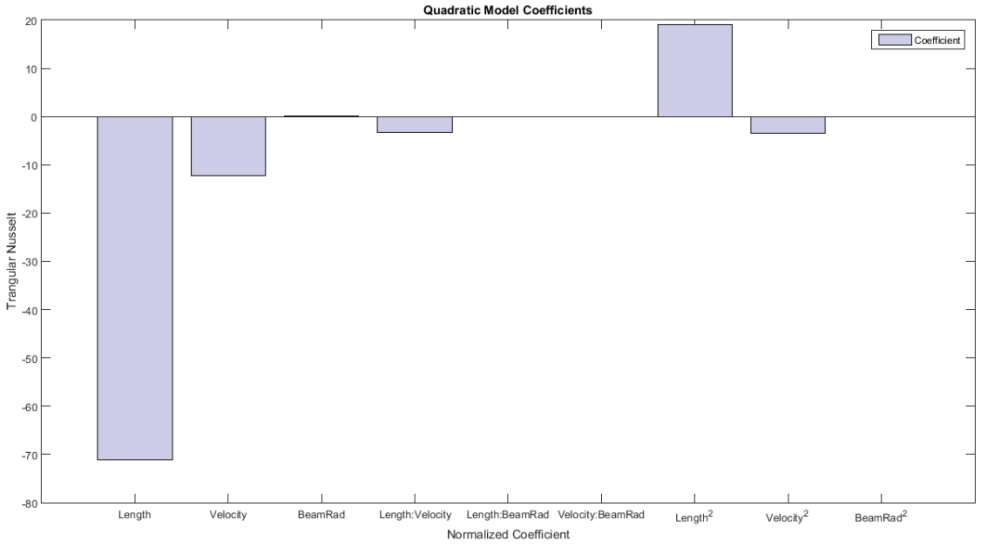

(b)

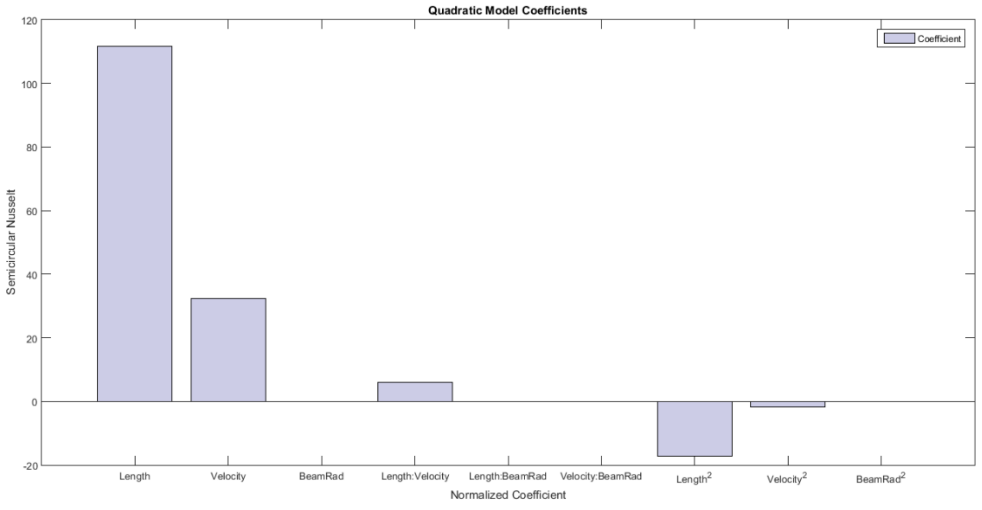

Figure 4.9 Full quadratic response surface coefficient of determination of triangular and Semi-circular Nusselt number; (a) Triangular response surface coefficient of determination; (b) Semi-circular response surface coefficient of determination

In fig.4.9 a and b, a full quadratic model was fited to the design of experiment table using the multiple regression and a mathematical model was predicted and the response was ploted

as coefficient of determination. The quadractic effect of length and velocity is more prominent as shown by the long bar above and below zero for both shapes. The mathematical model for the triangular and semicircular shape with the coefficients of the terms and the p-value of 0.572 and 0.0609 for the triangular and semicircular shape respectively.

In fig.4.9, the interaction between the length of the flow and the internal diameter of the copper pipe is much more dominant than the individual effect. The implication on the design is that the diameter and the length must be at their optimum to obtain a good heat transfer enhancement for the shapes.

4.9.2.2 Design of experiment result

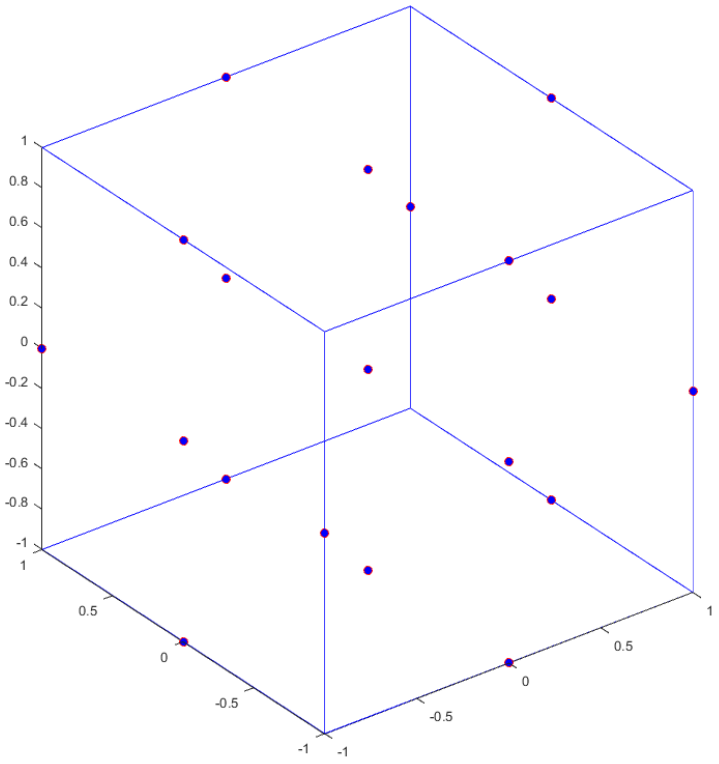

Figure 4.10 Box-Behnken design cube for design of experiments of the design variables on the Nusselt response

In fig. 4.10, the design of experiment design cube shows the codded values or normalised variables in the range [-1,0, +1], -1 represent the lower bounds of the variable, 0 represent the mid-point and +1 the upper bounds. The design points are all located at the midpoint, a typical characteristic of the Box-Behnken statistical experimental design.

(a)

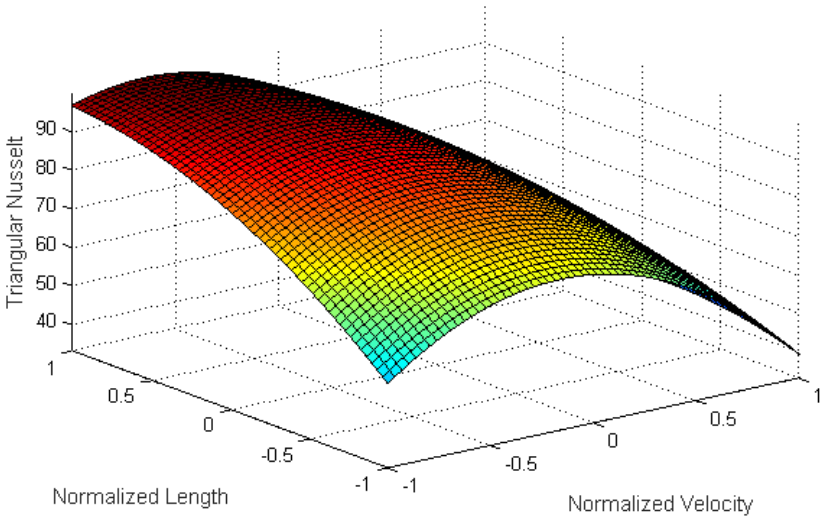

(b)

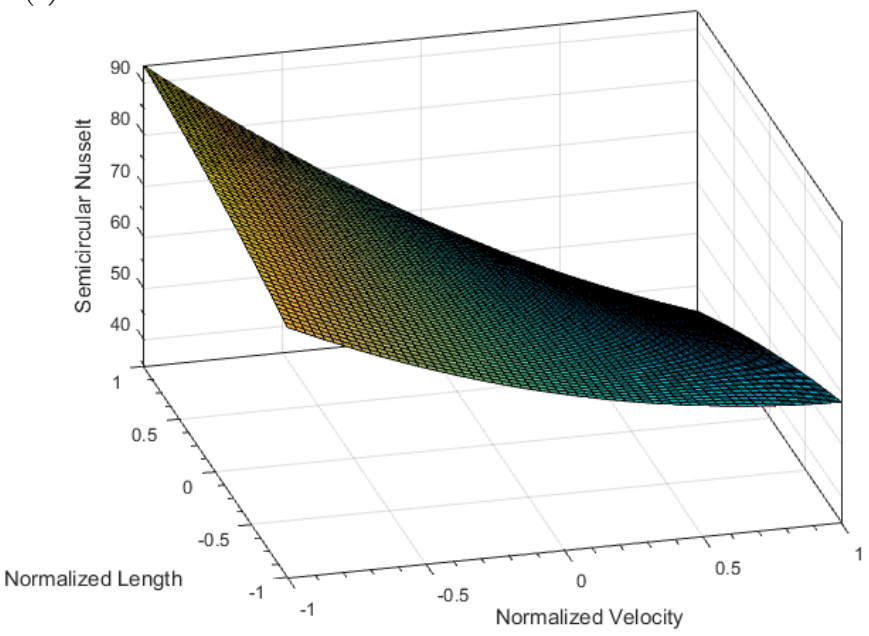

Figure 4.11 3D response surface plot of Nusselt number Vs receiver length and inlet velocity of the heat transfer fluid; (a) Triangular 3D response Nusselt and the normalised design variables; (b) Semicircular 3D response Nusselt and the normalised design variables

In fig. 4.11 a and b, a 3D visualisation of 2 variables (velocity and length) with the Nusselt number for both shapes, showing where the optimum Nusselt number with their corresponding design variables (velocity and length). This occurs at Nusselt number 98 and 90 for the triangular and semi-circular respectively.

4.9.2.3 Multi-objective optimisation results

Multi-objective NSGAII Optimisation for both shapes was written in as MATLAB function with the 5 design space variables and 2 objective functions.

4.9.2.3.1 Triangular shape optimisation result

The triangular shape optimisation results include the Pareto Front, average spread, selection function and rank histogram. The Pareto front shows a sets of non-dominated design of Fanning friction factor versus Nusselt number. The optimum values of the Nusselt number and the Fanning friction factor was obtained using decision support Pareto efficiency of 70%. In figure 4.32a, the Pareto front shows a high degree of crowdedness about the Utopian of the non-dominated solution set of the objectives. The global optimum for the design variables was found to be 3 m length, 0.00050001 m/s inlet velocity, 1000 W/m^2 and Nusselt of 1119.7 after imposing the Pareto efficiency decision support. In figure 4.32b, 34 individuals in total population are ranked 1 and 2 with a least rank of 12 for 1 individual. In fig. 4.12c a maximum of 24 children were selected from 20 individuals and minimum of 7 children was selected from 90 individuals. In fig. 4.12d, are evenly spread with a value of 0.59146 about the mean of a distribution of 300 generations. Fig.4.12e, shows the genealogy visual distribution more mutated children coloured in red than the crossover children as indicted by the few blue lines.

4.9.2.3.2 Semi-circular shape optimisation result

The semi-circular shape optimisation results include the Pareto Front, average spread, selection function and rank histogram. The Pareto front shows a point of non-dominated design of Fanning friction factor versus Nusselt number. The same approach of optimum values of the Nusselt number and the Fanning friction factor was obtained using decision support Pareto efficiency of 70%. In fig. 4.13a, the Pareto front shows a single non-dominated solution for the objectives. The global optimum for the design variables was found to be 0.8 m length, 0.00050021 m/s inlet velocity, 999 W/m^2 and Nusselt of 119.83 after imposing the Pareto efficiency decision support. In figure 12b, 70 individuals in total population are ranked 1 and least rank of 4 for 1 individual the diversity is not as well spread as the triangular shape. In fig. 4.13c a maximum of 24 children were selected from 20 individuals and minimum of 6 children was selected from 90 individuals. In fig. 4.12d, are evenly spread about the mean of a distribution of 300 generations. Fig 4.13 e, shows the genealogy visual distribution less mutated children coloured in red than the crossover children as indicted by the few blue lines.

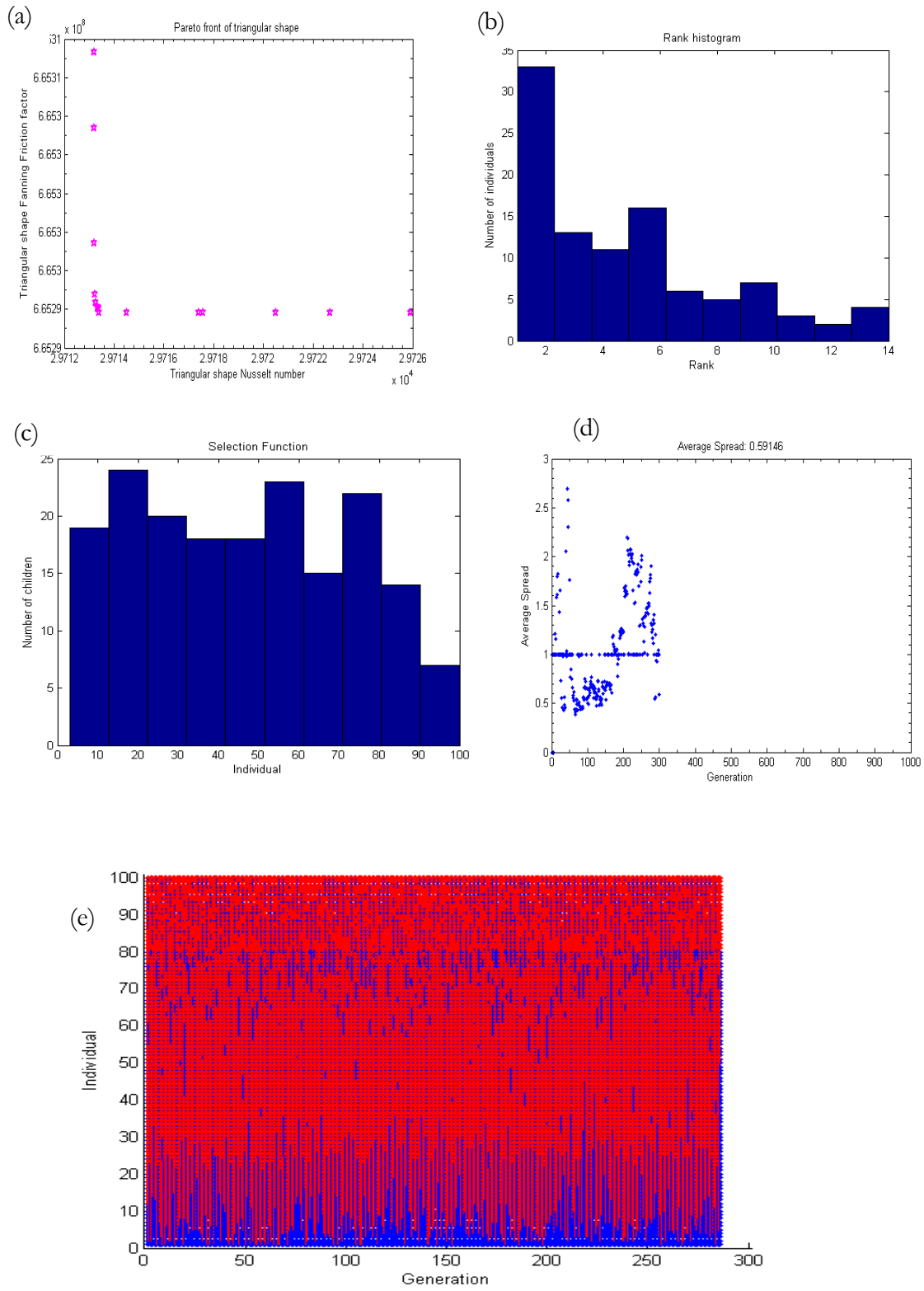

Figure 4.12 Triangular shape multi-objective optimisation plots; (a) Pareto front of the 2 objective, Nusselt Number and Fanning friction factor; (b) Rank histogram; (c) Selection function; (d) Average spread; (e) Genealogy of individuals and generation

4.9.2.3.3 Semi-circular optimisation shape result

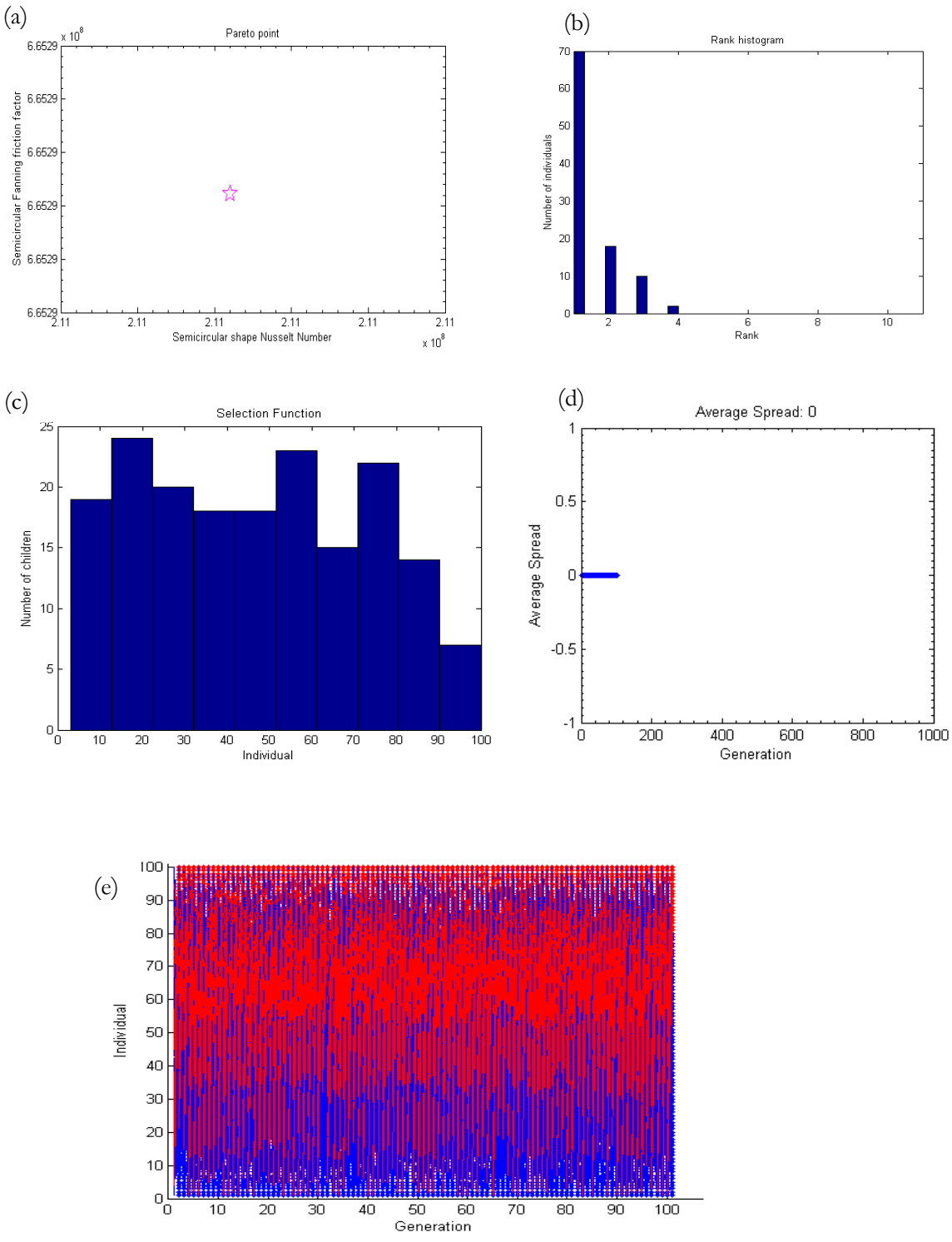

Figure 4.13 Semi-circular shape multi-objective optimisation plots; (a) Pareto front of the 2 objective, Nusselt Number and Fanning friction factor; (b) Rank histogram; (c) Selection function; (d) Average spread; (e) Genealogy of individuals and generation

4.9.2.3.4 Robust Six-sigma design results

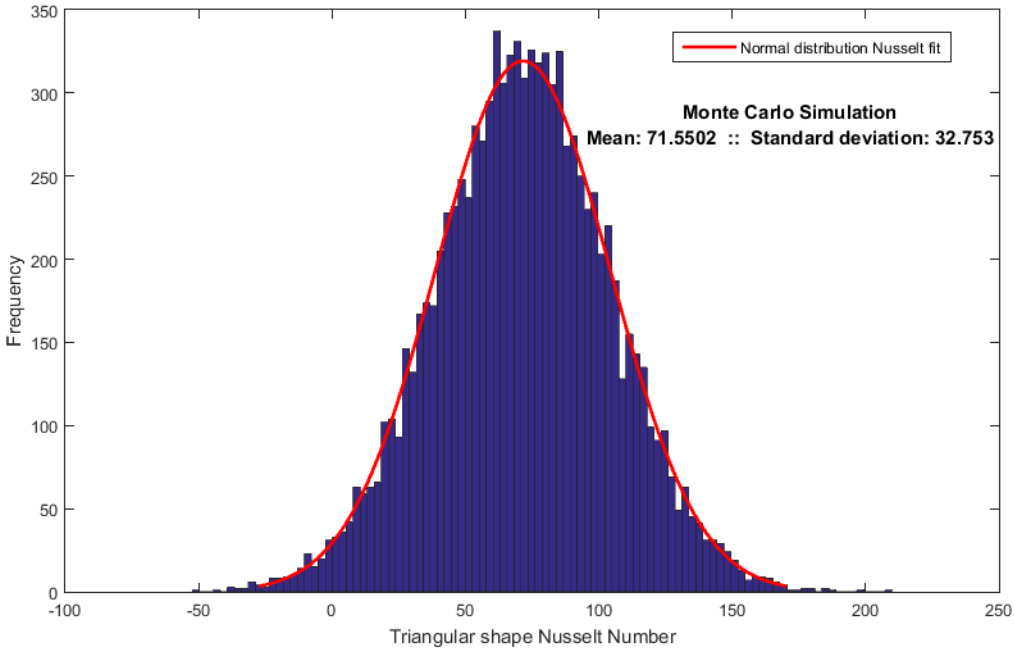

Figure 4.14 Six-sigma Monte Carlo simulation of 10000 samples of design variables of triangular shape

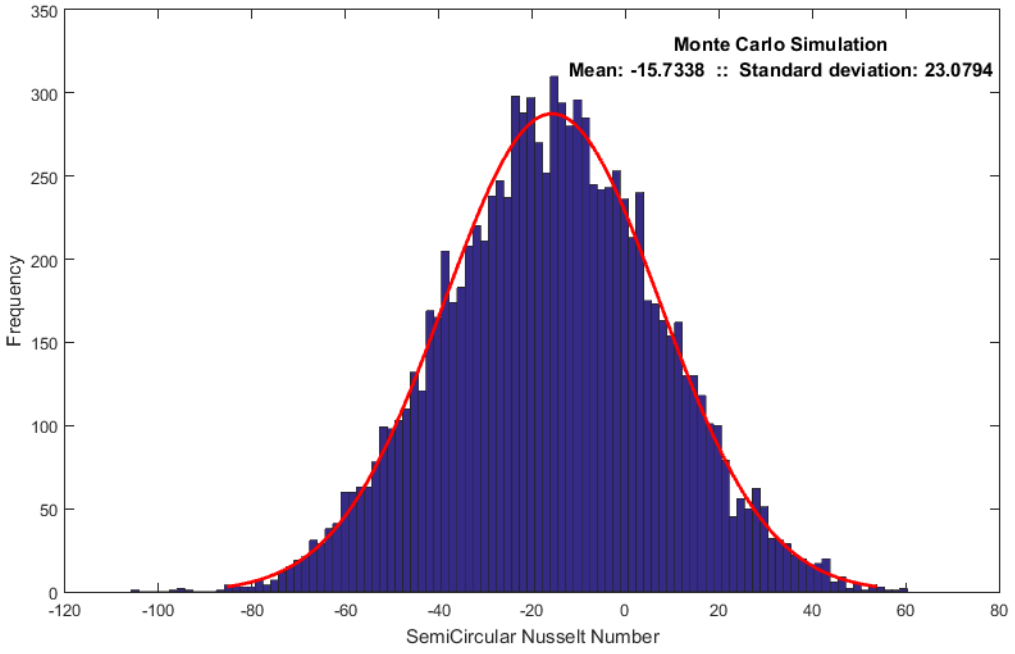

Figure 4.15 Six-sigma Monte Carlo simulation of 10000 samples of design variables of Semi-circular shape

The Six-Sigma Monte Carlo simulations histogram normal distribution fit in fig. 4.14 shows a mean Nusselt number of 71.55 with a standard deviation of 33.75. The results indicate that

99% of the time, 71.55 Nusselt number will be achieved with the triangular shape. In comparison, fig. 4.35, show a rather negative mean of -15.74 for the semi-circular shape and a standard deviation of 23.08. The results show a loss of heat 99% most of the time for the semi-circular shape. The result is an indication of the superiority of the triangular shape over the semi-circular shape.

4.9.2.3.5 Capability result for manufacturing the shapes

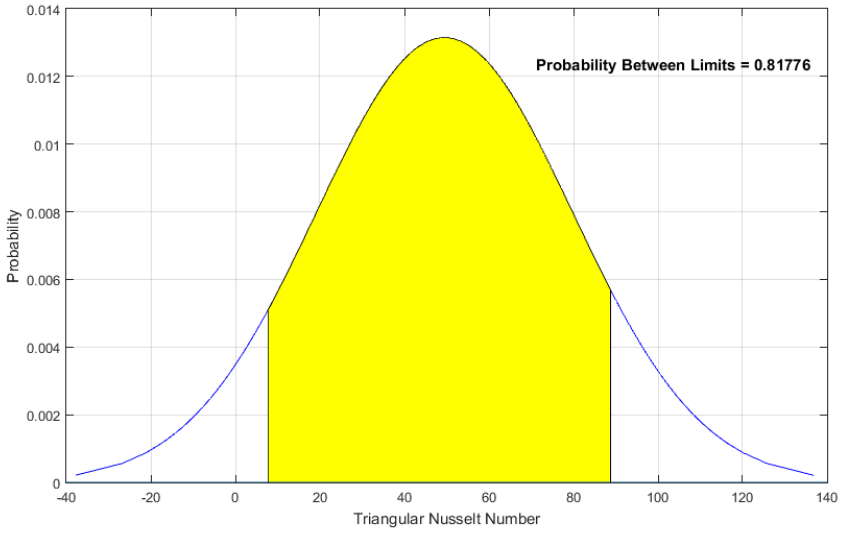

Figure 4.16 Capability probability of manufacturing the triangular shape

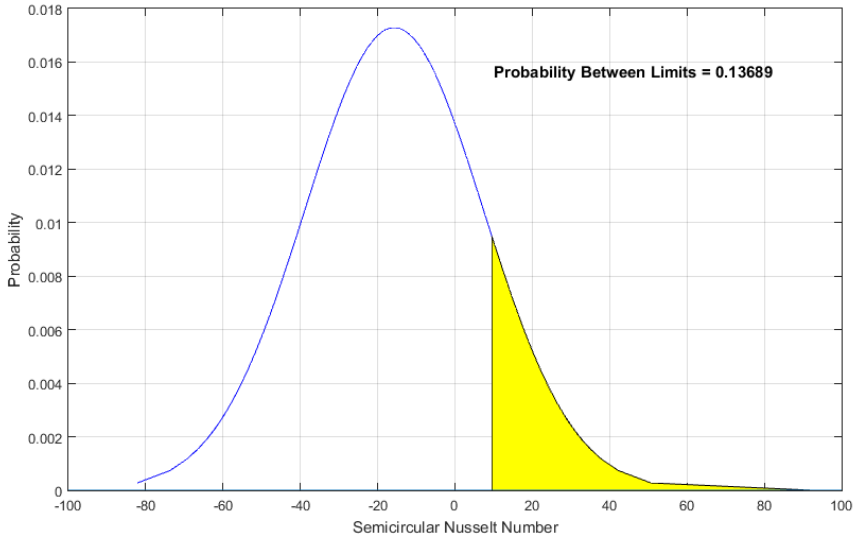

Figure 4.17 Capability probability of manufacturing the Semi-circular shape

In fig. 4.16 and 4.17, the process of manufacturing the shapes and meeting performance requirement of the design Nusselt number at a capable probability are visually represented

in a capability plot. Fig. 4.16 shows a more promising 82% certainty of the triangular shape meeting performance and design requirement as against 14% for the semi-circular shape.

4.10 Verification and validation of results obtained

In verifying and validating the design, the numerical mass balances and the design optimisation statistical approach will suffice. In addition to the optimisation and the statistical work, a validation using Nusselt number estimated from the Petukhov (1970) correlation was also used in verification of the numerical code. The validation results and comparison plot are presented in fig. 4.18 and 4.19 as follows;

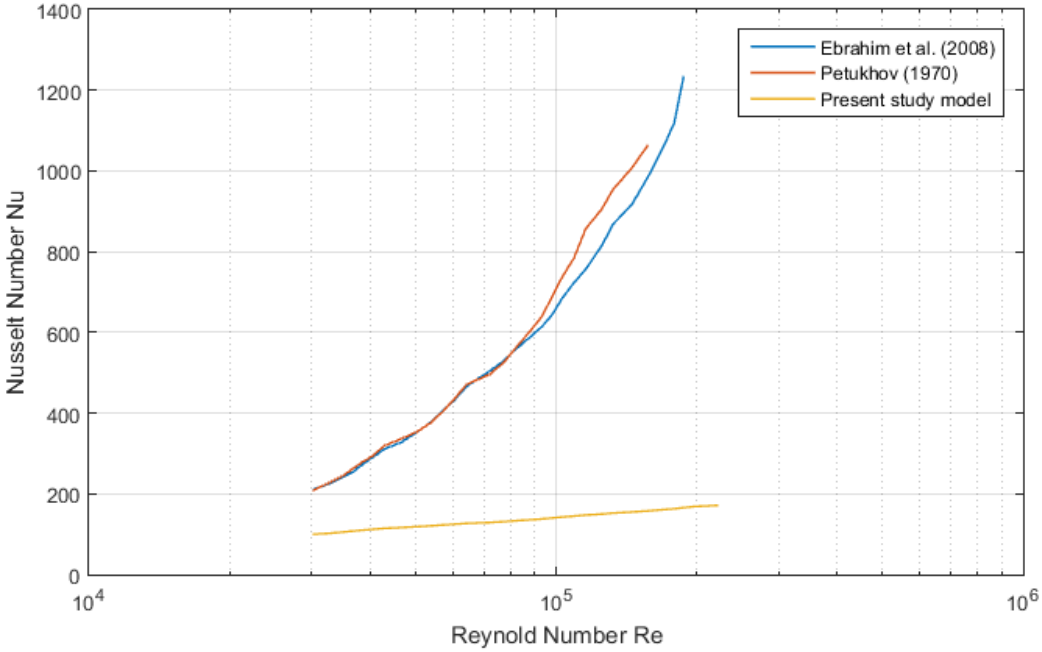

Figure 4.18 Nusselt number versus Reynolds number comparison of the semi-circular shape receiver with parabolic trough receiver of Ebrahim and Petukhov empirical correlation at constant heat flux along the length of the receiver

The deviation is about an average of 18% from that of Ebrahim and the Petukhov. The error is mostly due to tracing of the data from the digitizing software. The concentration ratio was applied by Ebrahim et. al while a concentration ratio of 1 was used in the study. The empirical correlations are given in Eqs. (4.21) and (4.22) as follows;

$$Nu = \frac{\left(\frac{f}{8}\right) Re\ Pr}{1.07+12.7\left(\frac{f}{8}\right)^{\frac{1}{2}}\left(Pr^{\frac{2}{3}}-1\right)} \qquad for\ 10^4 \leq Re \leq 5 \times 10^6 \qquad (4.21)$$

$$f = (0.79 log Re - 1.64)^{-2} \qquad (4.22)$$

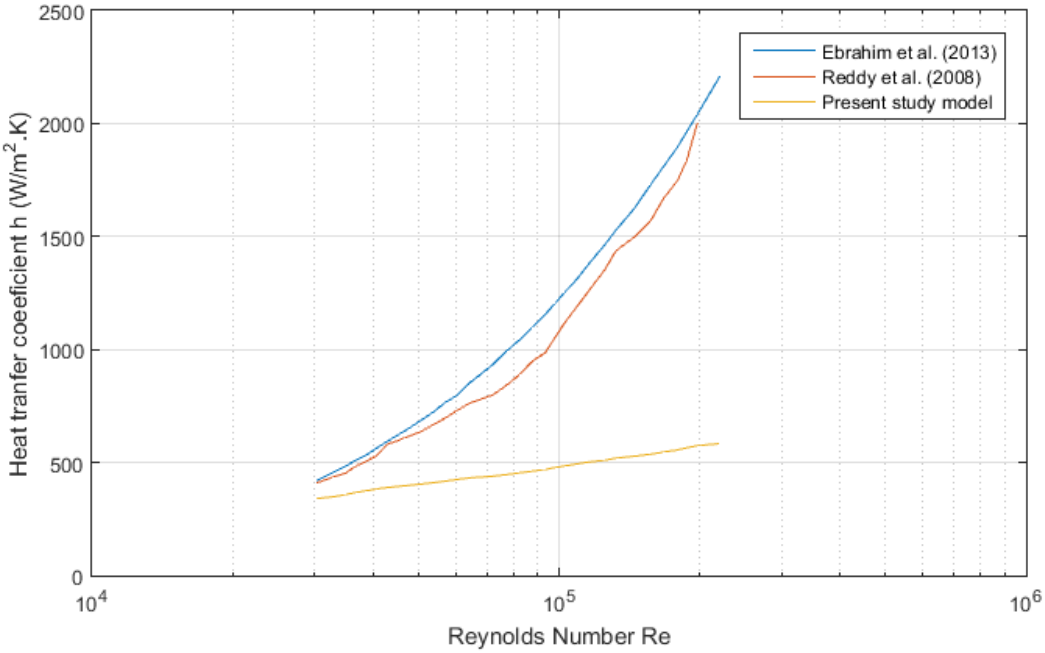

Figure 4.19 Heat transfer coefficient versus Reynolds number comparison of the semi-circular shape receiver with parabolic trough receiver of Ebrahim et al. (2013) and Reddy et al. (2008) empirical correlation at constant heat flux along the length of the receiver

The deviation of the present model from that of Reddy et al. and Ebrahim is also attributed to the error introduced in tracing the data point from the original source and the concentration ratio applied by the authors.

4.11 Summary and concluding remark

A multidisciplinary and co-simulation approach with numerical analysis and inverse-design optimisation methodology was used to determine and select the best shape for capturing heat from the sun. The tools used in selecting the shapes are MATLAB, Statistics toolbox, Machine learning toolbox (Patel, 2016) and ANSYS workbench. The triangular shape has been established to be a better shape than the semi-circular counterpart, with global optimal design variables of 3 m length, 0.00050001 m/s inlet velocity, 1000 W/m2 and Nusselt of 1119.7 while the semi-circular global optimum design variables of 0.8 m length, 0.00050021 m/s inlet velocity, 999 W/m^2 and Nusselt of 119.83. The triangular shape can achieve Six sigma benchmark of 3.4 number of failures of the triangular shape part manufacture out of a lots of 10000000 with a mean of 71.55 Nusselt number will be achieved. On the other hand, the semi-circular shape will not achieve Six sigma as a results of the negative mean of -15.74.

Conclusively, the triangular shape is a better shape for extracting and capturing heat from the sun solar radiation as a result of the higher Nusselt number. The pumping fanning

friction factor for both shapes are essentially the same, the only factor that will enhance the pumping friction factor is to reduce the viscosity of the heat transfer fluids.

4.12 What next

A shape selection design optimisation study based on ANSYS Fluent and MATLAB, established the right shape. The triangular was selected and was found to enhance the heat transfer rate by a factor of 10, which is significantly impressive and provides a means for using the shape in the system dynamics in chapter 5.

Chapter 5 Dynamical system modelling & Analysis of HCCHPS

5.1 Introduction

In chapter 2, it follows from the related work on combined heating and power (CHP) is already well established technology. However, there are huge gaps in the dynamical or time evolution behavioural modelling of the classical CHP and it is even non-existing in the emerging combined cooling heat and power system (CCHP). There are few work on the combined cooling heat and power using empirical pseudo-first order equations and static models. These approach am afraid lacked a detailed analysis of the dynamic behaviour, stability, inter-subsystem interactions, fast and slow dynamics characteristics of dynamical systems and system level interaction for loop pairing and decoupling that characterised control ready model. In this chapter a subsystems and system level dynamical model will be developed to established subsystems and system level interactions and time evolution over time. There are 3 types of computational models are the equation based model, Agent based model and Network model. The equation based models also known as top-down models drive the dynamics of system and already well established. They are obtained from underlying physics of the system, which includes ordinary and partial differential equations. The second type is Agent based models or the bottom-up models that do not drive the dynamics of the system. Agent-based models concentrate on the behaviour of different individuals at the system-level observations of the system. The Network model is based on network theory where each subsystem is considered as a network node. Internet of things, social network, supply chain management and the power grid are all kinds of Network model.

In this chapter, the computational top-down model based on ordinary differential equations are considered for each subsystem. A state-space subsystem representation, system response driven by vector differential equations, transition matrix, Eigenvectors analysis, controllability and observability, phase plane or phase portraits system simulation are considered. Also, system stability analysis based on equilibrium points stability, Relative Gain Array (RGA) and Niederlinki's Index (NI) Nyquist's and Singular Value Decomposition analysis will be discussed.

The physics based dynamic model of the 10 subsystems namely solar thermal parabolic trough PVT, wind turbine, battery, electrolyser, hydrogen storage, fuel cell, thermal storage adsorption cooling and heating system will be derived and established. The models will be analysed using time and frequency domain dynamic analysis tools such as stability, inter subsystem interactions, decoupling and control loop paring and obtain a reduced order control ready system model. The model obtained are linear and non-linear ordinary

differential equations. A block diagram model approach was used to decomposed the differential equation into manageable input-out system. The dynamical system analysis is an important prerequisite for supervisory control to established the inner and the outer loop in the decentralise hierarchical supervisory control highlighted in the literature.

5.2 Hypothesis from literature

Following the citations form previous dynamics and control study, it could be hypothesised that;

(i)The thermal time response time constant is the slowest compared to electrochemical, electronic, electrical, chemical and mechanical systems and will act as storage buffer in the overall HCCHP system

(ii) It therefore follows from (i) that inner loop will systems with faster time constant such as electrochemical and chemical process system will be in the outer loop while the thermal energy generation, storage and thermally activated technologies subsystems (adsorption chillers) remain in the inner loop for stability of the overall control scheme.

5.3 Research Approach

The research approach is based on the model based design (MBD) methodology and MATLAB and SIMULINK are the software tools for delivering or deploying MBD.

5.3.1 Model based design

Model based design is a systematic process of enabling faster, more cost effective development of dynamic, control, communication and signal processing system. It starts with a system model, where requirement and ideas are captured and transformed executable C code to target an embedded electronic control hardware. In model based design methodology, a system model is at the heart of the overall development process from requirement analysis, through design, implementation and testing. System emulation paradigms such as software, processor and hardware in loop simulation is used to determine if the model developed works correctly. It involves the following steps and the workflow is represented in figure 1:

- Defining the system
- Identifying system components
- Modelling the system with equations
- Building the system SIMULINK block diagram
- Running the simulation
- Validating the simulation results

5.3.2 MATLAB and SIMULINK

The MATLAB and SIMULINK are two most crucial tools for implementing MBD. The software MATLAB is an acronym for MATrix LABoratory, a programming construct with matrix as it backbone, all written and developed in C language. SIMULINK is a block diagram with all the block libraries for expressing and mathematical relation with plethora of toolbox for diverse multi-disciplinary application. It runs on MATLAB.

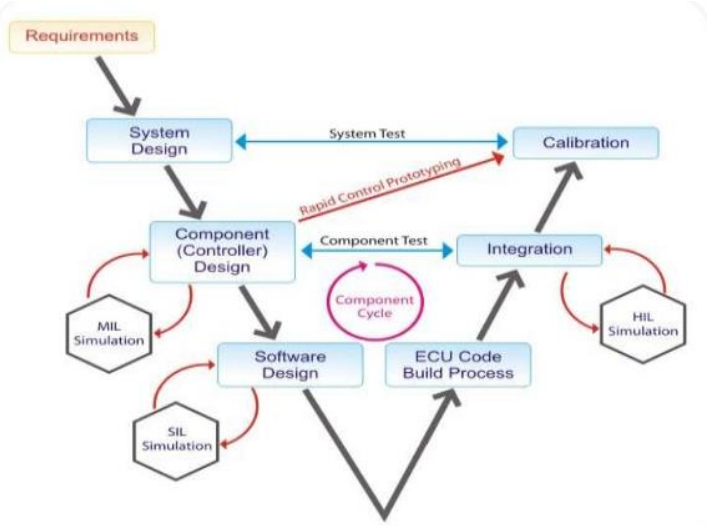

Figure 5.1 Model based design "V" work flow, starting with requirement analysis to system design through model in the loop, software in the loop to hardware in the loop simulation

In the fig. 5.1 the work flow commences with a requirement specification where the way system should behave is provided and send as input to the system model design. The system model could be obtained from experimental test bed or from first principle model and the output of the system model serves as input to the controller design. The controller is fine tune through model in the loop and software in the loop simulation until a functional software is obtained. The software design is tested on a hardware called the electronic control unit and the hardware and the software integrated by hardware in the loop integration and calibration.

The dynamical systems phase portraits provide a time evolution visualisation of the state vector of a system qualitatively through direction fields. The direction fields are arrows with curves or line superimposed on the direction fields showing vectors. The results of the phase portrait are provided in the results section on a components and subsystems basis.

5.4 The hydrogen Energy Hub Concept system modelling of HCCHP

The energy hub concept brings all the energy flow systems such as hydrogen, heat and electricity into a single unified scheme and is illustrated in figure 2 as follows;

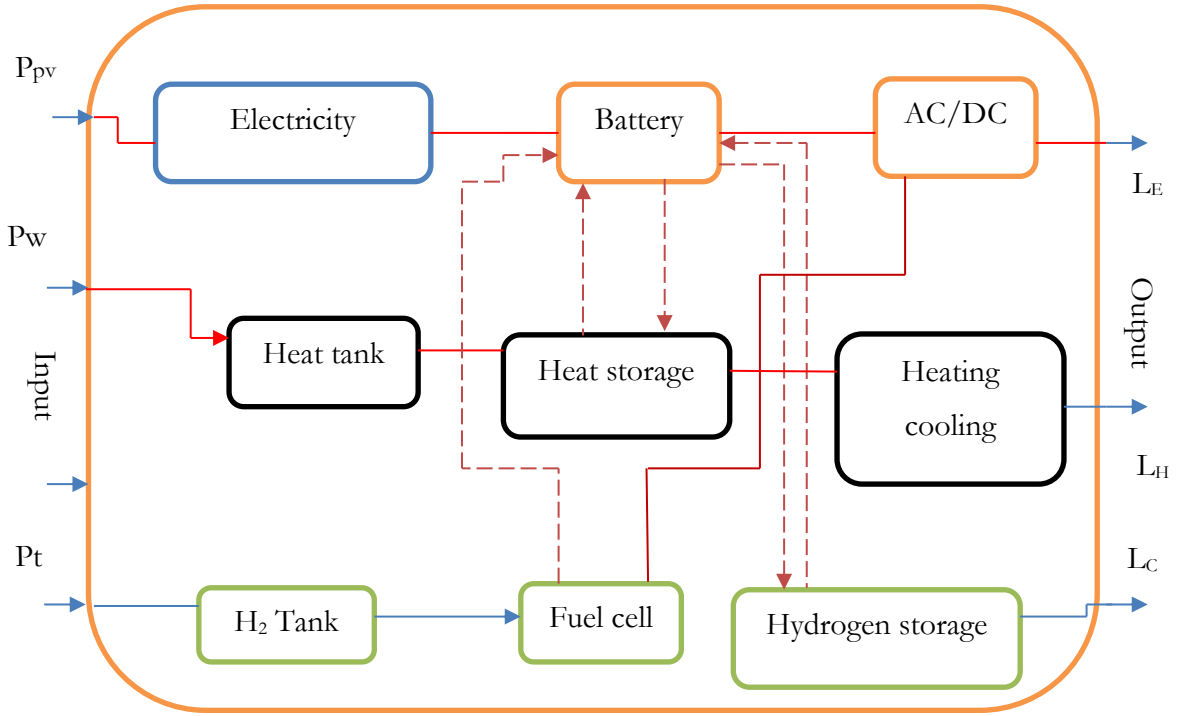

Figure 5.2 Energy hub unified concept combining hydrogen gas, heat and electric current transportation between all the subsystems; P_{pv} is electrical power produced by the PV panel, Pw is the electrical power produced by the wind turbine and Pt is the thermal power produce the trough receiver system as input to the hub; L_E, L_H and L_C are the electrical, heating and cooling load as output to the hub

5.5 The parabolic trough PVT Subsystem

The subsystems consist of the solar thermal trough PVT system and the heat storage and heat exchanger. The trough receiver PVT system is represented by a 3×3 state space in Eqs. (5.8) to (5.9) as follows, which is a decomposition of seven ordinary differential Eqs. (5.1) to (5.7).

$$\rho_T C_{p,T} A_T \frac{dT_T}{dt} = q_{\text{conv t-a}} + q_{\text{cond t-f}} + q_{\text{cond t-m}} + q_{\text{cond t-tedeva}} + q_{\text{cond t-p}} + q_{\text{cond t-g}} + q_{\text{rad sky-t}} + q_{\text{inso tot}} \quad (5.1)$$

$$\rho_f C_{p,f} A_f \frac{dT_f}{dt} = q_{\text{conv t-f}} + q_{\text{cond t-f}} + q_{\text{cond m-f}} + q_f \quad (5.2)$$

$$\rho_m C_{p,m} A_m \frac{dT_m}{dt} = q_{\text{conv m-f}} + q_{\text{cond t-m}} + q_{\text{cond m-f}} + q_{\text{cond tedeva-m}} \quad (5.3)$$

$$\rho_{tedeva} C_{p,tedeva} A_{tedeva} \frac{dT_{tedeva}}{dt} = q_{\text{cond t-}tedeva} + q_{\text{cond t-}tedeva} + q_{\text{cond m-}tedeva} \quad (5.4)$$

$$\rho_p C_{p,p} A_p \frac{dT_p}{dt} = q_{\text{cond g-}p} + q_{\text{cond }tedeva-p} + q_{\text{cond t-}p} + q_{inso\ beam} \quad (5.5)$$

$$\rho_g C_{p,g} A_g \frac{dT_g}{dt}$$
$$= \mathrm{q}_{\mathrm{conv\ a}-g} + \mathrm{q}_{\mathrm{cond\ p}-g} + \mathrm{q}_{\mathrm{cond}\ eva-g} + \mathrm{q}_{\mathrm{cond\ t}-g} + \mathrm{q}_{\mathrm{rad\ sky}-g} + \mathrm{q}_{\mathrm{rad\ con}-g}$$
$$+ q_{inso\ beam} \tag{5.6}$$

$$\rho_{con} C_{p,con} A_{con} \frac{dT_{con}}{dt} = \mathrm{q}_{\mathrm{conv\ a}-con} + \mathrm{q}_{\mathrm{rad\ sky}-con} + \mathrm{q}_{\mathrm{rad\ con}-g} + \mathrm{q}_{\mathrm{inso}\ total} \tag{5.7}$$

The 7 equations for the trough receiver systems was transformed and decomposed into state space representation of the 3 states, temperature of heat transfer fluid, copper metal and the photovoltaic panel in equation (8) to (11).

$$\dot{x} = Ax + Bu \tag{5.8}$$

$$\begin{pmatrix} \dot{T_f} \\ \dot{T_m} \\ \dot{T_p} \end{pmatrix} = \begin{pmatrix} \frac{h_{tf} d_f}{\rho_f C_{pf} A_f} + \frac{k_f}{\rho_f C_{pf} d_f} - \frac{k_f}{\rho_f C_{pf} d_m} + \frac{m_f \varepsilon}{\rho_f C_{pf} A_f} & \frac{k_f}{\rho_f C_{pf} d_f} & 0 \\ \frac{k_m}{\rho_m C_{pm} d_m} + \frac{h_{mf} d_f}{\rho_m C_{pm} d_m} & \frac{h_{mf} d_f}{\rho_m C_{pm} d_m} - \frac{3k_m}{\rho_m C_{pm} d_m} & 0 \\ 0 & 0 & -\frac{3k_p}{\rho_p C_{pp} d_p} \end{pmatrix} \begin{pmatrix} T_f \\ T_m \\ T_p \end{pmatrix}$$
$$+$$
$$\begin{pmatrix} \frac{k_t W_t h_{ta}}{k_t W_t h_{ta} + h_{tsky} A_t} - \frac{m_f \varepsilon}{\rho_f C_{pf}} & 0 & 0 \\ 0 & 0 & 0 \\ \frac{k_p h_{ag} A_g k_g}{\rho_p C_{pp} d_p (k_g h_{ag} A_g + A_g)} & 0 & \frac{C_r \eta_{opt} \eta_r \beta_r T_{ref}}{\rho_p C_{pp}} + \frac{C_r R_{con} \alpha_g}{\rho_p C_{pp}} \end{pmatrix} \begin{pmatrix} T_{in} \\ I_{total} \\ I_{beam} \end{pmatrix} \tag{5.9}$$

$$y = Cx + Du \tag{5.10}$$

$$y = \begin{pmatrix} 1 & 0 & 0 \\ 0 & 1 & 0 \\ 0 & 0 & 1 \end{pmatrix} \begin{pmatrix} T_f \\ T_m \\ T_p \end{pmatrix} + (\,0\ 0\ 0\,) \begin{pmatrix} T_{in} \\ I_{total} \\ I_{beam} \end{pmatrix} \tag{5.11}$$

5.5.1 Solar thermal parabolic trough PVT system

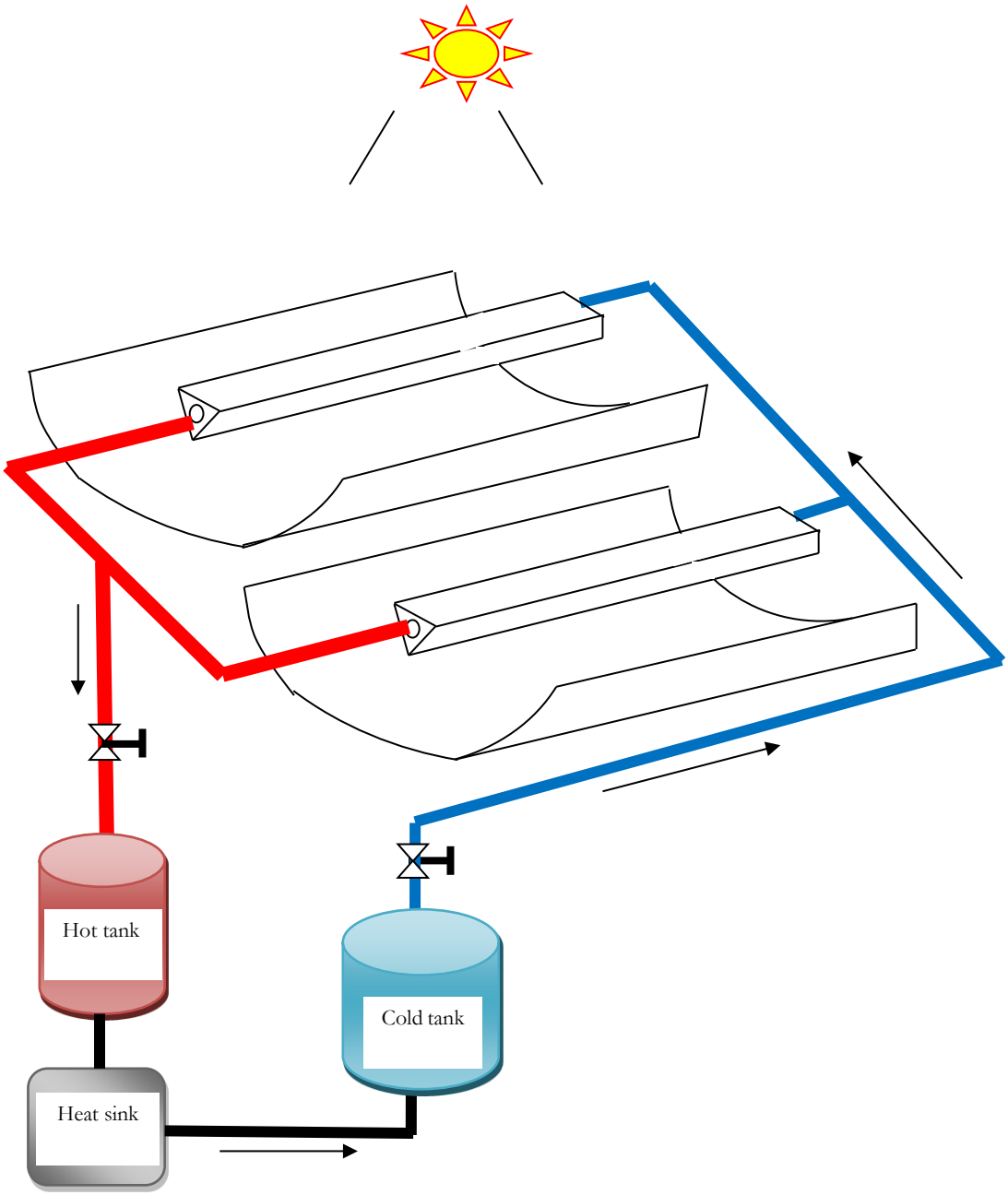

Figure 5.3 solar fields consisting of solar thermal parabolic trough with solar module place at the focal line. Cold water tank water or heat transfer fluid is pumped to through the triangular aperture of the solar collector the water is converted into steam or hot oil and stored in a hot oil tank or steam collector the hot oil is super-heated or regenerated in the heat sink or regenerator

Modelling the solar multiple (Hot water tank, cold water tank and the heat sink)

In modelling the thermal energy storage block, a hot tank, a shell and tube heat exchanger boiler with heat transfer fluid flowing in the tube, water in the shell to absorbed the heat and transforming the heat to hot water and cold tank to return the heat transfer fluid back to the trough receiver subsystem.

Tank in series modelling of the thermal energy storage tank

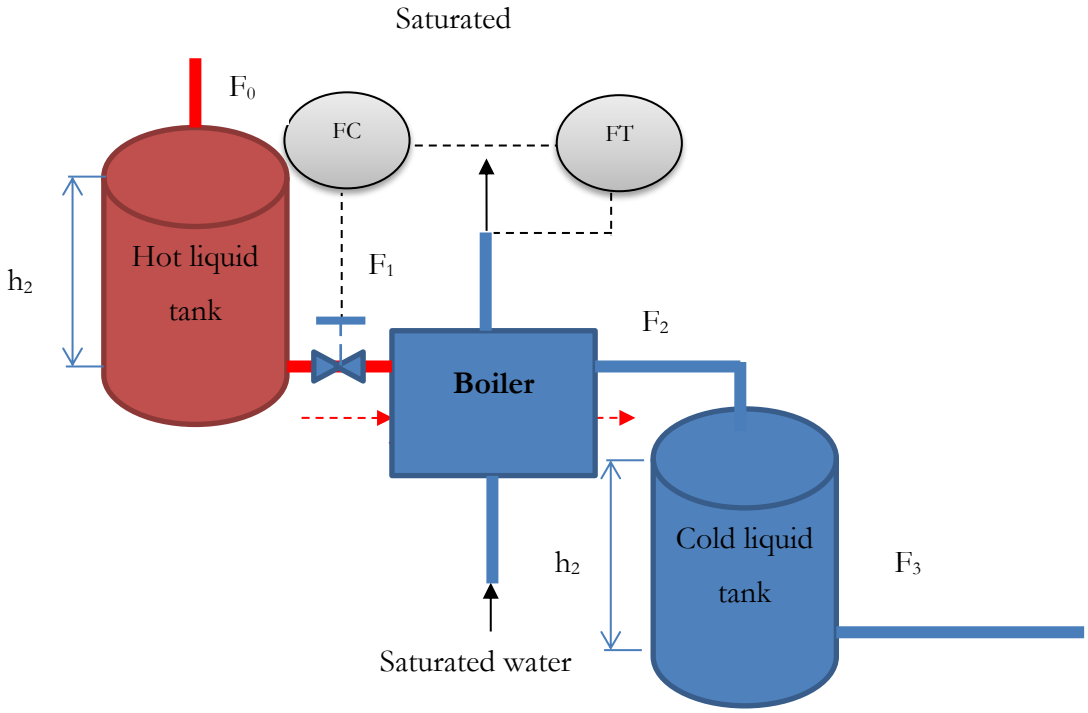

Figure 5.4 Tank in series modelling of solar multiple thermal energy storage of hot and cold tank with a boiler as the heat sink

Mass balance around the hot and cold liquid tank

From fig. 5.4 the material and energy balance of the cold and hot fluid tank will be modelled, while the energy balance of the boiler heat exchanger or heat sink was obtained from the heat conservation equation. The following assumptions were made

Constant density of the hot and cold liquid was assumed

Constant area for the tanks was assumed

Mass balance around the hot liquid tank

$$\rho_{FH} A_H \frac{dh_1}{dt} = F_0 - F_1 \qquad (5.12)$$

Energy balance around the hot liquid tank

$$\rho_{FH}A_H\frac{d(T_Hh_2)}{dt} = C_{FH}(T_0F_0 - T_HF_1) - UA_{tH}(T_H - T_{air}) \quad (5.13)$$

Mass balance around the cold liquid tank

$$\rho_{FC}A_C\frac{dh_2}{dt} = F_2 - F_3 \quad (5.14)$$

Energy balance around the cold liquid tank

$$\rho_{FC}A_C\frac{d(T_Ch_2)}{dt} = C_{FC}(T_2F_2 - T_CF_3) - UA_{tC}(T_C - T_{air}) \quad (5.15)$$

Mass and energy balance around the boiler heat exchanger

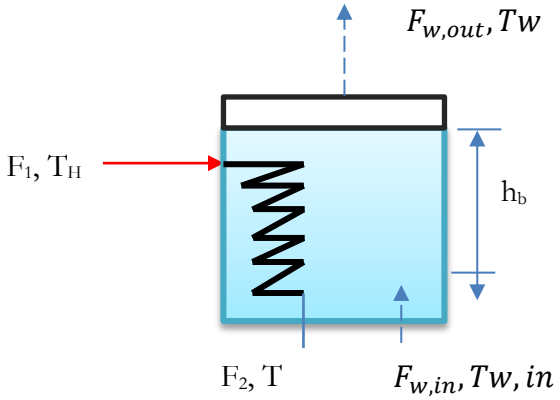

Figure 5.5 A boiler heat exchanger as the heat sink

Mass balance around the boiler heat exchanger

$$A_b\frac{dh_b}{dt} = F_{w,in} - F_{w,out} - F_H - \beta h_b \quad (5.16)$$

Energy balance of HTF in the tube of boiler heat exchanger

$$m_{HTF}Cp_{HTF}\frac{dT}{dt} = Cp_{HTF}F_1T_H - Cp_{HTF}F_2T + h_w\,A_w(\,T_w - T) \quad (5.17)$$

Energy balance of water in the shell of boiler heat exchanger

$$m_wCp_w\frac{dT_w}{dt} = F_{w,in}Cp_w(T_{w,in} - T_w) + h_w\,A_w(\,T_w - T) + F_{w,out}\Delta H_{\,v} \quad (5.18)$$

The flow out of the hot and cold tank are square root function as results of pipe valve flow characteristics. The Tylor series linearisation was use to obtain the equilibrium point in the phase plane diagram.

5.5.2 Wind turbine generation system

Wind turbine is a multi-domain system consisting of major components such as rotor, hub and blades; a drive train consisting of low-speed rotating shaft, a gearbox and high-speed

rotating shaft; generator and power converter; tower and foundation; and finally controls. Vertical axis wind turbine 3-mass mechanical drive train

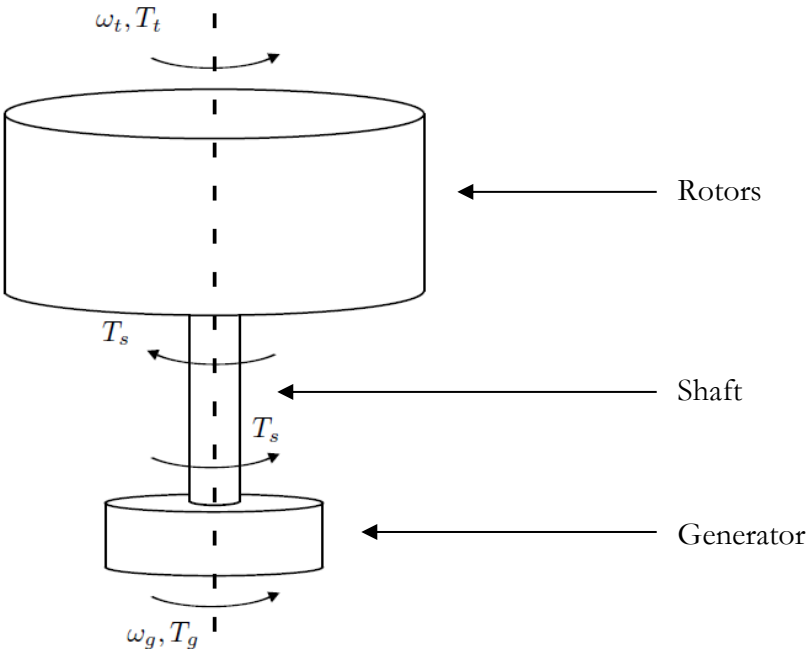

Figure 5.6 A 3-mass representation of the VAWT mechanical system

Mathematical model of the 3-mass system

Torque balance about the generator:

A mechanical components or parts are modelled by a generator, turbine rotational speed and the shaft torque (ω_g, ω_t, T_s) described by Eqs. (5.19), (5.20) and (5.21) as follows (Alverbäck, 2012)

$$J_g \frac{d\omega_g}{dt} = T_s + T_g + D(\omega_t - \omega_g) \tag{5.19}$$

$$J_g \frac{d\omega_t}{dt} = T_t - T_s - D(\omega_t - \omega_g) \tag{5.20}$$

$$\frac{dT_s}{dt} = k_s(\omega_t - \omega_g) \tag{5.21}$$

Electro-Mechanical and power electronics vertical axis wind turbine system

The system consists of electro-mechanical permanent magnet synchronous generator and the voltage source converter. The PMSG meant to convert the mechanical power into electric power. The voltage source converter matches the differential synchronous machine speed of the PMSG and the wind turbine variable speed to ensure that the voltage is in phase with the electric grid. This is achieved with a voltage source converter consisting of a six pulse diode bridge, a direct current line and a DC/AC inverter as shown in the fig. 5.7.

Kirchhoff's law representation of the electro-mechanical and power electronics dynamics of the system in fig 5.7(b) are described by the ODE's (5.22), (5.23) and (5.24) as follows (Alverbäck, 2012).

$$C_{DC}\frac{dU_{DC}}{dt} = I_R - I_{out} \tag{5.22}$$

$$L_{tot}\frac{dI_R}{dt} = -U_{DC} - R_{tot}I_R + \frac{2}{3}\Lambda\omega_g + \epsilon \tag{5.23}$$

$$\frac{d\Delta T_t}{dt} = -\delta\Delta T_t + w \tag{5.24}$$

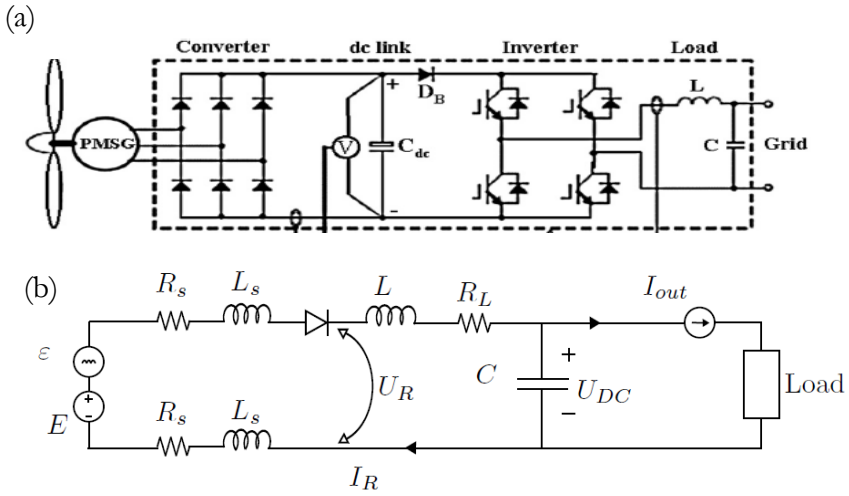

Figure 5.7 Electro-mechanical and power electronics description of the wind turbine system; (a) is the rotor-permanents magnet synchronous generator to a full bridge rectifier AC/DC converter, Dc link DC to AC converter and the load; (b) is the reduced or simple representation of the DC voltage source and the voltage ripple (ɛ)

Generation bus system

The generation bus is a point aggregation of the power produce from the renewable energy. It is also part of the system battery state of charge hysteresis prioritization and allocation of charge and discharge cycles of the storage and heating and cooling are triggered. The differential equation is time derivative of the Direct current power as a difference between power generated and power consumed and presented in Eq. (5.25) as follows;

$$U_{DC}\frac{dU}{dt} = \sum P_g - \sum P_s \tag{5.25}$$

5.5.3 Electrolyser model

Electrolysers are excellent electrochemical cell for hydrogen production. The electrolyser represented in Figure 8 is a system consisting of 4 main subsystems; anode, cathode,

membrane and voltage subsystems. The other subsystem called the auxiliaries and the balance-of-plant these include; hydrogen and oxygen separator, water pump, filter and valves as illustrated in fig. 5.8 There a several models of electrolyser, the comprehensive for a Proton Exchange Membrane (PEM) electrolyser is the work of Gorgun, (2006). The dynamic model was able to account for membrane redox reactions and proton and electron transfer and described by the ODE's in Eqs. (5.26) to (5.29) (Gorgun, 2006).

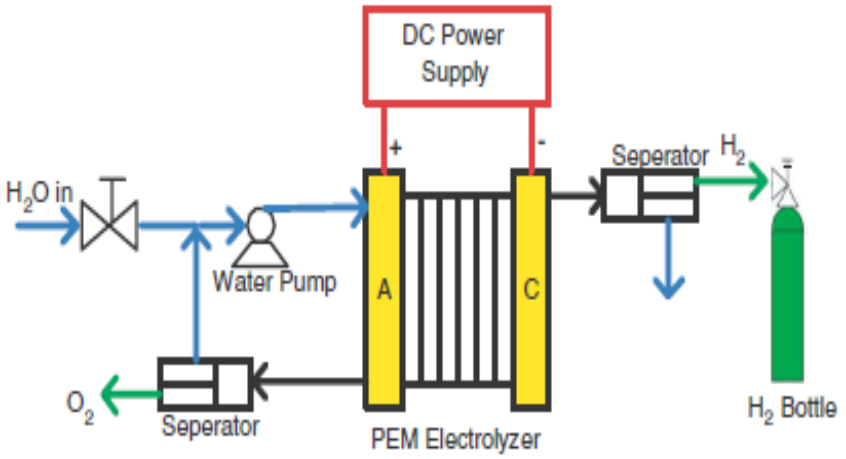

Figure 5.8 Proton Exchange Membrane electrolyser system components and subsystems; anode subsystem, cathode subsystem, DC voltage subsystem and the membrane subsystem. Hydrogen and oxygen separators, valves, water pump and filter are auxiliaries and balance of plant

Material balance around the anode

$$\frac{dN_{O_2}}{dt} = F_{O2}^{in} - F_{O2}^{out} + \frac{nI}{4F}\eta_F \tag{5.26}$$

$$\frac{dN_{H_2O}}{dt} = F_{H2O}^{in} - F_{H2O}^{out} - F_{H2O}^{d} - F_{H2O}^{eod} \tag{5.27}$$

Material balance around the cathode

$$\frac{dN_{H_2}}{dt} = F_{H2}^{in} - F_{H2}^{out} + \frac{nI}{2F}\eta_F \tag{5.28}$$

$$\frac{dN_{H_2O}}{dt} = F_{H2O}^{in} - F_{H2O}^{out} + F_{H2O}^{d} + F_{H2O}^{eod} \tag{5.29}$$

Energy balance of the system

$$M_{ele}C_{ele}\frac{dT_{ele}}{dt} = \dot{Q}_{gen} - \dot{Q}_{loss} - \dot{Q}_{cool} \tag{5.30}$$

The five ODE's above are control oriented and describe the physics of the PEM electrolyser Voltage subsystem calculates electrolyser applied voltage level by using Nernst Equation, ohmic polarization and activation polarization. Membrane subsystem computes water

content, electro-osmotic drag, water diffusion and conductivity of the membrane. The anode subsystem dynamically calculates oxygen and water flows and partial pressures. Similarly, hydrogen and water partial pressures and their flows are obtained in the cathode subsystem.

5.5.4 Fuel cell model

Fuel cell is part of the overall system of the hydrogen storage model, it basic function is to convert the hydrogen and oxygen as feeds to the anode and the cathode to produce water, heat and electrons as direct current through redox electrochemical reactions as illustrated in Fig. 5.9. Physics based and accurate plant model is the linchpin of control system development using Model-Based Design. A well-constructed plant model, engineers can verify the functionality of their control system, conduct closed-loop model-in-the-loop tests, tune gains via simulation, optimize the design, and run what-if analyses that would be difficult or risky to do on the actual plant. A model is only as accurate as its assumptions allow it to be. An understanding of the assumptions provides the limit of the model limitations and also provides a basis for the interpretation of the results. The most common assumptions made in fuel cell modelling and the system is described by ODE's in Eqs.(5.31) to (5.35) follows:

- Ideal gas properties,
- Incompressible flow,
- Laminar flow,
- Isotropic and homogeneous electrolyte, electrode, and bipolar material structures,
- A negligible ohmic potential drop in components,
- Mass and energy transport is modelled from a macro perspective using volume-averaged conservation equations,
- A porous area including membrane, catalyst layers and gas diffusion layers are considered to be isotropic

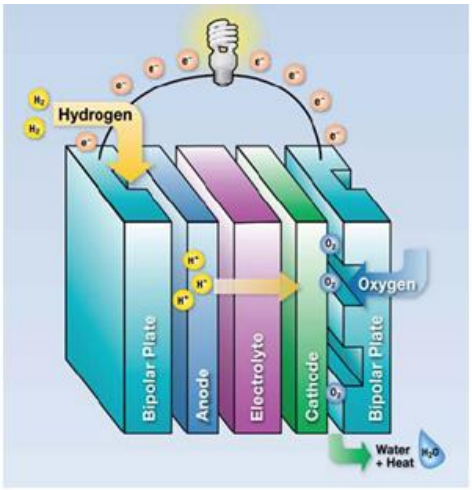

Figure 5.9 Fuel cell material and energy flow with hydrogen and oxygen gas in counter-current flow into the anode and cathode respectively. The output is a water and direct currents at the bipolar plate

Mass balance of oxygen, water and nitrogen about the cathode

$$\frac{dN_{O_2}}{dt} = F_{O2}^{in} - F_{O2}^{out} - \frac{nI_{fc}}{4F} \tag{5.31}$$

$$\frac{dN_{H_2O}}{dt} = F_{H2O}^{in} - F_{H2O}^{out} - \frac{nI_{fc}}{2F} - F_{H2O}^{mem} \tag{5.32}$$

$$\frac{dN_{N_2}}{dt} = F_{N2}^{in} - F_{N2}^{out} \tag{5.33}$$

Mass balance of hydrogen gas about the anode

$$\frac{dN_{H_2}}{dt} = F_{H2}^{in} - F_{H2}^{out} - \frac{nI_{fc}}{2F} \tag{5.34}$$

Energy balance about the cathode

$$M_{fc}C_{fc}\frac{dT}{dt} = \dot{Q}_{chem} - \dot{Q}_{elect} - \dot{Q}_{sen\,\&\,Lat} - \dot{Q}_{loss} \tag{5.35}$$

5.5.5 Hydrogen metal hydride storage model

The hydrogen storage model is based on a concentric cylindrical aluminium metal hydride tank. The hydrogen gas enters from the bottom and the gas is absorbed by the tank metal hydride powder. The physics of the process is represented by a mass and energy conservation as partial derivatives (Brown et al, 2008). The mass conservation and energy equation are given in Eqs.(5.36) and (5.37) as follows;

$$\frac{\partial m_s}{\partial t} = -C_a e^{\left(\frac{E_a}{RT}\right)} \log\left(\frac{P_g}{P_{VH}}\right)(\rho_{full} - \rho_{node})V_s \tag{5.36}$$

$$V_s\, C_h\, \rho_{node} \frac{\partial T_s}{\partial t} = k_s A \frac{\partial T_s}{\partial x} - C_a e^{(\frac{E_a}{RT})} \log\left(\frac{P_g}{P_{VH}}\right)(\rho_{full} - \rho_{node}) V_s\, \Delta H \qquad (5.37)$$

where $\log\left(\frac{P_g}{P_{VH}}\right) = \frac{\Delta H}{RT_g} - \frac{\Delta S}{R}$, $V_s = (1 - \varepsilon)V_{node}$

Table 5.1 Steady state metal hydride hydrogen storage tank parameters

Parameter	Description	Value
Hydrogen tank metal hydride steady state parameters		
C_h	Hydride specific heat (J/kg. K)	418.7
C_a	Adsorption desorption rate constant (s^{-1})	2800
ρ_h	Density of solid hydride (kg/m^3)	8300
ρ_m	Density of Aluminium metal container (kg/m^3)	2700
ε	Solid porosity	0.44
E_a	Activation energy ($Jmol^{-1}$)	31000
ΔH	Enthalpy ($Jmol^{-1}$)	30800
ΔS	Entropy ($Jmol^{-1}K^{-1}$)	108
R	Universal gas constant (J/mol.K)	8.314
ks	Hydride conduction coefficient (W/m. K)	1

The models are highly nonlinear and of hyperbolic partial differential equation type. Consequently, Laplace transforms and Tylor series linearization technique was used in making the model system analysis and control oriented ready. The procedure involves a Laplace transforms in the s space, combing the transfer functions with delays manually and converting it to state space form for analysis.

5.5.6 The battery model

The battery model is a simple voltage source connected to series resistance to account for the internal resistance of the electrolyte in the battery. The voltage and the resistance are functions of the state of charge (SOC) of the battery. The SOC is a conditioning monitoring function of the battery for visually display it health status. The equivalent circuit diagram is shown fig. 5.10 as follows (Kim and Ha, 1997)

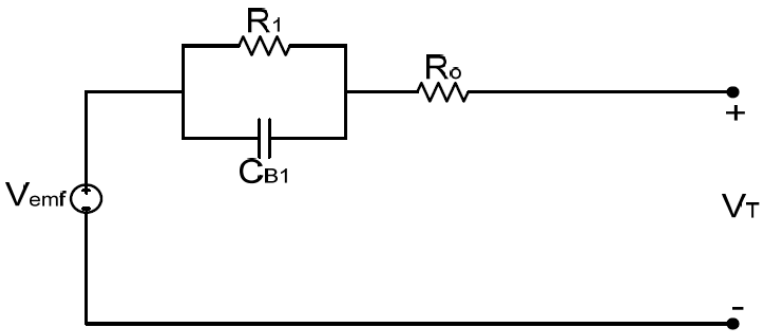

Figure 5.10 A simple equivalent circuits of a Lead acid battery with a voltage source internal resistance and capacitance; a terminal voltage as output or point of connection to the load

$$\frac{d(SOC)}{dt} = \frac{I_{bat}\, V_{EMF}}{E_{bat}} \tag{5.38}$$

$$\frac{dV_{bat}}{dt} = \frac{(I_2 - I_{bat})}{C_1} \tag{5.39}$$

$$I_2 = \frac{V_{EMF} - V_{bat}}{R_1} \tag{5.40}$$

$$V_{EMF} = V_{EMF_{min}} - k_e\, SOC \tag{5.41}$$

$$V_T = V_{bat} - I_{bat}\, R_0 \tag{5.42}$$

Substituting the algebraic equations in Eqs.(5.38) -(5.42) in the ODE for SOC and V_{bat}, the state space equation can be written as;

$$\begin{pmatrix} \dot{SOC} \\ \dot{V}_{bat} \end{pmatrix} = \begin{pmatrix} -\frac{k_e}{E_{bat}} & 0 \\ -\frac{k_e}{R_1 C_1} & -\frac{1}{R_1 C_1} \end{pmatrix} \begin{pmatrix} SOC \\ V_{bat} \end{pmatrix} + \begin{pmatrix} -\frac{V_{EMF_{min}}}{E_{bat}} & 0 \\ -R_1 & \frac{1}{R_1 C_1} \end{pmatrix} \begin{pmatrix} I_{bat} \\ V_{ref} \end{pmatrix} \tag{5.43}$$

$$y = \begin{pmatrix} 1 & 0 \\ 0 & 1 \end{pmatrix} \begin{pmatrix} SOC \\ V_{bat} \end{pmatrix} + [0] \begin{pmatrix} I_{bat} \\ V_{ref} \end{pmatrix} \tag{5.44}$$

The battery is one of the major system that works in tandem with the supervisory controller in chapter 7 for charging and discharging cycles of the storage interplay in the centralised control structure.

5.5.7 Solar space heating and airconditioning modeling

There is a renewed call by the European commission to promote or encourage 25% renewable heating and cooling to be supplied by renewables by 2020 according to Treberspurg & Djalili, (2011). The United Kingdom is just 1% of total world population yet the carbon emission level is a 2.3%, as postulated in the work of Fawcett, Hurst & Boardman

(2002). From the study, the UK is making tremendous contribution to cutting emission but this effort will require a significant effort in the building energy sector in reducing energy demand in space heating. In a study by Herring, Hardcastle, & Phillipson (2000); DTI. Digest of UK energy statistics, (2001), space heating contributes 25% of building carbon emission and 40% of energy cost in the residential sector.

Fundamentally, most space heating and domestic hot water system today especially in the develop nations such as Europe and America, work with a domestic boiler driven by natural gas for heating water circulated through room radiator (Boait & Rylatt, 2010). In a study conducted by BRECSU and reported in General Information Report No. 40 (1996), estimated that 90% of heating systems were inefficiently operated due to inadequate control, and calculable for the huge cost in industry and commerce, amounting to £500 million per annum in additional energy consumption. A more comprehensive treatment of absorption refrigeration is provided in the work of Srikhirin (2001), in which a detailed review of absorption refrigerated technology was presented with variation in the design and different configurations of the absorption heat pumps.

The room-heater-cooling controller model in fig. 5.11 is a simplified form of a space heating air-conditioning system. The protocol touch more on refrigeration or space cooling account for 40% of total electricity supplied to domestic dwellings in a conventional fossil fuels generation system. To reduce the impact of this effect on the climate, other means of providing cooling to domestic, commercial and industrial systems must be sought. Solar refrigeration is one of the most viable alternatives as cooling demand increases with increase in the intensity of solar insolation as reported in the work of Kim & Ferreira, (2008).

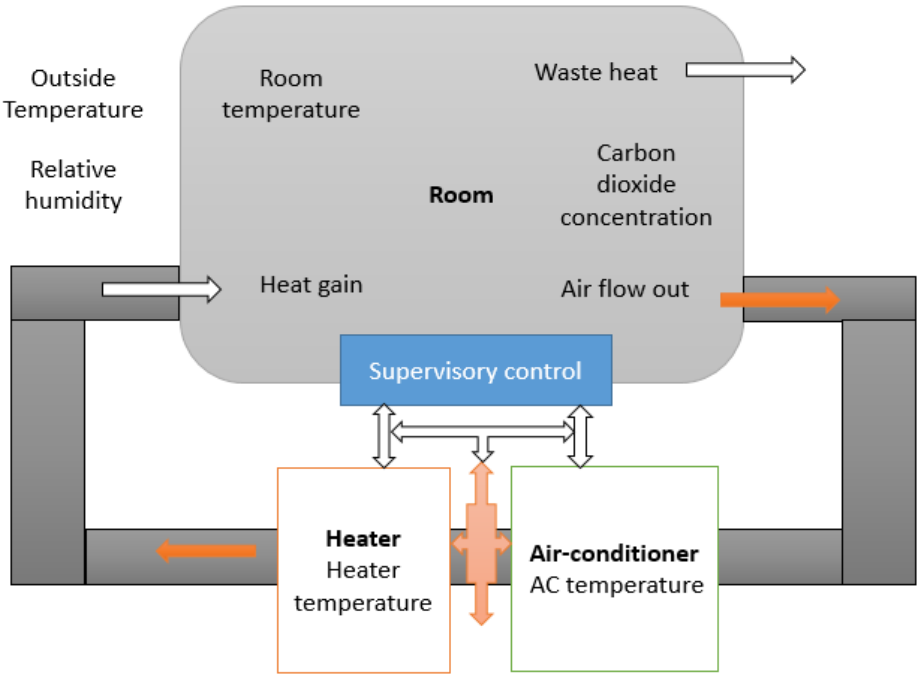

Figure 5.11 An integrated room space heating and air-conditioning system, with heater, room space, supervisory controller, 3-way control valve and air ducts. Carbon dioxide concentration and relative humidity are model in the conceptual heating and cooling system

5.5.8 Space heating and cooling models

Rate of heat gain and loss between the room and the heater or cooler is modelled as convection of heated air, from the heater and cooled air from the air-conditioner. The models are presented in equation (5.45) and (5.49) as follows;

$$\frac{dQ_{gain,H}}{dt} = M_{heater\ air}\, c_{air}(T_{heater} - T_{room}) \tag{5.45}$$

$$\frac{dQ_{loss,C}}{dt} = M_{AC\ air}\, c_{air}(T_{AC} - T_{room}) \tag{5.46}$$

The rate of thermal energy loss from the room with the outside, is driven by conduction through the walls and windows is presented in Eq. (5.47);

$$\frac{dQ_{loss}}{dt} = \frac{T_{room} - T_{outside}}{R} \tag{5.47}$$

The change in room temperature for heating and cooling model is given in Eqs. (5.48) and (5.49) as follows;

$$\frac{dT_{room,H}}{dt} = \frac{1}{m_{room,air}\ c_{air}} \left\{ \left(M_{heater\ air}\, c_{air}(T_{heater} - T_{room})\right) - \left(\frac{T_{room} - T_{outside}}{R}\right) \right\} \tag{5.48}$$

$$\frac{dT_{room,C}}{dt} = \frac{1}{m_{room,air}\ c_{air}} \{ \left(M_{AC\ air}\ c_{air}(T_{AC} - T_{room})\right) - \left(\frac{T_{room} - T_{outside}}{R}\right)\} \quad (5.49)$$

Humidity ratio room in and outside and carbon dioxide concentration in the room are represented and presented in (5.50) and (5.51) (Kang, Park, Park, & Baek, 2014) as follows;

$$\frac{dH}{dt} = \frac{60F}{V_s}(Hs - H) + \frac{M_0}{\rho_a V_s} \quad (5.50)$$

$$\frac{dC_s}{dt} = \frac{C_g}{V_s} + (1 - \mu)\frac{C_s}{V_s} \quad (5.51)$$

Table 5.2 Steady state cooling and heating parameters

Parameter	Description	Value
Cooling and heating steady state parameters		
ρ_a	Air mass density (kg/m^3)	1.19
V_{he}	Volume of heat exchanger (m^3)	1.72
V_s	Volume of thermal space for heating and cooling (m^3)	102
C_{pa}, c_{air}	Specific heat of air (J/kg. K)	1004.83
H_s	Humidity of air supplied (kg/kg)	0.0070
M_0	Moisture level (kg /s)	0.021
Q_0	Sensible heat load (kW)	2256
C_g	Carbon dioxide concentration (kg/m^3)	0.4
T_0	Temperature of outdoor air (^{0}C)	29.44
h_{fg}	Enthalpy of water vapour (0-100^{0}C) (kJ/mol)	40.65
T_{room}	Room temperature (^{0}C)	20
μ	Air circulation rate	0.5
T_{Heater}	Heater temperature (^{0}C)	50
F	Mass flow rate of air (kg/s)	1

$M_{Heater,air}$	Mass flow rate of heater air (kg/s)	1
$M_{AC,air}$	Mass flow rate of AC air (kg/s)	1
T_{AC}	AC temperature (^{0}C)	18
R	Thermal resistance (s. ^{0}C/J)	4.33e-7

5.5.9 System Analysis tools of HCCHP

A state space model representation of all the subsystem constituting hydrogen combined cooling heat and power, provides a compact and efficient way of qualitatively and quantitatively analysing the behaviour of each subsystem in time and frequency domain. The system analysis tools for analysing a system includes but are not limited to the following; phase portrait, singular value decomposition, Relative gain array, controllability, Bode diagram, Nyquist diagram.

5.5.9.1 Phase Portrait

It is a qualitative and graphical means of visualising the dynamics of system as a vector fields and direction vectors in 2 dimensional plane or 3 dimensional hyper plane. Phase portrait provides a visual means of interpretation of control actions.

5.5.10 Singular value decomposition (SVD)

Singular value decomposition (SVD) is a method of data analysis aimed at obtaining low-dimensional approximation descriptions of high-dimensional processes.

Lemma 1: *For any matrix $H \in R^{m\times n}$ exists a unitary matrix, $U^{-1} = U^T$, $U \in R^{m\times m}$ which its columns form an orthonormal basis, a unitary matrix $V \in R^{n\times n}$ which its columns form an orthonormal basis and a diagonal matrix decreasing order $\Sigma \in R^{m\times n}$ i.e.,*

$$\Sigma = \begin{pmatrix} \sigma_1 & 0 & \cdots & 0 \\ \vdots & \sigma_2 & \ddots & \vdots \\ 0 & 0 & \cdots & 0 \end{pmatrix} ; \sigma_1 \geq \sigma_2 \geq \dots \sigma_m \tag{5.52}$$

Such that,

$$H = U\Sigma V^T \tag{5.53}$$

The diagonal entries σ_1 of Σ are called the singular value of H. Σ's elements which are the singular values, are the square roots of the eigenvalues of UU^T and U^TU. The columns of U are called left singular values of H which are the eigenvectors of H^TH. The columns of V are called right singular values and are the eigenvectors of HH^T.

The Left Singular Vectors provide the most appropriate coordinate system for viewing the process sensors. This coordinate system is such that the first singular vector (U_1) indicates the easiest direction in which the system can be changed. The second singular vector (U_2) is the next easiest direction. The third is the next easiest, and so on....

The Right Singular Vectors provide the most appropriate coordinate system for viewing the manipulated variables. This coordinate system is such that the first singular vector (V_1) indicates the combination of control actions which has the most effect on the system. The second singular vector (V_2) is the combination which has the next strongest effect, and so on...

The Singular Values provide the ideal decoupled gain of the open loop process. The ratio of the largest singular value to the smallest is the Condition Number of the gain matrix and is a measure of the difficulty of the decoupled multivariable control problem. Large condition numbers indicate that the degrees-of-freedom are such that the number of control objectives need to be reduced.

5.5.11 Index of controllability

One important aspect of the physical significance of the Singular value analysis can be seen in the Condition Number. The condition number is the ratio of the largest to the smallest singular value and is used in numerical computation to quantify the "condition" of a set of equations.

$$\text{Condition Number (CN)} = \frac{\sigma_{max}}{\sigma_{min}} \tag{5.54}$$

5.5.12 Analysis of level of coupling or interaction

The degree of interactions between input and output can be quantitatively defined using the Relative gain array and the Niederlinski index.

5.5.13 Relative Gain Array (RGA)

Type of interaction-decoupled, partially coupled and fully coupled-input output pairing calculation of the relative gains for all combinations of input/output pairs in a multivariable system leads to the following matrix known as the relative gain array (RGA) or the Bristol Array. A Multivariable process is said to have interaction when process input affect more than one process output. The RGA is expressed mathematically in Eq. (5.55) as follows;

$$RGA = G_0 .* inv(G_0)^T \tag{5.55}$$

where G_0 is the steady state coefficient matrix of the state variable and $inv(G_0)^T$ is the inverse of steady state matrix transpose.

The RGA is weak in capturing the dynamics of the system, making it deficient input output signal pairing and must use in conjunction with Niederlinski index. In addition, it is established in control practice that, pairing with negative RGA-element is not desirable since this will cause the gain to change sign when the other loops are closed. Further investigations made by Grosdidier et al. (1985) have shown that pairings with negative RGA-elements may cause instability. Another result to consider in order to avoid pairings that may lead to instability is Niederlinski's theorem introduced by Niederlinski (1971) and refined by Grosdidier et al. (1985) is given in (5.56) as follows;

$$NI = \det\big(G(0)\big) / \prod_{i=1}^{p} G_{ii} \tag{5.56}$$

The necessary and sufficient condition for instability of the closed-loop system is that NI $<$ 0.

5.5.14 Stability

The stability of a multivariable control system is represented graphically using Nyquist plot based on the Nyquist stability criterion. Nyquist plot is a polar plot of the closed loop transfer function equal to the open-loop transfer function plus the number of encirclement around the (-1, j0) point on the complex plane.

The Nyquist stability criterion state that the number of unstable closed loop poles (z) is equal to the number of unstable open-loop poles (P) plus the number of encirclements (N) of the point (-1, j0). A multivariable system is stable if all poles of the transfer function lie in the LHP; otherwise it is unstable.

5.5.15 Controllability

A system is controllable if the controlled variables can be maintained at their set points, in the steady state, in spite of disturbances entering the system. In designing a control system, a linear time-invariant (LTI) systems model is used. It can be proposed that a system is reachable if and only if its **controllability matrix**, ζ, has a full row rank of p, where p is the dimension of the matrix A, and $p \times q$ is the dimension of matrix B. The controllability matrix ζ is defined as (Wikibooks, 2017);

$$\zeta = [\mathrm{B}\ \ \mathrm{AB}\ \ A^2B \ldots A^{p-1}B] \in R^{p \times pq} \tag{5.57}$$

A system is controllable when the rank of the system matrix A is p, and the rank of the controllability matrix is equal to (Wikibooks, 2017);

$$\mathrm{Rank}\ (\zeta) = Rank(A^{-1}\zeta) = \mathrm{p} \tag{5.58}$$

5.5.16 Analysis and findings of result obtained

5.5.16.1 Phase portrait plots

Phase portrait trajectory of copper metal temperature versus heat transfer fluid temperature. In fig. 5.12 the trajectory indicated by the arrows direction fields and the direction vectors moving in and diverging from a common saddle point at (0.0041177, 0.0040274). The trajectories indicated by the eigenvectors of the negative eigenvalue initially start at infinite-distant away from the plane of the paper, move toward and eventually converge at the critical point. The trajectories that represent the eigenvectors of the positive eigenvalue move in exactly the opposite way i.e. start at the critical point then diverge to infinite-distant out of the plane of the paper. Every other trajectory starts at infinite-distant away, moves toward but never converges to the critical point, before changing direction and moves back to infinite-distant away. This type of critical point is called a saddle point represented by the red point on the phase portrait. This type saddle critical point is unstable and validated by the eigenvalues poles and zero, Nyquist plot and Niederlinski's index in table 5.6. The phase portrait is a visual validation of the dynamic behaviour of the heat transfer fluid temperature and the receiver temperature. Instability can be cancel out or remove by adding a new variable control system such as pole placement and PID classical control. The details of this procedure is provided in chapter 6.

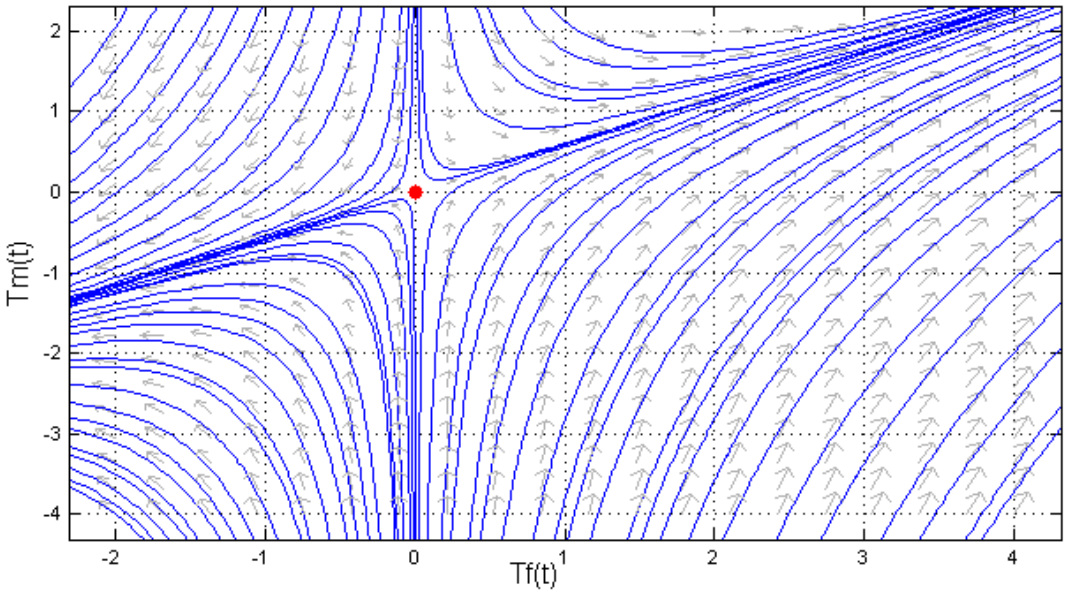

Figure 5.12 Phase portrait trajectory of copper metal temperature (T_m) versus heat transfer fluid (T_f) module temperature

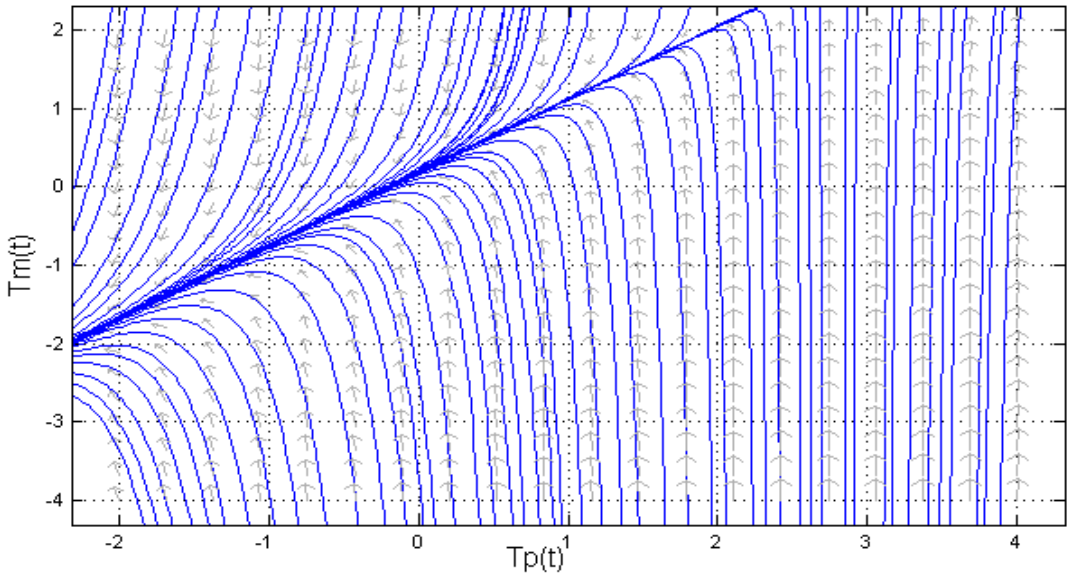

Figure 5.13 Phase portrait trajectory of copper metal temperature (T_m) versus PV module temperature (T_p)

There are two critical points in the phase portrait between the temperature of the PV module and the receiver metal. In the first part represented ¾ part of the paper, the direction vectors come from in infinite position from top and bottom end of the towards a common line at a ¾ part of the plane of the paper and converged towards a common line of the paper out of the plane of the paper. This type critical point is called a degenerate stable nodal line and it is stable. The stability could be inferred from the fact that the entropy or the degree of disorderliness is less or non-existence in solid-solid thermal dynamics between the solar PV module and the copper receiver. The second part is represented by the ¼ part of the paper come from the bottom parts and moves out of the plane of the paper. The second critical point is an infinite number of node and is unstable. The conclusion drawn from the plot is that the system is unstable.

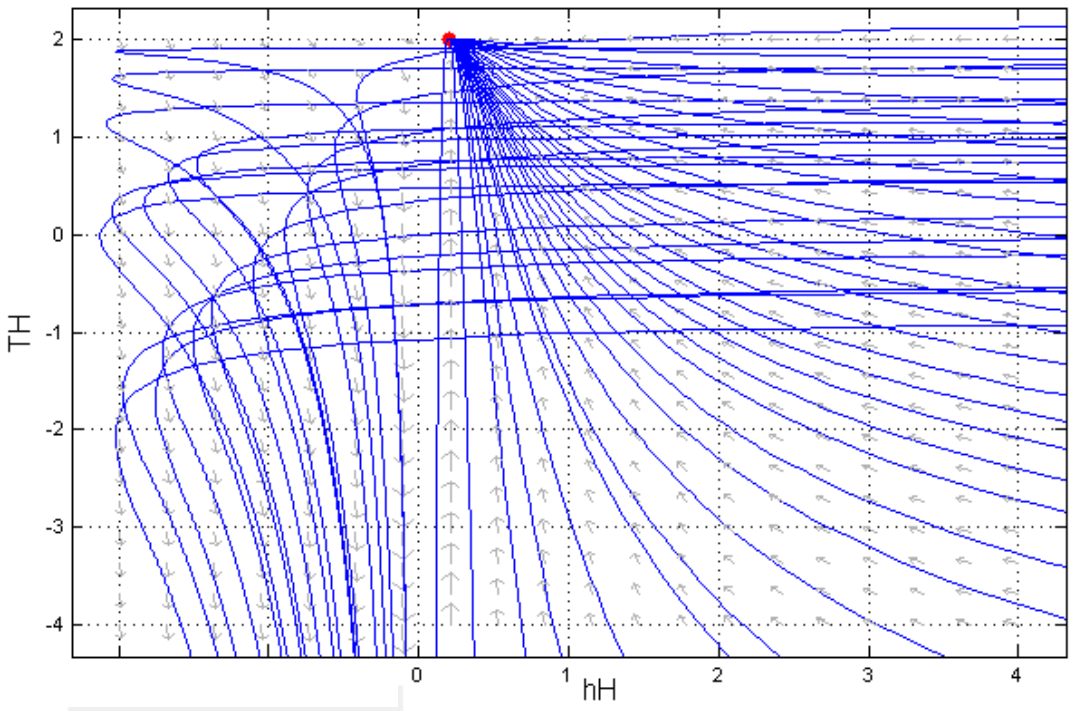

Figure 5.14 Phase portrait of temperature against height of the tank trajectory with the equilibrium point at the zero point on the height axis

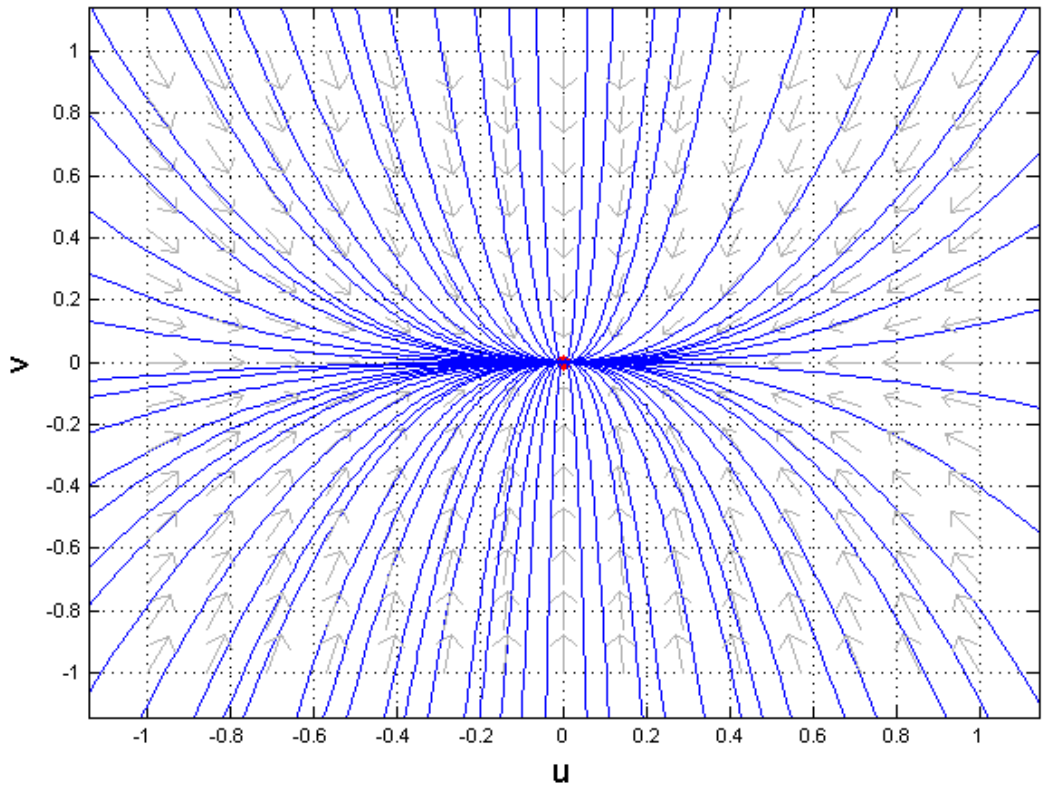

Figure 5.15 Phase portrait of a linearization hot storage tank

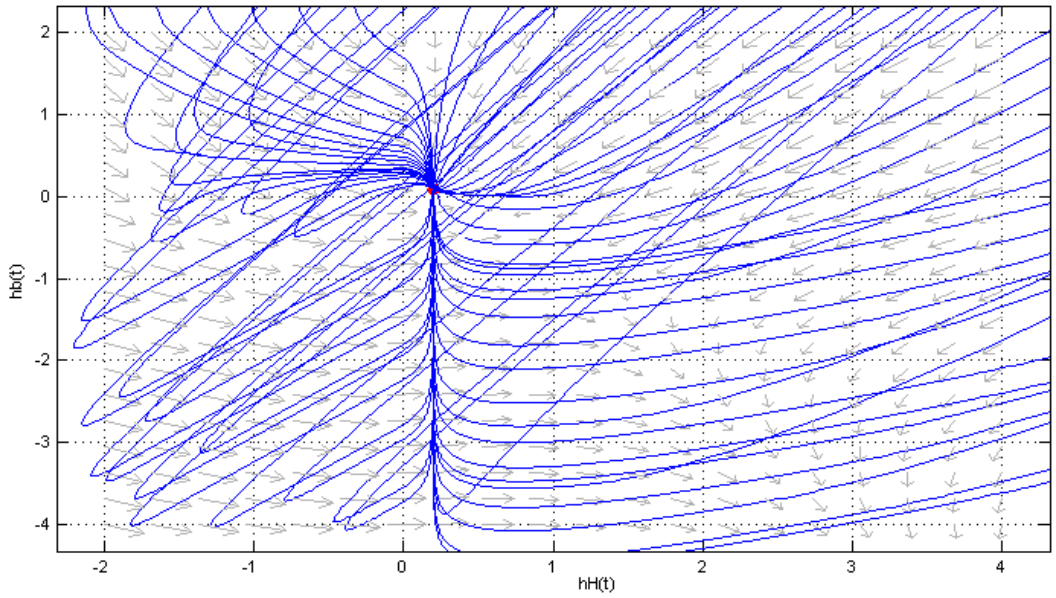

Figure 5.16 Phase portrait and Phase portraits linearization of height of hot and boiler storage tank

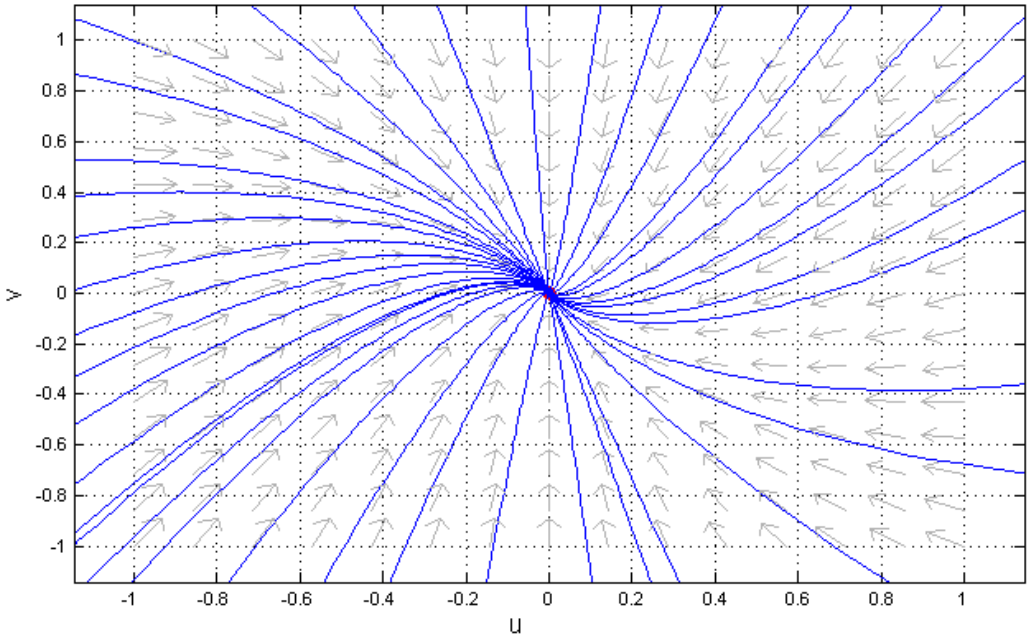

Figure 5.17 Phase portrait of linearized boiler heat exchanger

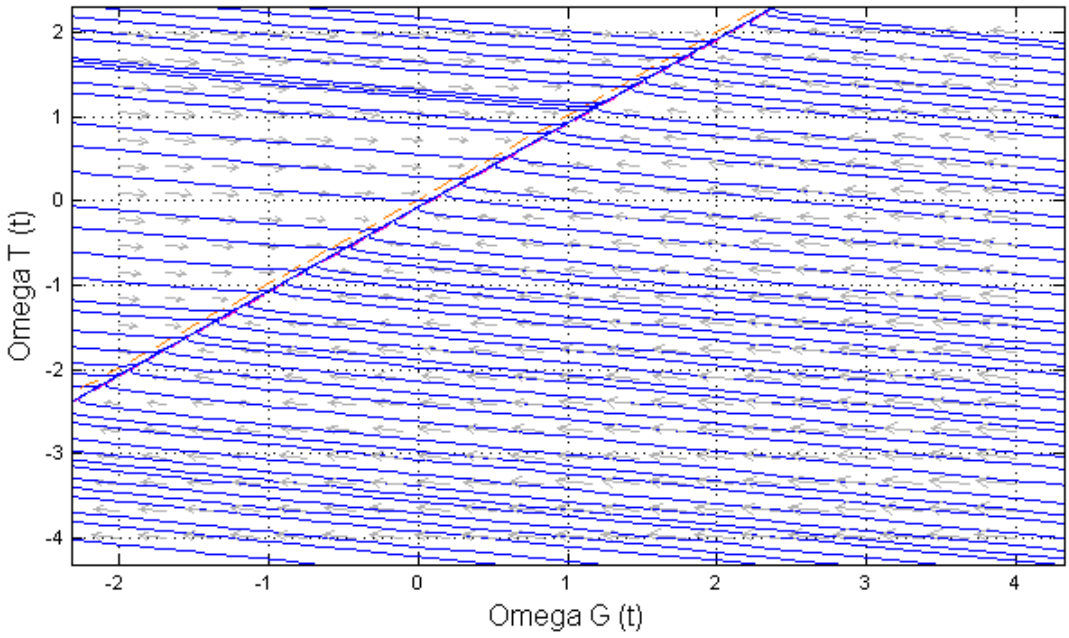

Figure 5.18 Phase portrait of the wind turbine generator rotational speed and the turbine rotational speed

The phase portrait of the wind turbine generator rotational speed and the turbine rotational speed in fig. 5.18, is type critical point called a degenerate stable nodal line and it is stable. the direction vectors come from in infinite position from top left and bottom and top end of the right of the paper, towards a common line at a ¼ part of the plane of the paper and converged towards a common line of the paper out of the plane of the paper.

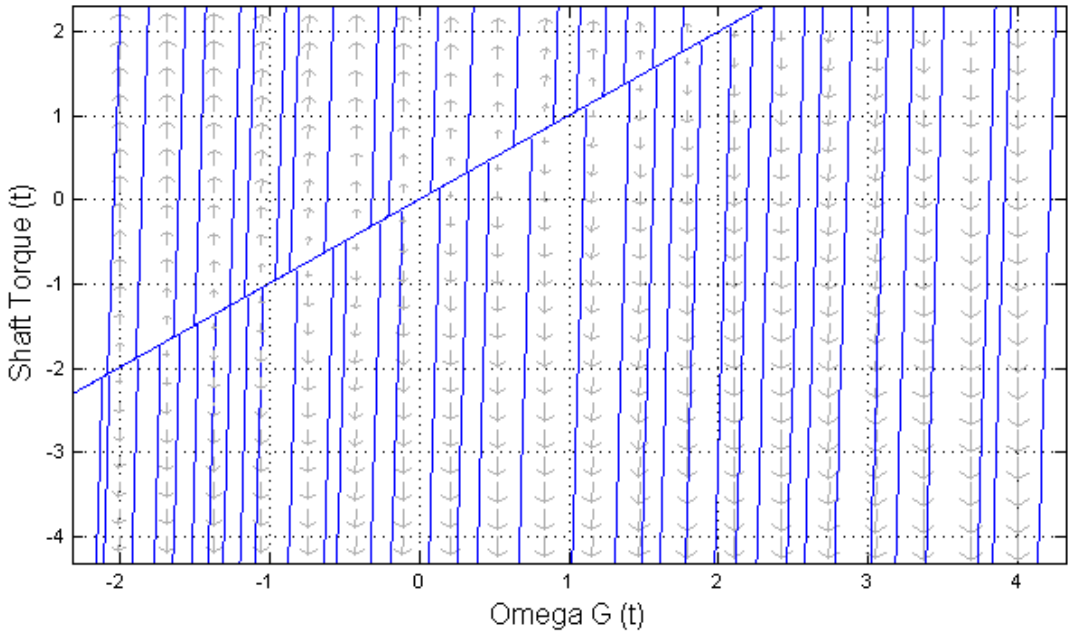

Figure 5.19 Phase portrait of the wind turbine generator rotational speed and the turbine rotational speed

The phase portrait of the shaft torque and the rotation speed of the generator in fig. 5.19 is an unstable degenerate nodal line. The direction eigenvectors are positive and moves away from the nodal degenerate line out of the plane of the paper and partition the plane of the paper into ¾ parts. The system from the trajectories is unstable degenerate node.

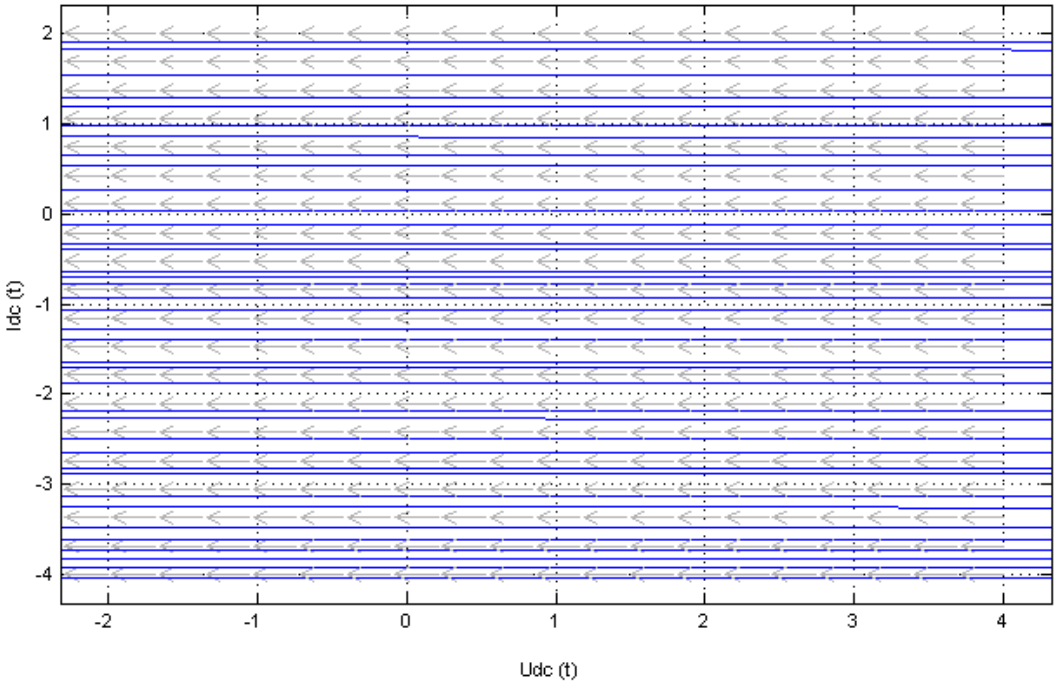

Figure 5.20 Phase portrait of converter DC current (I_{DC}) versus voltage (U_{DC})

The phase portrait in fig. 5.20 of the power electronics direct currents and the direct voltage is a critical point with infinite number of point along the y-axis with direction field vectors from the left plane of the paper towards the right of the paper. This is an unstable critical point, hence the dynamics of the DC power electronics is unstable.

Table 5.3 Mechanical, electrochemical, DC link and LC filter steady states parameter values for wind turbine subsystem analysis and control studies

Parameter	Description	Value
Wind turbine mechanical steady state parameters		
P_{rated}	Rated power of the wind turbine (kW)	15
V_{rated}	Rated voltage of the wind turbine (V)	400
N_p	Number of Poles	102
ω_s	Rated rotational speed (rps)	150
V_{tip}	Rated tip speed (m/s)	4
J_g	Generator Moments of inertia ($kg.m^2/s^4$)	386.85
J_t	Turbine Moments of inertia ($kg.m^2/s^4$)	2256
T_t	Turbine nominal torque (N.m)	4
T_s	Turbine shaft torque (N.m)	260
D_s	Drive train damping coefficient (N.m/rad. s)	18630
k	Drive train spring constant (N.m/rad)	2602.89
λ		0.192
Wind turbine electromechanical, DC link & LC filter steady state parameters		
V_g	Permanent Magnet Synchronous Generator Voltage (V)	400
f	Frequency (Hz)	50
R_p	Phase resistance (Ω)	0.06
L_p	Phase inductance (mH)	1.89
P_g	Rated power of PMSG (kW)	17
ω_g	Generator speed (rps)	750
T_g	Generator Torque at full load (N.m)	1401

C_f	LC filter capacitance (MF)	6.50
R_f	LC filter resistance (Ω)	0.0076
L_f	LC filter inductance (mH)	9.90
C_{DC}	DC capacitance link (μF)	1000

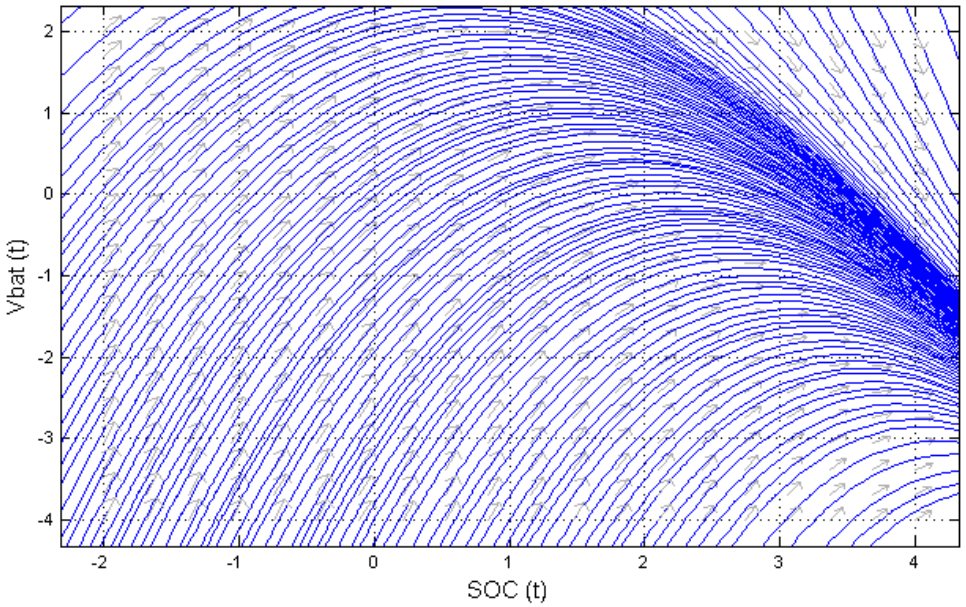

Figure 5.21 Phase portrait between battery state of charge (SOC) and the voltage with the gradient and the dirction vectors arrow diagram

The battery state of charge (SOC) and the battery voltage phase portrait in fig. 5.21 presents an interesting dynamic behaviour depicting a spiral node critical points moving out of the plane of the paper at the lower right end of the paper. The critical point is a spiral node at infinite position outside the plane of the phase portrait.

Table 5.4 Steady state parameters and constant used in the analysis of battery subsystem

Parameters	Description	Value
AGM deep cycle Trojan 12v c20 charging rate		
R_0	Battery ohmic resistance (Ω)	0.157
R_1	Energy loss charge transfer resistance in the double layer (Ω)	0.063
C_{B1}	Internal battery capacitance (F)	5.283
K_e	Battery EMF voltage versus SOC constant	1.5
I_{bat}	Average battery current from sizing in chapter 3 (A)	131
V_{emf}	Battery EMF voltage (V)	11.5
E_{bat}	Battery rated capacity (Ah)	200

Table 5.5 Steady state parameters and constant used in the analysis of electrolyser subsystem

Parameter	Description	Value
Pure gen 30 kW electrolyser state parameters		
C_{ele}	Overall thermal capacitance of electrolyser (J/K)	625
F	Faraday's constant (C/mol)	96485
R_t	Overall thermal resistance of electrolyser (W/K)	0.167
C_{pw}	Specific heat capacity of water (J/mol. K)	4200
R	Universal gas constant (J/K.mol)	8.315
V_a	Volume of anode (m^3)	2
V_c	Volume of cathode (m^3)	2
U	Pure gen electrolyser voltage from sizing chapter 3 (VAC)	400

I_{ele}	Pure gen electrolyser current from sizing chapter 3 (A)	70.25
M_{ele}	Mass of Pure gen 30 kW (kg)	440
P	Electrolyser operating pressure (N/m^2)	101325
n	Number of cells	3
T_{ele}	Electrolyser operating temperature (K)	300
η_{ele}	Electrolyser efficiency	0.75

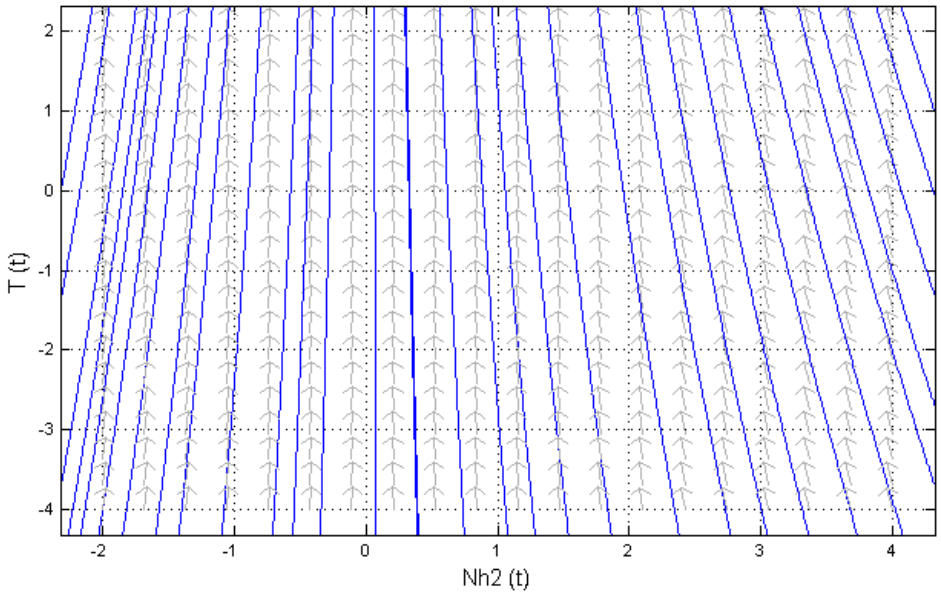

Figure 5.22 Phase portrait between electrolyser moles of hydrogen produce and the temperature with the gradient and the direction vectors arrow diagram

The phase portrait of the electrolyser is an infinite number of critical point from the bottom part of the paper and migrating towards the top to an infinite location outside the plane of the paper. The system temperature of the electrolyser and the number of moles of hydrogen gas produced by the electrolyser is unstable as a result of the infinite number of critical equilibrium point.

Table 5.6 A tabular summary results of the state space A and B matrix, rank and controllability of each subsystem, condition number from the singular value decomposition analysis, poles and zero values from eigenvalues and Nyquist stability criterion, Nierdlinki Index and stability classification

	State space model A&B matrix	Rank & Controllability	Condition number	Poles and zeros	NI	stability
Subsystem						
Trough PVT thermal	6×6 & 4×4	6, controllable	490200	-25, -0.328,0.0208,0.2330,0.1709,0.0001	0.0677	unstable
Trough PVT Mechanical tracking						
Wind turbine mechanical	3×3 & 3×3	4, not controllable	2.8×10^{24}	-28.21+66.407i, -28.21-66.407i, 3.4×10^{-15} +0i	-inf	unstable
Wind turbine electronics	3×3 & 3×3	3, controllable	655880000	-0.0000202, -0.770 and 3.2	-inf	unstable
Battery	2×2 & 2×2	2, controllable	10.2083	3 and -0.98	1	unstable
Electrolyser	3×3 & 3×3	3, controllable	2.9059	0.0123, -0.0123 and -0.0123	1	unstable
Fuel cell	4×4 & 4×4	4, controllable	5856	-0.0017+0i, -1.0959+1.8334i, -1.0959-1.8334i,1.2581+0i	-inf	unstable
Heater cooling	3×3 & 3×3	3, controllable	84777000	-0.6993,35.6153,0.0360	-19.8	unstable

The results in table 5.6 is compilation of the results obtained from the computation using MATLAB control system toolbox functions. The trough subsystem was set of linear autonomous first order differential equations by a 6×6 coefficient matrix or gain matrix and

4×4 input matrix. The rank of the A and B matrix was computed using rank (ctrb (A, B)) function. The rank of the 6×6 A matrix and 4×4 input matrix, returned a value of 6. The trough system is controllable since the rank is equal to the rank of the 2 matrix. The trough receiver subsystem is tightly coupled and can be controlled by multivariable control from the condition number of 490200 obtained from the singular value decomposition analysis. The poles and zero is an indication of the instability since there exist a positive real numbers of 0.0208,0.2330,0.1709,0.0001. The instability is validated by a positive value obtained from eigenvalues, Nyquist stability criterion and Nierdlinki Index. The trough receiver system is controllable and can be controlled by poles placement with procedure provided in chapter 6. The same explanation and analysis applies to the other subsystems except for the tracking whose model is 3D CAD mechanical system.

The electrolyser and the battery subsystem can be decoupled and treated as a decentralised control since their condition numbers are both less than 20. However, both subsystems are unstable and can be controlled from the rank order of 3 and 2 and the matrix order of 3 and 2 respectively. The mechanical wind turbine subsystem is the only subsystem that present a challenging result of not being controllable since the rank order of the matrix is of a higher order of 4 compared to the coefficient matrix order of 3.

Table 5.7 A tabular summary of the relative gain array (RGA) matrix of each subsystem, the input-output combinations or pairing and the type of interactions relationships for a decentralised multivariable control architecture

Subsystems	RGA matrix	Input-output pairing	Input-output interactions relationship type
Trough PVT thermal	$\begin{bmatrix} 0.063 & 0.94 & 0 & 0 & 0 & 0 \\ 0.94 & 22.6 & -22.6 & 0 & 0 & 0 \\ 0 & 22.6 & 21.12 & 2.42 & 0 & 0 \\ 0 & 0 & 2.42 & -1.03 & -0.39 & 0 \\ 0 & 0 & 0 & -0.39 & 1.39 & 0 \\ 0 & 0 & 0 & 0 & 0 & 1 \end{bmatrix}$	u_2->y_2, u_2->y_1 u_2->y_3, u_3->y_4 u_4->y_5, u_4->y_6	Fully coupled
Wind turbine mechanical	$\begin{bmatrix} -\infty & \infty & \infty \\ \infty & -\infty & -\infty \\ -\infty & \infty & Nan \end{bmatrix}$	u_1->y_2, u_2->y_1 u_2->y_3	coupled
Wind turbine electronics	$\begin{bmatrix} 0 & 1 & 0 \\ 1 & 0 & 0 \\ 0 & 0 & 1 \end{bmatrix}$	u_1->y_2, u_2->y_1 & u_3->y_3	2 coupled and 1 decoupled
Battery	$\begin{bmatrix} 1 & 0 \\ 0 & 1 \end{bmatrix}$	u_1->y_1, u_2->y_2	Fully decoupled
Electrolyser	$\begin{bmatrix} 1 & 0 & 0 \\ 0 & 1 & 0 \\ 0 & 0 & 1 \end{bmatrix}$	u_1->y_1, u_2->y_2 & u_3->y_3	Fully decoupled

Fuel cell	$\begin{bmatrix} 0 & 1 & 0 & 0 \\ 0 & 0 & 1 & 0 \\ 1 & 0 & 0 & 0 \\ 0 & 0 & 0 & 1 \end{bmatrix}$	u_1->y_3, u_2->y_1, u_3->y_2 & u_4->y_4	3 coupled and 1 decoupled
Heater cooling	$\begin{bmatrix} -0.0504 & 0 & 1.0504 \\ 0 & 1 & 0 \\ 1.0504 & 0 & -0.0504 \end{bmatrix}$	u_1->y_3, u_2->y_2 & u_3->y_1	2 coupled and 1 decoupled

In table 5.7, the results of the computation of the relative gains for all possible combinations of input/output pairs in column 3. The outcome of the gain is a matrix presented in column 2 for each subsystems known as the relative gain array (RGA) or Bristol Array. The trough PVT subsystems in row 1 column 3 u_2 is used to manipulate and control the EVA and Tedler temperature y_2 (T_{et}), the top temperature of the receiver y_1 (T_t) and the temperature of the metal tube y_3 (T_m). A second actuator or valve u_3 is used to manipulate and control the heat transfer fluid temperature y_4 (T_f) and actuator u_4 is used to manipulate and control PV temperature y_5 (T_p) and mirror temperature y_6 (T_c). In this decentralised architecture, a single manipulated variable or actuator can control more than one variable. The interaction is a fully coupled relation as indicated by the large value of the conditioned number in table 5.7. In the wind turbine mechanical subsystem, manipulated variable input u_1 control generator speed ω_g (y_2) and actuator input u_2 is used to manipulate and control turbine speed ω_t (y_1) and the shaft torque T_s (y_3). The infinity values in the gain matrix is as result of the large values of the steady state turbine parameters in table. The input/output interactions are coupled revealed by the large value of the condition from the singular value decomposition analysis (2.8×10^{24}). The power electronics subsystem of the wind turbine, the u_1 is used to manipulate and control the DC link current I_R (y_2), u_2 manipulate and control voltage of the AC to DC converter U_{DC} (y_1) and u_3 control the torque from the air mass noise ΔT_t (y_3). The interaction is coupled since there are 2 fully couple loops and validated by the condition number of 655880000.

In the battery subsystem, it is a decoupled system since input u_1 is used to manipulate and control the state of charge (SOC) y_1 and input u_2 is used to manipulate and control the battery terminal voltage V_{bat} (y_2). The SVD analysis condition validate the outcome of the RGA analysis with a condition number of 10.2083, a number less than 50. The same analysis follows for the electrolyser, fuel cell and the heating and cooling subsystems.

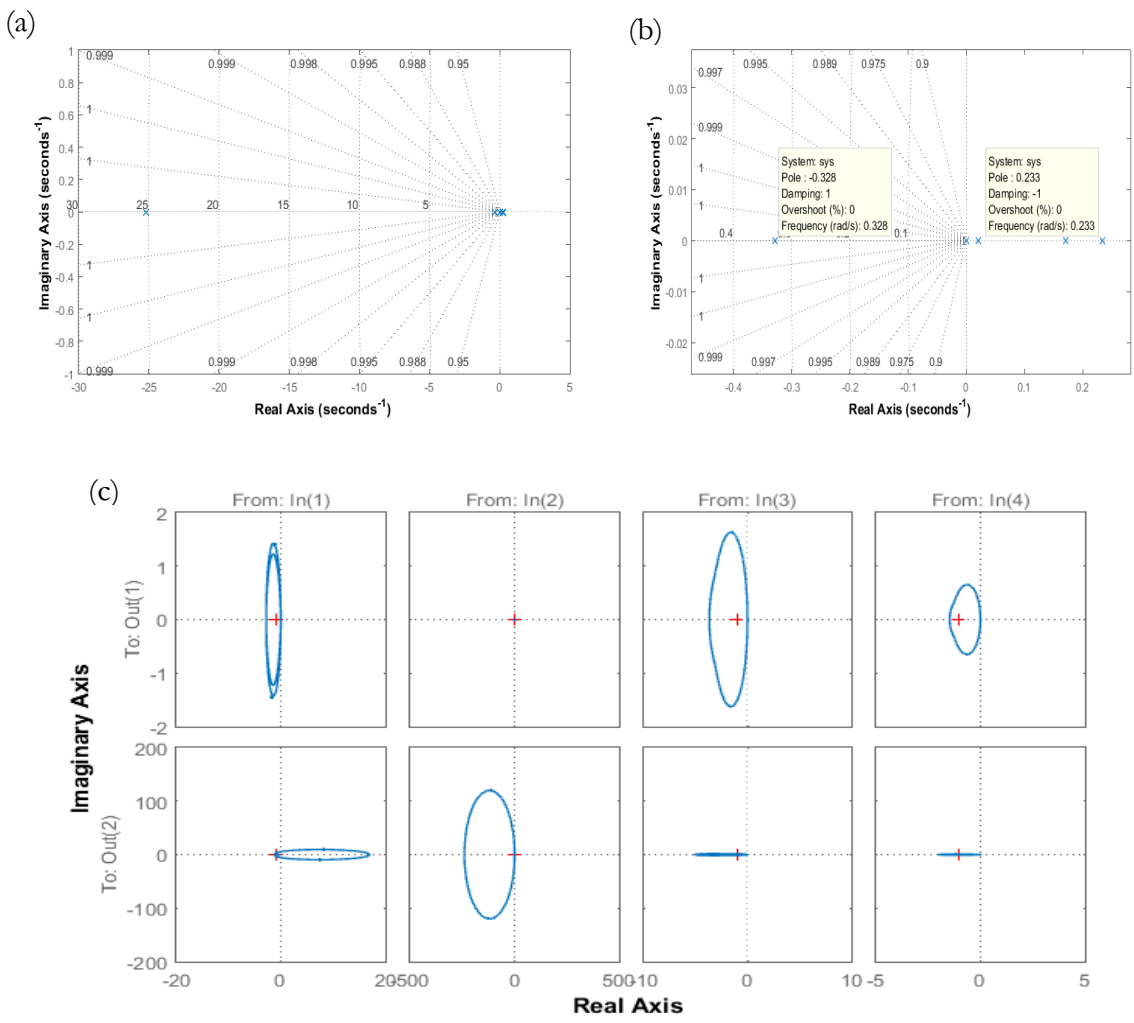

Figure 5.23 (a) Pole Zero map of trough with 6 poles along the zero real axis;(b) a zoom view of five crowded poles about the zero of the real axis;(c) The Nyquist plot of the 4 input total and beam radiation, flow rate and ambient inlet temperature by 2 output temperature of the heat transfer fluid and the PV module temperature

The pole and zero maps in fig. 5.23 (a) and (b), shows the locations of the poles and zeros six states of the trough system. The pole of two of the states are located in the left hand of the complex plane while the other four are located on the right hand of the complex plane. The implication of having 4 poles out of the six poles on the right hand plane is that the overall system behaviour in the open loop is unstable.

(a)

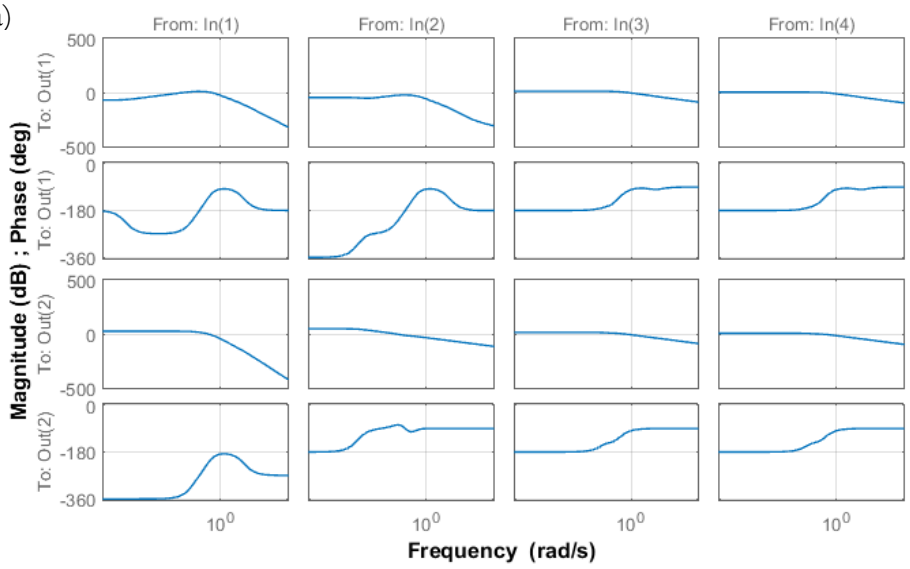

(b)

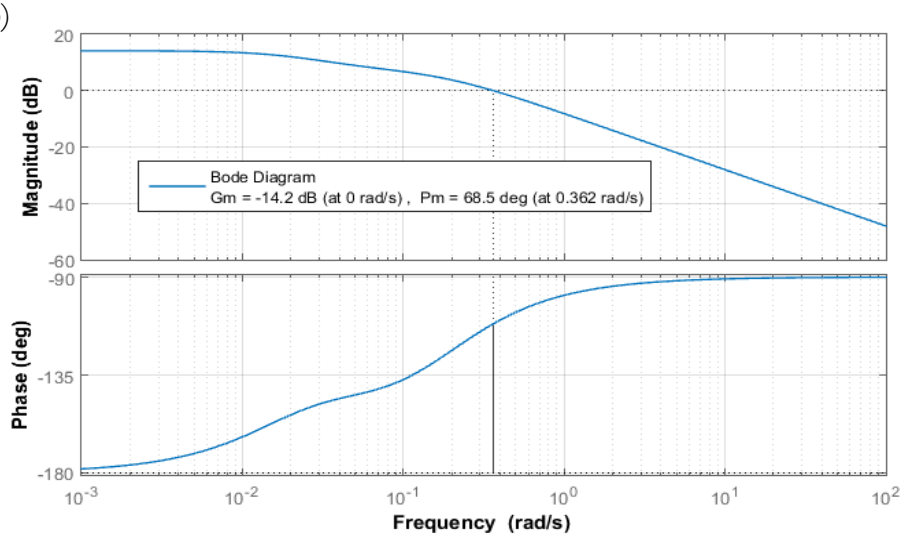

Figure 5.24 (a)Bode plots of the trough PVT of 4 input by 2 output total and beam radiation, flow rate and ambient inlet temperature by 2 output temperature of the heat transfer fluid and the PV module temperature multivariable system;(b) Bode plot of beam radiation effect on PV module output temperature with gain and phase margin and their corresponding crossover frequencies

The Bode plots of the trough subsystem in figure 5.24 a, is open loop dynamics of between the 2 inputs and the 4 output on a log scale with gains in magnitude and phase in degree as a function of frequency. Fig. 5.24b is Bode plot of indicating instability in the PV module dynamics.

(a)

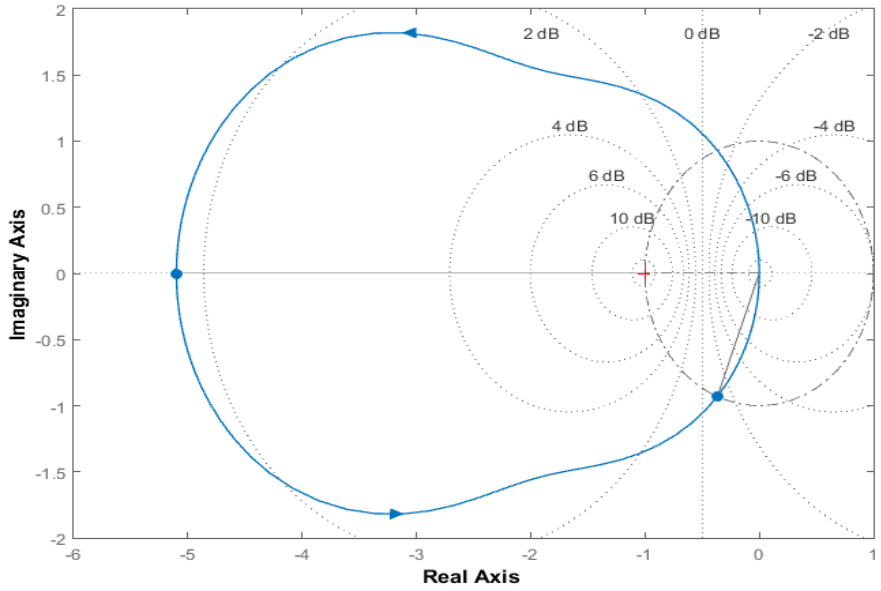

(b)

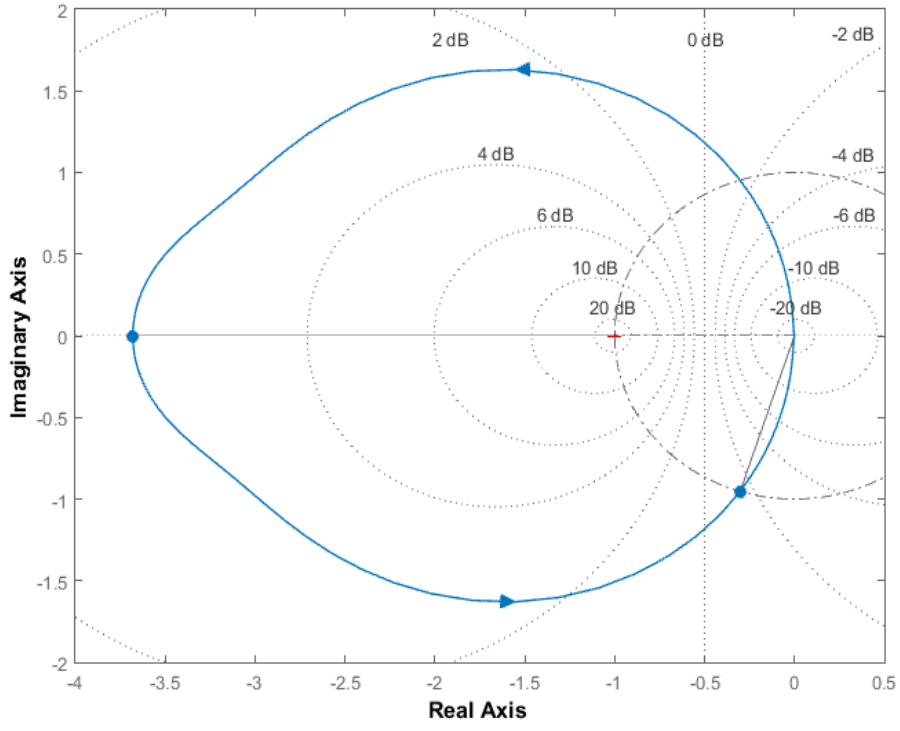

Figure 5.25 (a) Nyquist plot of beam radiation input and PV module temperature;(b) Nyquist stability plot of frequency response dynamics of flow rate input and heat transfer fluid temperature output

In fig 5.25(a), the beam radiation input interaction with the PV module temperature overall stability and peak stability margin is confined to the -4 decibels dotted circle. The implication is that the close loop performance or stability with respect to the beam radiation and the PV module temperature can be attained if the gains are maintained within the dotted cycle. The blue cycle shows the encirclement of the open-loop poles with respect to it close loop poles in an anticlockwise direction and facing the right plane of the complex plane. The dynamics of the heat transfer fluid temperature output with respect to the flow rate of the heat transfer fluid, follows the same reasoning but with anticlockwise direction in the left hand plane of the complex plane in figure 5.25 (b).

5.6 Summary and concluding remark

A detailed dynamical system analysis of the open-loop hydrogen combined cooling heating and power system was implemented using tools Phase Plane Analysis (PPA), Singular value decomposition (SVD), Relative, Gain Array (RGA), Controllability, Nyquist stability criterion and Niederlinski's index. The PPA indicated instability in all of the subsystems with saddle, spiral and infinite critical points of the direction and gradient vector fields in a 2 dimensional Cartesian plane. The singular value decomposition (SVD) dimension reduction technique all except the battery and electrolyser subsystems are fully decoupled, unstable and can be control using decentralised control architecture.

The other subsystems that highly tangled or coupled are unstable too and can be controlled using a centralised control architecture. The Nyquist stability criterion and Niederlinski's index was used to establish the instability and the position of the poles and zero. A controllability analysis was used to establish that all subsystems were indeed controllable except the wind turbine mechanical subsystem is not controllable. At this point, the plots for the other subsystems will be exclude because of space and limit for the thesis.

5.7 What next

The dynamical analysis of the HCCHP reveal that all the subsystems are controllable and the poles of the system was obtained, a pole placement optimal robust control architecture called Linear Quadratic Regulator (LQR) will provide an optimal placement of the poles in the complex argand plane.

Chapter 6 Control structure, architecture and strategies of hydrogen combined cooling heating and power system

6.1 Introduction

As a sequel to the perceived gaps identified in the related work, this chapter will focus on control strategies for each subsystems models developed from chapter 5. A detailed dynamical system analysis both in the time domain and frequency domain in chapter 5 shows that all the subsystems are open-loop unstable. Also, the battery and the electrolyser subsystems are the only 2 that can be decouple and control with decentralised architecture, the rest requires centralised control strategies. The first control challenge is to use optimal robust control to place the unstable open-loop pole in the left hand complex plane and determined their feedback gain. The main control problems with solar plants are related to sun tracking and control of circumferential temperature spikes. It is common control practice to track the sun using open loop control and implement a closed loop control for temperature of the receiver. This age-old practice is suboptimal as solar plants exhibit varying dynamics, nonlinearities, and uncertainties, characteristics that result in detuned performance with classical PID control. An advanced control strategy that can handled these issues are required for better performance and for reducing the cost per kilowatt-hour of thermal and electrical energy generated. A combined or mixed Linear Quadratic Regulator open-loop and closed-loop control architecture is proposed for the parabolic trough plant. A Linear Quadratic Gaussian control with specific consideration of suppression of torsional effect is considered for the wind turbine. The cooling and heating system control is based on multivariable LQR control architecture. The fuel cell, electrolyser and storage tanks will be based on model predictive LQR control architecture.

6.2 Research approach and methodology

The research approach is based on the model based design (MBD) methodology and MATLAB, SIMULINK, SIMSCAPE, SIMULINK design optimisation and control system toolbox are the software tools for delivering or deploying MBD.

6.2.1 Model based design

Model based design is a systematic process of enabling faster, more cost effective development of dynamic, control, communication and signal processing system. It starts with a system model, where requirement and ideas are captured and transformed compiled as executable C code to target an embedded microcontroller, microprocessor or electronic control hardware. The model are block diagrams that are converted into manageable code snippet.

6.2.2 Programming software tools

The control systems architecture mention in the introduction, requires software programming tools for their implantation. The subsystems models are of high order and hand calculation though possible but prone to error as a result of the share mathematical rigor required. The tools provided by Mathworks; MATLAB, SIMULINK, SIMSCAPE, SIMULINK design optimisation and the control system toolbox was used for the implementation of the control architecture and control strategies. The details of this tools are provided as follows;

6.2.3 SIMULINK

SIMULINK is a block diagram programming construct driven by MATLAB text programming language or modelling continuous dynamic system. The block for constructing the dynamic systems preloaded as libraries, blockset and toolboxes such as control, signal processing, communications, optimisation etc.

6.2.4 SIMSCAPE

Simscape is a blockset for enabling the creation of dynamic models of physical systems within the Simulink canvas. It provides the tools, for building physical component models based on physical connections that integrate seamlessly with block diagrams from other modelling domains. The Simscape tool can model systems such as electric motors, bridge rectifiers, hydraulic actuators, and refrigeration systems, by assembling fundamental components with realistic input/output port into a schematic. Also, add-on in Simscape provide more complex components and analysis capabilities that aids the development of control systems and test system-level performance. Apart from the existing blocks provide in the defaults package, custom component models using the MATLAB based Simscape language, which enables text-based for authoring of physical modelling components, domains, and libraries can be created. Parameterization capabilities for models using MATLAB variables and expressions, and design control systems for your physical system in Simulink is provided by the tool (Mathworks, 2016).

6.2.5 SIMULINK design optimisation

Simulink Design Optimization is blockset that provides functions, interactive tools, and blocks for analysing and tuning dynamic model parameters. It aids in improving system design characteristics such as response time, bandwidth, and energy consumption in control system. In addition, a joint optimization of physical plant parameters and algorithmic or controller gains capability is provided by the tool. Control system parameters can be tuned to meet time-domain and frequency-domain requirements, such as overshoot and phase margin, and custom requirements (Mathworks, 2015).

6.2.6 Control system toolbox

Control System Toolbox are set of blockset and tools that provides algorithms and graphical user application interface for systematically analyses, design, and tuning of linear control systems. The interface enables specification system model as a transfer function, state-space, zero-pole-gain, or frequency-response model. The tool provides applications and functions, such as step response plot and Bode plot, for you analysing and visualizing system behaviour in the time and frequency domains. Also, compensator parameters can be tune using interactive techniques such as Bode loop shaping and the root locus method. In addition, the toolbox automatically tunes both Single Input Single Output (SISO) and Multiple Input Multiple Output (MIMO) compensators, as well as Proportional Integral Differential (PID) controllers. The compensators can include multiple tunable blocks covering several feedback loops which can be tuned simultaneously. A more advanced technique such as gain-scheduled controllers and specification of multiple tuning objectives, such as reference tracking, disturbance rejection and stability margins can be implemented. Finally, design can be validated by verifying rise time, overshoot, settling time, gain and phase margins, and other requirements ("Control System Toolbox For Use with M ATLAB," 1999).

6.3 Control architecture and strategies

As a sequel to dynamical system analysis of HCCHP system in chapter 5, the trough PVT, wind turbine power electronics, battery, electrolyser, fuel cell and heating and cooling systems are controllable. The general rule is that if a system is controllable, the system poles can be place anywhere. The placement of this poles anywhere is ill-defined as placement of the poles to far from it open-loop poles put the controller in a very difficult position as more control effort is required to control the system. The other recommendation is that the closed-loop poles should be placed close to the open-loop poles which is still a challenge, since questions like how closed to the open-loop poles is open ended.

The solution to this control problem is to have an optimal and quantitative measure of accurately placing the poles to meet performance and sensitivity requirement such as rise time, settling time, overshoot, damping ratio, offset and peak input signal values. A typical quantitative optimal performance index is a quadratic measure of future behaviour, using the origin as the target. The index is called Linear quadratic regulator (LQR) and is defined mathematically and presented in Eq. 6.1 as follows (Bosgra, 2002);

$$J = \int_0^\infty (x^T Q x + u^T R u)\, dt \tag{6.1}$$

Q Implicitly measures convergence rate for rise time, settling time, overshoot, damping ratio, offset

R Penalises the aggressive use of the input signals

LQR is model predictive control (MPC) with an infinite horizon represented by the upper bound of the performance index integral in Eq. 6.1. The rise time, settling time are captured implicitly by $x^T Qx$ term in Eq.6.1

The next question is how is the performance index J optimised? This is achieved using dynamic programming with respect to the state feedback K and presented in Eqs. 6.2, 6.3 and 6.4 as follows;

$$\underbrace{min}_{K} J = \int_0^\infty (x^T Q x + u^T R u)\, dt \tag{6.2}$$

Subject to;

$$\dot{x} = Ax + Bu \tag{6.3}$$

$$u = -Kx \tag{6.4}$$

$$K = R^{-1} B^T P \tag{6.5}$$

6.4 Subsystem control structure and architecture

6.4.1 Parabolic trough PVT system

Control problem specification for the parabolic trough PVT system are two-fold;

- The ultimate objective of one axis tracking of parabolic trough system is to maximised the incident direct radiation by minimising the angle of incidence
- the second control problem is to control the temperature of the heat transfer fluid to meet temperature difference ΔT and the temperature of at the surface of the PV cells

The main challenge is the arrangement of the two-fold control loops, which give rise to control structure or architecture. The process flow diagram in figure 1 must be decomposed into a block diagram and the and is presented as follows in figure 6.2;

6.4.2 Mechanical tracking system

The plant consists of three subsystems or subassemblies, the receiver subsystems, the parabolic trough mirror subsystems and the four bar link mechanisms subsystems.

6.4.2.1 Physical plant high fidelity model of the trough PVT link system

A high fidelity models are models representing the real full size mechanical, electrical, process, thermal behaviour of a system. In another definition perhaps, a more thorough and in-depth elucidation of the meaning by Simulation Group (2015), Fidelity connote the extent

to which a model or simulation replicate the state, behaviour and attribute of a real world object, feature or condition. In simple terms, it is a measure of realism of a model or simulation. Hays & Singer (1989) concisely defined it as the degree of similarity between the real model and simulated model. The following subsystems the trough mirror, Receiver PVT and the 4 bar Link mechanism was

created in Solidworks with their materials properties in a native 3D CAD. The subsystems are presented in details in the sections below.

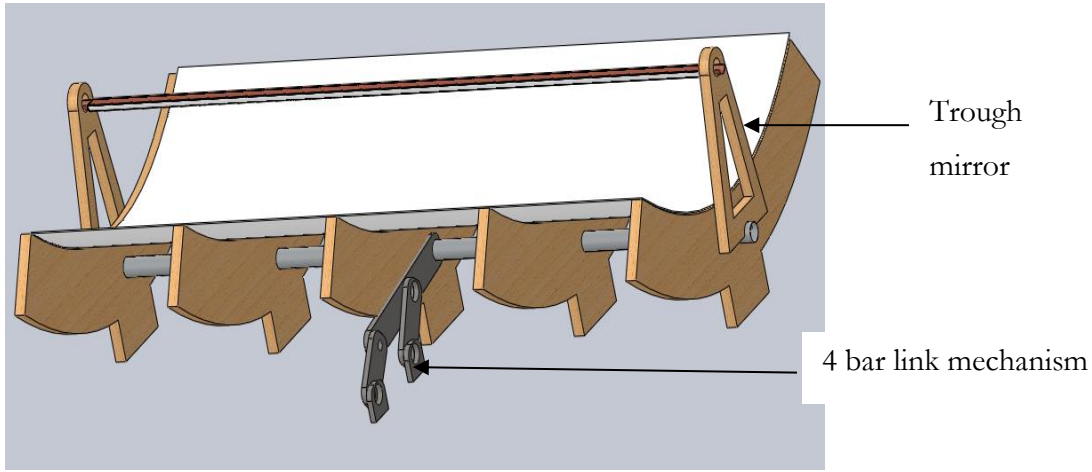

Figure 6.1 A 3D native CAD model of the parabolic trough mirror PVT and the four-bar link mechanism, realised in solidworks

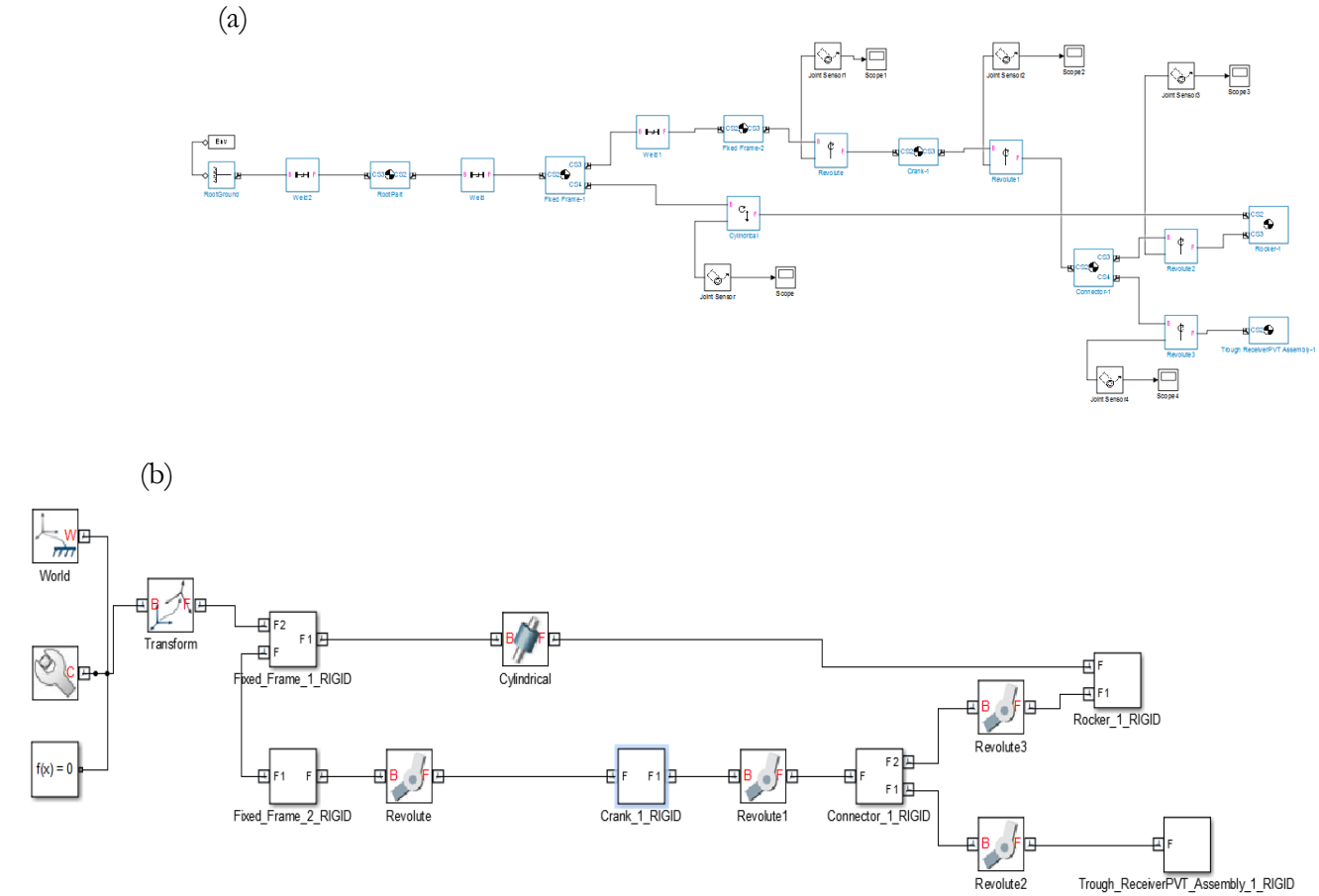

Figure 6.2 High fidelity SIMMECHANICS model of the parabolic trough mirror receiver PVT system and the four bar link mechanism; (a) first generation CAD translation; (b) second generation CAD translation

Two degree-of-freedom PID controller design and development

It is a known fact that a control system is as good as it as the fidelity of the plant or process model. The model is the linchpin of model based controller. The two degree of freedom is a variant of the classical proportional differential integral control architecture with an extra degree of freedom for weighing the set point as it passes through the proportional and the derivative channel. The control architecture is shown in fig 6.3.

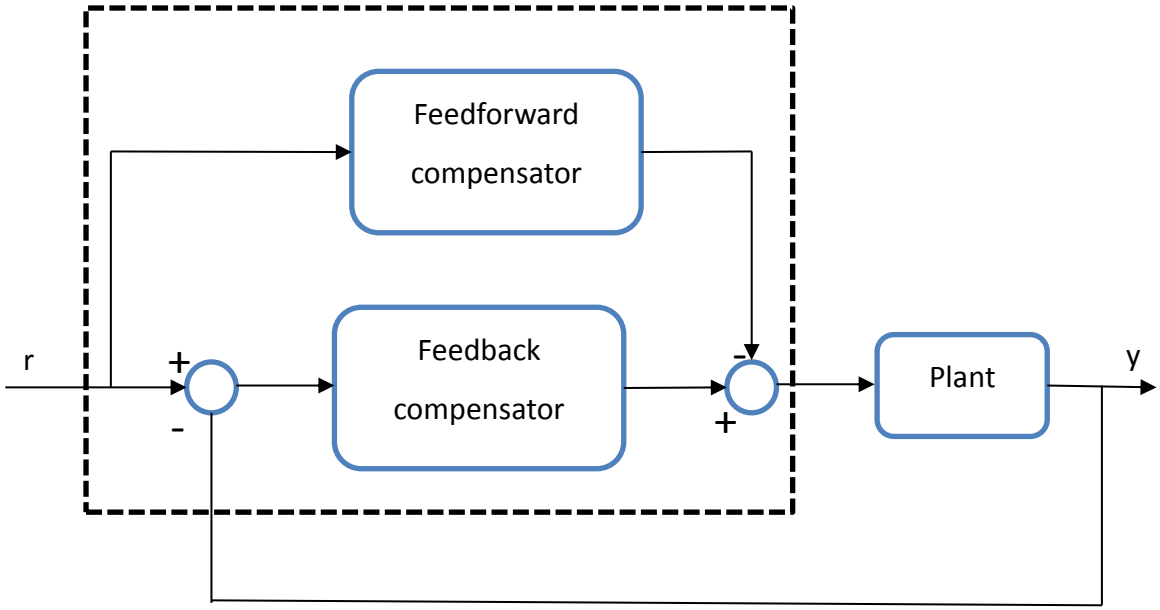

Figure 6.3 two-degree of freedom PID Controller

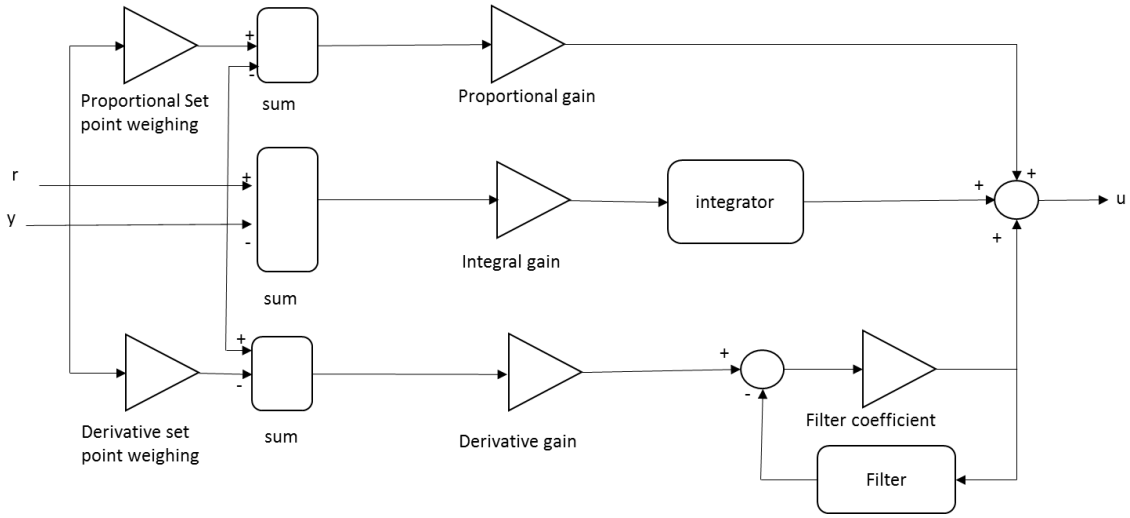

Figure 6.4 A more detailed implementation of the 2 degree of freedom architecture

6.4.2.2 Physical model of a DC servo motors

Motor modelling complete dynamics to captures rotor inertia, rotor damping is a complex and deriving the differential equations is challenging and time consuming task. A viable alternative to this is to build the complex actuator such as motor is use physical components with energy conserving ports that are high fidelity representation of physical connections. The DC linear actuator was implemented with physical blocks and represented in fig. 6.5.

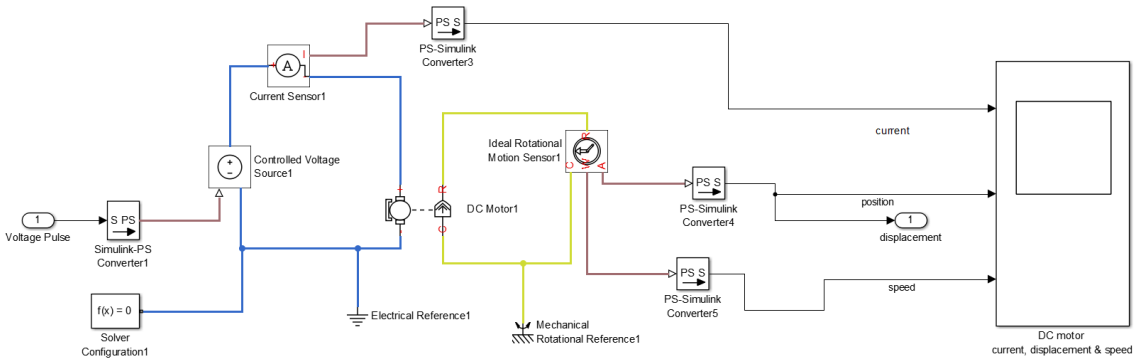

Figure 6.5 physical components high fidelity model of a DC motor

6.4.3 Process thermal system

The control of the trough system was done using linear quadratic control, an advanced robust optimal control technique for ensuring optimal placement of poles to stabilize the system and obtained optimal gain that respect performance, robustness and at optimum control effort. The output of the trough thermal control is used as input to the hot boiler exchanger and cold tank control.

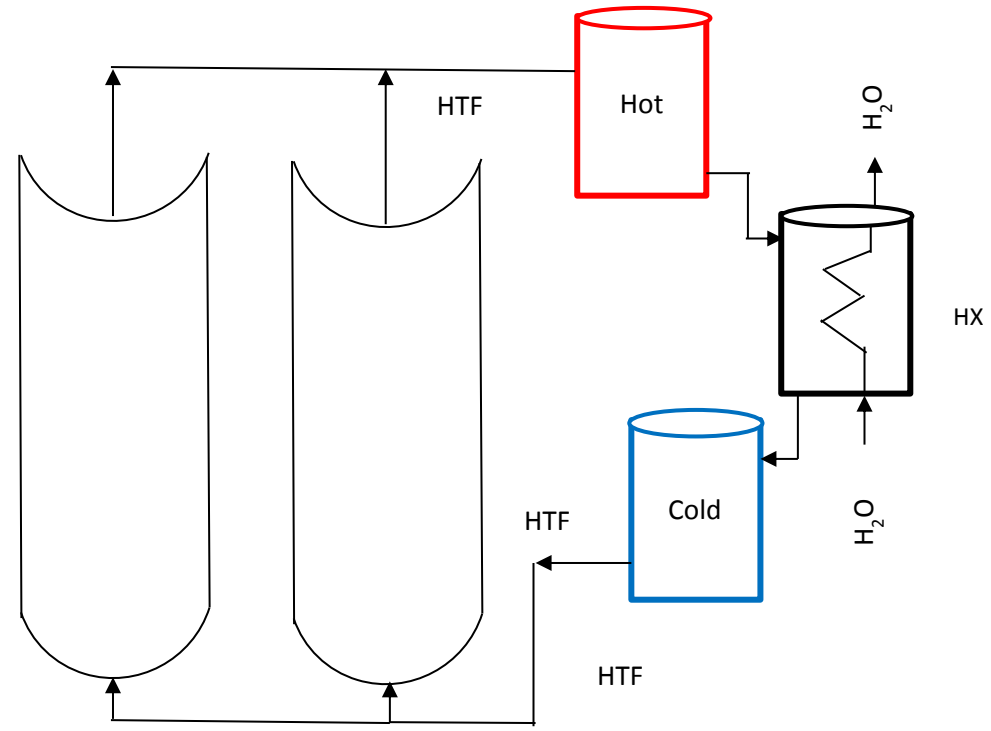

Figure 6.6 Parabolic trough plant process flow diagram (PFD);Hot tank heat transfer fluid (HTF); Cold tank heat transfer fluid; Heat Exchanger (HX) water flowing in the tube and heat transfer fluid in the shell

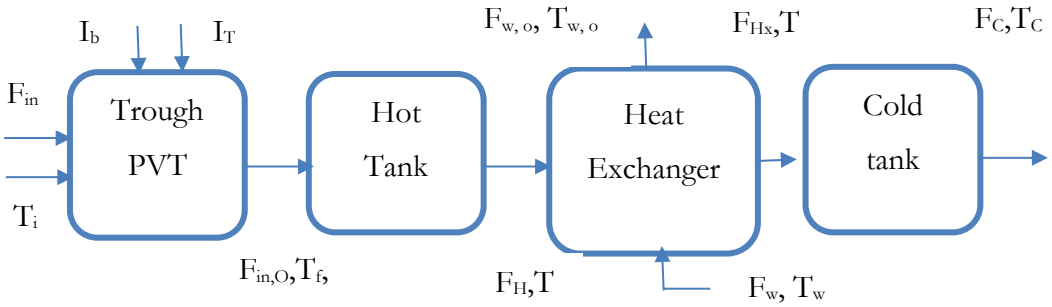

Figure 6.7 Block diagram decomposition of the process flow diagram in fig. 6.6; inputs to the trough PVT system are flow rate in F_{in} and the inlet temperature T_{in}, I_b and I_{tot} are beam radiation and the total radiation, the outputs are F_{in}, o temperature of the heat transfer fluid and the surface temperature of the solar PV cells T_p ; Output from the F_{in}, o and T_f are input to the hot heat transfer fluid tank with output F_H,T_H; The heat exchanger output are F_{Hx},T_{HX} and $F_{w,o}$, $T_{w,o}$ and inputs F_H,T_H and F_w, T_w; cold tank inputs are F_{Hx},T_{HX} with output F_C,T_C

The overall control structure and architecture of the parabolic trough system will be a cascade control with the tracking dynamics as the faster loop and will be the inner loop or the slave while

the slow thermal dynamics of the heat transfer fluid and PV cell temperature as the outer loop or the master.

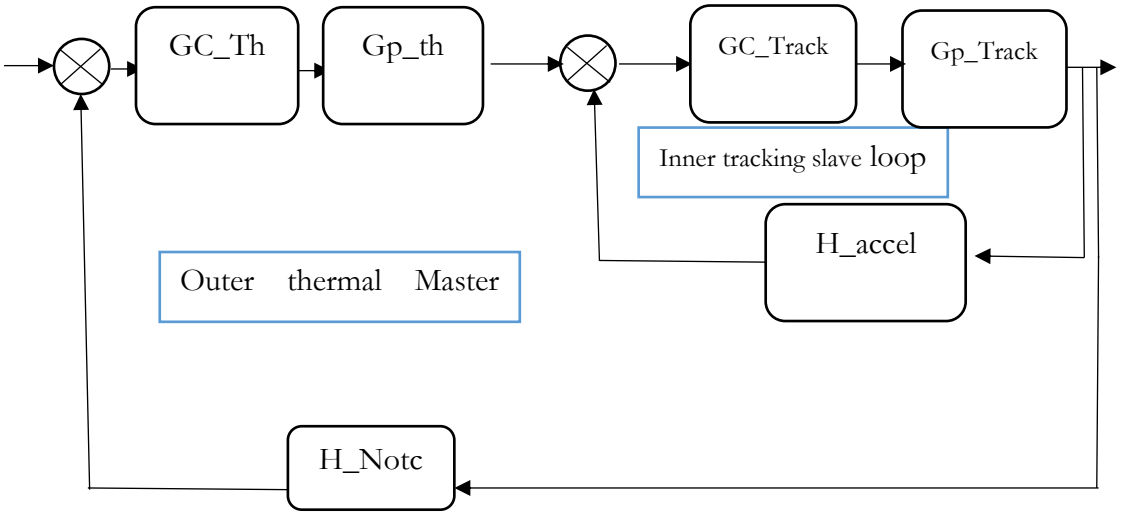

Figure 6.8 Control structure and architecture of the thermal and mechanical one-axis tracking of the parabolic trough PVT system

6.4.4 Full state feedback multivariable LQR control architecture of subsystems

The control strategies of the is a mixed architecture type. The tracking system input is a step signal, pulse, sine and sun azimuth and elevation angle of the sun converted to voltage pulse to control the speed of the linear actuator or motor. In the architecture, a manual switch is used to select the signal of interest, to drive the tracking system. The output of the tracking is position of the trough relative to the position of the sun, at minimal incident angle. The control is contained as the inner closed loop. The output of the tracking is used as input to other thermal temperature control loop whose

output is the optimum heat transfer temperature. The optimum trough heat transfer fluid temperature is a function of the controlled trough position from tracking inner loop. The output of the temperature serves as input to the hot storage tank and the hot tank output becomes the input of the boiler heat exchanger. In the same vain, the output of the heat exchanger boiler is the input to the cold tank. The output of the cold tank becomes the input to the thermal trough. The control system is a PID feed forward/feedback, LQR, PID for the tracking, trough thermal and series hot tank-boiler heat exchanger-cold tank trio respectively.

The control system architecture is presented in fig 6.4, 6.5, 6.6 and 6.7 as follows

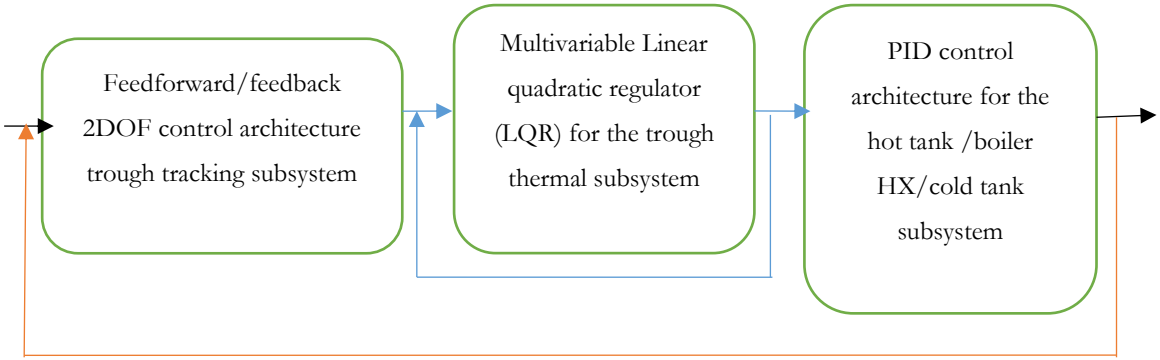

Figure 6.9 Overall control strategies and architecture for the trough tracking and thermal system

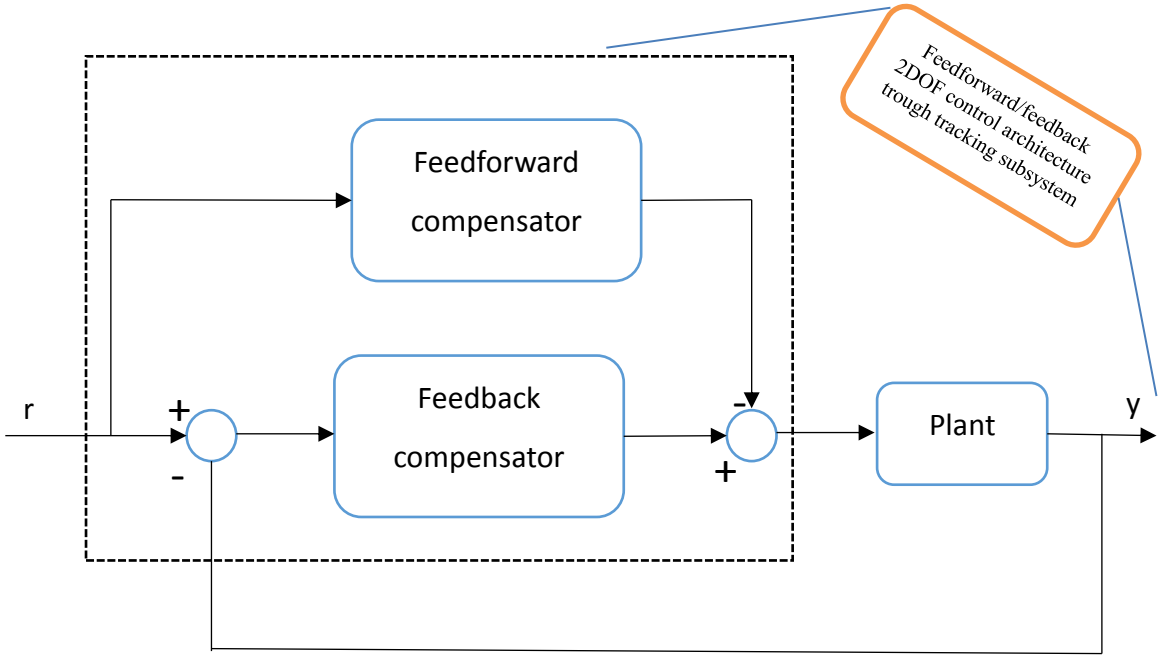

Figure 6.10 tracking subsystem block feedback feedforward control architecture detail

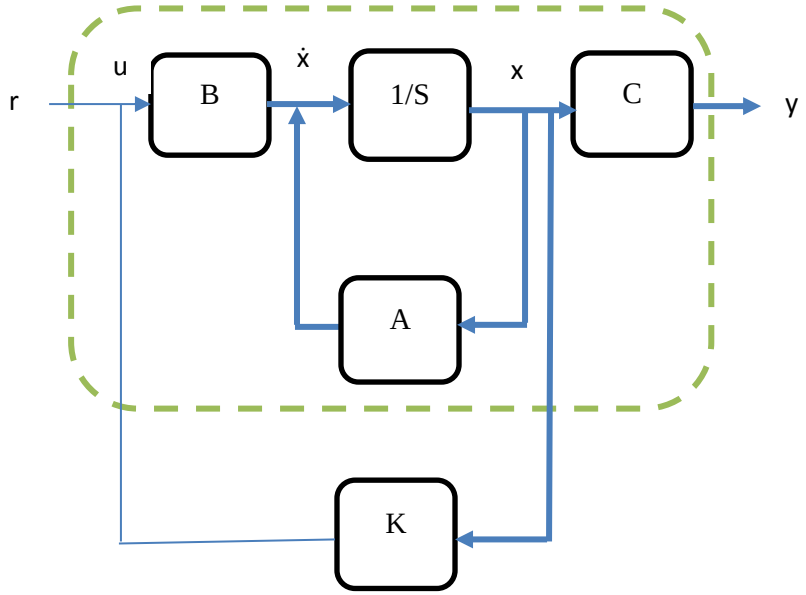

Figure 6.11 Multivariable State Feedback Linear quadratic regulator (LQR) control strategy and architecture with the open-loop within the dash box reference r, input u, state differential ẋ, state vector x, input matrix B, pure integrator 1/S, Output matrix C, the state coefficients matrix A and the full feedback controller gain K

In fig. 6.11, the overall control architecture and strategies of the trough system are combined as mixed multi-loop control. The first loop is the control of the velocity of the direct current motor to actuate and position the trough to follow the sun. The second loop is a centralised LQR multivariable control of the thermal temperature of the heat transfer fluid and the temperature of the PV cells using flow rate of the fluid. The third loop is a PID control of the level of the hot tank and third loop is the temperature and the level of the hot fluid in the heat exchanger/boiler. The fourth loop is a PID control of the height and temperature of the cold tank. The decomposition of the entire trough PVT subsystem is a complex task and requires a painstaking and patience effort to arrive at the control structure.

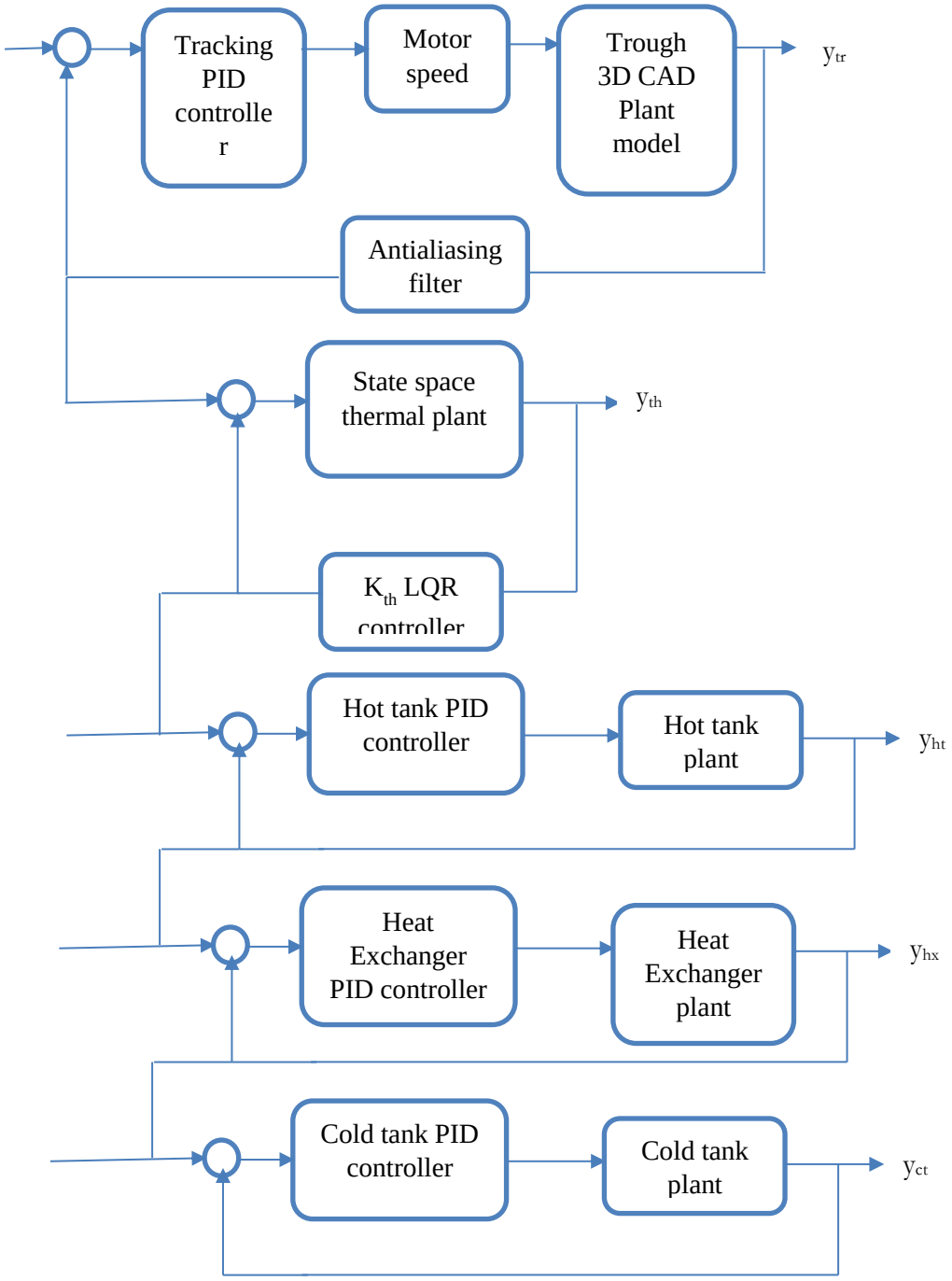

Figure 6.12 Multi-loop control strategies and architecture for the full parabolic trough tracking, thermal temperature, hot tank storage, Heat exchanger-boiler and the cold storage tank

6.4.5 Wind turbine system

6.4.5.1 Control of the wind turbine system

Control of the wind turbine system consists of the wind speed, the aerodynamics, mechanical transmission and gearing, the electrical generator, the power electronics converter system and the load

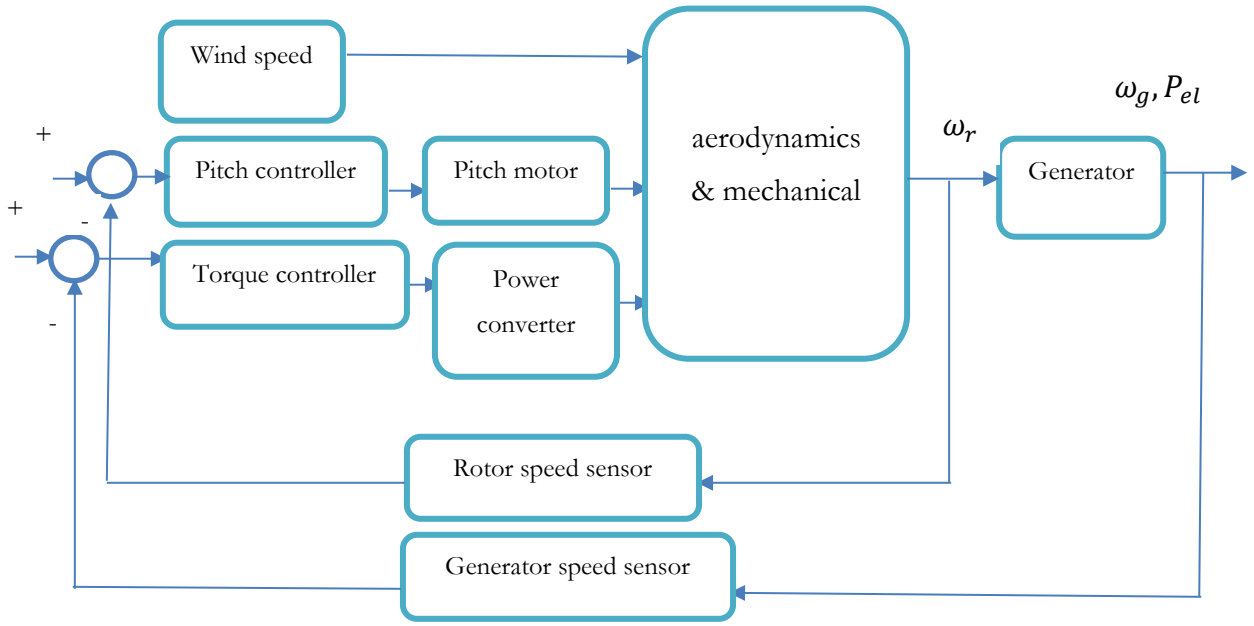

Figure 6.13 Control structure and architecture of wind turbine system with rotor speed control as inner loop and generator speed control as outer loop and rotor, generator angular velocity and electromagnetic torque (Electrical DC/AC power) as outputs

A multivariable control of the wind turbine system is structure with the outer mechanical loop and an inner electrical and power electronics loop. The generator and the rotor speed are used as feedback to the torque and pitch controller respectively. The strategies are combined in fig. 6.13 for optimal pole placement because of the unstable open loop behaviour and the non-controllable behaviour of the mechanical subsystem. The linear quadratic regulator was able to stabilised the system using the B_w and the B_{we} matrix and the eigenvalues of the design all falls in the left hand plane of the complex plane. The approach provides a cost function that keeps performance and robustness at the same advantage using the weighing factor in the LQR dynamic optimisation algorithm.

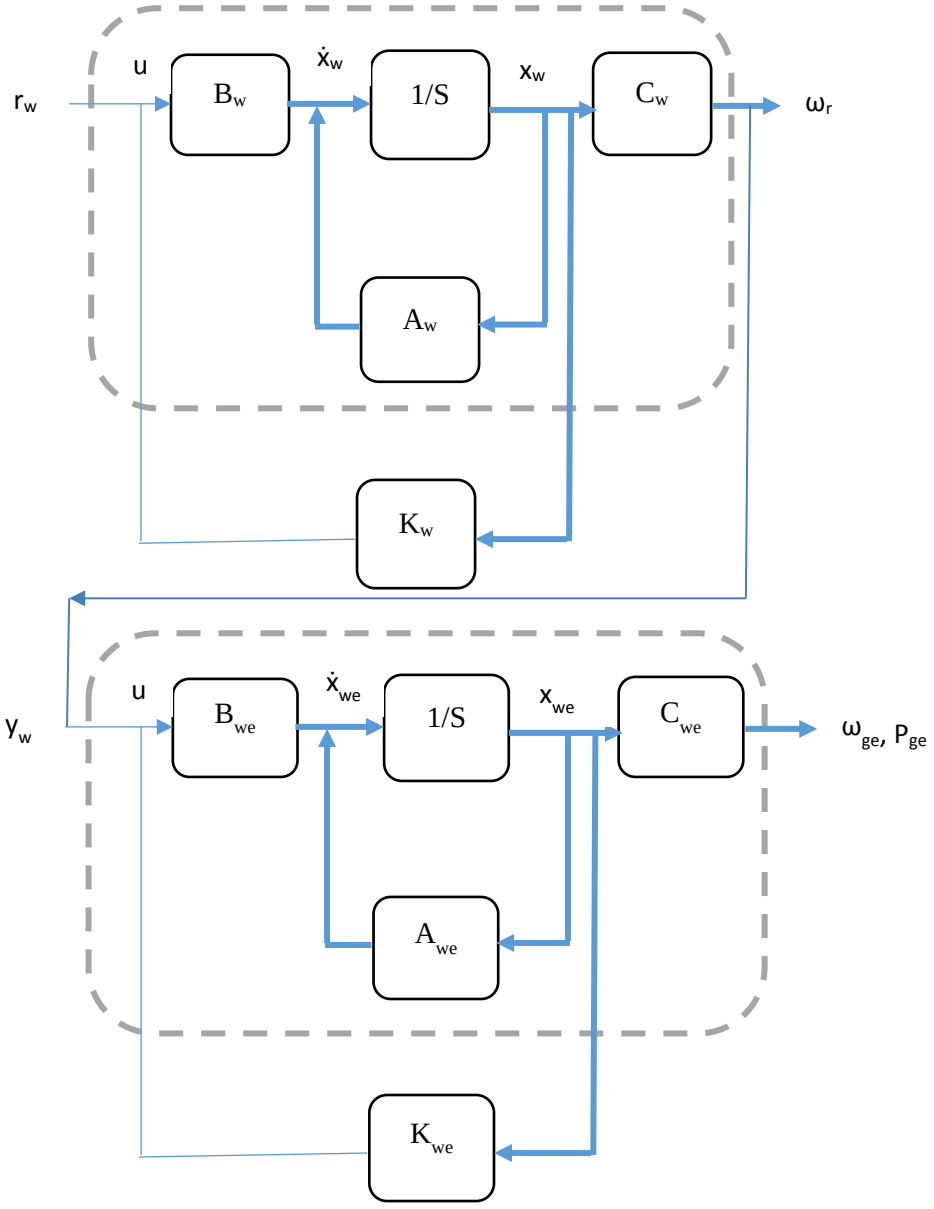

Figure 6.14 Full multivariable centralised Linear Quadratic Regulator (LQR) implementation of the wind turbine mechanical subsystem control with reference input r_w, input u, differential state variable $\dot{x}_w$, x_w state variable, A_w is state variable coefficient matrix , B_w control matrix and C_w output coefficient matrix wind turbine. K_w is control the gain matrix obtained from the LQR dynamic optimisation.Wind turbine electrical with output from mechanical system as reference input y_w, input u, differential state variable $\dot{x}_{we}$, x_{we} state variable, A_{we} is state variable coefficent matrix , B_{we} control matrix and C_{we} ouput coefficient matrix wind turbine. K_{we} is control the gain matrix obtained from the LQR dynamic optimisation

6.5 Hydrogen storage system

6.5.1.1 Electrolyser system

6.5.1.1.1 Control structure of the electrolyser system

The control architecture in the electrolyser follows a cascade control structure as the inner pressure loop is used to trigger the current input to the electrolyser when the input pressure of the hydrogen storage tank pressure approach the maximum permissible storage tank pressure. The control structure is a cascade control with a slave pressure loop to ensure that the pressure in the hydrogen storage tank is maintained below the maximum permissible pressure of the hydrogen tank. The outer master loop is activated using the feedback from the inner loop as illustrated in fig. 6.15, as soon as the pressure drops significantly below the maximum permissible. The two control variables are the tank pressure and the direct current to the electrolyser.

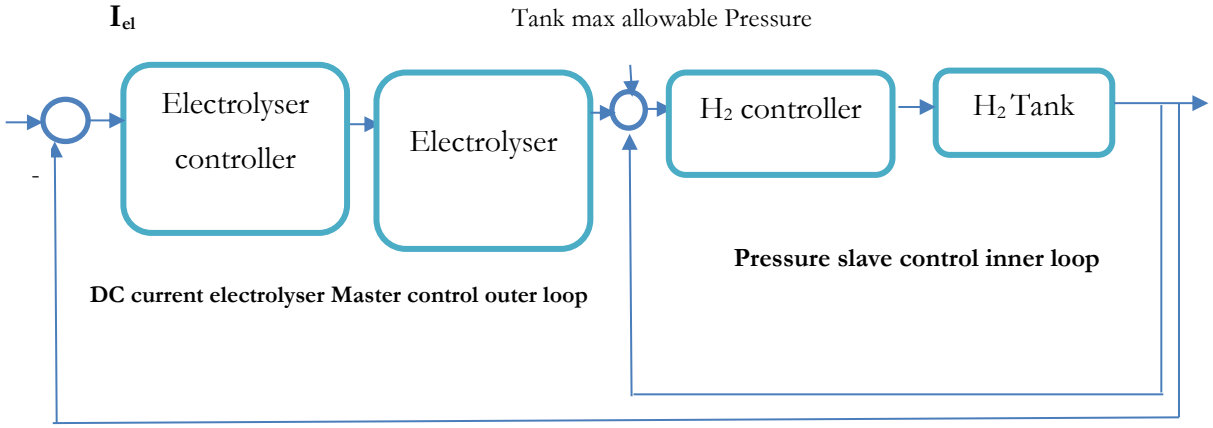

Figure 6.15 Control architecture of the electrolyser with and inner pressure loop and outer electrolyser controlled direct current; The feedback hydrogen tank pressure is used to activate the current loop when the pressure falls significantly below the maximum permissible value

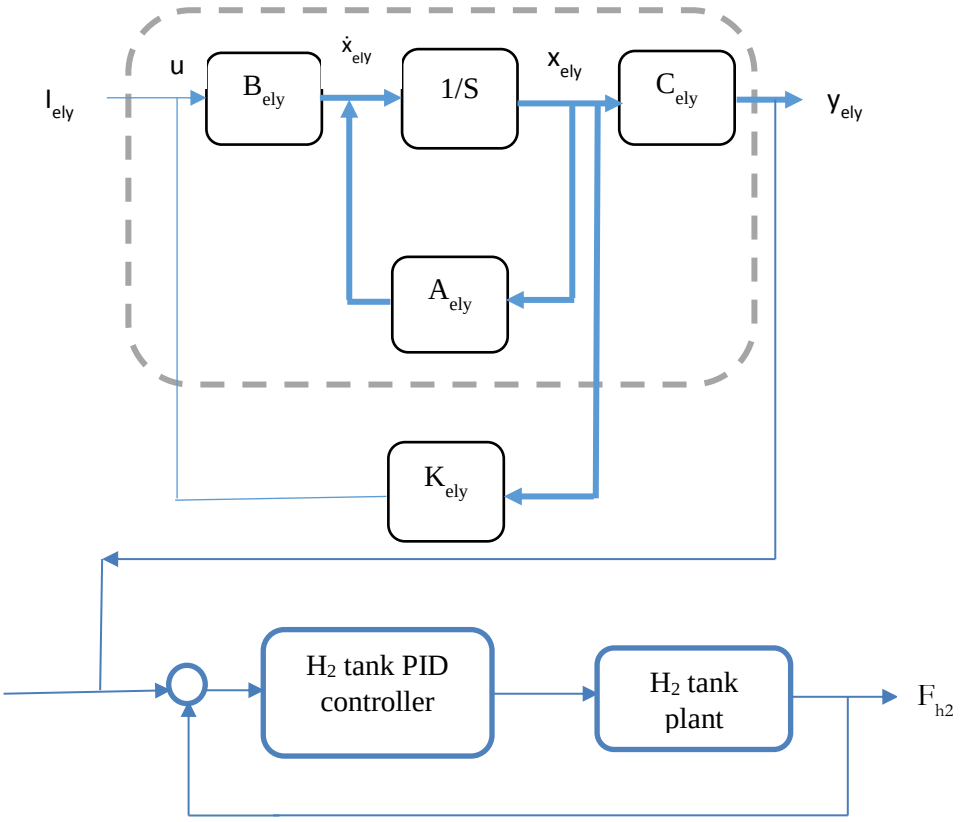

Figure 6.16 Full multivariable centralised Linear Quadratic Regulator (LQR) implementation of the wind turbine mechanical subsystem control with reference input I_{ely}, input u, differential state variable $\dot{x}_{ely}$, x_{ely} state variable, A_{ely} is state variable coefficient matrix, B_{ely} control matrix and C_{ely} output coefficient matrix of the electrolyser. K_{ely} is control the gain matrix obtained from the LQR dynamic optimisation. The H_2 tank inner loop is a decoupled PID control architecture with control flow rate of the hydrogen gas F_{h2}

6.6 Hydrogen metal hydride tank system

The hydrogen storage is a system of partial differential equations of the temperature of the bed and the mass flow of the hydrogen gas in the chapter. The control is based on the transfer function of the temperature of the bed and the flowrate.

6.6.1 PEM fuel cell system

6.6.1.1 Control architecture of the fuel cell

The control architecture for the fuel cell is based on the hydrogen gas capacity utilisation and the flow rate as the control variables. The flow rate is used to control the current output of the fuel cell. The inlet flow is compared with the flow rate computed as a fraction of the capacity of utilisation of the hydrogen gas from the hydrogen storage tank. The inner loop is triggered as soon

as the current output drops below the set-point. The full architecture of the hydrogen tank and fuel cell is shown in fig.6.17 and 6.18.

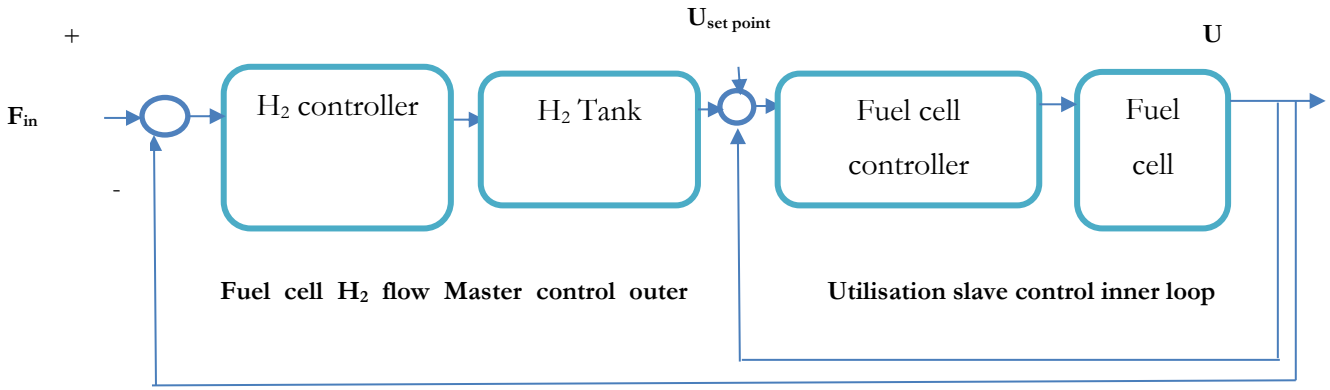

Figure 6.17 Control architecture of the fuel cell with a hydrogen fuel utilisation and outer master loop hydrogen gas flow rate; The utilisation factor flow fraction, control the flow and the DC current output of the fuel cell

The hydrogen tank control is already part of the control loop for the fuel cell and the electrolyser. Consequently, the storage does not require a separate control architecture.

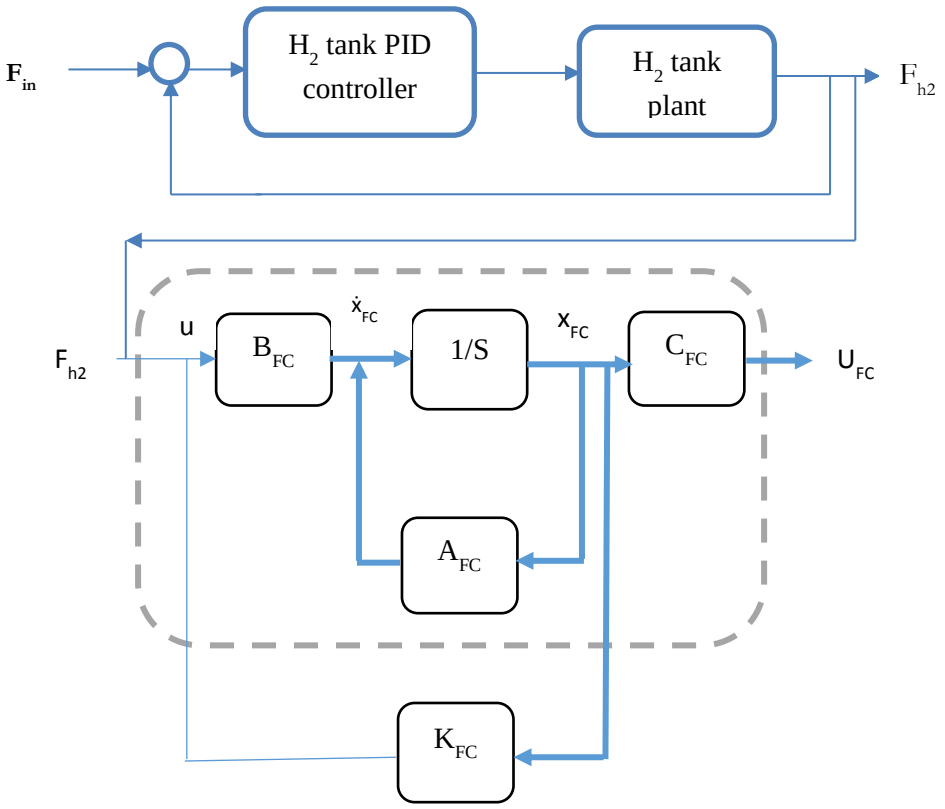

Figure 6.18 The H_2 tank inner loop is a decoupled PID control architecture with control flow rate of the hydrogen gas inlet flow F_{in} and controlled flow rate F_{h2}. Full multivariable centralised Linear Quadratic Regulator (LQR) implementation of the Fuel cell subsystem control with reference input F_{h2}, input u, differential state variable $\dot{x}_{FC}$, x_{FC} state variable, A_{FC} is state variable coefficient matrix, B_{FC} control matrix and C_{FC} output coefficient matrix wind turbine. K_{FC} is control the gain matrix obtained from the LQR dynamic optimisation

6.7 Battery storage control system

The battery is one of the most important subsystem in the HCCHP since it is responsible for providing a short time storage buffer for the other subsystems and for handling charge and discharge operations of the secondary heat storage and primary hydrogen storage. The control system provides a strong protection around the battery to prevent overcharging and undercharging through an intelligent charging algorithm to monitor the state of health of battery.

The control architecture and strategies is two loop decoupled control algorithm with an inner Proportional Integral (PI) current loop and an outer Proportional Integral (PI) voltage loop shown in fig. 6.19.

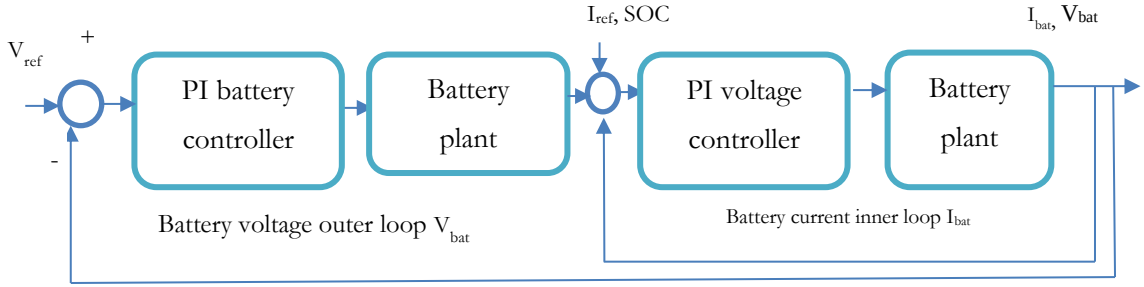

Figure 6.19 A two loop inner battery PI and outer battery controller with V_{ref} and I_{ref} as manipulated variable and I_{bat} and V_{bat} as controlled variables the input to the control structure is selected based on the battery SOC values

6.8 Cooling and heating system

Heating and cooling forms a major part of human life, living space are cold during summer when temperature climb above the threshold. In winter, space heating is used to provide comfort to the inhabitant in residential or public space. Control systems are used to regulate and control temperature. In this research work, a 3-input, 3-output MIMO system with volumetric air flow rate, the chilled water flow rate inputs and the outdoor air flow rate. The outputs are temperature, humidity ratio, and CO_2 concentration of the thermal space. A linear quadratic regulator controller is implemented to maintained the temperature of the thermal space during summer and winter. The architecture of the controller is shown in figure 6.20 as follows

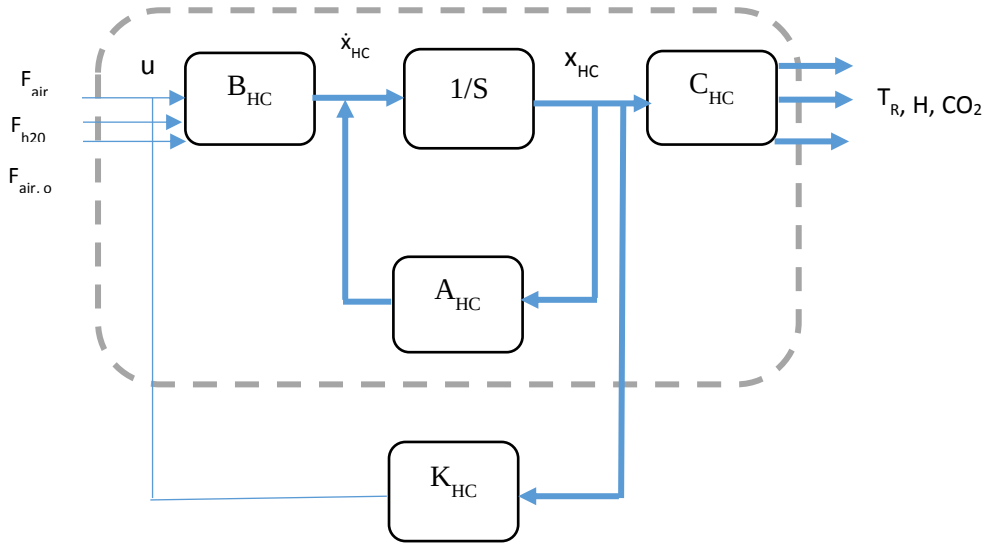

Figure 6.20 A multivariable Multiple Input Multiple Output (MIMO) LQR control architecture of Full multivariable centralised Linear Quadratic Regulator (LQR) implementation of the Heating and cooling subsystem control with reference inputs water flowrate F_{h20}, inside air flowrate F_{air}, and outside air flowrate $F_{air,\,o}$ input u, differential state variable $\dot{x}_{HC}$, x_{HC} state variable, A_{HC} is state variable coefficient matrix, B_{HC} control matrix and C_{FC} output coefficient matrix wind turbine. K_{HC} is control the gain matrix obtained from the LQR dynamic optimisation. The control outputs are room temperature, relative humidity and carbon dioxide concentration in room T_R, H, C_{CO2}

6.9 Analysis of result obtained

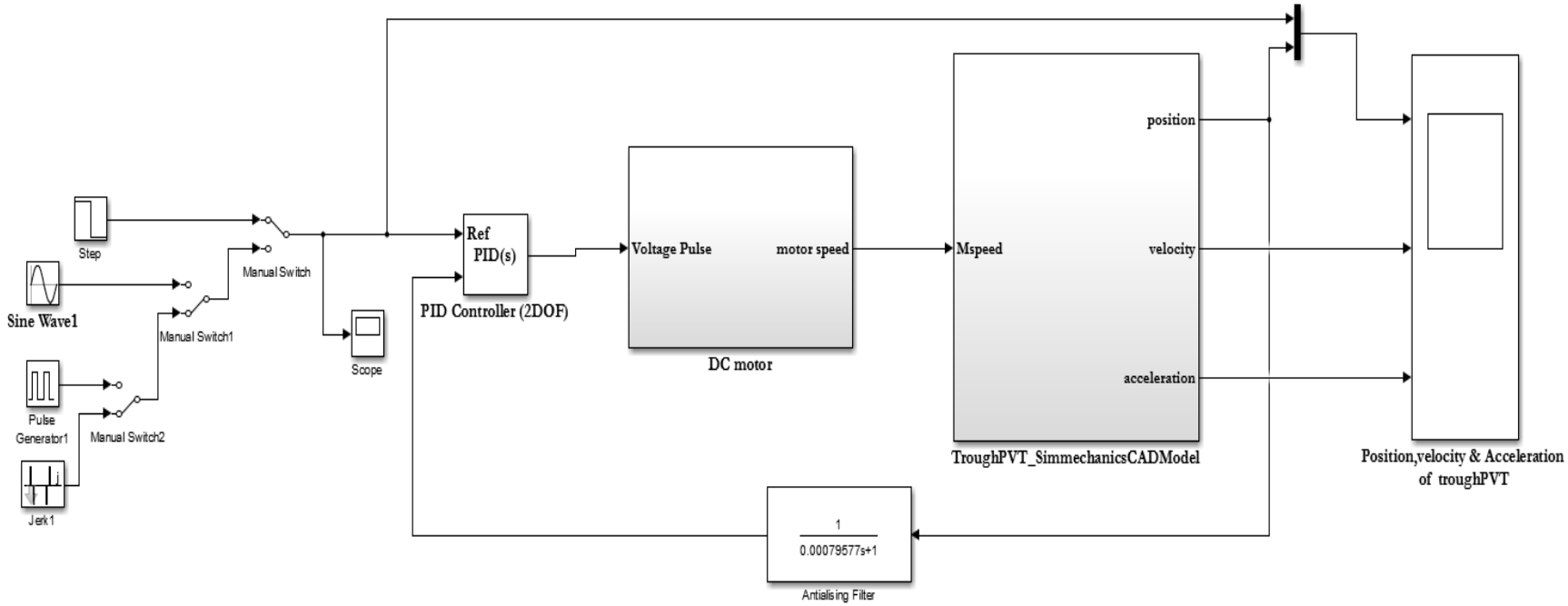

Figure 6.21 Trough PVT mechanical tracking PID control strategies and architecture with step, sinusoidal, pulse and advanced set-point motion driving input signals. A 2 degree of freedom PID controller is use to control the velocity of a DC motor to actuate a parabolic trough PVT 3D CAD high fidelity model. An antialiasing filter place at the feedback backward path as compensator

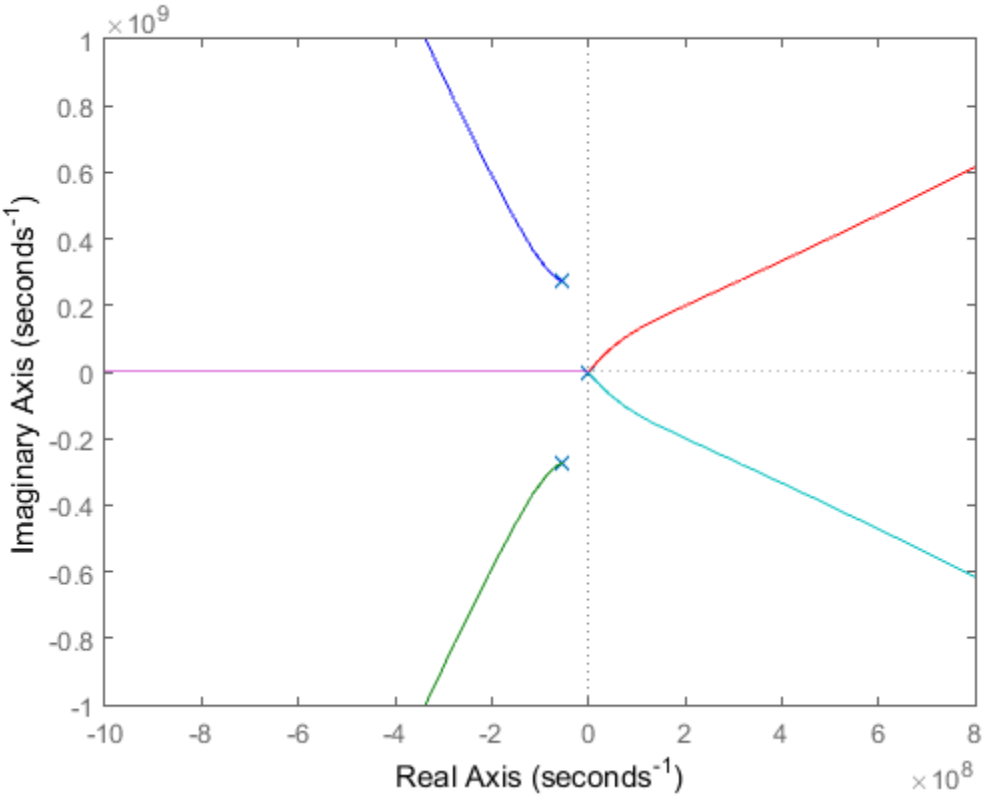

Figure 6.22 A root locus plot of the trough mechanical tracking subsystem with poles at the zero and left hand plane of the complex plane

The root locus plot in fig. 6.22 shows the poles location of the 2 DOF PID controller with an antialiasing filter. From the figure, the poles are all located in the left hand plane of the complex plane. A mechanical parabolic trough tracking system is usually open-loop stable but closed-loop unstable. The antialiasing filter added a new equation and dimension to the stability and performance of the controller on the tracking. The poles on the plot can be moved to a new location using the control system application.

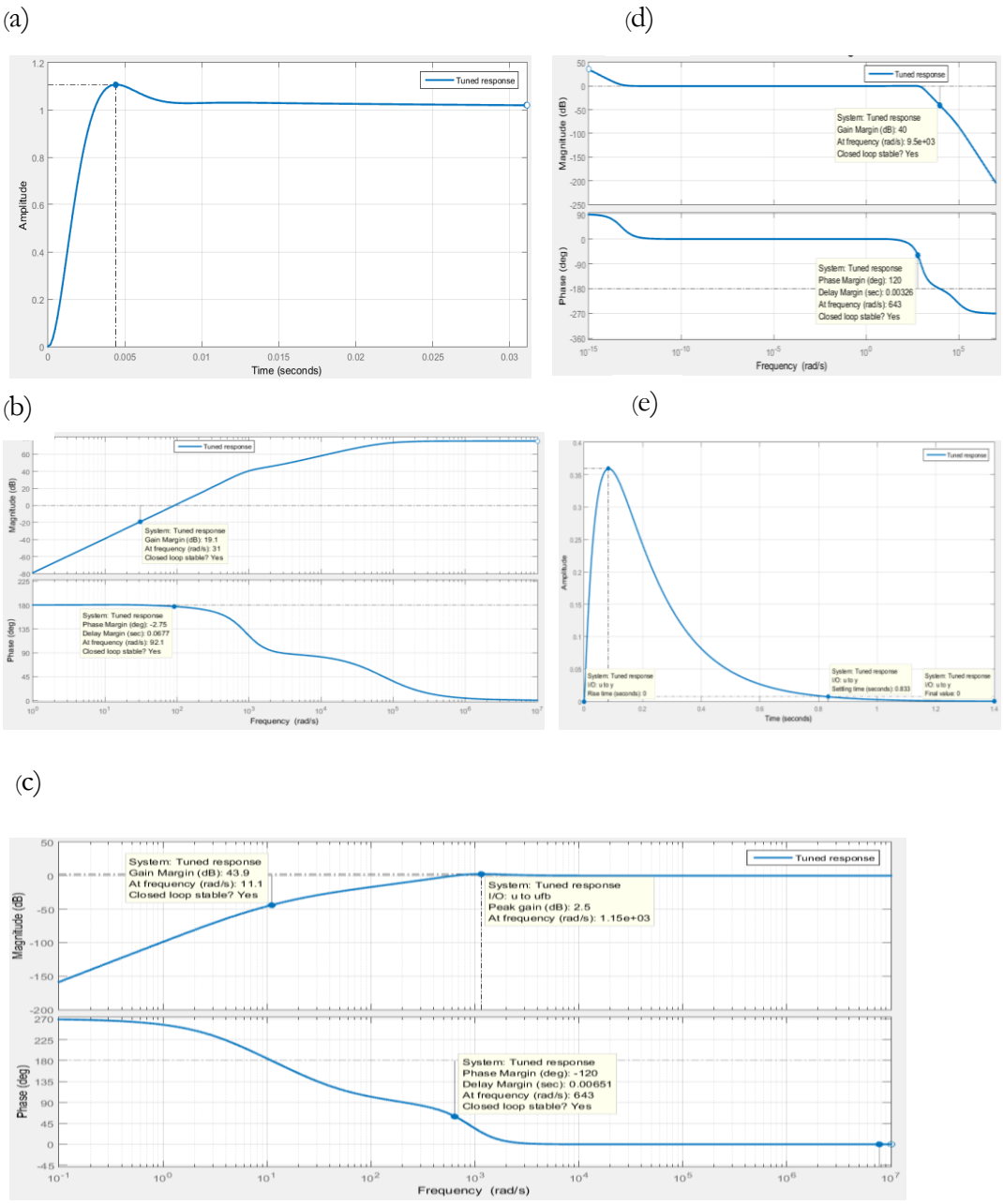

Figure 6.23 (a) Time domain step response of tuned 2DOF PID controller with antialiasing filter compensator; (b) 2DOF PID controller effort in frequency domain(c) Bode plot of output disturbance rejection in frequency domain (d) Bode frequency response of tuned 2DOF PID controller; (e) Input disturbance rejection of 2 DOF controller in time domain

In fig. 6.23, the tuned 2DOF PID controller was able to hold the trough tracking dynamics with a stable closed loop at response time of 0.00311 s. The control parameters obtained from the PID control system tuner are proportional gain (P) 2.202, integral gain (I) 9.805, differential gain (D) 0.08161, filter coefficient (N) 7.348×10^4, and set-point weight of 1. The tuned trough is characterised with robustness of 0.6. The tuned system response in

frequency domain represented in 23(d) in a Bode plot, shows that the control system response to reference tracking is good since the rule-of-thumb is that the gain margin should be at least 2 decades above the zero dB line. The control phase margin is 40dB, which is 2 decades above the minimum threshold. The high and steep roll-off shows that the controlled trough tracking system will have a good noise rejection characteristics at high frequency.

In fig. 6.24, the motor current (d), displacement or position (e) and speed (f) as a result of the response from the PID controller output shows the oscillatory dynamics of the trough tracking system. The controlled speed of the DC motor, position the trough relative to the sun. The algorithm is a simplified for this research work, a more rigorous approach is to use look-up table as reference signals to the input of the controller which the motor follow as a path trajectory of the sun's position. In fig. 6.24 c it can be seen that the PID controller does a good job in keeping the acceleration about a reference.

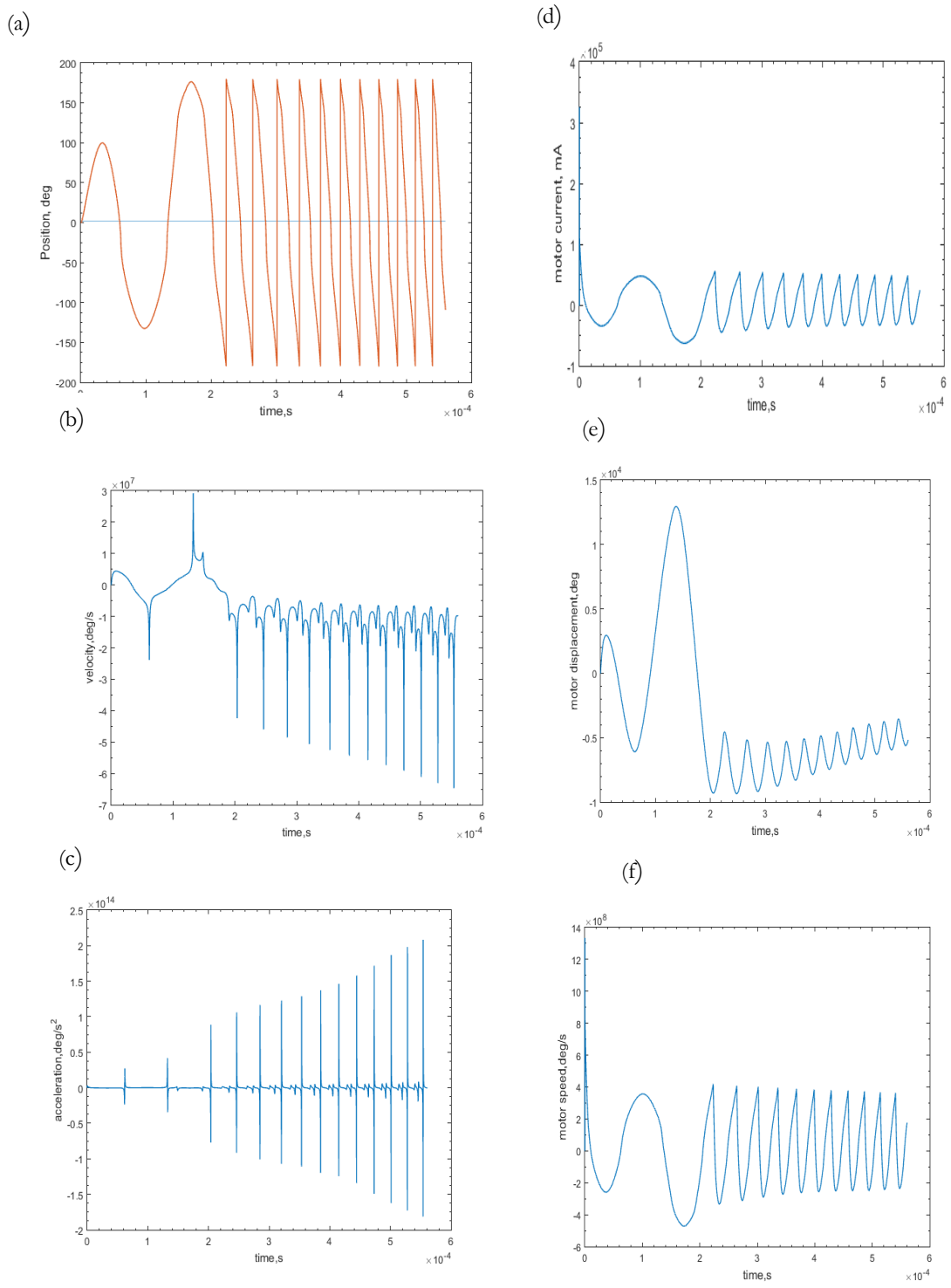

Figure 6.24 (a) Trough PVT position in pace relative to the tracking angle position of the sun;(b) Trough velocity response to motor speed actuation to position the trough;(c) Trough rate of change of velocity during actuation;(d) Motor current requirement for actuating positioning the trough;(e) motor displacement relative to the trough and sun position;(f) motor velocity for positioning the trough

Subsystems MATLAB/SIMULINK implementation of LQR full feedback controller design

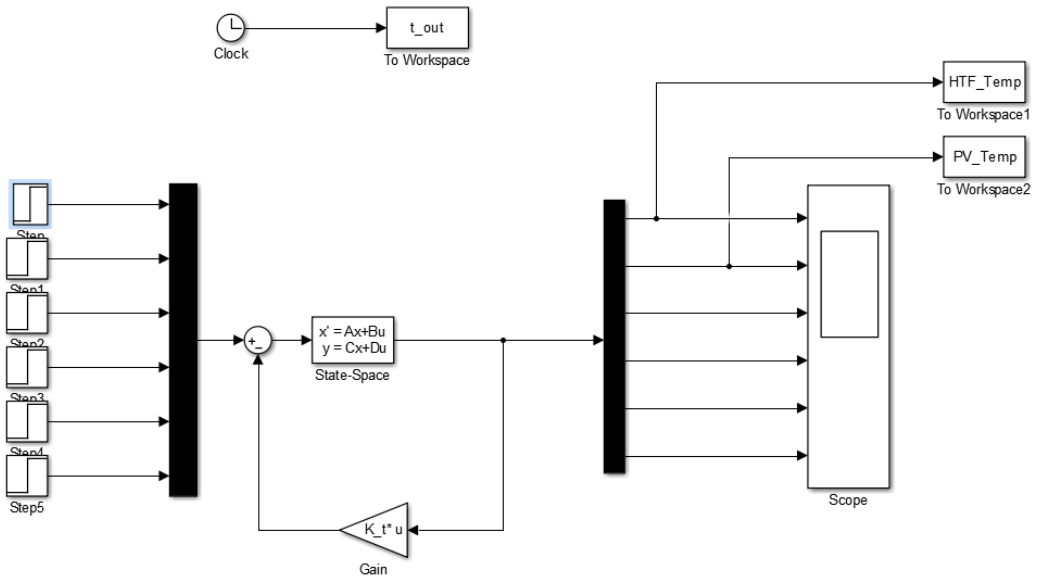

Figure 6.25 Full feedback centralised multiple-input multiple output multivariable optimal Linear quadratic regulator (LQR) controller with 6 step inputs, multiplexed and the gain K_t subtracted and fed as error signal to the State space block implemented the state vector x and output y. The feedback is implemented with a gain block, the outputs are multiplexed into output signals

In fig. 6.25, the control output of the temperature of the heat transfer fluid and the temperature of the PV module the system is characterised with a time delay of 1 seconds, a rise time of about 5 seconds and settling time of 1.5 seconds. The performance for both heat transfer fluid and the is already being met but the system overall performance can be improved with a careful tuning of the LQR controller using the weighting inner matrix of the Q matrix. It is important to state that coming from a system that was unstable and meeting the performance with the results stated above is to say the least encouraging. The transient delay represented by the fig. 6.26 in a and b, is a typical characteristics of thermal system that the control cannot ignore. A further increase in the controller gain K, could improve or eliminate the delay but will come at a huge cost of the control effort which means bigger control actuators. The implication of having bigger or larger control actuator is more cost for the control engineer to handle.

(a)

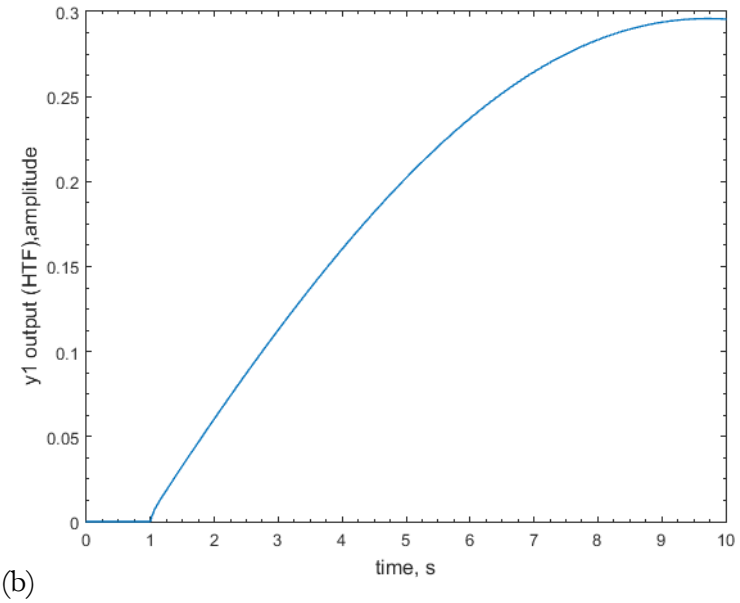

(b)

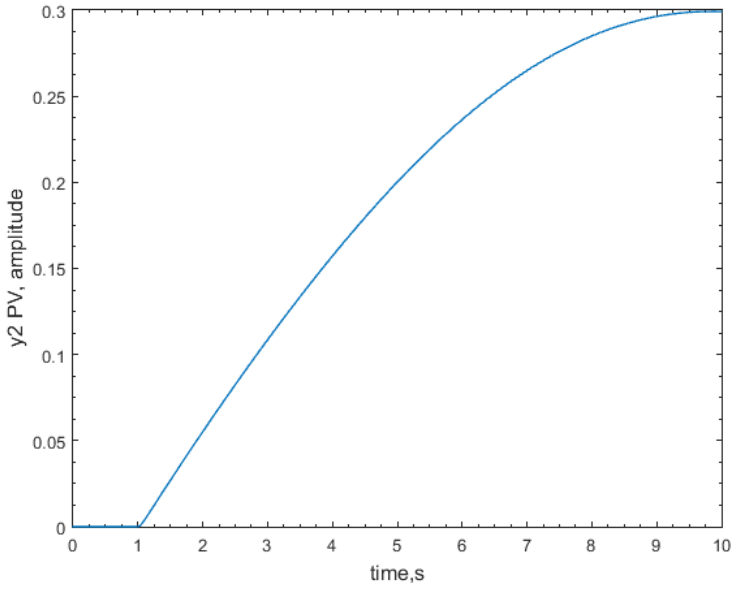

Figure 6.26 (a) Step response of step input obtained from LQR controller design in figure 16 of the Heat transfer fluid temperature in the trough PVT thermal subsystem; (b) Step response of step input obtained from LQR controller design in figure 16 of the PV temperature in the trough PVT thermal subsystem

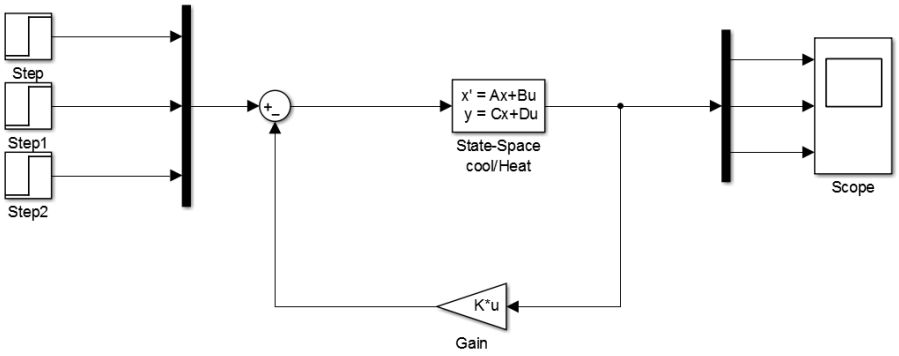

Figure 6.27 Cooling/Heating subsystem full feedback Linear Quadratic Regulator Controller with state space state equation and output block. The Gain block contains the row vector multiply by the input control u. Inputs are step signals

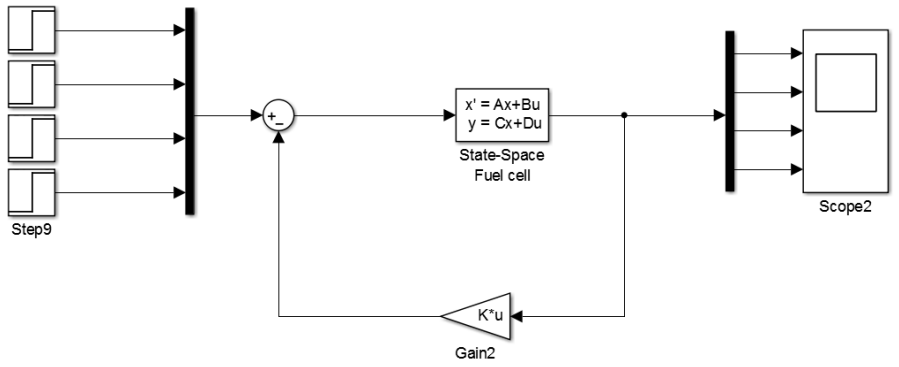

Figure 6.28 Fuel cell subsystem full feedback Linear Quadratic Regulator Controller with state space state equation and output block. The Gain block contains the row vector multiply by the input control u. Inputs are step signals

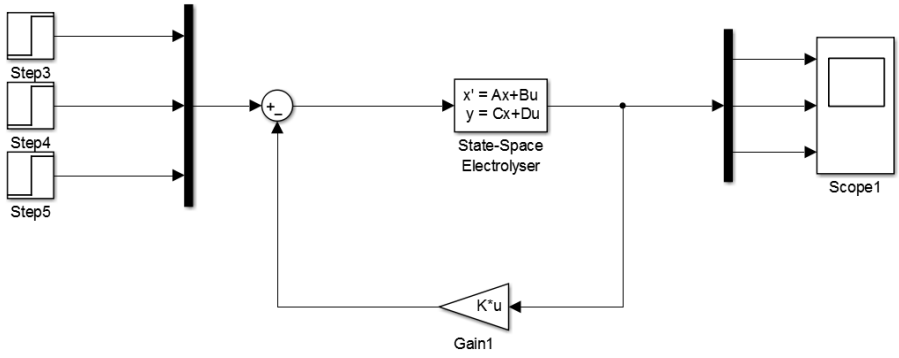

Figure 6.29 Electrolyser subsystem full feedback Linear Quadratic Regulator Controller with state space state equation and output block. The Gain block contains the row vector multiply by the input control u. Inputs are step signals

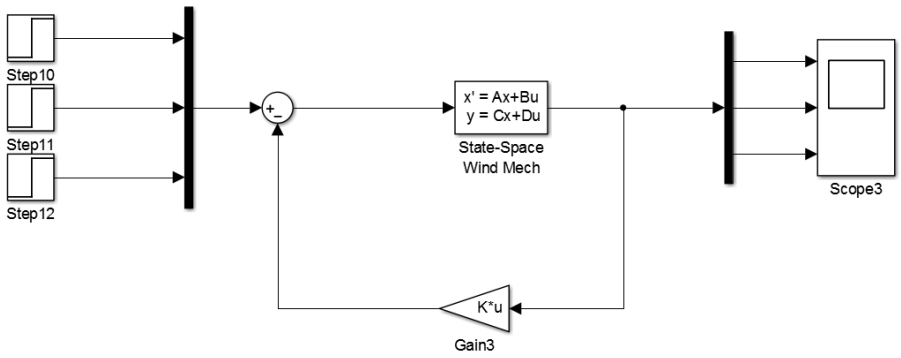

Figure 6.30 Wind turbine mechanical subsystem full feedback Linear Quadratic Regulator Controller with state space state equation and output block. The Gain block contains the row vector multiply by the input control u. Inputs are step signals

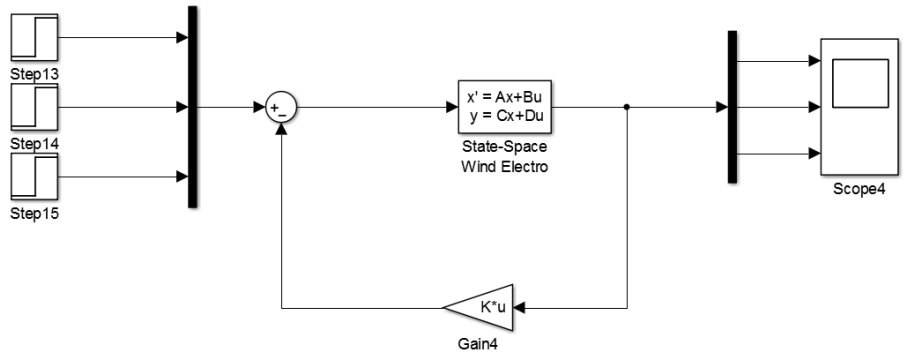

Figure 6.31 Wind turbine electrical subsystem full feedback Linear Quadratic Regulator Controller with state space state equation and output block. The Gain block contains the row vector multiply by the input control u. Inputs are step signals

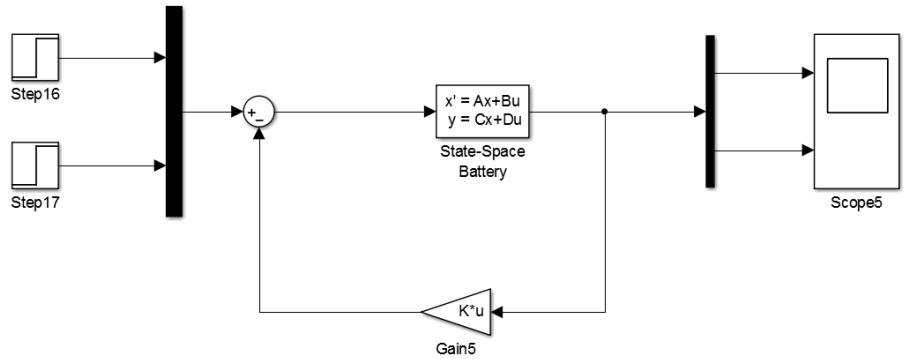

Figure 6.32 Battery subsystem full feedback Linear Quadratic Regulator Controller with state space state equation and output block. The Gain block contains the row vector multiply by the input control u. Inputs are step signals

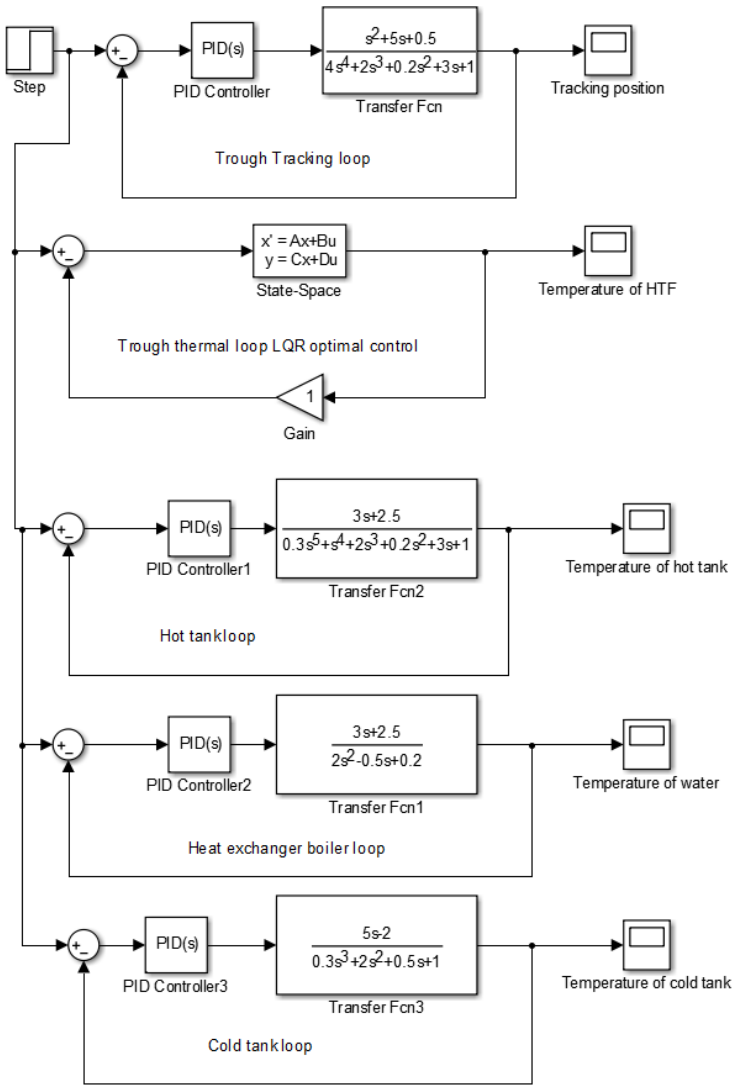

Figure 6.33 Multi-loop mixed architecture and control strategies implementation of block diagram in fig. 6.6 in MATLAB/SIMULINK

6.10 Subsystems Linear Quadratic Regulator controller design

The LQR controller design for the optimal state feedback gain K, the Riccati matrix, S and the eigenvalues, E of the stabilised closed-loop system (A-BK) for the continuous time linear time invariant (LTI) system is presented in table 6.1 as follows;

Table 6.1 LQR optimal controller design using the (6.1) for controller loops with full LQR feedback of system ((A-BK), B, C, D)

Subsystems	Full feedback LQR gain (K)	Eigenvalues (E)
Trough PVT thermal	[0.72 5.53 5.31 17.52 32.99 119.37]	-25.20 -0.33 -0.24 -0.16 -0.041 $-7.4E-5$
Wind turbine Mechanical	[0.71 -0.71 -0.01]	$-28.21+66.41i$ $-28.21-66.41i$ $-0.002+0.01i$
Wind turbine Electrical	[9.3E-14 -4.23E-15 6.55]	-0.77 $-2.02E-5$ -3.35
Heating & Cooling	[2.04 -71.66 2.88]	-60.84 -1.81 -0.02
Electrolyser	[-73.01 36.51 146.03]	-0.0125 -0.0121 -0.0123
Fuel cell	[-0.798 0.423 0.950 -0.043]	$-8.64+0.0001i$ $-1.88+1.7991i$ $-1.88+1.7991i$ $-0.0017+0.0001i$
Battery storage	[2.499E3 -2.205E3]	-0.984 -3.000

The result in table 6.1, is a summary of the result of the dynamic programming optimisation based on the linear quadratic regulator control algorithm implemented in MATLAB. The design codes are presented in Appendix B. The cell mode scripting approach with subsystem in each section with a double %% separating each subsystems section. The results in tables 6.1 shows the unstable open-loop systems in the previous dynamical study in chapter 5 have been stabilised as indicated in the column eigenvalues (E). In the table, the wind turbine mechanical and fuel cell subsystem eigenvalues contain real and imaginary poles with all the

real poles as negative values. The others subsystems all have real negative values. The negative real poles all lie on the left plane of the complex plane. Hence the subsystems have been stabilised by the optimal LQR controller by placing the poles at an optimal position without violating the cost penalty function. This is an interesting finding, as my control knowledge at the undergraduate level was based on the notion that when an open-loop system is unstable, such system cannot be stabilised. The LQR optimisation based control is an advanced model predictive control with an infinite horizon that provide the space dimension to stabilise a controllable system. The necessary and requisite condition for a system to be stabilised is that the unstable system must be controllable.

Table 6.2 The Riccati matrix obtained from the optimal LQR controller design

Subsystems	Riccati Matrix (S)	Stabilisation B Matrix column
Trough PVT thermal	$\begin{matrix} 0.6 & 3.6 & 3.4 & 11.2 & 21 & 65 \\ 3.6 & 80 & 79.4 & 262 & 493.64 & 2.28E3 \\ 3.39 & 79.36 & 78.95 & 263.3 & 498 & 2.56E3 \\ 11.16 & 262 & 263.3 & 902.4 & 1.72E3 & 1.1E4 \\ 21 & 494 & 498 & 1.73E3 & 3.3E3 & 2.4E4 \\ 64.75 & 2.23E3 & 2.56E3 & 1.1E4 & 2.4E4 & 9.5E7 \end{matrix}$	First column matrix B (:,1)
Wind turbine Mechanical	$\begin{matrix} 271.97 & 271.97 & -4.17 \\ 271.97 & 271.97 & -4.17 \\ -4.17 & -4.17 & 0.06 \end{matrix}$	First column matrix B4(:,1)
Wind turbine Electrical	$\begin{matrix} 4.26E8 & 0.05 & 9.30E-14 \\ 0.01 & 0.65 & -4.23E-15 \\ -9.3E-14 & -4.23E-15 & 6.55 \end{matrix}$	Third column matrix B5(:,3)
Heating & Cooling	$\begin{matrix} 0.84 & 543.63 & 0.089 \\ 543.63 & 9.35E6 & -46.92 \\ 0.09 & 46.92 & 0.09 \end{matrix}$	First column matrix B1(:,1)
Electrolyser	$\begin{matrix} 2.17E5 & -1.08E5 & -4.34E5 \\ -1.08E5 & 5.42E4 & 2.17E5 \\ -4.34E5 & 2.17E5 & 8.67E5 \end{matrix}$	First column matrix B2(:,1)
Fuel cell	$\begin{matrix} 0.9279 & -0.4105 & -0.0025 & -0.019 \\ -0.4105 & 0.4044 & -0.0485 & -0.0408 \\ -0.0025 & -0.0485 & 0.124 & 0.0059 \\ -0.0182 & -0.0408 & 0.0059 & 293.58 \end{matrix}$	First column matrix B3(:,1)
Battery storage	$\begin{matrix} 1.041E6 & -9.183E5 \\ -9.183E5 & 8.104E5 \end{matrix}$	First column matrix B6(:,1)

In designing the full feedback control based on LQR, the selection of the right control column matrix B to stabilised the system. The algorithm returns an error if the matching column is not selected. A typical error message is returned such as "The "lqr" command failed to stabilize the plant or find an optimal feedback gain". The solution to the

computational problem is that all unstable poles of the A state matrix of the system are controllable through B (use MINREAL to check)

The weights Q and R matrix was modified to make [Q N; N' R] a positive definite, using EIG to check positivity. In table 6.1 all systems but the wind turbine electrical subsystem was stabilised using the first column of their B matrix.

Subsystem controller tuning

Heating and cooling system Optimal LQR controller design with pre-compensator

Controller tuning for LQR controller

The controller can be tuned by changing the nonzero elements in the Q matrix to achieve a desirable response. The 2 extremes of the Q matrix non-zero matrix were explored $Q=\begin{bmatrix}10000 & 0 & 0\\ 0 & 0 & 0\\ 0 & 0 & 20000\end{bmatrix}$ and $\begin{bmatrix}0.00001 & 0 & 0\\ 0 & 0 & 0\\ 0 & 0 & 0.00002\end{bmatrix}$ and both could not achieve a stable step response of the LQR controller for the heating and cooling system. These 2 extrema provided a means or bounds until half the Q (1, 1) =0.5 and Q (3, 3) =1 $\begin{bmatrix}0.5 & 0 & 0\\ 0 & 0 & 0\\ 0 & 0 & 1\end{bmatrix}$ of the leading diagonals of the Q matrix was able to control the heating and cooling plant.

The step response for the temperature signal is shown in fig.34. From the figure the room temperature step response signal has a peak amplitude of 0.814 with an overshoot of 0%, a rise time of 34 seconds and a final steady state value of -0.196. The performance for the heating and cooling system are peak amplitude of -0.178 at 0% overshoot, a rise time of 56.6s, a settling time of 70.5s and a steady state final values of 0.172.

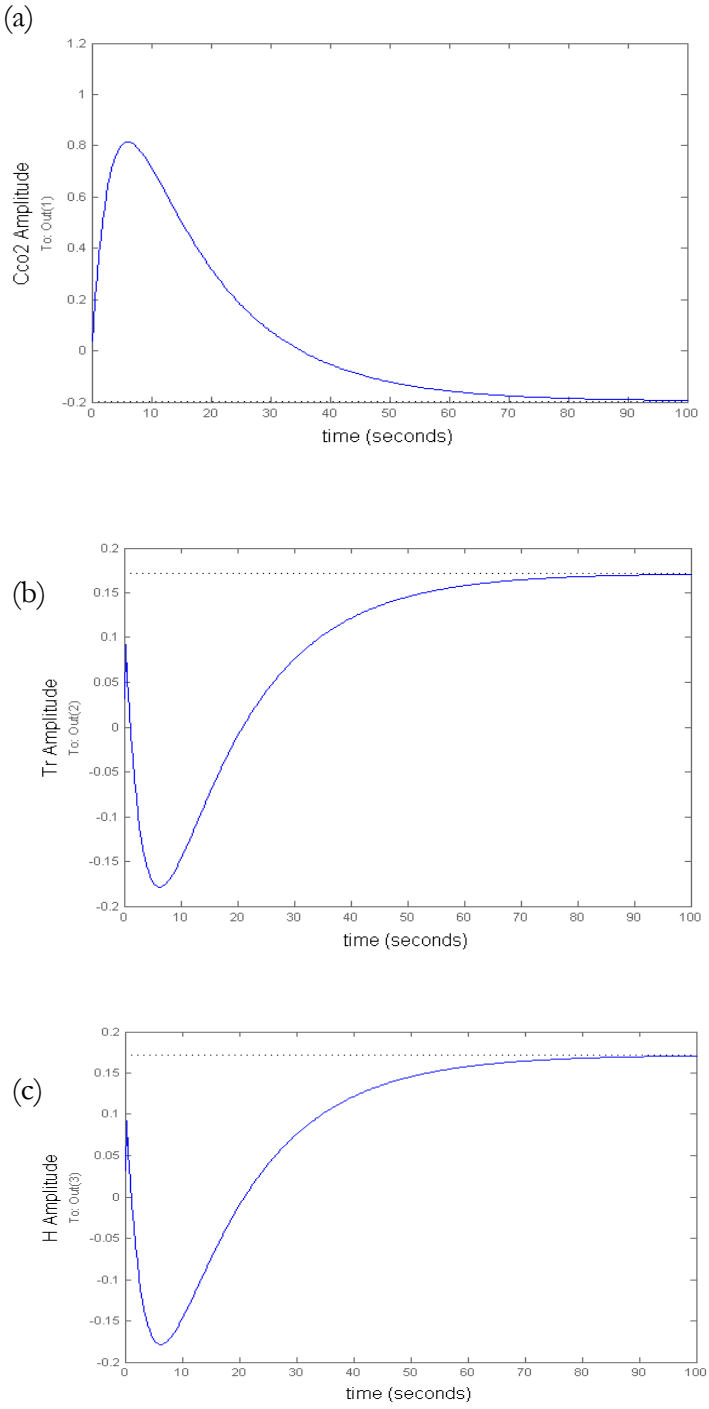

Figure 6.34 A step response plot for the heating and cooling subsystem; (a) carbon dioxide concentration step response to unit step input; (b) Step response of room temperature to unit step input; (c) Humidity step response to unit step input

The performance for the heating and cooling system are peak amplitude of -0.178 at 0% overshoot, a rise time of 56.6s, a settling time of 70.5s and a steady state final values of 0.172.

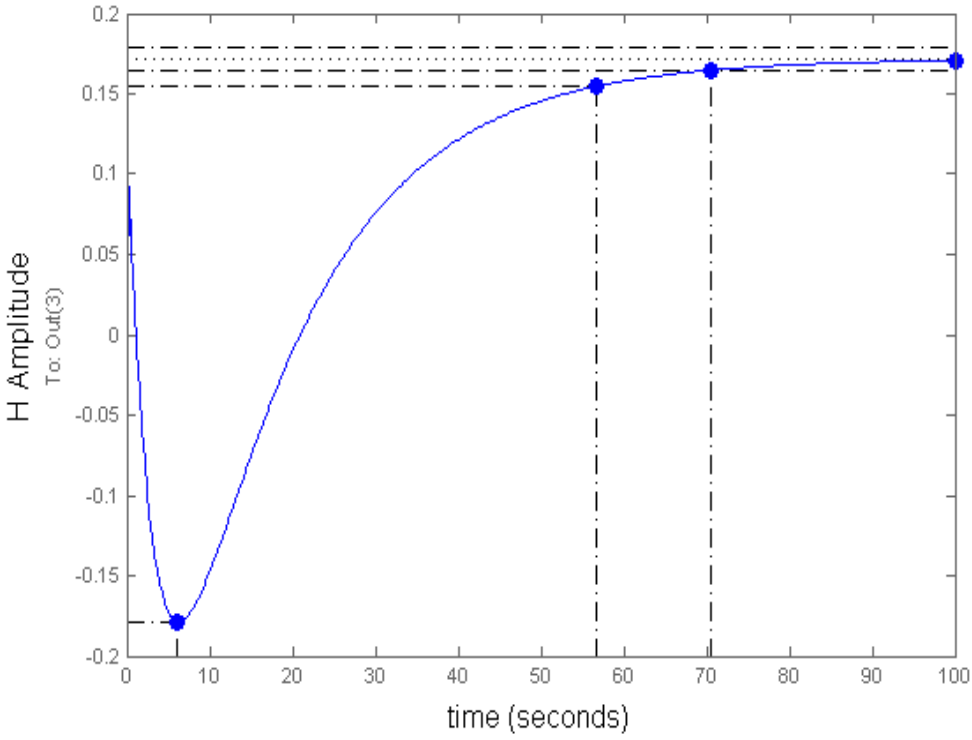

Figure 6.35 A typical step plot with performance position and locations

6.10.1 Electrolyser controller tuning with pre-compensator

All bounds of the Q matrix of the electrolyser system was explored and the same step control response of the original Q matrix. The control response for the electrolyser temperature was obtained. The performance of the electrolyser expressed in terms of the overshoot of 0% and peak amplitude of 0.00515 for 44.9 s, a settling time of 3.99 s and a steady state value of -4.4×10^{-18}. The electrolyser hydrogen gas flow rate performance is characterised with a rise time of 187 s, settling time of 383s and steady state value of -0.00891

(a)

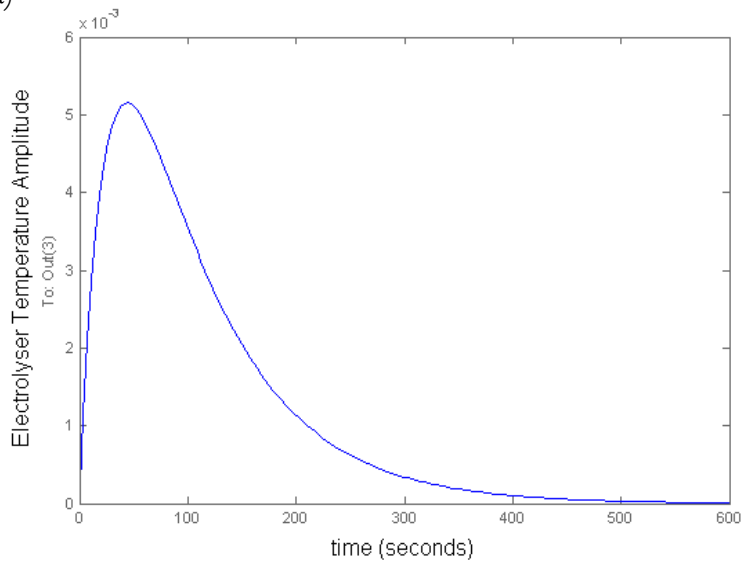

(b)

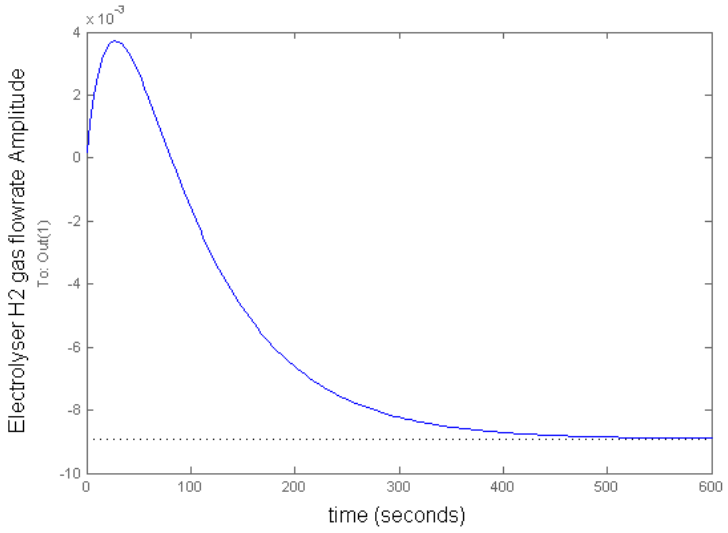

Figure 6.36 Electrolyser step response to step input of an LQR controller with a pre-compensator; (a) electrolyser temperature step response to unit step input;(b) flowrate of hydrogen produce step response to a unit step input

6.10.2 Fuel cell controller LQR tuning with pre-compensator

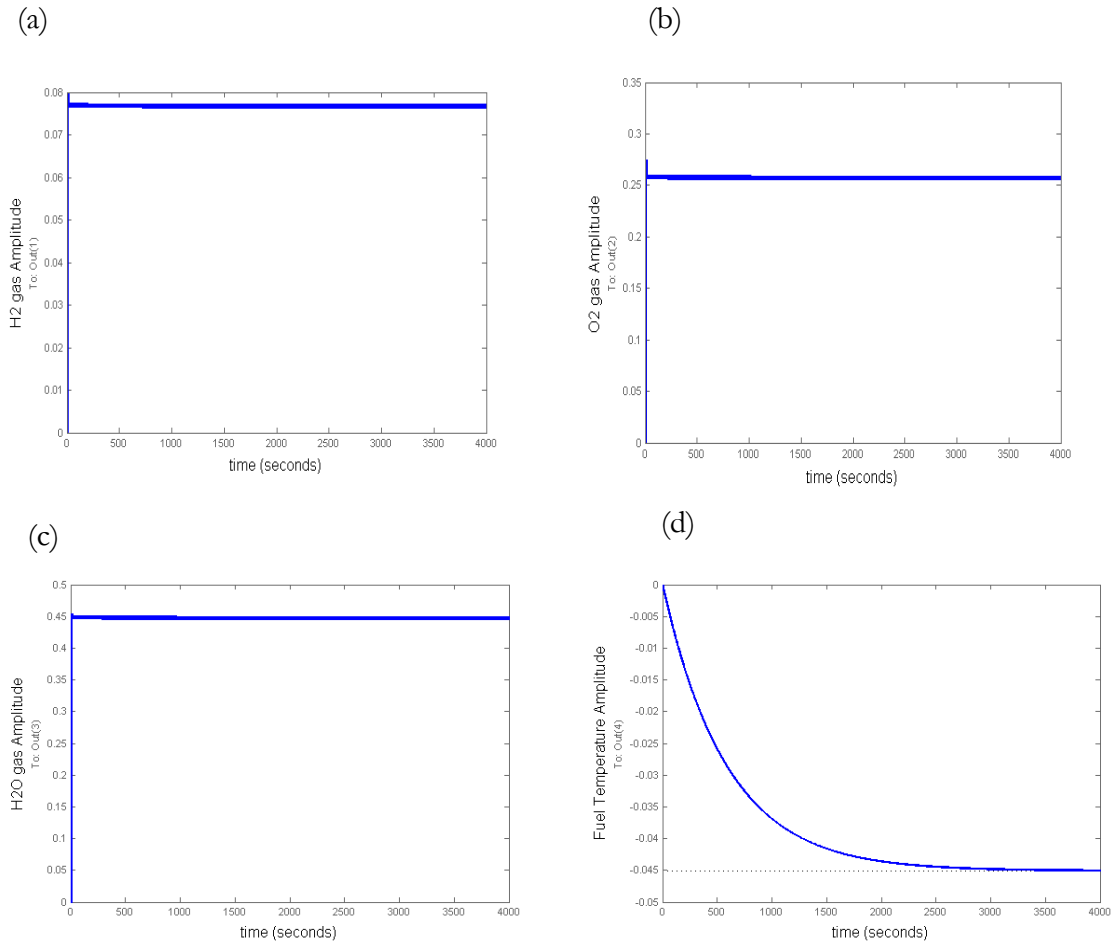

Figure 6.37 Fuel cell step response LQR controller tuning with pre-compensator;(a) Hydrogen gas consumption flowrate step response to input;(b) Oxygen gas consumption flowrate step response to input;(c) water production flowrate of fuel cell step response to step input; (d) fuel cell temperature step response to unit step input

H2 gas LQR controller tuning performance in fig.6.37 is characterised with an overshoot of 4.32s at peak amplitude of 0.08 at 1.62 s, a settling time of 2.24 s, rise time 0.78 s and steady state value of 0.0767. The O2 gas performance is characterised with an overshoot of 7.01% at peak amplitude of 0.275 at 1.08s. The water flowrate step response performance is characterised with an overshoot of 1.74% at peak amplitude of 0.455 at 0.27s, a settling time of 0.186s, a rise time of 0.113s and steady state value of 0.447. The fuel cell temperature step response has a settling time of 2290 s, rise time of 1290 s and steady state value of -0.0451.

The fuel cell flow rate LQR controller in fig. 6.37 shows a very tight control characteristics compared to the temperature control with a very high settling and rise time. Perhaps is as result of very slow behaviour of the thermal temperature process, characterised by time delays. The LQR controller with compensator N was able to keep the overall fuel cell system

under control but the thermal system response to the controller is extremely slow, a more advance intelligent genetic algorithm will be applied to optimised the system and make the response faster. This extra controller implementation is beyond the scope of this research and forma the basis of study for the future research direction.

6.10.3 Wind turbine mechanical system LQR controller tuning with pre-compensator

The original non-zero element in the Q matrix did provide the control performance expected after adding a pre-compensator. The wind turbine mechanical system LQR optimal controller with pre-compensator shows performance of the wind turbine generator and rotor rotational speed according to the fig. 6.38 are characterised with overshoot of 0%, rise time of 597 s, settling time of 1060 s and steady state value of 0.354. The result shows that the controller though was able to hold and keep the rotational speed of the generator and rotor at set point values but at huge time. The system can be optimised to respond faster with a genetic algorithm based controller. Overall, the controller did a good job by eliminating torsional vibration since the controller is stable without oscillations.

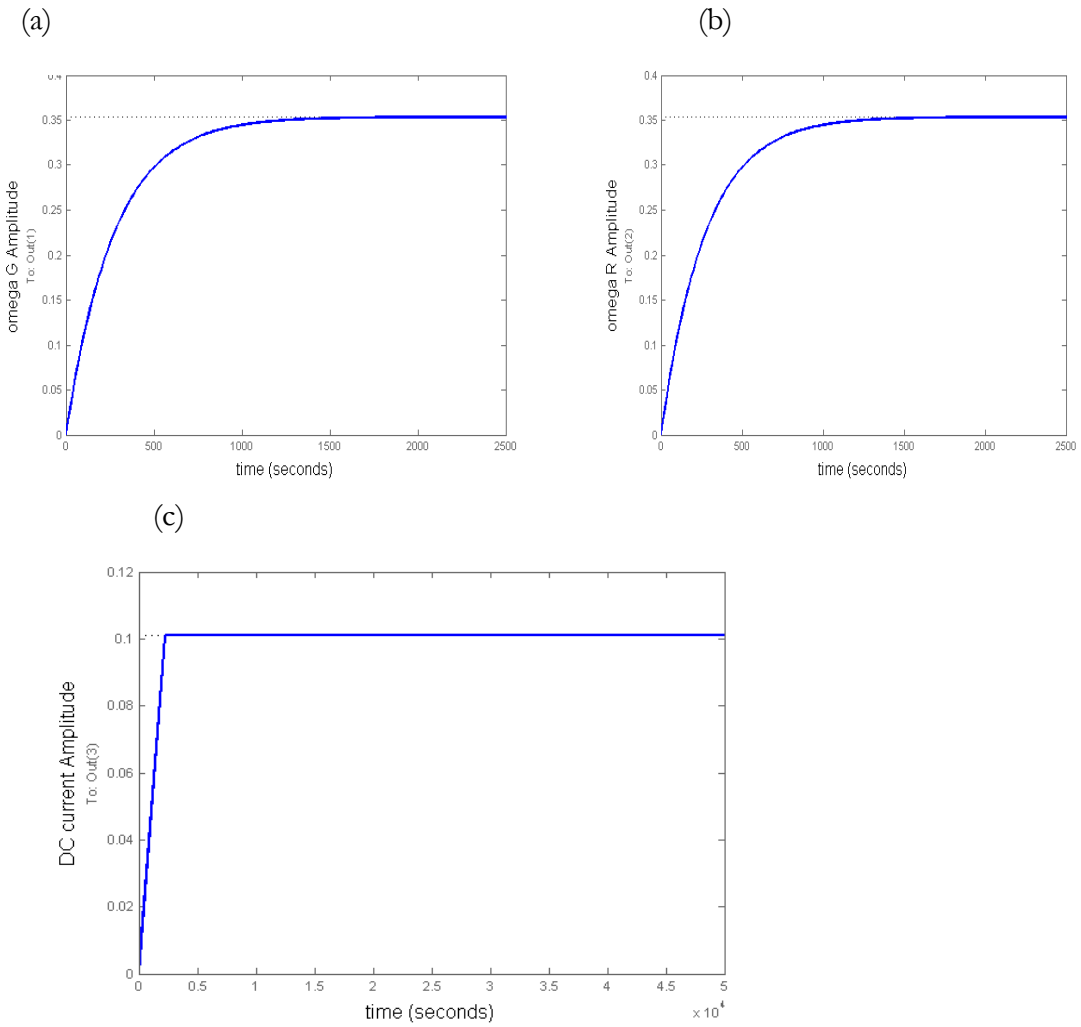

Figure 6.38 Wind turbine subsystem LQR controller tuning with pre-compensator step response to a unit step input;(a) Step response of generator rotational speed to a unit step input;(b) Rotor step response to unit step input;(c) direct current response to unit step input

The electrical DC current has the performance characteristics with 0% overshoot, settling time of 2230 s, rise time of 1820 s and steady state value of 0.101.

6.10.4 Battery LQR controller tuning with pre-compensator

The non-zero element of the Q matrix was able to control the battery plant without trying different non-zero element in the Q tuning matrix.

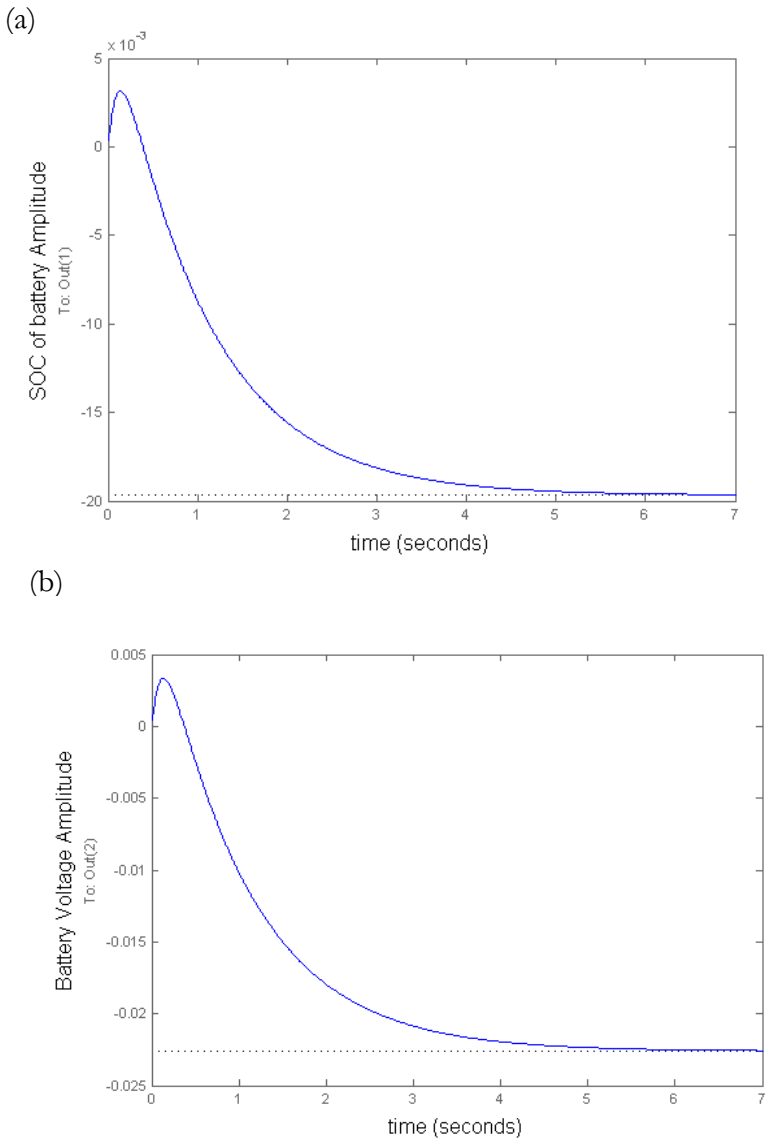

Figure 6.39 Battery LQR controller response to a unit step input tuned with a pre-compensator; (a) Battery state of charge (SOC) step response to a unit step input; (b) Battery voltage response of LQR controller to a unit step input

The following battery performance was obtained from the step response plot in fig. 6.39 battery voltage has an overshoot of 0% at > 7s with peak amplitude of <=-0.0226, a settling time of 4.24 s, rise time of 2.24 s at steady state value of -0.0226. The battery state of charge (SOC) has an overshoot of 0% at > 7 s and peak amplitude of -0.0196, settling time of 4.24 s, rise time of 2.24 s and steady state value of -0.0197.

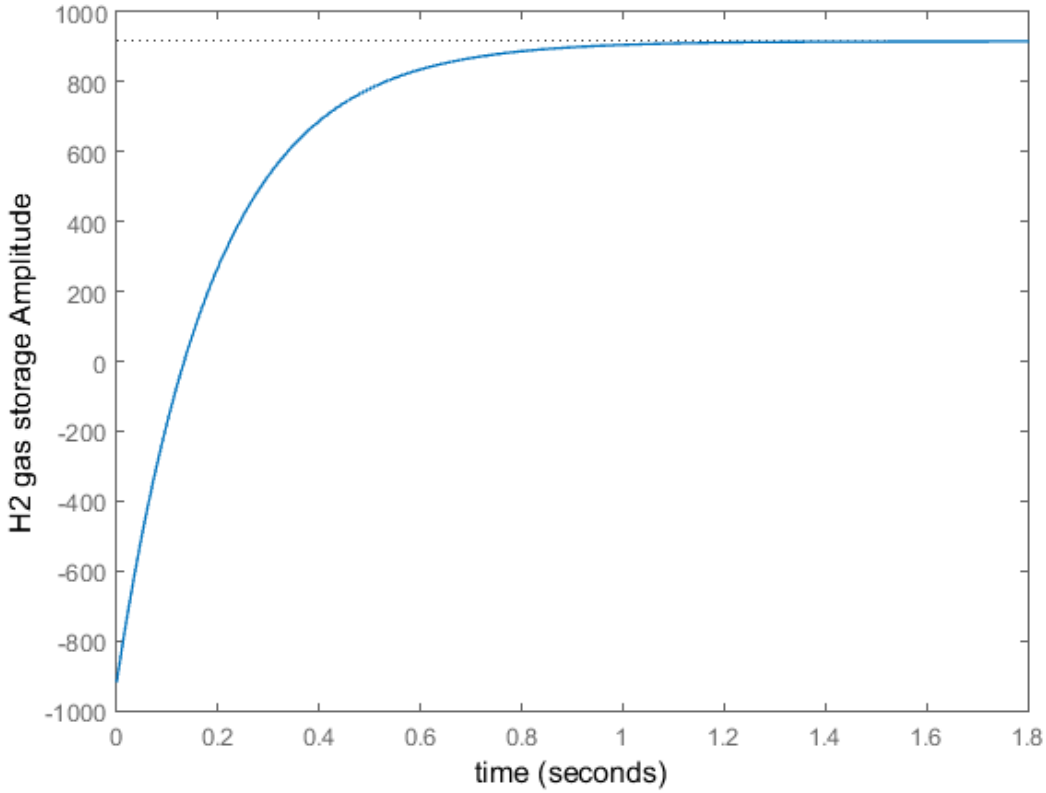

Figure 6.40 Hydrogen gas storage tank step response to unit step function of the transfer function with a PID controller

The performance of the hydrogen storage tank in fig. 6.40, is characterised with an overshoot of 0%, rise time of 0.423 s, a settling time of 0.756 s and steady state value of 917.

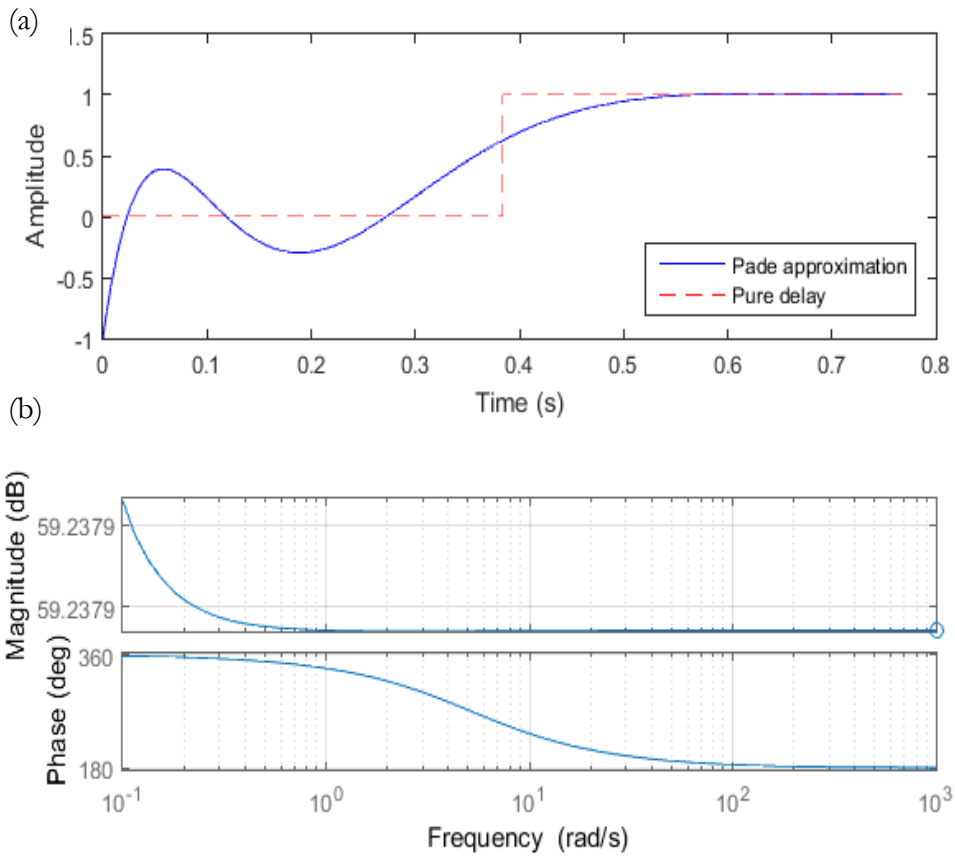

Figure 6.41 (a) Pade approximation of order 3: step response comparison; (b) the Bode plot of the frequency domain behaviour of the hydrogen storage tank temperature

The Pade approximant in fig. 6.41a is the best approximation of the temperature partial differential equation function by a rational function of order 3. The approximation was compared with a pure delay function and fits it within the limit of computational error.

6.11 Summary and conclusions

A detailed subsystem by subsystems control was implemented using MATLAB/SIMULINK, SIMSCAPE, controller designer and Simulink design optimisation as tools for realising model-based design computer aided control design paradigm. The LQR optimisation based, proportional, integral differential (PID) 2 degree of freedom and it variant (PI) was also implemented in a mixed mode, centralised multivariable multiple input multiple output (MIMO) and multi-loop control architecture and strategies, indicated a good controller response to step response. It is important to note that some of the subsystems were inherently slow to controller response. The response to the dynamics of the controller is as a results of the extra-dimension added to alter the dynamics of the open-loop unstable behaviour of the subsystems in chapter 5. The LQR controller design with a pre-compensation is a very powerful model predictive controller with infinite horizon that was

successful in stabilising the unstable open-loop plant dynamics for all the subsystems in the previous dynamical studies.

The delays were particularly prevalent in subsystem components with thermal transient dynamics, a more rigorous LQR controller tuning with an observer may reduce or eliminate the delay. The other suggestion or recommendation is to introduce a genetic algorithm based controller to improve the dynamics of the step response of the thermal process. This could form the basis for future research directions in the control of combined cooling heat and power system. The response to the dynamics of the hydrogen and heat storage was omitted because of the non-linear behaviour and may introduce a new challenge of Lyaponov stability and non-linear tuning which as result of time, is beyond the scope of this study.

In conclusion, it been a very challenging task to produce the state space models from differential equations, though the mechanical trough tracking system model was developed using native computer aided design software and discretised into SIMMECHANICS blocks using extensible mark-up language (xml) and translated to high fidelity plant model. The DC motor actuator is also a high fidelity model with input-output port representing real physical connections. The unit step input was used in all the subsystem to simplify the control on a subsystem by subsystem basis. In control practice, step input is often used because they excite an infinite range of frequencies and provide control engineers with a good idea of not only the performance of the controller but the overall stability of the system. A performance criteria was not specified in the beginning for each subsystem, as this will make the controller design overwhelmingly challenging to implement and manage. The systems control response to step input can be concluded to have provided good tracking of set-point changes. The control system has more than ever reveal the multiscale of the various subsystem electrical, mechanical, electrochemical and thermal systems response to controller step input in fractions of seconds and minutes for subsystems with rise and settling time of order of 10^3 seconds as presented in the performance characteristics of the controllers. The electrical and electrochemical systems occur at the electron transfer scale which is a subatomic level, the thermal system happens at atomic level and molecular level making the system a multidimensional.

Chapter 7 Fabrication of experimental rig and synthesis of Nanofluids

7.1 Introduction

The challenge of using the solar radiation form the sun was addressed by designing a solar emulator or simulator, to provide light conduct experiment on the parabolic trough. The parabolic trough and the receiver shape was fabricated from ground-up using the innovative Frugal engineering approach, which is essentially getting things done at lower cost and short time to market. From the literature cited in chapter 2, an experimental rig consisting of sun simulator, parabolic trough receiver system, flowmeter, pump, top and bottom tank and the synthesis of mono propylene Nanofluids.

7.2 Research approach and methodology

The chapter methodology was based on hardware systems integration of various parabolic trough PVT, sun simulator, light spectrometer subsystems from components parts. The integration is driven by cost as result of an extremely meagre budget, resulting in a new cost engineering technique called frugal engineering.

The second methodology was based on the experimental synthesis of graphene oxide from graphite using top-down modified Hummer's method. The graphene oxide was reduced using green reduction method with ascorbic acid and dilute solution of Ammonia. The solution was sonicated with some green amphoteric gum Arabic surfactants to obtain a stable graphene Nanofluids dispersed in deionised water, Mono ethylene glycol, Mono propylene glycol, binary mixture of water/Mono ethylene glycol and water/Mono propylene glycol.

7.3 Frugal engineering methodology approach

The concept of frugal engineering, a phrase credited to Carlos Ghoshn, who heads Renault-Nissan, connoting and signifying achieving more with fewer resources (James, 2010). It is of much more fundamental interest to recognize the revolution in product-design philosophy that frugal engineering embodied. Others have described similar ideas under terms such as reverse innovation, Gandhian innovation or even "Indo-vation." The method was adopted in fabrication of the experimental rig because of the tight budget and limited funding available (Anand, 2010).

7.3.1 The solar simulator subsystem

The solar simulator subsystem consists of the Cree LED boards, the driver, cooling fans, heat sink, the audio cable, the controller, reflector and the power supply module.

7.3.1.1 Cree LED boards

The LED board contain 12 units of warm white and 12 units of Royal-Blue per foot of cool-white Cree XT-E high power LEDs. The board is cleverly design to with screw terminals for mounting on the heat sink. The back and the front side of the board is shown in fig.7.1.

(a)

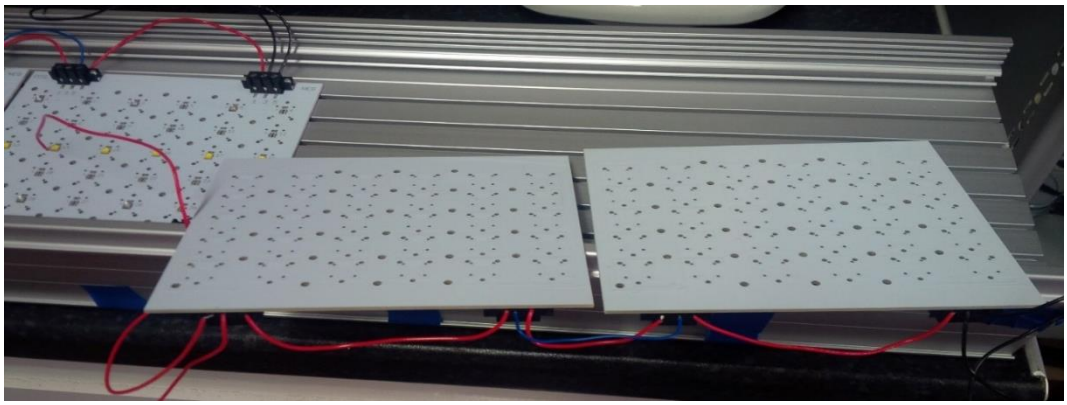

(b)

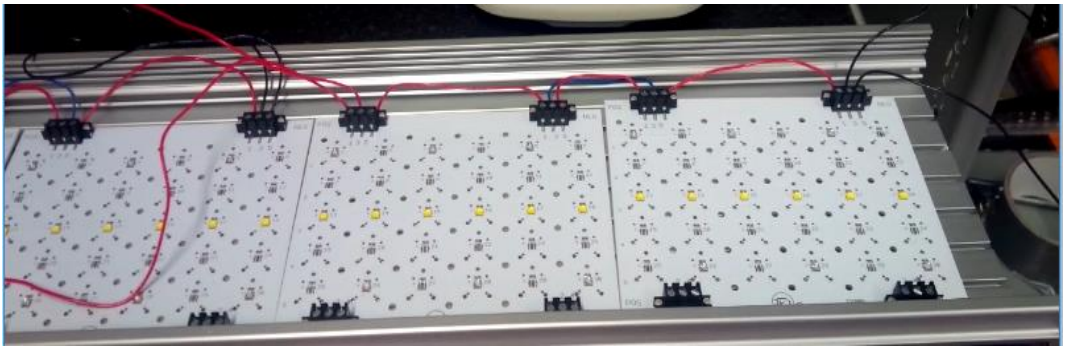

Figure 7.1 (a) Back view of CREE LED boards with holes for the thermal paste; (b) Front view of the CREE LED boards with connecting wires between boards

7.3.1.2 Driver

The driver in fig. 7.2 is a 48Vdc power input, for driving up to 28 LEDs, a fan, and an optional controller. The driver provides two dimming channels, each capable of driving 14 LEDs. Internally the MakersDRIVER 2UP PRO includes user-replaceable Meanwell LDD series LED drivers and a dimming options with integrated knobs for varying the intensity of the LED light during operation.

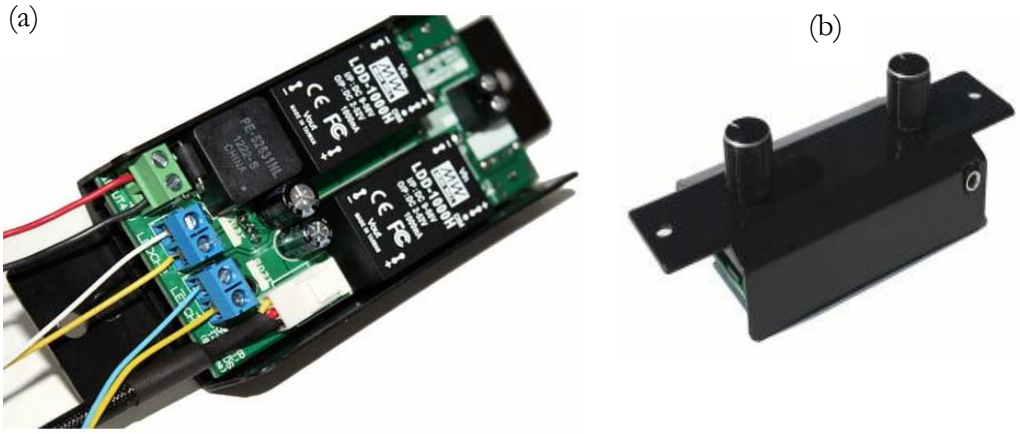

Figure 7.2 (a) up-turn view of Maker driver up pro with the blue connectors for connecting each LED printed circuits board, green connector for connecting each power supply unit to the driver and Molex female connector for the cooling fan; (b) top view of Maker driver up pro with the dial for increasing and decreasing the contrast of the LED's (LED supply, (2016))

7.3.1.3 Cooling fans

The cooling fans are 12 volts and provide cooling when the intensity of the LED light is greater than 10%. The LED get really hot at high intensities and fan and the thermal paste provides and effective means of dissipating the heat. The female Molex connector connect to the fan connector in the LED driver. The fan cools a pair of Cree LED boards.

Figure 7.3 (a) The 4 12 V cooling fan for each CREE LED boards for removing heat at intensity values ≥ 10%; (b) Heat sink for mounting and installing LED's, fans, drivers and for dissipating heats

7.3.1.4 Heat sink

The Makers LED heatsink is engineered with integrated t-slots making it easy to mount Cree LED boards. The heatsink kit includes: anodized heatsink, splash guard, end caps, fan and LED mounting hardware. The heat sink is shown in fig.7.3b.

7.3.1.5 Controller and audio data cable

The Makers Controller in fig 7.4, works with the driver to create sunrise, sunset and other special effects throughout the day. Although the Makers DRIVER 2UP PRO does include a manual dimming option via 2 turn knobs, we highly recommend adding the Makers CONTROLLER to your kit. As stated above, the controller provides sunrise, sunset as well as cloud cover, high-noon and simulates lightning storms.

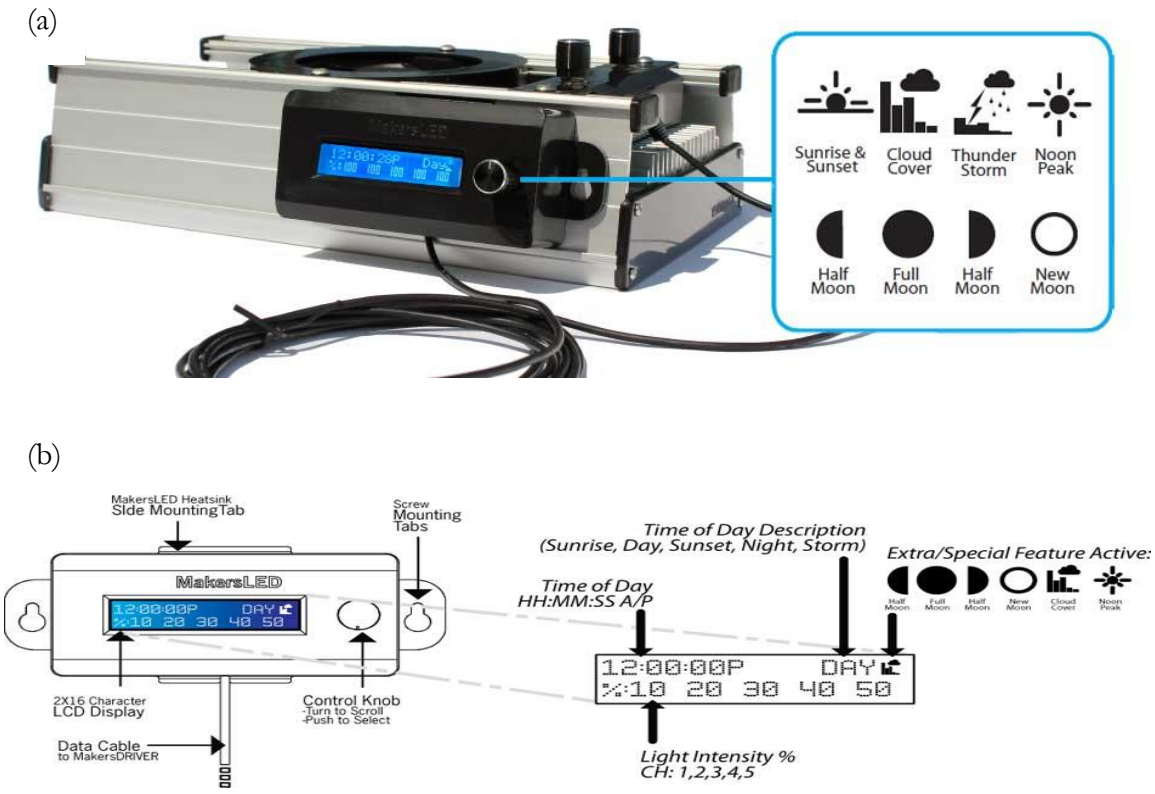

Figure 7.4 (a) Controller mounted on the heat sink with the audio data cable;(b) details of the controller with knob, LCD character display with sunrise, day, sunset night and storm features (LED supply, (2016))

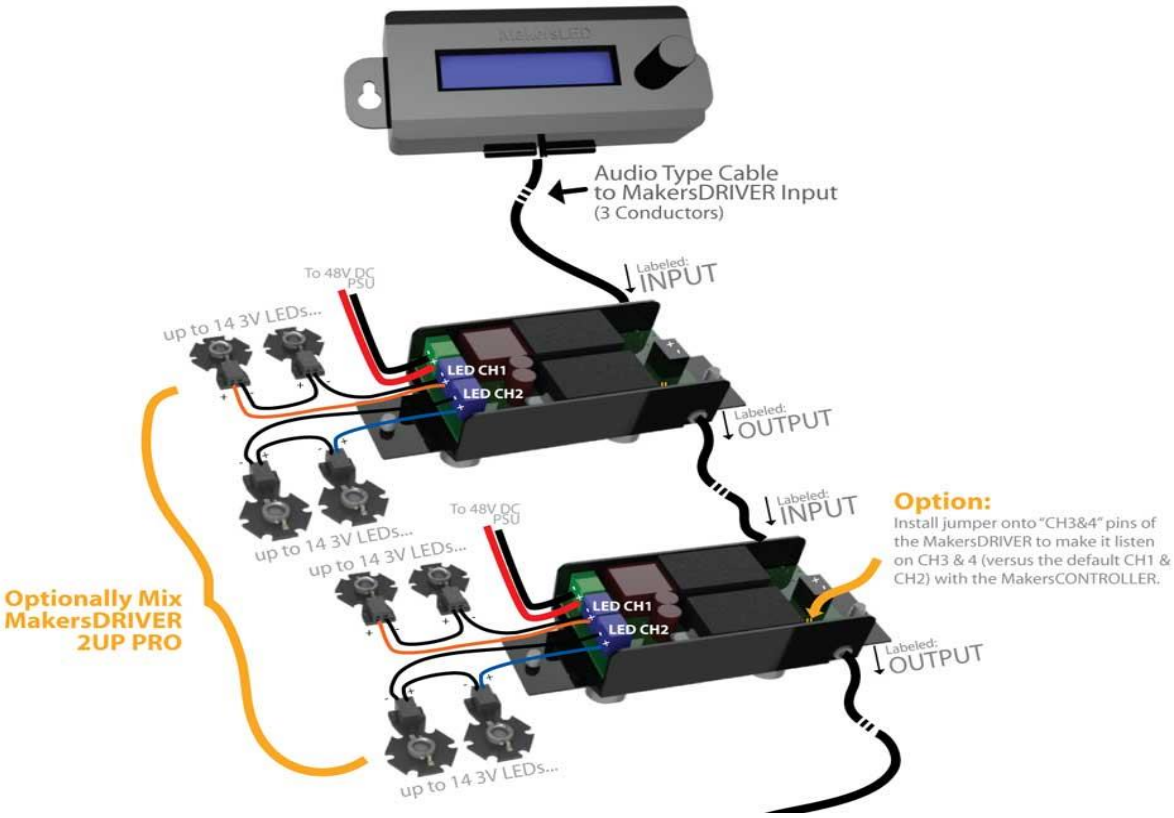

Figure 7.5 Connections schematics of drivers to drivers with audio data cable to controller, LED's to LED's and the output (LED supply, (2016))

7.3.1.6 Power supply module

The power supply module takes in a 240 VAC power at steady 48V Open Frame Power Supplies. Open Frame Switching Power Supplies, as you can see from the picture, are power sources where the circuit board and components are not totally enclosed, as with a desktop or wall wart power supply. Rather, they are encased in a metal casing with small holes throughout. This aids in air flow and cooling as the components are all open to the outside air. There are 4 of the power supply module, for a driver, fan and 2 LED Cree solderless board. The four power supplies are connected and contained in an electrical enclosure box with thermal circuit breakers for each power supply module. In the electrical box enclosure, 2×12 rechargeable VDC battery connected in series with a 24 V charger and the flow meter. The connection diagram is presented as follows;

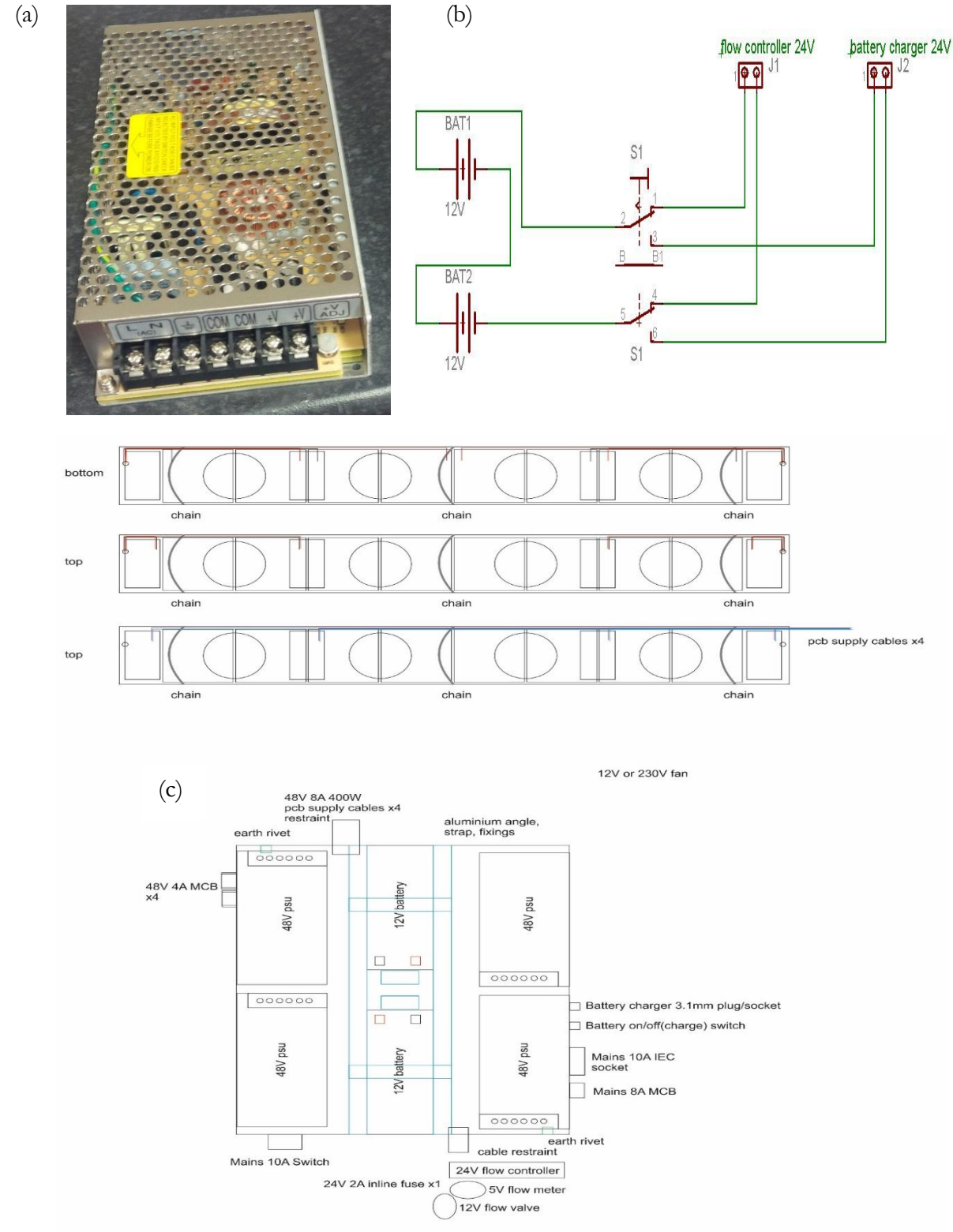

Figure 7.6 (a) the 48 V power supply unit (PSU); (b)the wiring connection of battery 1 and 2 to the 24 V flow meter and the 24 V battery charger in the control panel box enclosure; (c) Interior of the control panel enclosure box with the control panel buttons to the right

7.3.1.7 Reflector

The reflector function as a light focusing unit to reduce the scattering of the Cree LED light during operation. A triangular frustum geometry was selected because of the rectangular shape of the heat sink containing the LED boards. In figure 7(a), the reflector is used to test and calibrate the power of the simulator concentrated to 7.4 with a coefficient of utilisation about 50%.

(a)

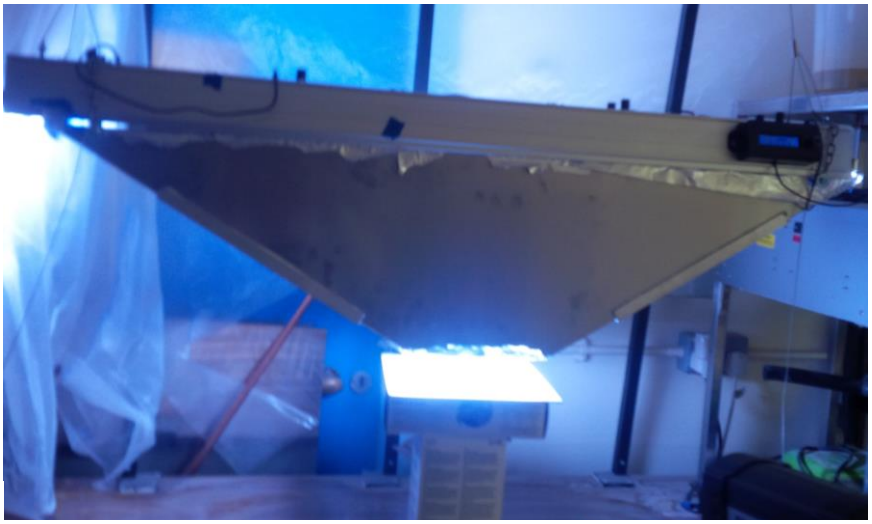

(b)

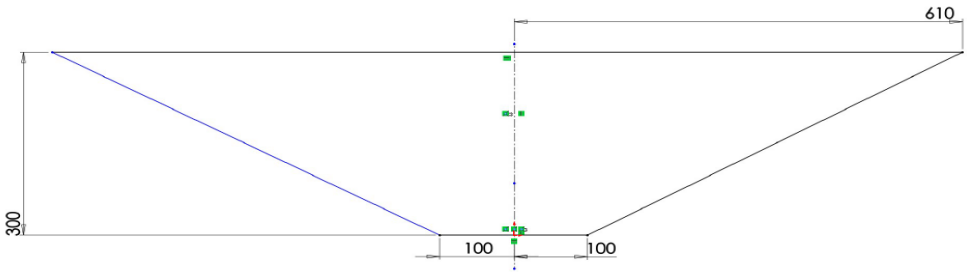

Figure 7.7 (a) Solar sun simulator with reflector under a lambertian target test calibration; (b) dimension of triangular part of the reflector

7.3.1.8 Hanging kits

The hanging kit is used to hang the simulator from a higher elevation. The hanging rope is used to adjust the height of the simulator to meet user requirements. The user requirement is the best position to pace or position the simulator before taking measurement. The complete hanging kits and it components part are shown in fig. 7.8.

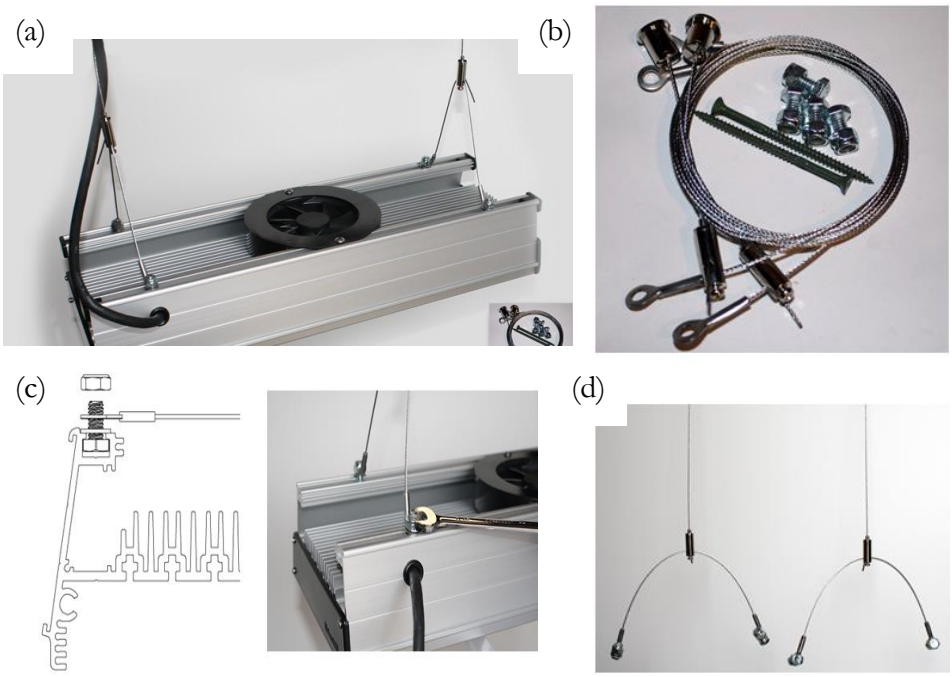

Figure 7.8 (a) Simulator hanging kits with all the accessories for installing the hanger; (b) 4 nylon washers, 4 stainless steel hex cap screws, and 4 stainless hex lock nuts to mount to MakersLED fixture and 2 2.5 inch screws for top stud installation;(c) installation of the hanger eylette, and the lock nut. Using a 7/16" open face wrench to tighten down the lock nut; (d) y-hager cable for suspending the heat sink from the top (LED supply, 2016)

7.3.2 Solar simulator theory

In designing and building a sun simulator for terrestrial applications, the concept of Air Mass value is used to bench mark the solar simulator based on the it location on the earth surface. In Fig. 7.9, the sun irradiance on before reaching the atmosphere has a one sun value of 1360 W/m^2 and classified as AM0 but drops or attenuate the light intensity and change the make-up spectrum of the light. The constituent of the light usually includes ultraviolet, visible and infrared. The path of the light that travels straight to the equator is called AM 1 whereas the path travels towards the north pole through continental and western Europe and north America is called AM 1.5. The classification of this sun solar simulator is based on spectral uniformity, spatial match and temporal stability. A detailed treatment of the sun simulator theory is espoused by Duffie & Beckman (2006); Mrinalini (2014).

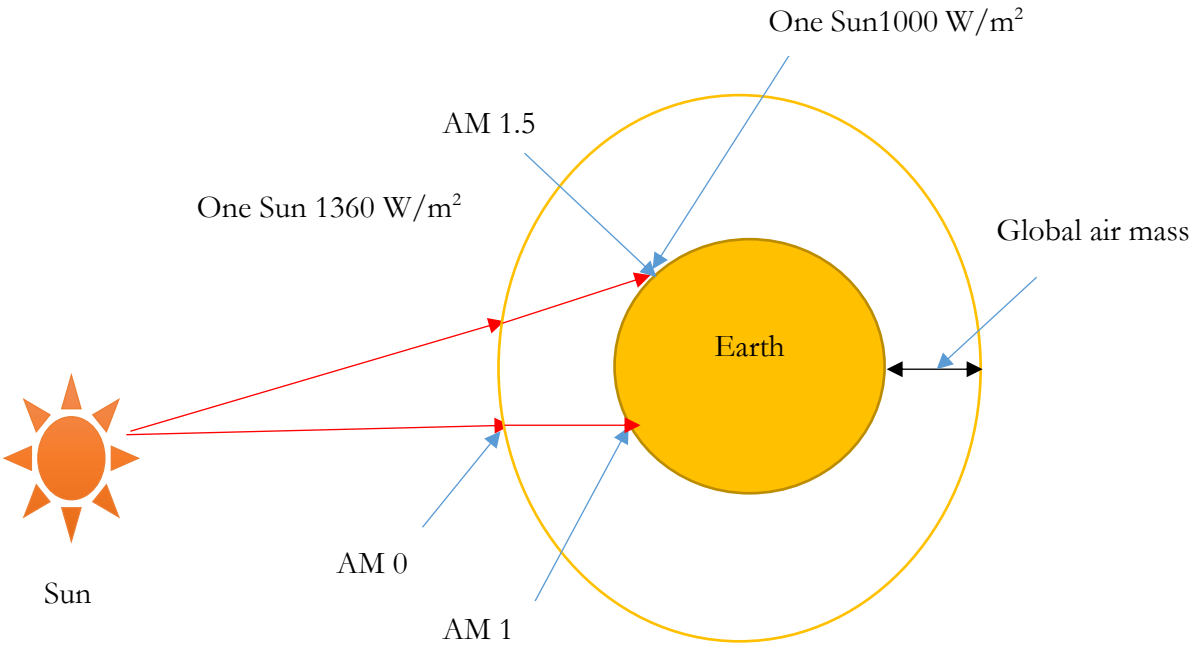

Figure 7.9 The sun solar irradiance on the earth surface with the atmosphere covering for illustrating the concepts of 1 sun, Air mass (AM) 0, 1 and 1.5 at different locations on the earth surface

7.3.2.1 Sun simulator power versus intensity calibration curve

The controller was calibrated for intensity but the power of the light is also required to match each light intensity to the power dissipated by the light. A solar radiation meter was used to measure the power for varying values of intensity. A plot of the power against the intensity was obtained as a power-intensity calibration curve. The curve is presented in fig. 7.10 as follows;

Table 7.1 Solar simulator heat Flux calibration data obtained using solar power meter TM-206.

Solar heat flux (W/m²)	Intensity (%)
1825	100
1387	95
1156	90
1099	85
976	80
872	75
761	70

686	65
580	60
488	55
403	50
385	45
279	40
233	35
215	30
195	25
140	20
93	15
46	10
22	5
0	0

7.3.3 Calibration of the solar simulator irradiance

A TM-206 power meter was used to measure the light irradiance corresponding to the light intensity already provided and indicated in the controller. The simulator was set to day intensity setting dial. The intensity was varied from 0-100% at interval of 5%. The result was tabulated in table 7.1. The calibration plot is presented in fig. 7.10 as follows;

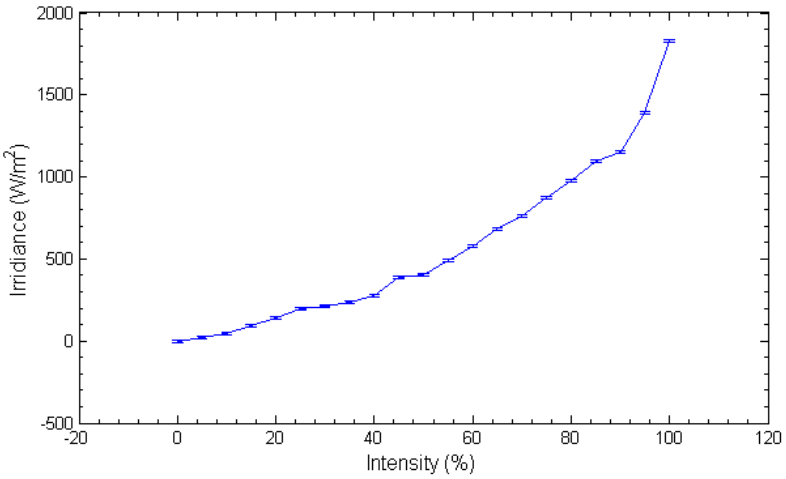

Figure 7.10 Sun simulator solar power versus intensity curve, obtained by measuring the light corresponding to an intensity value on the solar controller

Figure 7.11 Ambient Weather TM-206 Solar Power Meter (Pyranometer)

7.4 The spectrophotometer subsystem

The spectrophotometer was built to measure the spectrum of light from the Cree LED as a system and not as individual LED's. The spectrophotometer consists of the slit, a diffraction grating, the enclosure, a CMOS camera and the learnlight acquisition and analysis software.

7.4.1 Spectrometer slit unit

The spectrometer slit optics unit is 1mm gap made by to thin sharpe-edges of a tiger blade. The slit was constructed by cutting a 2.5×2.5cm square on the enclosure box and securing the 2 sharpe edges of a razor blade with a gap of exactly 1mm. The main function of the slit is to allow a very small path of 1mm for the light to go through before making impact with the diffraction grating. It helps to reduce the effect of ambient light on the light spectrum measurement.

7.4.2 Spectrometer diffraction grating unit

The is a 1000 lines/mm linear diffraction grating capable of measuring the spectrum of any visible light between 300 and 700 nanometres. The light falls on the front side placed at the back of the slit and the other side refract or separate the light into it component red, yellow and blue light. The diffraction grating is shown in fig. 7.12 as follows;

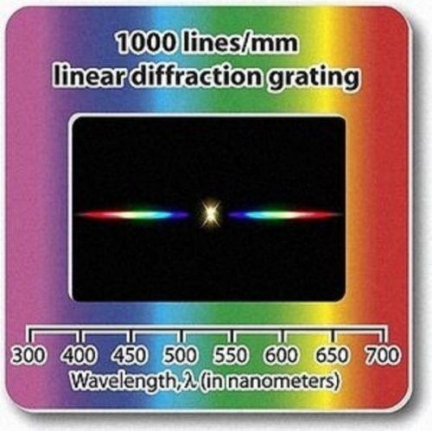

Figure 7.12 A linear diffraction grating with 1000 lines/mm and a measurement range of between 300 and 700 nm

7.4.3 Spectrometer enclosure

The is cardboard box of 25×20×2cm dimension. The front side of the box contains the slit and the back side holds the linear diffraction grating. The front side faces the visible light while the backside is used to acquire the spectrum of any visible light. The camera lens is used to at the centre of the diffraction grating.

7.4.4 CMOS mobile camera

The camera is the sensor or measurement unit for measuring the spectra of the light. The requirement for quantitative measurements, camera should be manually controlled and focus, short exposure time and white balance. Virtually any modern mobile phones have a CMOS sensor for digitizing spectrum images.

7.4.5 Learnlight acquisition and analysis software

The learnlight software is a mobile and a desktop application for analysis of visible light spectrum. It provides a means of comparing sample spectrum acquired from a camera and the reference in the software database to plot intensity, transmittance and absorbance of their visible wavelength. The mobile Android application comes with an extra email screen shoot image capture and email csv files for Excel (or any other spreadsheet software).

7.5 The flowmeter piping subsystem

The flowmeter piping consists of flowmeter, flow sensor, flow solenoid valve pipe connectors and pipe tape seal. The heat transfer fluid in the cold overhead tank flow down through the flow sensor and the fluid is actuated through and open and close means of the solenoid valve. The flow controller is used to select the flow rate and the run button is used to state the flow of the heat transfer fluid. The components of the flowmeter are shown as follows in figure 7.13 as follows;

Figure 7.13 Flowmeter and piping subsystem components installation; (a) ZJ-LCM digital display flow controller with buttons and numeric; (b) Sabocn water flow sensor with Molex connector to the flow meter; (c) solenoid valve for turning-on and turning-off flow;(d) connection of flow meter, flow sensor and solenoid valve;(e) connection of flow meter, flow sensor, solenoid valve and piping from the top storage tank and to the receiver inlet

7.6 Parabolic trough receiver subsystems

7.6.1 Trough mirror subsystem

The trough subsystem consists of 5 parabola profile rails, 2 end rails, 2 trough target support, and 1 aluminium frame pipe. The primary function of the parabolic trough mirror system is to focus and concentrate the light from the sun onto the receiver subsystem.

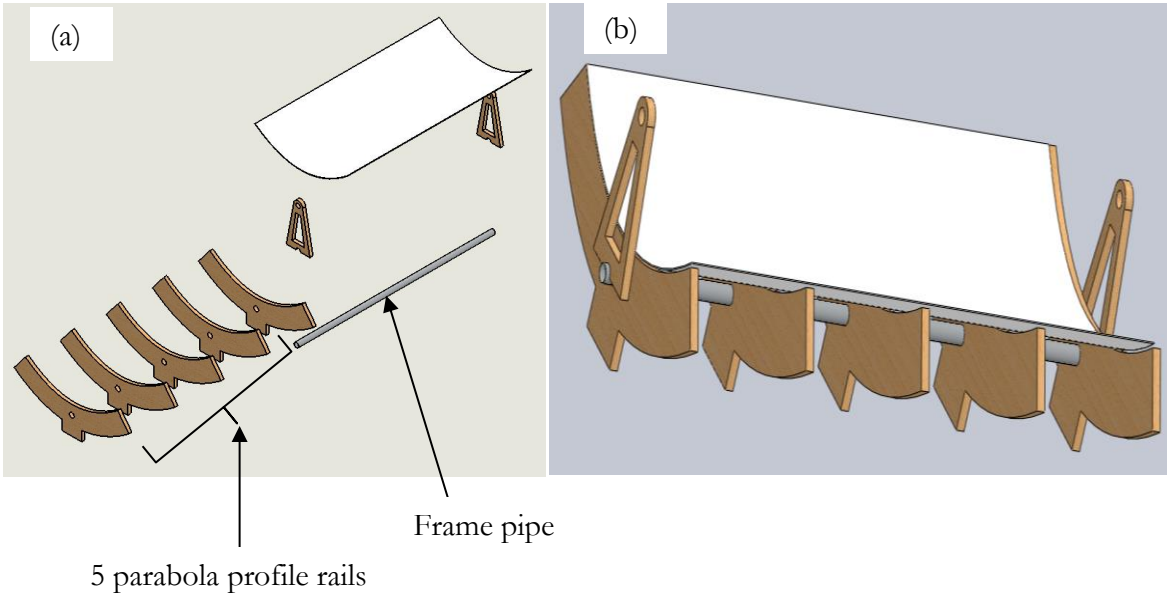

Figure 7.14 (a)An exploded view of the parabolic trough mirror and (b) the assembly view of the subsystem

7.6.2 Receiver PVT subsystem

The receiver subsystem consists of sandwiches of half glass cover, an EVA film, a thin film solar photovoltaic module, EVA film, a Tedlar backsheets, a half copper tube a heat transfer fluid and a copper plate cover. The function of the receiver PVT subsystem is to produce electricity and heat from the thin film module and as the heat transfer fluid flow through the copper tube and remove the heat from the stainless steel back of the module.

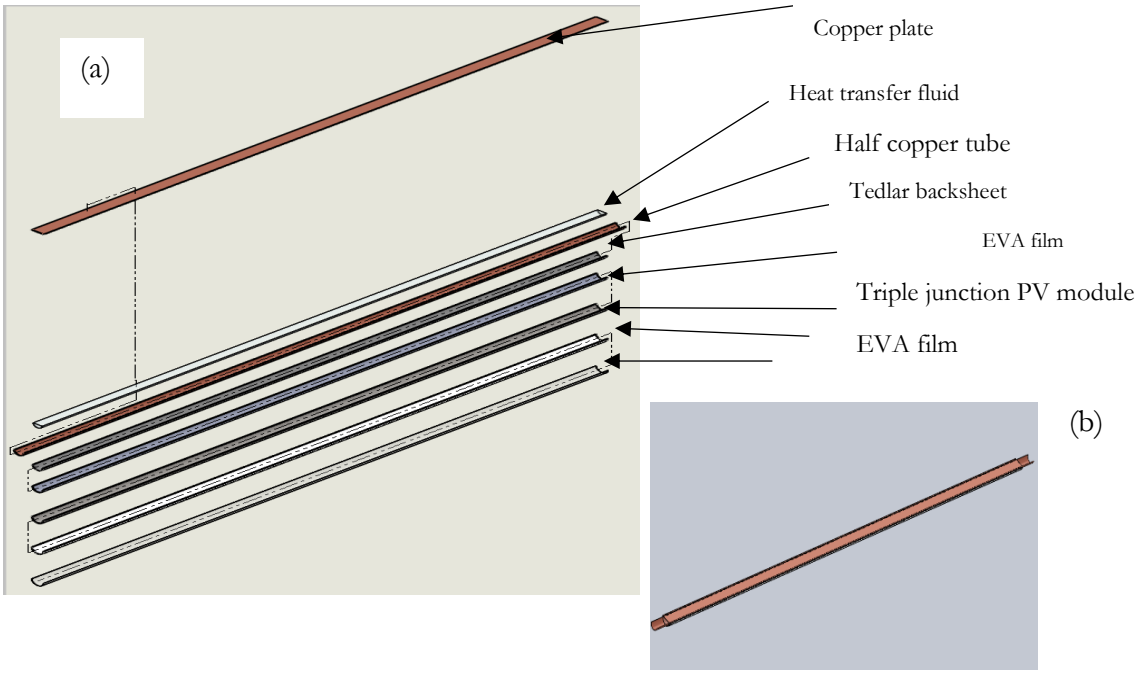

Figure 7.15 (a) An exploded view of the receiver PVT and the (b) the assembly view of the receiver PVT subsystem

7.6.3 4 bar Link mechanism subsystem

The link mechanism in fig.7.16 consists of 2 frame, a crank, a rocker and a connector. The 4 bar link machine mechanism functions as motion transformer with a specific objective of translating the linear motion of a linear actuator to the rotary motion of the parabolic trough PVT system to follow that azimuth path of the sun, with a mechanical advantage. There are variant of the four bar link mechanism, the Evans linkage design was adopted for the study as the crank goes through a complete rotation, as a result most suitable as input connection to the drive system and the parabolic trough PVT receiver system.

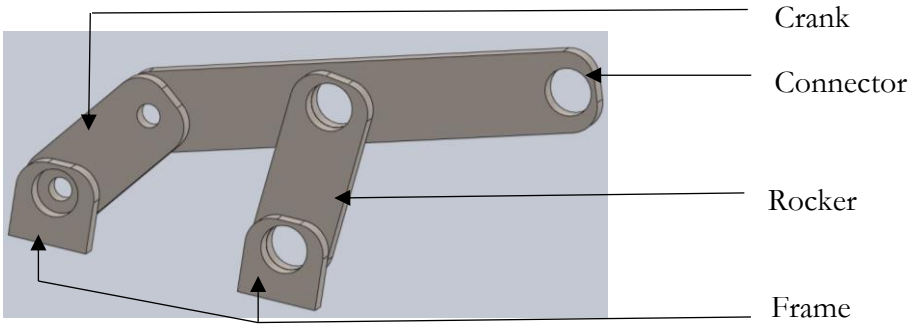

Figure 7.16 Four bar link mechanism with 2 fixed frame, a crank, rocker and a connector. It is an Evans four link variants of the four-bar link mechanism

7.6.4 Complete trough PVT system

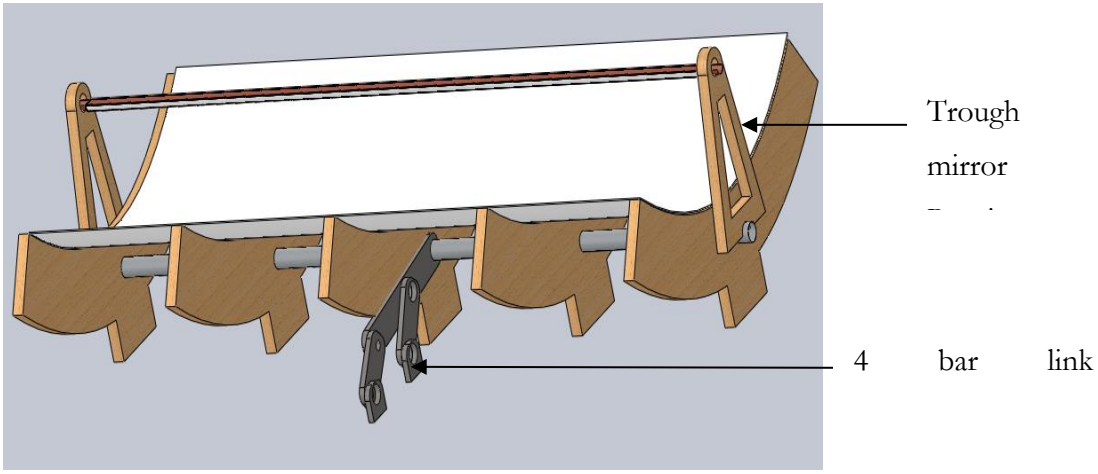

Figure 7.17 A 3D native CAD model of the parabolic trough mirror PVT and the four bar link mechanism, realised in solidworks

7.7 Preparation of graphene Nanofluids

The synthesis of the Nanofluid involves preparation of graphene oxide, reduction of graphene oxide to graphene, sonication of graphene in solvent and stabilisation of Nanofluid with gum Arabic amphoteric surfactant.

7.7.1 Preparation of graphene oxide

The modified Hummers method called the Tour method was used in synthesis of graphene oxide.

Materials

Micronized graphite, Potassium Permanganate, 98% H_2SO_4, 85% H_3PO_4, 35% Hydrogen Peroxide (H_2O_2), Deionised ice water, Ethanol, Kern balance, IKA heater stirrer, Thermo scientific centrifuge, Fisher scientific bath sonicator, Thermo scientific probe sonicator, an analytical high precision weighing balance and 3 600 mL beaker.

7.7.2 Experimental procedure

3g of micronized graphite was measure and pour into a 600 mL capacity beaker. Using the same beaker, 18g of $KMnO_4$ was weighed and mixed with the 3g of the micronized graphite. A mixture of 360mL of 98% H_2SO_4 and 40mL of 85% H_3PO_4 prepared in another 600mL beaker and poured into the first beaker containing 3g of micronized graphite powder and 18g of Potassium Permanganate. A green solution was formed after pouring the acid into the mixture of micronized graphite and potassium permanganate. The green mixture was place on a mixer stirrer at 50^0C, at a speed of 700 mot/min. The mixture was stirred for 17

hours to complete the reaction. The mixture was allowed to cool to room temperature and poured over a 400 mL deionised iced water. To complete the reaction, 6 mL of hydrogen peroxide was added to the mixture to obtain a bright yellow mixture of graphene oxide. The mixture for left to settle for about 2 weeks and washed with tap water twice. The mixture was sifted through a metal 300-micron sieve and then filtered through polyester fibre. The filtrate was centrifuged using the centrifuge in Fig.18 (c) at 8000 rpm for 2 h, and the supernatant was decanted away. The remaining solid material was then washed in succession with 200 mL of water, 200 mL of 30% Hydrochloric acid, and 200 mL of ethanol twice for each wash, the mixture was filtered through sieve and then filtered through polyester fibre with the filtrate being centrifuged (8000 rpm for 2 h) and the supernatant decanted away. The supernatant was allowed to settle and the graphene oxide layer settles to the bottom the beaker and the water was gently poured away leaving the residue was poured into a glass bowl with large surface area. After 5 days, flakes of graphene oxide was obtained.

7.7.3 Reduction of graphene oxide

The graphene oxide produced above is soluble in deionised water when it is sonicated. The solution was reduced into graphene using environmentally benign approach of a mixture of ascorbic acid and 8.5% ammonia solution. A weighing val was gently placed in an analytical high precision balance after calibration. A spatula was used to gently add the graphene oxide flake until 217g was recorded on the balance. The graphene oxide was transfer into a 500 mL beaker and 400 mL of deionised water was added and stirred with a magnetic stirrer with a turbine and dispersed for 15 mins to obtained a golden solution of graphene oxide. 5g of ascorbic acid and 6 mL of 8% ammonia solution was added to the graphene oxide solution.

7.7.4 Sonication of graphene in solvent

The mixture of graphene oxide, ascorbic acid and ammonia was place in a sonicator for 2 hours and at a temperature of 35^0C to obtain a black solution of graphene. The solution obtained was label as graphene oxide in deionised water. The process of preparing the graphene in solution in Mono-ethylene glycol and Mono-propylene glycol was done taking the graphene solution from the reduction of graphene oxide and placing it on a magnetic stirrer and adding the 200 mL of the oil to the solution and transferring it back to a bath and probe sonicator in fig. 7.18 (a) and (b) for 2 h.

Figure 7.18 (a) A Fisher scientific bath sonicator with Nanofluids with 3/4 water level; (b) Probe sonicaor with control panel and graphene-MEG Nanofluid; (c) A Thermo scientific centrifuge with LCD display of rpm (8000), time (2 h) and operating temperature (25^0 C); (d) Centrifuge Vals tubes with sediment of graphene oxide on the walls; (e) Centrifuge bucket with Val and Counter-Val during loading of sample

7.7.5 Stabilisation of Nanofluid with gum Arabic

The Nanofluids obtained below in Fig.7.19(e) settles after 2 weeks, especially the oil based Nanofluids. The fluids are stabilised with gum Arabic. The Nanofluids were all stabilised with 0.01 mg of gum Arabic in 10 mL of deioned water and sonicated using a probe sonicator for 1 h. The solution gets very hot, as a result the solution was left to cool to room temperature at intervals of 15 mins. The Nano fluids obtained as shown in fig 7.19 a, b, c and d were stable for a long period. The stability of the observed after 2 weeks and presented as follows in figure 7.19;

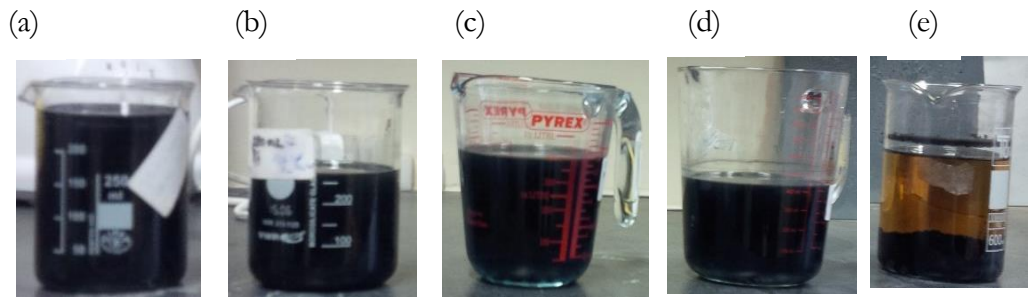

Figure 7.19 Graphene Nanofluids prepare using Tours Modified Hummers method and stabiliseb by 0.01mg/mL; (a) 0.1 mg/mL graphene-Monoethylene glycol (250 mL of MEG + 28 mg of graphene); (b) 0.1 mg/mL graphene-Mono propylene glycol (250 MPG + 28 mg graphene);(c) 0.1 mg/mL graphene-Deionised H_2O (500 mL of Deionised H_2O + 50 mg of graphene);(d) 0.1 mg/mL graphene-Monoethylene glycol-Deionised H_2O (200 of MEG + 300 of Deionised H_2O +28 mg of graphene);(e) 0.1 mg/mL of sedimented unstablised graphene-Monopropylene glycol-Deionised H_2O (200 of MEG + 300 of Deionised H_2O +28 mg of graphene) after 2 weeks

7.8 Summary and concluding remark

A detailed description of the experimental rig and the synthesis of Nanofluid was presented in this chapter. The trough and receiver subsystem 3D CAD model design in solidworks was presented. The Nanofluids prepared from physical examination indicate stability. The experimental rig is still a work in progress and still under development. The sun simulator shows very good performance with all the functions, day, night, thunderstorms showing good response during testing and measurement.

In conclusion, the rig is ready for taking measurement with the Nanofluid prepared and a detailed procedure for acquiring experimental data is presented in chapter 8.

Chapter 8 Experimental measurement and validation

8.1 Introduction

Sequel to the citations in review chapter, infrared thermography was identified to be the most viable method for investigating the temperature distributions in the receiver in the solar thermal plant. As a non-contact method that will eliminate the risk of exposing operators taking measurement and routine maintenance to exposure of concentrated solar radiation containing high infrared and ultraviolet rays. The measurement of thermal signature temperature of the heat transfer fluid using non-contact computer infrared thermometry is still new and emerging field. The classical approach prior to this study was to use thermocouples and this rather not efficient and prone to measurement error. Currently, there are limited report of application of IR thermometry in measuring temperature for carbon based Nanofluid for investigating boiling heat transfer reported by Moo et al., (2014). In this chapter, infrared thermography was applied in studying the thermal temperature distribution for water, and graphene carbon based Nanofluid prepared in chapter 9. The results obtained is used to validate the computational results obtained in the previous chapters

8.2 Research approach and methodology

The research method are experimental infrared thermography and optical spectrometry. The details of both methods are detailed as follows;

8.2.1 Experimental infrared thermometry

The infrared electromagnetic radiation is converted to temperature after scanning the object and condensing the signal. The signal is usually weak as a result it is conditioned or amplified with power electronics transistors. The amplified image is converted into colour map of the object in a visual display unit. The display image is constantly scanned by synchronising the acquired image with the incoming image calibrating the input and the output image. Thermal image data acquired is transferred to a PC through high speed Gigabit Ethernet interface. Thermal image is a coloured up pixel by pixel based on temperature map. The fig. 8.1 illustrate the working principle of infrared thermometry and fig. 8.2 shows the operating range of the infrared temperature spectrum.

8.2.2 Experimental optical spectrometry

In fig. 8.3, the light source passes through the monochrometer and through the narrow slit and finally through the beam splitter. The beam splitter separates the light into its constituent's colours. A sample of known spectrogram is compared with the unknown light before hitting the detector which is usually a Charge Couple Device (CCD) or

Complementary Metal Oxide Semiconductor (CMOS) sensor. The image of the spectrum is display of visual display unit.

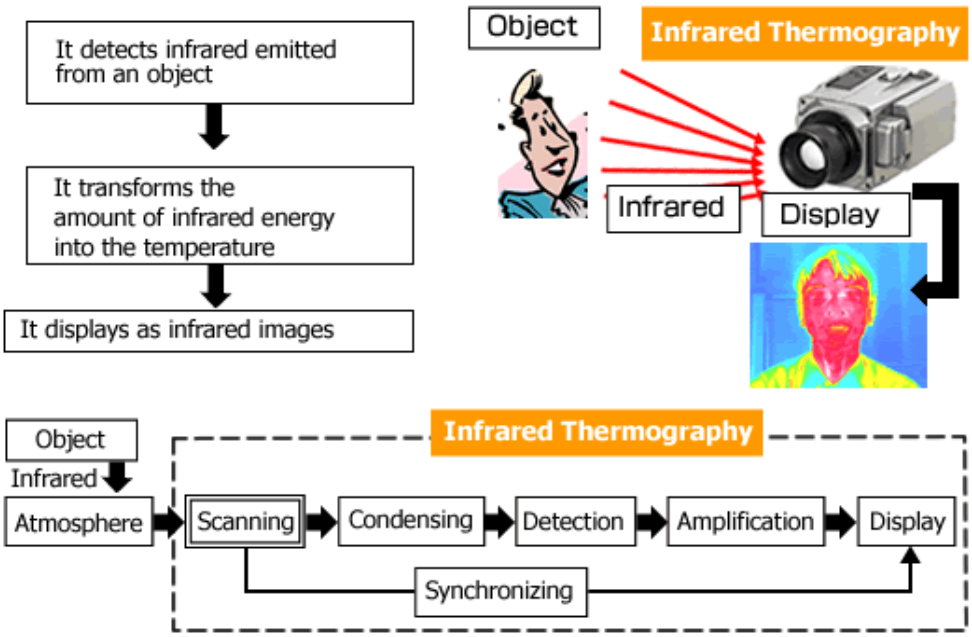

Figure 8.1 Working principle of infrared thermography from object infrared radiation emission sensing or detection to display of the image with the colour temperature map (Nippon Avionics, 2016)

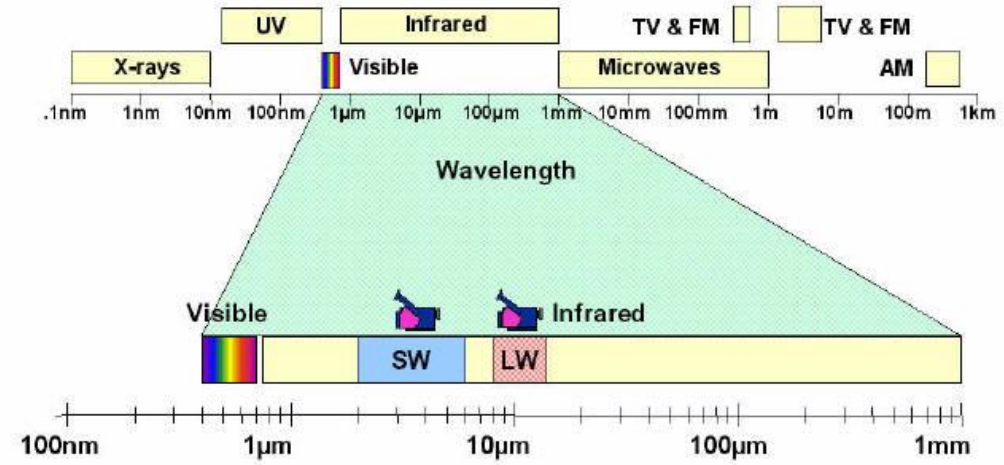

Figure 8.2 Part of the electromagnetic spectrum measured by infrared camera (Lowe, 2008)

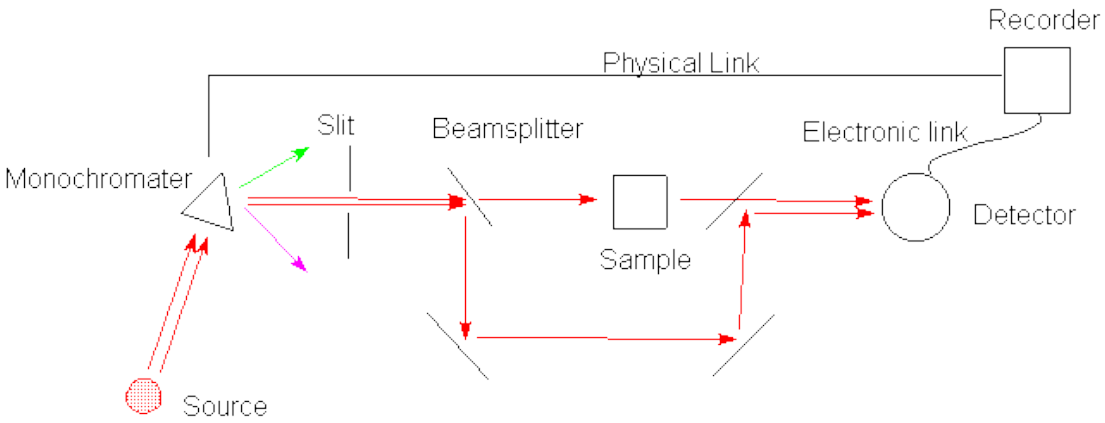

Figure 8.3 Working principle of visible light spectroscope (Gable, 2013)

8.3 Experimental setup

The setup consists of the LED sun simulator, the parabolic trough mirror receiver system, top cold graphene Nanofluid and water tank, bottom collecting tank, the pump, flow sensor, flow meter, solenoid valve, the FLIR IR camera and research IR data processing and computer data acquisition software. The setup is presented in fig. 4a and 4b as follows;

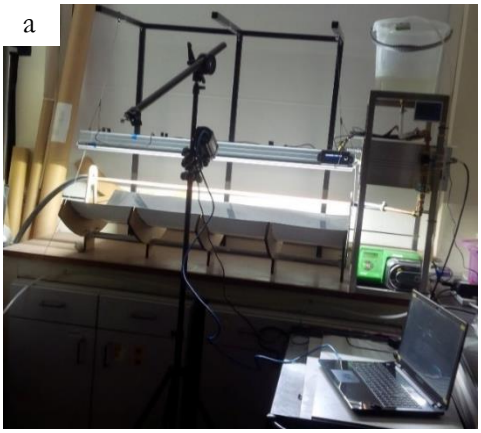

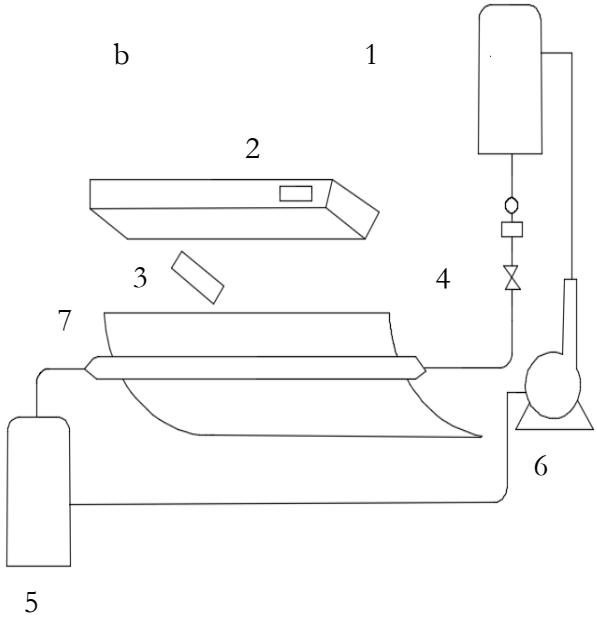

1. Cold tank 2. sun simulator

3. IR camera 4. Mirror parabolic trough

Figure 8.4 (a) Pictorial installation of the IR thermometry setup; (b) a schematic view of the experimental apparatus and instrumentation

8.4 Infrared camera setup, calibration and focusing

The IR camera was setup with a flexible pod and a tripod to face the receiver and track the fluid as it flows from the cold water and graphene Nanofluid tank located on top. The liquid

flows by gravity through the flow sensor, the flow meter and finally through the solenoid valve to the inlet of the receiver. The temperature is measured by the Infrared camera the thermal signature is transferred to the FLIR research IR acquisition software. The live video is saved as a window media file, image as Jpeg, while the temperature signatures along the axial and radial length as line plot with the line tool and an average plot using the rectangle area plot tool. The calibration was done by clicking the calibration button in the research IR software. The same procedure was done for the focussing with the focus button. The image and the plot was acquired after a clear image is obtained.

Figure 8.5 FLIR 325sc infrared camera used for acquiring the thermogram, x-y plots and csv data exports; (a) front view of the camera in front and the point of connection to tripod by the side;(b) back view of the sowing the power connector screw terminal, Gigabit Ethernet port RJ-45 connector and the digital I/O screw terminal

8.5 Measurement of temperature and acquisition of thermal signature of IR image

The procedure for taking measurement was first by turning on the sun simulator and allowing it to heat-up for 10 minutes and selecting the day settings of the simulator. The IR camera was turn-on to track the temperature of the receiver without the heat transfer fluid. The flow controller was turn-on and the flow rate is measured based on the settings selected. The solenoid valve is opened and the fluid flow through the pipe to the receiver and the IR camera track and measure the temperature as the fluid is heated and flow along the length of the open channel flow receiver. The temperature was acquired as explained in the preceding section.

8.6 Measurement, calibration, and acquisition of LED simulator spectrum

The software user interface for spectrophotometer and calibration of the image of the spectrum acquired is presented in fig 8.6. Fig. 8.6(a) is a snapshot of the image capture with a camera phone with a CMOS sensor, with a narrow slit at the middle and the spectrum resolved into 2 on the far right and left. The image in 8.6 (b) and (c) are the calibrated measured spectrum of the white and royal blue CREE XT-E high power LEDs and the reference spectrum from the database of software, with a green line calibrating both images before post-processing. Fig. 8.6 (d) is the post-processing interface with tools for plots and exporting of image as MS excel csv file format for further post-processing in third-party software packages.

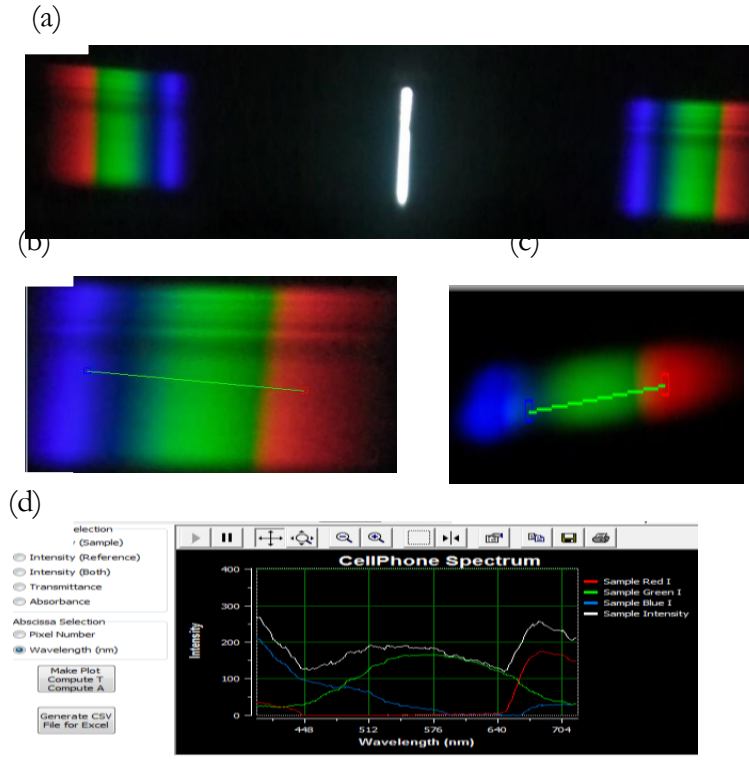

Figure 8.6 Software post-processing interface for analysing the spectrogram obtained from the spectrophotometer and a cell phone CMOS detector; (a) Spectrum image of the white light in channel 1 of the sun simulator obtained from a mobile phone camera showing the spectrum resolved into 2 image with the split in the middle; (b) is the simulator spectrum acquired with a mobile phone with a green calibration lines to match the red and blue colour of in (a);(c) is the reference image acquired from the database of the software with a green calibration lines to match the red and blue colour; (d) Plot options radio buttons, x-axis pixel number or wavelength options, make plot and csv fie export to Microsoft excel button and the plotting canvass

8.7 Importance and limitation of the research

8.8 Analysis and findings of experimental result obtained

8.8.1 Thermal signature measurement & axial and radial profiles

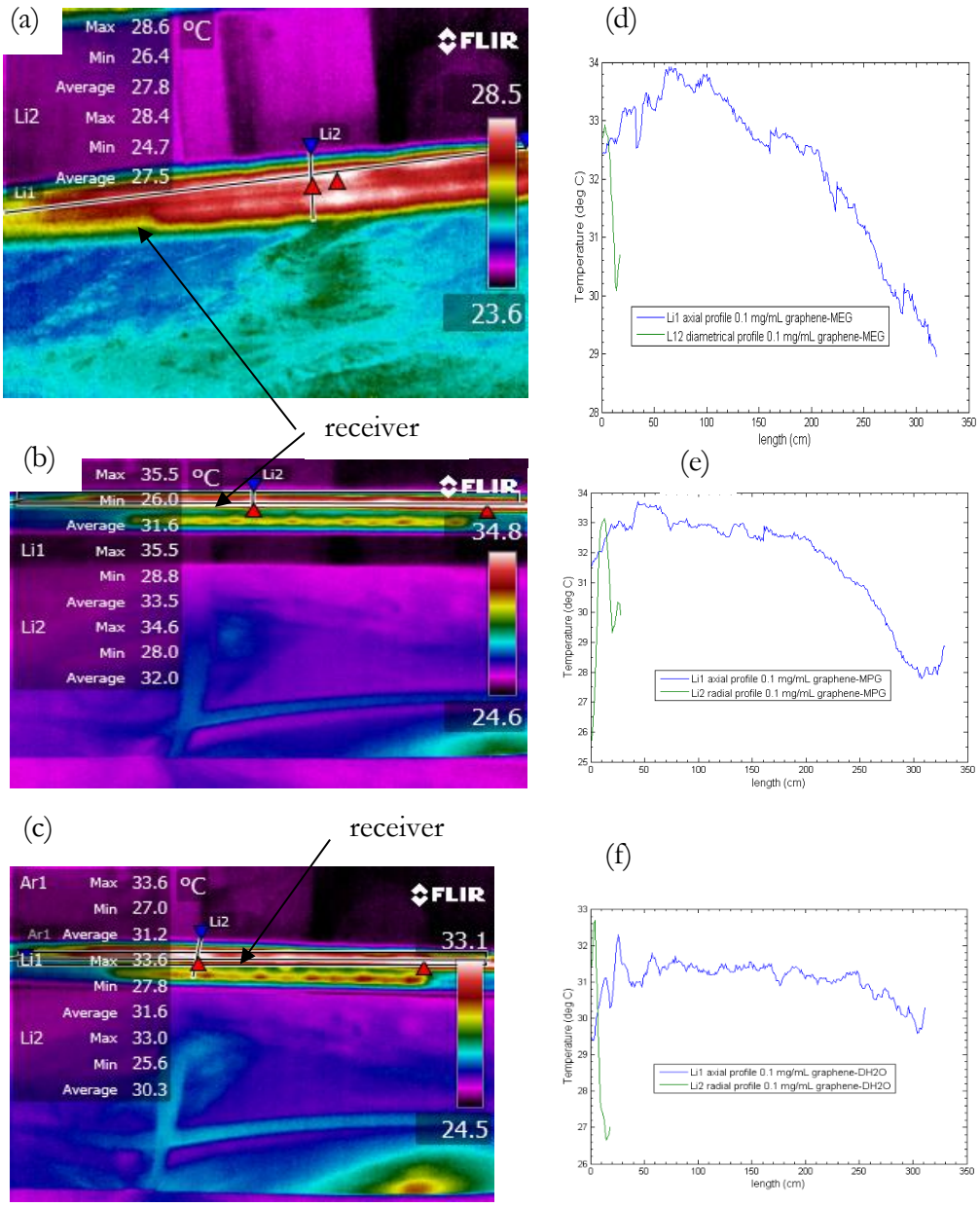

Figure 8.7 (a)Thermogram of 0.1 mg/mL graphene-MEG (250 mL Monoethylene glycol + 28mg graphene) of after 10 min of introducing Nanofluid into the receiver; (b)Thermogram of 0.1 mg/mL graphene-MPG (250 mL 28g of mono-propylene glycol); (c)Thermogram of 0.1 mg/mL graphene- DH_2O (50g of graphene + 500 mL mono-ethylene glycol after 10 mins of heating in the receiver; (d) 0.1 mg/mL graphene-MEG temperature profiles; (e) 0.1 mg/mL graphene-MPG temperature profiles;(f) 0.1 mg/mL graphene-DH_2O temperature profiles

In fig 8.7, the thermal signatures of sun simulator and the temperature profiles axially and radially represented by the blue and green lines respectively. The simulator was position at about 15 cm from the receiver containing the heat transfer fluids 0.1 mg/mL graphene-MEG (250 mL Monoethylene glycol + 28mg graphene), graphene-MPG and graphene-DH_2O. The fluid flows from the top by gravity through the flowmeter and piping and the infrared camera is focused on the receiver acquire the temperature profiles. In the thermogram (8.7 (a), (b) and (c)), Li1, Li2 and Ar1 represent lines drawn along the length, across the diameter and rectangle over the receiver with the line and rectangle tool in FLIR research IR software. The temperature profiles in fig. 8.7 d, e and f, indicate that the graphene-Monoethylene glycol outperforms graphene-Monopropylene glycol and graphene-deionised water Nanofluids.

8.8.2 Comparison plots of the 3 Nanofluids

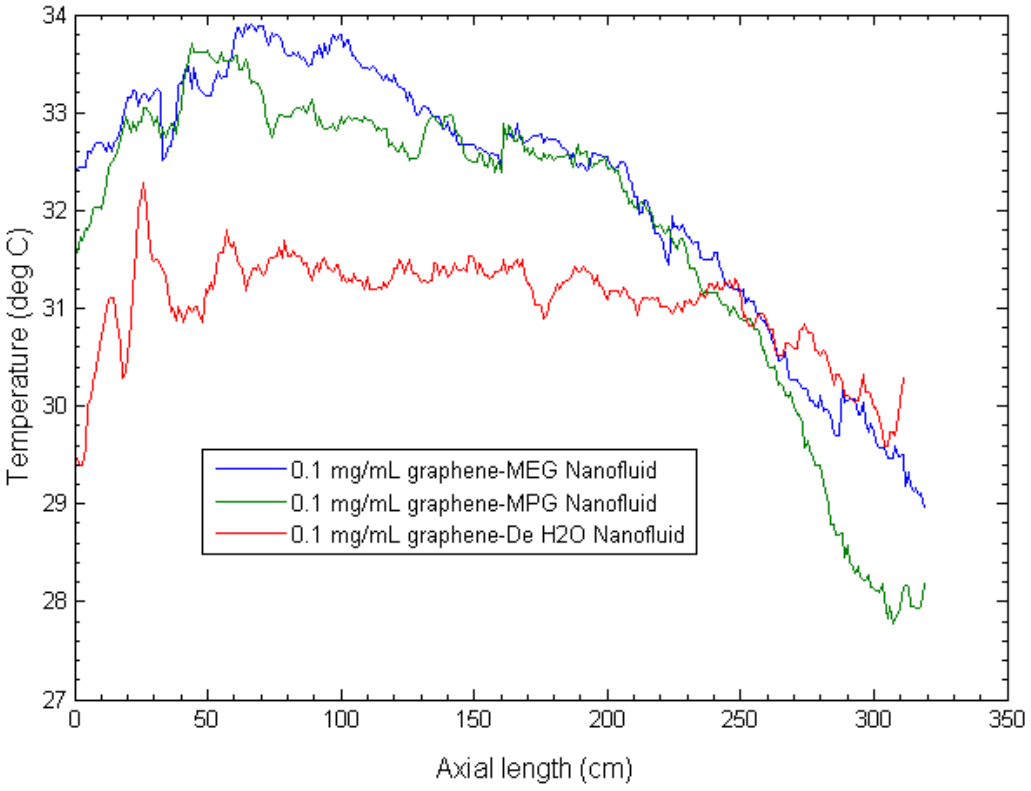

Figure 8.8 Infrared temperature thermal signature measurement along the axial length of the trough PVT receiver of 3 Nanofluids heat transfer fluids; 0.1 mg/mL of graphene 28 mg in 250 mL of Monoethylene glycol (MEG); 0.1 mg/mL of graphene 28 mg in 250 mL of Monopropylene glycol (MPG); 0.1 mg/mL of graphene 50 mg in 500 mL of Deionised water stabilized with 0.01 mg/mL of amphoteric gum Arabic solution

In fig 8.8, a comparison plot of the 3 Nanofluids graphene-MEG, graphene-MPG and graphene-DH_2O shows that there is a marked enhancement in solar absorption with the graphene-MEG and graphene-MPG compared to graphene-DH_2O. The enhancement in solar absorption is due to the thermal properties of Monoethylene and Monopropylene glycol as heat transfer fluids. Generally, the two fluids are the most widely used in process industries for transferring heat in process unit operations. It can also be deduce from the figure that graphene-MEG performance is slightly better than MPG. In comparison with water, the absorption of the solar radiation less than that of the graphene-MEG and graphene-MPG. This is because water is not a good heat transfer fluid. The graphene is also a major contributor to enhance solar absorption because of it high thermal conductivity and optical properties. The thermal properties of the overall heat transfer fluid is the combined properties of the base fluids and the graphene nanoparticles, usually estimated using empirical correlations. There is a deviation from the expected trend in the graphene-Monopropylene glycol in fig. 8.9, which could be as result of the noise introduced by drill during the measurements process. The graphene-Monoethylene and graphene-deionised water profiles follows the trends observed in axial profile in fig. 8.7.

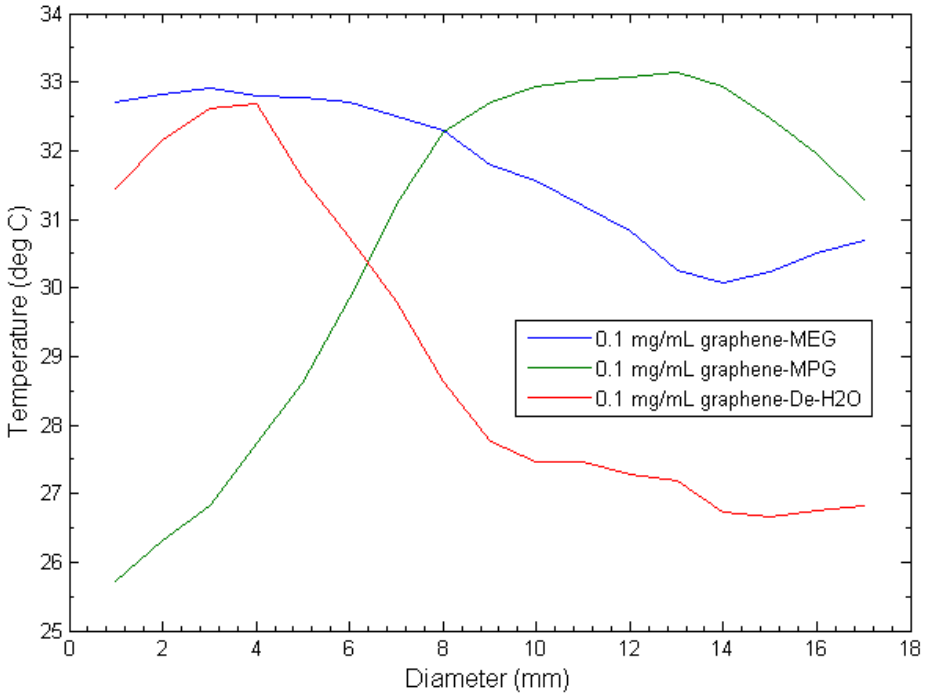

Figure 8.9 Infrared temperature thermal signature measurement along the diameter of the trough PVT receiver of 3 Nanofluids heat transfer fluids; 0.1 mg/mL of graphene 28 mg in 250 mL of Monoethylene glycol (MEG); 0.1 mg/mL of graphene 28 mg in 250 mL of Monopropylene glycol (MPG); 0.1 mg/mL of graphene 50 mg in 500 mL of Deionised water stabilized with 0.01 mg/mL of amphoteric gum Arabic solution

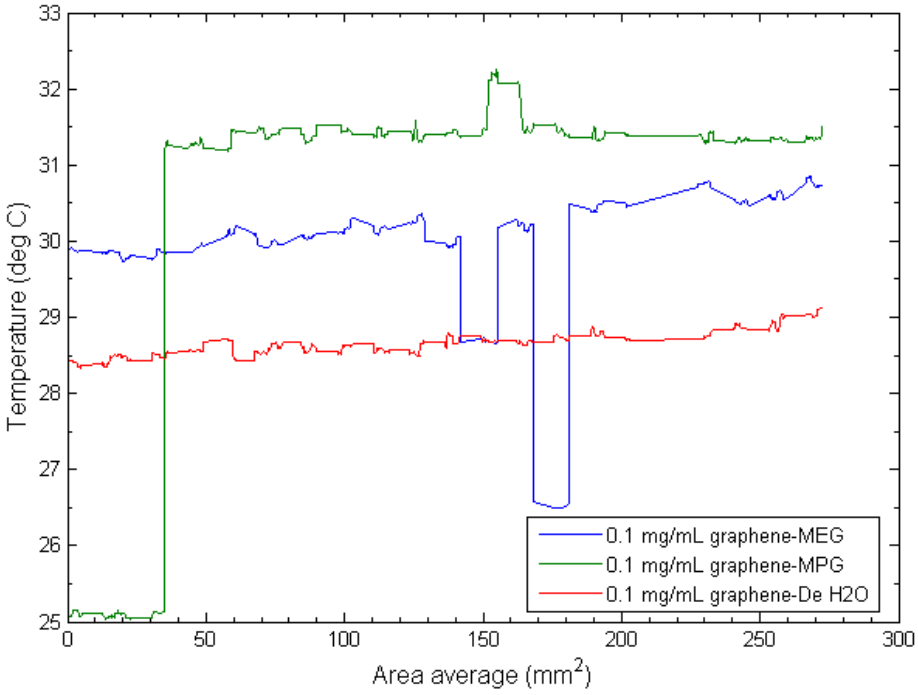

Figure 8.10 Infrared temperature thermal signature measurement of area average of the trough PVT receiver of 3 Nanofluids heat transfer fluids; 0.1 mg/mL of graphene 28 mg in 250 mL of Monoethylene glycol (MEG); 0.1 mg/mL of graphene 28 mg in 250 mL of Monopropylene glycol (MPG); 0.1 mg/mL of graphene 50 mg in 500 mL of Deionised water stabilized with 0.01 mg/mL of amphoteric gum Arabic solution

In fig. 8.10, an area plot using the rectangle tool was used to show the trend of the temperature about an area represented by the Ar1 in fig.8.7. The trends seem to favour the graphene-Monopropylene glycol as the best Nanofluid in absorbing the LED lights compared to graphene-Monoethylene glycol and graphene-deionised water Nanofluids. The diametrical profile surrounding noise introduce by the drill was responsible for the deviation from the expected trend. The infrared camera is very sensitive to background noise and may serve as source of measurement errors.

8.8.3 Sun and simulator spectrum matching

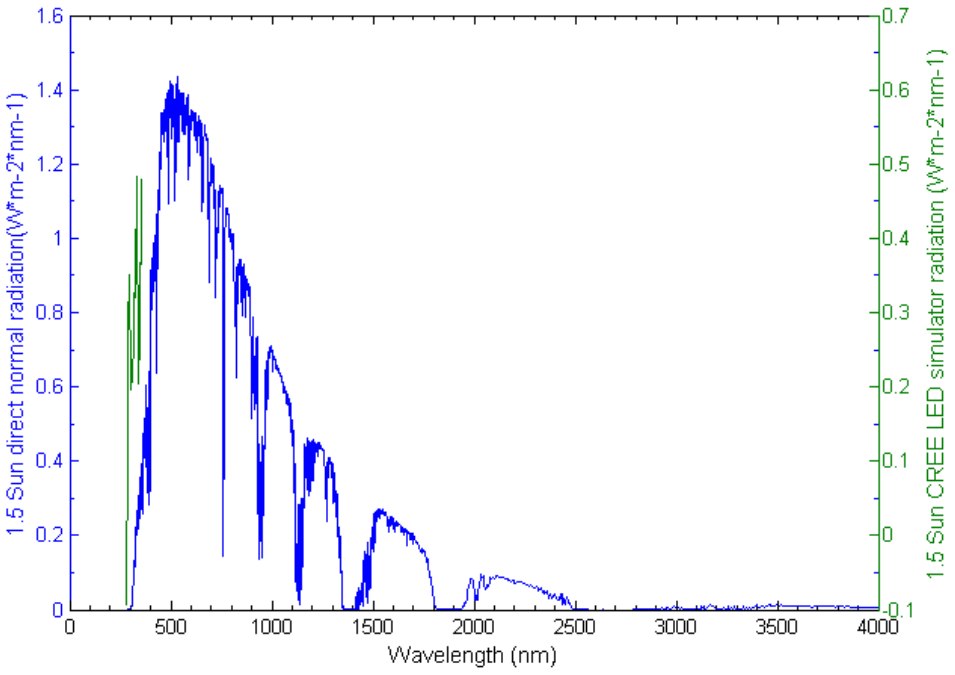

Figure 8.11 Spectral matching of the Sun direct normal radiation at 1.5 Air Mass in blue (1.5 AM ASTMG 173) and the spectrum of the CREE LED simulator radiation in green measured in the laboratory with fabricated Spectrum

Fig 8.11 is a spectral plot of the spectrum of the sun and that of royal-blue and cool-white Cree XT-E high power LEDs, juxtaposed on the same wavelength scale. It is a normal practice to benchmark a simulator with that of the sun. The extent of matching of the spectrum of the light source with the standard spectrum of the sun (AM1.5G) is an important parameter in quantifying the quality of the solar simulator. These important parameter is called Spectral Match (SM), one of the three parameters used in classification commercial solar simulators. The bands measure spectral matching is measured by dividing into six wavelength bands between 400 nm - 1100 nm region each of these contain a particular percentage of the total integrated irradiance as stipulated in ASTM E927 - 05. The spectral match is slightly outside the range of a class A solar simulator because the LED's were carefully selected as growing light but can still be class as A.

8.9 Validation of results obtained

In validating the results obtained from the shape optimisation studies investigated using conjugate heat transfer combined with inverse design optimisation, the thermal signature temperature measurement along the axial length of the receiver was compared with the numerical computation. The comparison was made using simulation with the receiver using Monopropylene glycol. In Fig.8.12 the trend between the predicted and the experimental

temperature profile shows that the predicted computational profile and the experimental follows the same trend up until 0.25 m along the axial length of the receiver. A different trend was become evident at receiver length greater than 0.3m with an over prediction of the axial temperature. The over prediction of the computational results compared to the experimental is that the fluid flow and heat transfer models for the laminar flow assumed ideal conditions such as smooth pipe roughness at the entrance of the pipe and at the walls. In the real experimental measurement, the pipes roughness at the entrance, wall and outlet are not ideal. Apart from the pipe properties, during measurement sensor noise interfere measurement data. From the result obtained, there is an over prediction of 2.2 % between the experimental and computational results. It is safe to say that within the limitation of 2.2% experimental error, the experimental and computational temperature profile show an agreement.

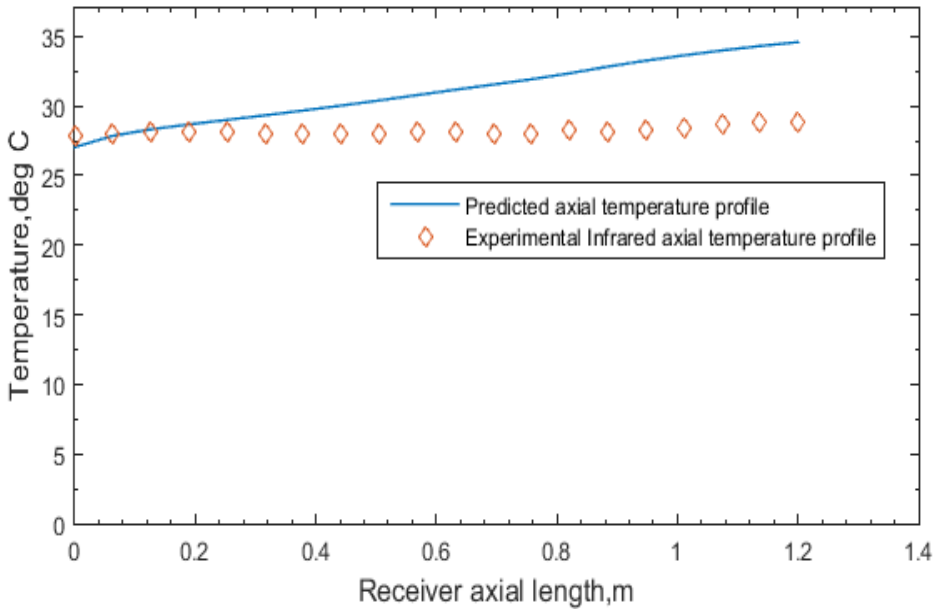

Figure 8.12 Validation of conjugate heat transfer computation against the infrared measurement obtained using FLIR IR 625 AC camera

8.10 Summary and concluding remark

In this chapter an infrared thermography measurement base methodology was used to measure and track temperature signatures of an open channel parabolic trough receiver. The Tours modified Hummers synthesis was used to synthesize Graphene-Monoethylene glycol, Graphene-Monopropylene glycol and Graphene-deionised water Nanofluid. A laboratory camera based spectrometry was used to measure spectrum of the Cree LED light of the simulator. The Nanofluid synthesise under the sun simulator shows that Graphene-Monoethylene glycol is better in absorbing solar radiation compared to Graphene-Monopropylene glycol. The trade-off is that Graphene-Monopropylene glycol is more

friendly than Graphene-Monoethylene glycol, hence the adoption of Graphene-Monopropylene glycol in the validation between the experimental and the computational temperature profile along the length of the receiver. The spectral matching of the sun simulator irradiance and that of the sun follows an air mass (AM) 1.5.

Conclusively, the experimental and computational temperature signature along the axial length of the receiver follows the same trend with an error margin of 2.2 %.

Chapter 9 Conclusions and scope for future research

9.1 Conclusions

A detailed research is performed successfully for sizing of hydrogen combined heat and power energy system to meet, electric, heat and cooling loads using design optimisation approach. The method is novel because of it machine learning statistical background. Also, an inverse design optimisation technique was applied for the first time in choosing the right shape that delivers the heat transfer requirement for solar receiver heat exchanger. A dynamical system analysis of the state space model of the subsystems in the hydrogen combined cooling heat and power system was realised, which revealed the internal structural behaviour of time evolution of each subsystem stability. It was clearly established through an optimisation based linear quadratic regulator control strategies. For the first time and unstable system was rendered stable by this advanced controller. Also, an experimental rig was fabricated from ground-up to study the characteristics of a receiver with nanoliquids synthesised and stabilised with noncontact temperature measurement techniques that is new in the solar thermal energy application. The three nanoliquids thermal signatures was for the time quantitatively measured and one of the nanoliquids performance validated with Multiphysics simulation. The major contributions are enumerated as follows;

In chapter 3, a hydrogen combined cooling and heating subsystems and components unit sizing model was develop. The systems were sized and met the electric, heating and cooling with the excess energy stored as long term hydrogen storage, medium term heat storage and short term battery storage. The model predicted short term storage of 4 hours during the day, 6 hours of heat between midnight and the early hours of the morning and can provide long term hydrogen storage for 5 days (115 h). The research questions based on hypothesis and proposed were addressed.

In chapter 4, two trough receiver shape (triangular and semi-circular) were proposed and the research question of the shape with a better performance with respect to multi-criteria optimisation was addressed. The triangular geometry was found to outperformed the semi-circular counterpart from a rigorous inverse design optimisation, statistical machine learning and robust Six sigma studies.

In chapter 5, a detailed dynamical analysis study of subsystems in the hydrogen combined cooling heat and power was investigated. The phase portrait, dimension reduction singular value decomposition (SVD), controllability and relative gain array (RGA) shows that all the subsystems except the electrolyser and battery were ill-defined with condition number well above 50, a threshold value for a well pose and defined system. All subsystems were unstable and controllable, hence the overall system can work together since they are controllable. The

outcome of the study addressed the research question of all subsystems in the energy system working together.

In chapter 6, a detailed system-of-system control of subsystem control architecture and strategies was defined and implemented in MATLAB, SIMULINK and control system toolbox. The unstable subsystems from the dynamical analysis studies in chapter 5, were all stabilised using infinite horizon multivariable model predictive linear quadratic regulator (LQR) control architecture. The LQR was able to place the poles on the left hand side of the complex plane optimally without violating the cost performance index function. A state space multivariable full controller was realised for all subsystems with system overshoot of 0%, settling and rise time of fraction of seconds for most subsystems. The control system revealed the multi-scale and multi-dimensional nature of the hydrogen combined cooling and heating energy system in the response time of each subsystem.

In chapter 7, a frugal engineering approach was used to fabricate from scratch the trough-mirror, sun simulator, piping system and preparation of Nanofluids for studying and validating the simulation analysis study in chapter 5. The sun simulator measurement was meet the expectation of standard laboratory instrument and can be classified as AM1.5 simulators. The Nanofluids prepared were stabilised using a green and environmentally benign amphoteric surfactant and the stability over a long period was impressive.

In chapter 8, a non-contact infrared computer thermography temperature measurement technique was applied to measure temperature signature of Nanofluids flowing through an open channel receiver. The thermal radiation absorption of Graphene-monoethylene glycol was best compared to the Graphene-monopropylene glycol and Graphene-deionised water Nanofluids.

9.2 Contributions of the Research

The contribution of this thesis to body of knowledge is divided into two categories: The contributions are highlighted as follows;

9.2.1 Primary Contributions

A hybrid tool based on enhanced deterministic and design optimisation for sizing a very daunting hydrogen combined cooling heat and power energy system was realised using model based design

A co-simulation analysis and model based design optimisation methodology algorithm is realised for selecting the best shape of a novel parabolic shape receiver

A dynamical modelling approach based on variable structure methodology was applied to analyse the system level behaviour of HCCHP system, an extension of the energy hub approach

A concept of system-of-system approach was applied for low level and supervisory level control of HCCHP was realised

An open channel flow full scale experimental model of a parabolic trough receiver shape for measuring Infrared temperature thermal signatures was realised

A sun simulator/emulator with full sun spectrum at 1.8 suns (1 sun= 1000 W/m2) was fabricated from ground with a very limited budget using system integration approach

A portable spectrometer was fabricated with low cost material and mobile phone CMOS sensor

A graphene based Nano fluid of monoethylene glycol, monopropylene glycol and water was synthesised for solar thermal radiation absorption was compared, monoethylene glycol shows a best performance

9.2.2 Derived Contributions

The derived contributions are in the modification the deterministic sizing algorithm to suite the sizing of HCCHP system. The algorithm was originally designed for wind turbine as the primary energy source whereas in the thesis, it was modified for solar thermal and solar PV as primary energy source.

The second derived contribution was an extension of the energy hub concept to include hydrogen in addition to the heat and electricity in the original energy hub concept.

9.3 Future outlook

The research has only scratch the surface considering the enormous research problem in model based system science, control and managing complex energy system-of-systems, solar thermal simulator, shape optimisation, carbon based Nanofluids and infrared thermometry for solar thermal applications. A new Vista of research opportunity for control of complex system and a basis for thermal solar parabolic trough temperature measurement have been provided. The lack of space and time limitation providing a much more detailed study, has prompted the following research directions;

- A hardware-in-the-loop rapid prototyping to test the LQR controller in chapter 6 on the mechanical tracking of the trough, using accelerometer, global positioning sensor, light dependent sensors, linear actuator direct current motor
- Model-based design of a system of cooperating set of parabolic trough receiver PVT system using a robotics cooperating algorithm to study, test and measure the effect of parabolic troughs weight, link mechanism, on motor size to established the optimum motor for particular numbers of troughs arranged in series and parallel
- Real-time deployment of embedded c code on a target real time electronic control unit (ECU) to measure and obtain voltage signals from input/output I/O port of the ECU real time target
- A real-time power hardware-in-the-loop of the distributed supervisory logic automation algorithm realised in chapter 7 on the entire hydrogen combined cooling heat and power system
- A detailed design of at least 500 suns using high power light emitting diodes of an automatic controlled solar thermal simulator to study the high temperature conditions of a parabolic trough with a thin film, multi-junction module and thermocells embedded in parabolic trough receiver for combined heat and power real time power and heating energy measurement and testing
- Design of heat, hydrogen and battery system for studying the transient during charge and discharge cycles
- Development of carbon based adsorption and absorbent materials for refrigeration and cooling
- A detailed dataacquision electrical and thermal load, and weather system for wind speed, solar radiation, humidity, residential and commercial carbon dioxide concentration measurement to forecast renewable resource availability
- A detailed Multiphysics study of the electrical, inverse kinematic, inverse dynamic, multiphase flow study of the parabolic trough PVT receiver system
- A study on the possible materials for 3D printing of the receiver with glass and PV modules and glass with PV modules
- Development of carbon and organic based battery and supercapacitor materials for energy storage applications

- A study on the switching characteristics of short time energy storage on long and medium energy storage during discharge and charge cycles at the system level using starter direct current motors
- A 3D Multiphysics and molecular simulation of carbon and organic based battery and supercapacitor materials for energy storage applications
- Plant simulation of parabolic troughs, Stirling engine and other power cycles to study and determine the best combinations for specific applications using ASPEN custom modeller
- Design, simulation, fabrication and development of Stirling engines for cooling and heating application in combined heat and power
- Development of advance electrolytic coating techniques for metals and non-metals for solar thermal energy storage applications
- Development of drones based infrared thermography for measurement and telemetry of solar thermal parabolic troughs power plants
- Development of library blocks toolbox for solar thermal unit operation subsystem using MATLAB and SIMULINK
- Development of 3d CAD models for horizontal and vertical axis wind turbine, Stirling engines with friction less magnetic levitation motion
- Development of high fidelity models of sensors, actuators, motor starters, bidirectional converters for energy storage and generation
- Matlab Simulink implementation of solar thermal generation and storage simulator for student and operator training
- Completion of data acquisition subsystem for the sun simulator
- Development of swarm robotics Drone approach for a system of cooperating drones to position and measure temperature and the flow fields using infrared thermography and particle image velocimetry of system of parabolic troughs
- Development of a high temperature thermocells using carbon based material
- Re-design of laboratory scale sun simulator spectrum analyser for characterisation and spectral uniformity and matching

List of References

Ackermann T, Andersson G, So¨ der L. Distributed generation: a definition. Electric Power Syst Res 2001; 57:195–204.

Angel Wind Energy. (2010). *Introducing our Proven line of turbines.* Available: http://www.angelwindenergy.com/aboutus.html. Last accessed June 2010.

Aguiar, A.B.M., Pinto, J.O.P., Andrea, C.Q., and Nogueira, L.A., 2007. Modelling and simulation of natural gas micro-turbine application for residential complex aiming technical and economical viability analysis. In: Electrical Power Conference, 25–26 October 2007 Montreal. IEEE, 376–381.

Akiki, H., Eng, C., & Avenue, T. (1998). A DECISION SUPPORT TECHNIQUE FOR THE DESIGN OF HYBRID SOLAR-WIND POWER SYSTEltlS, *13*(1), 76–83.

Alanne K, Saari A (Laboratory of Construction Economics and Management, Helsinki University of Technology). Sustainable small-scale CHP technologies for buildings: the basis for multi-perspective decision-making. Renew Sustain Energy Rev 2004; 8:401–31.

Alxneit I. & Dibowski G., R12.5 solar simulator evaluation report, PSI&DLR. August, 2011

Anand Giridharidas, Innovation without bells and whistles, International Herald Tribune, 10 April 2010, p.

Anderson B. D. O., Brinsmead T., Liberzon D., and Morse S., "Multiple model adaptive control with safe switching," International Journal of Adaptive Control and Signal Processing, vol. 15, pp. 445–470, 2001.

Åström, K.J. & Hägglund, T. (1995). *PID Controllers: Theory, Design, and Tuning (2nd Ed.).* Research Triangle Park, N.C.: International Society for Measurement and Control.

A Compilation of Summaries of the Papers Presented: NASA Conference on Thermal Radiation Problems in Space Technology, Langley Research Centre, 1960.

Alverbäck, A. (2012). LQG-control of a Vertical Axis Wind Turbine with Focus on Torsional Vibrations on torsional vibrations.

Arnold, R. D., & Wade, J. P. (2015). A definition of systems thinking: A systems approach. *Procedia Computer Science*, *44*(C), 669–678. https://doi.org/10.1016/j.procs.2015.03.050.

Bakule L., Decentralized control: an overview, Annual Reviews in Control 32 (2008) 87–98.

Bennett, C.L., 2008. Optimal heat collection element shapes for parabolic trough concentrators. *Journal of Solar Energy Engineering*, *130*(2), p.021008.

Bendt P., Rabi A., Gaul H.W., Reed K.A., "Optical Analysis and Optimization of Line Focus Solar Collectors", Solar Energy Research Institute report no. TR-34-092, (1979), especially see equation 2-18 on p. 11.

Barnett R. M., Thiele C., JPL Advanced Solar Simulator Design Type A, JPT Technical Memorandum No.33-141, 1963.

Barnett R. M. and Bartera R. E., Development of the Jet Propulsion Laboratory Solar Simulator, Type A, Technical Report 32-638, Jet Propulsion Laboratory, Pasadena, California, July 1964

Basic, S., Tools, S., & Planning, E. (2010). Some Basic Statistical Tools for Experiment Planning 8.1. *Statistics*, 355–386.

Bayón, R., Rojas, E., Valenzuela, L., Zarza, E., & León, J. (2010). Analysis of the experimental behaviour of a 100 kWth latent heat storage system for direct steam generation in solar thermal power plants. *Applied Thermal Engineering*, *30*(17–18), 2643–2651. https://doi.org/10.1016/j.applthermaleng.2010.07.011

Bazzi A. M., Klein Z., M. Sweeney, et al., Solid- State Solar Simulator, IEEE Transactions on Industry Applications, 48(2012), pp. 1195-1202.

Bernal-Agustin, J.L., and Dufo-Lopez, R., 2009a. Simulation and optimization of stand-alone hybrid renewable energy systems. Renewable and Sustainable Energy Reviews, 13 (8), 2111–2118.

Brandhorst H., Hickey J., Curtis H, Ralph E., Interim Solar Cell Testing Procedures for Terrestrial Applications, NASA TM X-71771, 1975.

Boait, P. J., & Rylatt, R. M. (2010). A method for fully automatic operation of domestic heating. *Energy and Buildings*, *42*(1), 11–16. https://doi.org/10.1016/j.enbuild.2009.07.005

Bosgra, O. H. (2002). Design Methods for Control Systems.

Brdys M.A., Grochowski M., Gminski T., Konarczak K., Drewa M., Hierarchical predictive control of integrated wastewater treatment systems, Control Engineering Practice 16 (2008) 751–767.

Brooks R.A, Elephants don't play chess. In P. Meas, editor, *Designing Autonomous Agents*. The MIT Press, Cambridge, Massachusetts, 1990.

Carek J., Space Power Facility for Testing Large Space Optical System, IEEE Aerospace Conference, 2006.

Casten TR. (WADE). The DG revolution—a second Indian miracle. 2004.

Chengzhang Z. CHP applications in US and Europe used for reference in China. Popular Utilization of Electricity 2003;2 (only in Chinese).

Codd D. S., Carlson A., Rees J., Slocum A. H., A Low Cost High Flux Solar Simulator, Solar Energy, 84(2010), pp. 2202-2212.

Canonsburg, T. D. (2013). Design Exploration User ' s Guide, *15317*(November), 724–746.

COGEN Europe (The European Association for the Promotion of Cogeneration, www.cogen.org). The European educational tool on cogeneration, 2nd ed. December 2001.

COGEN Europe (www.cogen.org). A guide to cogeneration. March 2001.

COGEN Europe (www.cogen.org). Decentralized generation technologies—potentials, success factors and impacts in the liberalized EU energy markets. Final report, October 2002.

Comsit M, Visa I. Design of the linkages type tracking mechanisms of the solar energy conversion systems by using multi body systems method. In: The 12th IFTOMM world congress; 2007.

Control System Toolbox For Use with M ATLAB. (1999). *Mathworks Inc.*

Cope D. S., Problems in the Construction of a Space Environment Simulator, NASA TN D-1917, 1964.

Cutler, C. R. & Ramaker, B. L. (1980). Dynamic matrix control—a computer control algorithm. *Joint Automatic Control Conference*. San Francisco, CA.

Daly, J.C., 1979. Solar concentrator flux distribution using backward tracing. Applied Optics 18 (15), 2696–2700.

Davison E.J., Ferguson I.J., The design of controllers for the multivariable robust servomechanism problem using parameter optimization methods, IEEE Transactions on Automatic Control 26 (1981) 93–110.

de Durana, J.M.G., and Barambones, O., 2009. Object oriented simulation of hybrid renewable energy systems focused on supervisor control. In: Proceedings of the 14th IEEE International Conference on Emerging Technologies & Factory Automation, 1–8.

Details, C. (2014). OpenAIR @ RGU The Open Access Institutional Repository at Robert Gordon University Sizing Hybrid Green Hydrogen Energy generation and Storage systems (HGHES) to enable an increase in renewable penetration for stabilising the grid.

Demiroren, A., and Yilmaz, U., 2010. Analysis of change in electric energy cost with using renewable energy sources in Go¨kceada, Turkey: an island example. Renewable and Sustainable Energy Reviews, 14 (1), 323–333.

Lesser Durfee V & E.H. Negotiating task decomposition and allocation using partial global planning. In L. Gasser and M. Huhns, editors, *Distributed Artificial Intelligence II*. Pitman Publishing, London, 1989.

EPA (www.epa.gov) Technology characterization: reciprocating engines. March 2002.

ERDA/NASA, Terrestrial Photovoltaic Measurement Procedures, NASA TM-73702, 1977.

Elliston, B., MacGill, I., & Diesendorf, M. (2013). Least cost 100% renewable electricity scenarios in the Australian National Electricity Market. *Energy Policy*, *59*, 270–282. https://doi.org/10.1016/j.enpol.2013.03.038.

Esteban, M., Zhang, Q., Utama, A., Tezuka, T., & Ishihara, K. N. (2010). Methodology to estimate the output of a dual solar–wind renewable energy system in Japan. *Energy Policy*, *38*(12), 7793–7802. https://doi.org/10.1016/j.enpol.2010.08.039

Elliston, B., MacGill, I., & Diesendorf, M. (2013). Least cost 100% renewable electricity scenarios in the Australian National Electricity Market. *Energy Policy*, *59*, 270–282. http://doi.org/10.1016/j.enpol.2013.03.038.

Ender, T.R., Murphy, J., and Haynes, C.L., 2010. A Framework for portfolio management of renewable hybrid energy sources. IEEE Systems Journal, 4 (3), 295–302.

Fazekas AI (Hungarian Power Companies Ltd.). Possibilities for The development of cogeneration in Hungary. 2004.

Ferber J. *Multi-agent Systems - An Introduction to Distributed Artificial Intelligence*. Addison-Wesley, Harlow, England, 1999.

Findeisen W., Bailey F.N., Brdys M., Malinowski K., Tatjewski P., Wozniak A., Control and Coordination in Hierarchical Systems, Wiley and Sons, 1980.

Franco E., Magni L, Parisini T., Polycarpou M., Raimondo D, Cooperative constrained control of distributed agents with nonlinear dynamics and delayed information exchange: a stabilizing receding-horizon approach, IEEE Transactions on Automatic Control 53 (2008) 324–338.

Gu, W., Wu, Z., Bo, R., Liu, W., Zhou, G., Chen, W., & Wu, Z. (2014). Modeling, planning and optimal energy management of combined cooling, heating and power microgrid: A review. *International Journal of Electrical Power and Energy Systems*, *54*, 26–37. http://doi.org/10.1016/j.ijepes.2013.06.028

Henten Van E.J., Bontsema J, Time-scale decomposition of an optimal control problem in greenhouse climate management, Control Engineering Practice 17(2009) 88–96.

Hangstrup M. E., Stoustrup J., Andersen P., and Pedersen T. S. "Gain-scheduled control of a fossil-fired power plant boiler," in Proc. of the 1999 IEEE International Conference on Control Applications, vol. 2, 1999, pp. 905–909.

Kaikko, J., and Backman, J., 2007. Technical and economic performance analysis for a microturbine in combined heat and power generation. 18th International Conference on Efficiency, Cost, Optimization, Simulation, and Environmental Impact of Energy Systems, 32 (4), 378–387.

Komor, P., & Glassmaire, J. (2012). Electricity Storage and Renewables for Island Power, (May), 48.

Kamjoo, A., Maheri, A., Putrus, G.A. and Dizqah, A.M., 2012. Optimal sizing of grid-connected hybrid wind-PV systems with battery bank storage. In *Proc. World Renewable Energy Forum*.

Keviczky T., Borrelli F., Balas G.J., Hierarchical design of decentralized receding horizon controllers for decoupled systems, in: Proceedings of the 43th IEEE Conference on Decision and Control, Atlantis, USA, 2004, pp. 1592–11597.

Keviczky T., Borrelli F., Balas G.J, Decentralized receding-horizon control of large-scale dynamically decoupled systems, Automatica 42 (2006) 2015–2115.

Laitner J (US EPA), Parks W (US DOE), Schilling J, Scheer R (Energetics, Inc.). Federal strategies to increase the implementation of combined heat and power technologies in the United States. 2000.

Lemar P, Honton EJ (Resource Dynamics Corporation). High natural gas prices and the updated market for CHP world energy engineering congress. September 2004.

Lund, H., 2007a. Renewable energy strategies for sustainable development. Energy, 32 (6), 912–919.

Lund, H., Duic, N., Krajac˘ic, G., and Carvalho, M., 2007b. Two energy system analysis models: a comparison of methodologies and results. Energy, 32 (6), 948–954.

Lunze J, Feedback Control of Large Scale Systems, Prentice-Hall, 1992.

Mesarovic M.D., Macko D., Takahara Y., Theory of Hierarchical Multilevel Systems, Academic Press, New York, 1970.

Mazhari, E.M., et al., 2009. Hybrid simulation and optimization based capacity planner for integrated photovoltaic generation with storage units. In: Proceedings of the 2009 Winter Simulation Conference, 1511–1522.

Mitigation, C. C. (2011). IPCC special report on renewable energy sources and climate change mitigation.

PBS. (20 April 2011). *Power surge.* Available: http://www.pbs.org/wgbh/nova/tech/power-surge.html. Last accessed 21 Jan 2016.

Glöckner R, et al.., *Market Potential Analysis for Introduction of Hydrogen Energy Technology in Stand-Alone Power Systems. Final report, EU/ALTENER Programme. Contract No. 4.1030/Z/01-101/200*. 2004, Institute for Energy Technology, Kjeller, NO-2027, 2004.

Tables for Reference Solar Spectral Irradiances: Direct Normal and Hemispherical on 37° Tilted Surface, ASTM standard G173-03, 1992.

Uguccini O. W., Pollack J. L., A Carbon-arc Solar Simulator, Paper 62-WA-241, ASME, 1962.

Wu, D. W., & Wang, R. Z. (2006). Combined cooling, heating and power: A review. *Progress in Energy and Combustion Science*, *32*, 459–495. http://doi.org/10.1016/j.pecs.2006.02.001

K. Gable. (2013). *FTIR Spectroscopy.* Available: http://chemistry.oregonstate.edu/courses/ch361-464/ch362/irinstrs.htm. Last accessed 26th Jan 2013.

Nippon Avionics. (2016). Infrared Thermography. Available: http://www.infrared.avio.co.jp/en/products/ir-thermo/what-thermo.html. Last accessed June 2015.

Steve Lowe. (2008). *A PRIMER ON INFRA-RED THERMOGRAPHY*. Available: http://www.thermalcities.com/HOWITWORKS.htm. Last accessed 2008.

Duffie, J., & Beckman, W. (2006). *Solar Engineering of Thermal Processes, 3th ed. Journal of Solar Energy Engineering* (Vol. 116). http://doi.org/10.1115/1.2930068

LED supply. (2016). *LED kits.* Available: http://www.ledsupply.com/led-kits. Last accessed July 2016.

Mrinalini, C. P. (2014). LED Based Solar Simulator. *Ieee*, 1–6.

James Lamont, The Age of Indovation Dawns," Financial Times, 15 June, 2010

Fidelity Implementation Study Group Report "SISO-REF-002-1999:". Simulation Interoperability Standards Organization. 1999. Retrieved January 2, 2015.

Gambier, A. (2011). Control of a Reverse Osmosis plant by using a robust PID design based on multi-objective optimization. *50th IEEE Conference on Decision and Control and European Control Conference (CDC-ECC)*, Orlando, FL, 7045–7050.

Gerro Prinsloo, Robert Dobson (August 2014). *Solar Tracking*. South Africa: University, Stellenbosch. p137-156.

Hays, R. T.; Singer, M. J. (1989*). Simulation fidelity in training system design:* Bridging the gap between reality and training. Springer-Verlag.

Lagunas-Jimenez, J. R., Moo-Yam, V., & Ortiz-Moctezuma, **B**. (2014). Two-degrees-of-freedom robust PID controllers tuning via a multiobjective genetic algorithm. *Computacion Y Sistemas*, *18*(2), 259–273. http://doi.org/10.13053/CyS-18-2-2014-031

Mathworks, C. (2016). Simscape ™ User ' s Guide R 2016 a.

Mathworks. (2015). MATLAB User ' s Guide R 2015 b.

Mathworks, C. (2016). Simscape ™ User's Guide R 2016 a.

Michael, K & Brett P. (2010). *Are Solar Thermal Power Plants Doomed?* Available: http://www.greentechmedia.com/articles/read/is-CSP-doomed. Last accessed October 18, 2010.

Naidoo P, Niekerk TIV, Brooks M. Intelligent control and tracking of a parabolic trough solar collector. First African Control Congress, University of Cape Town, Cape Town; 2003.

Splitt ME, Bahrmann CP. Detection of SIRS solar tracking problems with automated algorithms. In: The 9th ARM science team meeting; 1999.

Garcı´a, C. E. (1984). Quadratic dynamic matrix control of non-linear processes. An application to a batch reactor process. *AIChE Annual Meeting*. San Francisco.

Galiaev V. L., Large Space Chamber Environments Simulation for Solar Simulator Mirror Study, Proceedings of the Third International Symposium on Environmental Testing for Space Programmes, ESTEC, Noordwijk, The Netherlands, 1997.

Garg H. P., Shukla, et al A. R, Development of a Simple Low-Cost Solar Simulator for Indoor Collector Testing, Applied Energy, 21(1985), pp. 43-54. Feasibility Study: Development of a Solar Collector Certification Lab, Department of Mechanical Engineering, University of Minnesota, 2009.

Geidl M. and Andersson G. Optimal coupling of energy infrastructures. In Proceedings of PowerTech 2007, pages 1398–1403, Lausanne, Switzerland, July 2007.

Grimmer D. P., Bronisz L, Small-scale Solar Simulator for Indoor Testing of Collector Modules and Materials, International Solar Energy Society Meeting, Atlanta, Georgia, 1979.

Gorgun, H. (2006). Dynamic modelling of a proton exchange membrane (PEM) electrolyzer. *International Journal of Hydrogen Energy*, *31*(1), 29–38. https://doi.org/10.1016/j.ijhydene.2005.04.001

Gu, Q., Ren, H., Gao, W., & Ren, J. (2012). Integrated assessment of combined cooling heating and power systems under different design and management options for residential buildings in Shanghai. *Energy and Buildings*, *51*(March 2010), 143–152. https://doi.org/10.1016/j.enbuild.2012.04.023

Gu, W., Wu, Z., Bo, R., Liu, W., Zhou, G., Chen, W., & Wu, Z. (2014). Modeling, planning and optimal energy management of combined cooling, heating and power microgrid: A review. *International Journal of Electrical Power and Energy Systems*, *54*, 26–37. https://doi.org/10.1016/j.ijepes.2013.06.028

Hambsch, M. (2011). Photovoltaic systems thermography from the air using drones.

Hernandez, D., Olalde, G., Gineste, J. M., & Gueymard, C. (2004). Analysis and Experimental Results of Solar-Blind Temperature Measurements in Solar Furnaces. *Journal of Solar Energy Engineering*, *126*(1), 645. https://doi.org/10.1115/1.1636191

HK, V., & W, M. (1995). *An introduction to computational fluid dynamics* (Vol. M).

Hogan S. J., Status of IEC, ASTM, and IEEE Photovoltaic Standards, Solar Cells, 18(1986), pp. 327-333.

Hollingsworth R. T., A Survey of Large Space Chambers, Goddard Space Flight Center, NASA TN D-1673, 1963.

Ho K. T. K. & Loveday D. L., New Approach for Analyzing Solar Collectors Subjected to Unequal Front/Rear Ambient Temperatures: The Equivalent Ambient Temperature Concenpt, Part 2: Validation and Implications for Design, Journal of Solar Energy Engineering, 124(2002), pp. 268-275.

Hay J.E., Davies J.A., "Calculation of the Solar Radiation Incident on an Inclined Surface", Proceedings of the First Canadian Solar Radiation Workshop, pp. 59-72, 1980

Kenny S.P., Davidson J.H, Design of a Multiple-Lamp Large-Scale Solar Simulator, Journal of Solar Energy Engineering 116 (1994), pp.201-205.

Hatziargyriou, N., Asano, H., Iravani, R., and Marnay, C., 2007. Microgrids. Power and Energy Magazine, 5 (4), 78–94, IEEE.

Hirsch D., Zedtwitz P. V., Osinga, et al.T., A New 75kW High-Flux Solar Simulator for High-Temperature Thermal and Thermochemical Research, Journal of Solar Energy Engineering, 125(2003), pp. 117-129.

Hovd M., Skogestad S., Sequential design of decentralized controllers, Automatica 30 (1994) 1601–1607.

Hussain F., Othman M. Yatim, et al. Y. H, B., Fabrication and Irradiance Mapping of a Low Cost Solar Simulator for Indoor Testing of Solar Simulator for Indoor Testing of Solar Collector, Journal of Solar Energy Engineering, 133(2011), pp. 0445021-4.

Huang, W., Hu, P. and Chen, Z., 2012. Performance simulation of a parabolic trough solar collector. *Solar Energy*, *86*(2), pp.746-755.

IEA (International Energy Agency). Energy policies of IEA countries. Japan. 1999, review.

Iftar A., Decentralized estimation and control with overlapping input state and output decomposition, Automatica 29 (1993) 511–516.

Ikeda M., Siljak D.D., White D.E., Decentralized control with overlapping information sets, Journal of Optimization Theory and Application 34 (1981) 279–310.

Ikeda M., Siljak D.D., White D.E., An inclusion principle for dynamic systems, IEEE Transactions on Automatic Control AC-43 (1984) 1040–1055.

IIDE S., Sakazume N., Chikashi, et al C., 6M Diameter Space Simulation Chamber, Proceedings of the Third International Symposium on Environmental Testing for Space Programmes, ESTEC, Noordwijk, The Netherlands, 1997.

Jaber JO, Probert SD. Environmental impact assessment for the proposed oil-shale integrated tri-generation plant. Appl Energy 1999; 62:169–209.

Japan Cogeneration Centre (CGC). Current status and trends in Japan. 2003.

Jeter, S.M., 1986. The distribution of concentrated solar radiation in paraboloidal collectors. Journal of Energy Engineering 108 (1), 219–225.

Jennings N.R. and Wooldridge M., Eds., *Agent Technology: Foundations, Applications and Markets*. New York: Springer-Verlag, 1998.

Jiang, S., Hu, P., et al., 2010. Optical modelling for a two-stage parabolic trough concentrating photovoltaic/thermal system using spectral beam splitting technology. Solar Energy Materials & Solar Cells 94, 1686–1696.

Jieyi D. Development of gas-fired CHP projects in Japan. Int Electric Power China 2002; 6(4) (only in Chinese).

Johnson S. M. and Simon F. F., Evaluation of Flat-Plate Collector Efficiency under Controlled Conditions in a Solar Simulator, NASA TM X-73520, 1976.

Joseph EA, Roy-Aikins. Cogeneration in rural development. Energy 1995; 20(2): 95–104.

Kang, C. S., Park, J. Il, Park, M., & Baek, J. (2014). Novel modeling and control strategies for a HVAC system including carbon dioxide control. *Energies*, *7*(6), 3599–3617. https://doi.org/10.3390/en7063599

Kim, D. S., & Infante Ferreira, C. a. (2008). Solar refrigeration options - a state-of-the-art review. *International Journal of Refrigeration*, *31*(1), 3–15. https://doi.org/10.1016/j.ijrefrig.2007.07.011

Khambhampati C., Patton R. J., Casavola A., and Franze G., "Fault-tolerance as a key requirement for the control of modern systems," in Proceedings of the 6th IFAC Symposium on Fault Detection, Supervision and Safety of Technical Processes, 2006, pp. 26–36.

Komor, P., & Glassmaire, J. (2012). Electricity Storage and Renewables for Island Power, (May), 48.

Klucher T.M., "Evaluation of Models to Predict Insolation on Tilted Surfaces", Solar Energy, Vol. 44, pp. 111-114, 1979

Kolberg D., F. Schubert, N. Lontke, et al., Development of Tunable Close Match LED Solar Simulator with Extended Spectral Range to UV and IR, Energy Procedia,8(2011), pp. 100-105

Koutroulis, E., Kolokotsa, D., Potirakis, A., & Kalaitzakis, K. (2006). Methodology for optimal sizing of stand-alone photovoltaic/wind-generator systems using genetic algorithms. *Solar Energy*, *80*(9), 1072–1088. https://doi.org/10.1016/j.solener.2005.11.002.

Krusi P., Schmid R, Design of an inexpensive solar simulator, Technical Report, Department of Mech. Eng., University of Sydney, 1979.

Koronakis P.S., "On the Choice of the Angle of Tilt for South Facing Solar Collectors in the Athens Basin Area", Solar Energy, Vol. 36, No. 3, pp. 217-225, 1986

Krueger K. R., Davidson J. H, Lipiński W., Design of a New 45 kWe High-Flux Solar Simulator for High-Temperature Solar Thermal and Thermochemical Research, Journal of Solar Energy Engineering, 133 (2011), pp. 0110131-0110138.

Kuhn P. and Hunt A., A New Solar Simulator to Study High Temperature Solid-State Reactions with Highly Concentrated Radiation, Solar Energy Materials, 24(1991), pp.742-750.

Ley W., Survey of Solar Simulator Test Facilities and Initial Results of IEA Round Robin Tests Using Solar Simulators, DFVLR, 1979, Cologne.

Li, J., Wei, W., & Xiang, J. (2012). A Simple Sizing Algorithm for Stand-Alone PV/Wind/Battery Hybrid Microgrids. *Energies*, *5*(12), 5307–5323. https://doi.org/10.3390/en5125307 Pacific : Samoa. (2003), 1–4.

Liu B.Y. H., Jordan R. C. "Daily Insolation on Surfaces Tilted Towards the Equator", ASHRAE Journal, Vol. 3, pp. 53- 59, 1961.

Lo¨ ffler P. (COGEN Europe). Cogeneration in Europe: potentials, trends and EU policy responses. October 2002.

Marcano, D.C., Kosynkin, D.V., Berlin, J.M., Sinitskii, A., Sun, Z., Slesarev, A., Alemany, L.B., Lu, W. and Tour, J.M., 2010. Improved synthesis of graphene oxide. *ACS nano*, *4*(8), pp.4806-4814.

Michael, K & Brett P. (2010). *Are Solar Thermal Power Plants Doomed?* Available: http://www.greentechmedia.com/articles/read/is-CSP-doomed. Last accessed October 18, 2010.

Meng Q., Y. Wang, L. Zhang, Irradiance Characteristics and Optimization Design of a Large-Scale Solar Simulator, Solar Energy, 85(2011), pp. 1758-1767.

Minett S. (COGEN Europe). Micro-CHP needs specific treatment in the European directive on cogeneration. 2003.

Moon G. W., Cho H., Lee, et al.S. H., A Large Space Simulator (Φ8M X L10M) In Korea, Proceedings of the 5th International Symposium on Environmental Testing for Space Programmes, Noordwijk, Netherlands, 2004.

Mueller R. L., The Large Area Pulsed Solar Simulator (LAPSS), JPL Report, JPL Publication 93-22, 1993.

Navarro E, Diaz A. European network for the integration of renewables and distributed generation (the ENIRDGnet project partially supported by the European Commission under the 5th RTD Framework Program−Thematic priority: 'energy environment and sustainable development, under contract no ENK5-CT-2001-20528). 2004.

NASA No. NAS w-181 final report, NASA Space Environment Test Chamber and Solar Radiation Simulator, College of Engineering, The University of Rochester, 1961.

Nema, P., Nema, R.K., and Rangnekar, S., 2009. A current and future state of art development of hybrid energy system using wind and PV-solar: a review. Renewable and Sustainable Energy Reviews, 13 (8), 2096–2103.

Nwana H.S, Software agents: An overview. *Knowledge Engineering Review*, 11(3):1–40, September 1996a. Available athttp://www.labs.bt.com/projects/agents/publish/papers/agentreview.htm.

Tian Y. Q., R.J. Davies- Colley, P. Gong, B.W. Thorrold, "Estimating Solar Radiation on Slopes of Arbitrary Aspect", Agricultural and Forest Meteorology, Vol. 109, pp. 67- 74, 2001

Koronakis P.S., "On the Choice of the Angle of Tilt for South Facing Solar Collectors in the Athens Basin Area", Solar Energy, Vol. 36, No. 3, pp. 217- 225, 1986

Hay J.E., Davies J.A., "Calculation of the Solar Radiation Incident on an Inclined Surface", Proceedings of the First Canadian Solar Radiation Workshop, pp. 59- 72, 1980

Temps R.C., Coulson K.L., "Solar Radiation Incident upon Slopes of Different Orientations", Solar Energy, Vol. 19, pp. 179- 184, 1977

Klucher T.M., "Evaluation of Models to Predict Insolation on Tilted Surfaces", Solar Energy, Vol. 44, pp. 111- 114, 1979.

Lee W. S., Anderson B. D. O., Mareels I. M. Y., and Kosut R. L., "Onsome key issues in the windsurfer approach to adaptive robust control," Automatica, vol. 31, no. 11, pp. 1619–1636, 1995.

Patton R. J., Khambhampati C., and Uppal F. J., "Reconfiguration in networked control systems: fault tolerant control and plug-and-play," in Proceedings of the 6th IFAC Symposium on Fault Detection, Supervision and Safety of Technical Processes, 2006, pp. 151–156.

Perez R., Ineichen P., R. Seals, "Modelling Daylight Availability and Irradiance Components from Direct and Global Irradiance", Solar Energy, Vol. 44, pp. 271- 289, 1990

Petrasch J., P. Coray, et al., A Novel 50 kW 11,000 Suns High-Flux Solar Simulator Based on an Array of Xenon Arc Lamps, Journal of Solar Energy Engineering, 129 (2007), pp. 405-411.

Rawlings J.B., Stewart B.T., Coordinating multiple optimization-based controllers: new opportunities and challenges, Journal of Process Control 18 (2008) 839–845.

Resource Dynamics Corporation. Cooling heating and power for industry a market assessment. August 2003.

Richalet, J., Rault, A., Testud, J. L., & Papon, J. (1978). Model predictive heuristic control: applications to industrial processes. *Automatica*, 14 (5), 413–428.

Russel S. and Norvig P, *Artificial Intelligence - a modern approach*. Prentice-Hall International, Inc., Englewood Cliffs, New Jersey, 1995.

Srikhirin P, E. a. (2001). A review of absorption refrigeration tehnologies. *Renewable and Susainable Energy Reviews*, *5*, 343–372.

Perez R., Ineichen P., Seals R., "Modelling Daylight Availability and Irradiance Components from Direct and Global Irradiance", Solar Energy,Vol. 44, pp. 271-289, 1990

Pfänder, M., Lüpfert, E., & Pistor, P. (2007). Infrared temperature measurements on solar trough absorber tubes. *Solar Energy*, *81*(5), 629–635. https://doi.org/10.1016/j.solener.2006.08.016

Petrasch J., Steinfeld A., A Novel High-Flux Solar Simulator Based on an Array of Xenon Arc Lamps- Optimization of the Ellipsoidal Reflector and Optical Configuration, 2005 International Solar Energy Conference, ISEC2005-76009, Orlando, 2005.

Pv, T., Treberspurg, M., & Djalili, M. (2011). New technical solutions for energy efficient buildings State of the Art Report Photovoltaic / Thermal Systems, (July).

Rantzer A., "On prize mechanisms in linear quadratic team theory," in Proceedings of the IEEE Conference on Decision and Control, 2007, pp. 1112–1116.

Reicher D (Texas New Energy Capital). CHP roadmap workshop five years into the challenge. September 2004.

Rotkowitz M. and Lall S., "A characterization of convex problems in decentralized control," IEEE Transactions on Automatic Control, vol. 50, no. 12, pp. 1984–1996, 2005.

Seeling-hochmuth, G. (1998). Optimisation of Hybrid Energy Systems Sizing and Operation of PV-Hybrid Systems for remote Area Power Supply- Results and Evaluation of a Rural Case Study, Proceedings of the 14th EU PV Solar Conference, Barcelona.

Sharafi, M., ElMekkawy, T. Y., & Bibeau, E. L. (2015). Optimal design of hybrid renewable energy systems in buildings with low to high renewable energy ratio. *Renewable Energy*, *83*, 1026-1042.

Simon F.F., Flat-Plate Solar-Collector Performance Evaluation with a Solar Simulator as a Basis for Collector Selection and Performance Prediction, NASA TMX-71793, 1975.

Simon F. F., Standardized Solar Simulator Tests of Flat Plate Solar Collectors, NASA TM X-71738, 1975.

Simon F. F., Status of the NASA-Lewis Flat-Plate Collector Tests with a Solar Simulator, NASA TM X-71658,1975.

Simon F. F., Buyco E. H., Outdoor Flat-Plate Collector Performance Prediction from Solar Simulator Test Data, NASA TM X-71707, 1975.

Smouse SM, et al. Promotion of biomass cogeneration with power export in the Indian sugar industry. Fuel Process Technol 1998; 54:227–47.

Solanki S. C., Dubey S., Tiwari A., Indoor Simulation and Testing of Photovoltaic Thermal (PV/T) Air Collectors, Applied Energy, 86(2009), pp. 2421-2428.

Song H., Franklin S., and Negatu A. A fuzzy subsumption softbot. *Proc. of the ISCA Int. Conf. on Intelligent Systems*, 1996. Reno Nevada.

Standard Specification for Solar Simulation for Photovoltaic Testing, ASTM standard E927-05,

2005.

Simon F. F., Flat-Plate Solar-Collector Performance Evaluation with a Solar Simulator as a Basis for Collector Selection and Performance Prediction, Solar Energy, 18(1976), pp. 451-466.

Siljak D.D., Decentralized Control of Complex Systems, Academic Press, Cambridge, 1991.

Siljak D.D., Decentralized control and computations: status and prospects, Annual Reviews in Control 20 (1996) 131–141.

Shipley AM, Neal Elliott R. (The American Council for an Energy-Efficient Economy). Distributed energy resources and combined heat and power: a declaration of terms. April 2000.

Sun H. J., Moo W. S., Fabrication and Thermal Optimization of LED Solar Cell Simulator, Current Applied Physics, 10 (2010), pp. 537-539.

Takagi, Y., Nishitani, Y., and Nakamaru, T., 1999. An absorption chiller model for HVAC SIMþ. Building Simulation, 6, 1259–1266.

Temps R.C., Coulson K.L., "Solar Radiation Incident upon Slopes of Different Orientations", Solar Energy, Vol. 19, pp. 179-184, 1977

Tian Y. Q., Davies-Colley R.J., P. Gong, Thorrold B.W., "Estimating Solar Radiation on Slopes of Arbitrary Aspect", Agricultural and Forest Meteorology, Vol. 109, pp. 67-74, 2001

Tschudi, H. R., & Morian, G. (2001). Pyrometric Temperature Measurements in Solar Furnaces. *Journal of Solar Energy Engineering*, *123*(2), 164. https://doi.org/10.1115/1.1355035

Taylor C. Treatment of CHP in EU accession country national allocation plans. January 2004.

Ulleberg, O. (2003). Modeling of advanced alkaline electrolyzers: a system simulation approach. *International Journal of Hydrogen Energy*, *28*(1), 21–33. https://doi.org/10.1016/S0360-3199(02)00033-2

Ulleberg, Ø. (2004). The importance of control strategies in PV–hydrogen systems. *Solar Energy*, *76*(1–3), 323–329. https://doi.org/10.1016/j.solener.2003.09.013.

Van Dyke H. Parunak. Go to the ant: engineering principles from natural multi-agent systems. *Annals of Operations Research*, (75):69–101, 1997. Available at http://www.erim.org/vparunak/gotoant.pdf.

Vernon R. W., Initial Comparisons of Solar Collector Performance Data Obtained Out-of Doors and with a Solar Simulator, NASA TM X-71626, 1975.

Vlahinos, A. (2008). Applying six sigma to drive down product defects. *ANSYS Advantage*, *2*(2), 14–16.

WADE (www.localpower.org). New 'National Survey of DE in China—2003': China—substantial prospects for clean and efficient decentralized energy systems. March 2003.

WADE (www.localpower.org). World survey of decentralized energy. 2004.

Wuhua, H., Gaoxi, X., & Wen-Jian, C. (2011). PID controller design based on two-degrees-of-freedom direct synthesis. *2011 Chinese Control and Decision Conference* (CCDC), Mianyang, China, 629–634.

Wu, D. W., & Wang, R. Z. (2006). Combined cooling, heating and power: A review. *Progress in Energy and Combustion Science*, *32*, 459–495. https://doi.org/10.1016/j.pecs.2006.02.001.

Xinhua, L., Xutang, Z., Wenjian, L. (2007). Integration of CAPP and CAFD based agent technology. In: *International Conference on Mechatronics*, Kumamoto, Japan, 8–10 May, 2007.

Yaghoubi, M., Ahmadi, F., & Bandehee, M. (2013). Analysis of Heat Losses of Absorber Tubes of Parabolic through Collector of Shiraz (Iran) Solar Power Plant. *Journal of Clean Energy Technologies*, *1*(1), 33–37. https://doi.org/10.7763/JOCET.2013.V1.8

Yang, H., Lu, L., & Zhou, W. (2007). A novel optimization sizing model for hybrid solar-wind power generation system. *Solar Energy*, *81*(1), 76–84. https://doi.org/10.1016/j.solener.2006.06.010

Yang, H., Wei, Z., & Chengzhi, L. (2009). Optimal design and techno-economic analysis of a hybrid solar–wind power generation system. *Applied Energy*, *86*(2), 163–169. https://doi.org/10.1016/j.apenergy.2008.03.008

Yamamoto, S., Hirahara, H., Tanaka, A., & Ara, T. (2012).

Zaiontz, C. (2017). *Spearman's Rank Correlation.* Available: http://www.real-statistics.com/correlation/spearmans-rank-correlation/. Last accessed January 2017.

Zahler C., Luginsland F., Häberle A., Design, Manufacture and Installation of a Solar Simulator for the GREEN Laboratory at Pontifícia Universidade Católica de minas Gerais in Brazil, ISES Solar World Congress, Orlando, 2005.

Zahler C, S. Scherer, F. Luginsland, et al., Design, Manufacturing and Installation of a Combined Indoor and Outdoor Test Stand for Solar Thermal Collectors for the Centre for Solar Energy Studies (CSES) in Libya, 1st International Conference on Solar Heating, Cooling and Buildings, Lisbon, 2008.

Zecevic A.I. Siljak, D.D., Control of large scale systems: beyond decentralized feedback, Annual Reviews in Control 29 (2005) 169–179.

Zhao, J., Ge, X., et al., 1994. Theoretical and experimental study of the radiation flux distribution in the focal plane of a parabolic trough concentrator. Acta Energiae Solaris Sinica (Chinese) 15 (3), 262–267.

Zhang, J., Xie, Z., Zhang, J., Tang, Y., Song, C., Navessin, T., Holdcroft, S. (2006). High temperature PEM fuel cells. *Journal of Power Sources*, *160*(2), 872–891. https://doi.org/10.1016/j.jpowsour.2006.05.034.

List of Abbreviations

A_{co}	Area of parabolic trough collector (m^2)
A_{PV}	Area of photovoltaic module on the receiver (m^2)
A_W	Area of wind turbine generator (m^2)
C_{bat}	Capacity of Battery (Ampere-hour, kWh)
c_i	Specific heat
$C_{P\text{-}HTF}$	Specific heat capacity of Heat transfer fluid (J/kg.K)
C_{PV}	Specific heat capacity of Heat transfer fluid (J/kg.K)
$D_{no\text{-}sun}$	Days of no sun
$E_{H2\text{-}Tank}$	Energy store in hydrogen tank (kWh)
E_{re}	Energy required (kWh)
FF	Photovoltaic module fill factor
F_{KL}	Sky clearness index factor
G	Global solar radiation (W/m^2)
HHV	Hydrogen heating value (kWh/Nm^3)
h_{ref}	Wind turbine reference height (m)
I_b	Photovoltaic photon current (A)
I_{bat}	Battery current (A)
I_{SC}	photovoltaic current at standard condition (A)
$I_{SC\text{-}STC}$	photovoltaic current at standard condition and standard test condition (A)
I_{total}	Total radiation (w/m^2)
K_2	Fraction daily load during no sun
k_{SM}	thermal conductivity of storage medium (W/m. K)
K_V	Photovoltaic module temperature coefficient
L_{lv}	Latent heat of vaporisation (J/kg)

$m(t)$	Mass (kg)
m_i	Mass of phase change materials (kg)
$N_{MH, Start}$	H_2 content in MH at start time [NL]
$N_{MH\text{-}Norm\ Cap}$	total H_2 capacity in MH [NL]
N_P	Number of parallel photovoltaic module on the receiver
N_S	Number of series photovoltaic module on the receiver
P_{bal}	Balance of Power between supply and demand (kW)
P_{dem}	Power demanded (kW)
GC_Th	Transfer function of controller thermal trough system
GP_Th	Transfer function of plant thermal trough system
GP_Track	Transfer function of mechanical trough tracking system
GC_Track	Transfer function of mechanical trough tracking system
J	LQR controller cost quadratic performance index
Q	state square and symmetric weighting matrix
R	control square and symmetric weighting matrix
H_accel	Accelerometer transfer function
H_Notch	Notch filter transfer function
I_b	solar beam radiation (w/m^2)
I_{Tot}	solar total radiation (w/m^2)
F_{in}	Flowrate in (kg/s)
T_{in}	Temperature in (^0C)
$F_{in,O}$,	Flowrate out (kg/s)
T_f,	Heat transfer fluid temperature (^0C)
T_p	Heat transfer fluid temperature (^0C)
$F_{w, o}$	Flowrate of water out (kg/s)
$T_{w, o}$	Temperature of water out (^0C)
F_H	Flowrate of hot tank (kg/s)

T_H	Temperature of hot tank (^{0}C)
F_{Hx}	Flowrate of heat exchanger (kg/s)
T_{HX}	Temperature of hot tank (^{0}C)
$P_{el\text{-}load}$	Electric load (kW)
P_{ely}	Electrolyser power (kW)
P_{FC}	Fuel cell power (kW)
P_{gen}	Power generated (kW)
$P_{min\text{-}dem}$	Minimum power demanded (kW)
P_{PV}	Power of photovoltaic module (kW)
P_r	Rated power of selected photovoltaic module on the receiver (kW)
P_{store}	Energy stored (kWh)
P_{WG}	Power generated by wind generator (kW)
Q_{HTF}	Enthalpy of gain or loss by Heat transfer fluid (kJ/kg)
$r_m(t)$	Heat storage tube radius (m)
SOC(t)	Battery state of charge
$SOC_{MH\text{-}H2}$	Metal hydride hydrogen state of charge
T_C	Temperature of solar cell (K)
$T_{HTF\text{-}in}$	Inlet temperature of heat transfer fluid (K)
T_{long}	Long term storage time (h)
T_m	Melting temperature of phase change material (K)
T_{max}	Maximum temperature (K)
$T_{SOC\text{-}SM}$	State of charge of heat storage medium
$V_{cut\text{-}in}$	Wind generator cut-in speed (m/s)
$V_{cut\text{-}out}$	Wind generator cut-in speed (m/s)
V_h	Velocity of wind turbine at installation height (m/s)

$V_{H2\text{-}Elyser}$	H2 produced by the electrolyser (NL/min)
$V_{H2\text{-}Tank}$	H2 consumed by the fuel cell (NL/min)
$V_{Heat\text{-}Tank}$	Volume of heat storage tank (m^3)
V_{OC}	Open circuit voltage of solar cell
V_r	Wind turbine generator rated speed (m/s)
V_{ref}	Wind velocity of generator at rated speed (m/s)
x(t), x	steam quality, number of unit of subsystems in the optimisation decision space
α	Neutral stability condition factor of wind turbine
β_{PV}	Photovoltaic inclination angle
η_{Bat}	Efficiency of battery
η_{FC}	Efficiency of Fuel cell
η_{Heat}	Efficiency of heat storage
η_{th}	Efficiency of light to thermal conversion
ϱ_{HTF}	Density of heat transfer fluid (kg/m^3)
σ	Battery self-discharge rate
T_{ewt}	Entering heat temperature to the cooling and heating thermally activated unit (K)
$HP_{cool\ Abs}$	Hourly cooling rate of thermally activated unit
HP_{Heat}	Hourly heating rate of thermally activated unit
COP	Coefficient of performance of heating and cooling unit
d	Ranking difference
D_h	hydraulic diameter
f	Fanning friction factor, objective functions
g_y	Acceleration due to gravity along the y-axis m/s^2
h	Heat transfer coefficient W/m^2. K
k	Thermal conductivity W/m. K

L	Length of receiver in m
n	number of design point
Nu	Nusselt number, $\frac{hL}{k}$, $h = \frac{Q''}{\Delta T}$
P	Pressure of heat transfer fluid N/m^2
ΔP	Pressure drop
Pr	Prandtl number
Q	quantity of heat in J
q"	Heat flux in W/m^2
R_{xx}	inverse of correlation matrix
Re	Reynolds number
T	Temperature in K
u, v, w	velocity components in the x, y and z in m/s

Greek

μ, μ_t	Viscosity, Viscosity tensor
ϱ	Spearman rank correlation coefficient, Density in kg/m

Appendix A

The code snippet for the sizing, design optimisation and control

Sizing MATLAB script code snippet

```
% Hydrogen standalone combined cooling heat and power system Constant

% radiation model constants
beta= 0:0.25:90;
%beta= 0:0.010274:90; % Tilt angle variation from 0 degree to 90
degree
phi=34.0500;    % Latitude of the location of Loss angeles california
Long=118.25;    % Longitude of the location of Loss angeles california
DeltaGMT=-7;    % Local time difference between GMT and Loss angeles
LSTM=15*DeltaGMT; % Local standard time merridian
% fn=['weather_data\',fn];
% [fn,pn]=uigetfile('weather_data\sch*.xlsx','Specify an excel
Schedule File Name',fn);
% name=[pn,fn];
Day_No=xlsread('Day_No.xlsx','Day number');
Diffuse_horizontal_rad=xlsread('Diffuse_horizontal_rad','Diffuse
horizontal radiation');
Direct_Normal_rad=xlsread('Direct_Normal_rad','Direct normal
radiation');
Temperature_sur=xlsread('Temperature_sur','Temperature of
surroundings');
Clock_time=xlsread('Clock_time','Clock time');
Electric_load=xlsread('Electric_load','Electric demand Load');
Cooling_load=xlsread('Cooling_load','Cooling demand Load');
Heating_load=xlsread('Heating_load','Heating demand Load');
Wind_speed=xlsread('Wind_speed','Wind speed');
delta=23.45*sind((360.*(Day_No+284))./365); % Declination angle
B=(360.*(Day_No-81))./365;
EOT=(9.87.*sind(2.*B))-(7.53.*cosd(B))-(1.5.*sind(B));
TCF=4.*(LSTM-Long)+EOT;
Ts=Clock_time+(TCF./60);
w=15.*(Ts-12);
thetaz=acosd(sind(delta).*sind(phi)+cosd(delta).*cosd(phi).*cosd(w));
CosIn=sqrt((cosd(thetaz)).^2+(cosd(delta)).^2.*(cosd(w)).^2);
In_ang=acosd(CosIn);
% Empirical constant for comuting the thermal and electical incidence
angle modifier
a1=0.14;
b1=2*a1;
% if (In_ang< 60)
    IAM_th=(1-(a1*(1/CosIn-1)));
% else
%     IAM_th1=(1-a1*(1/CosIn-1))*(1-(In_ang-60)/30);
% end
%
% if (In_ang< 60)
    IAM_el=(1-(b1*(1/CosIn-1)));
% else
%     IAM_el1=(1-b1*(1/CosIn-1))*(1-(In_ang-60)/30);
```


```
% end
% IAM_th=real(IAM_th1);
% IAM_el=real(IAM_el1);
I_b=CosIn.*Direct_Normal_rad;
I_tot=Diffuse_horizontal_rad+I_b;
Tsky=0.914.*Temperature_sur;
nu_thermal=0.5;
nu_PV=0.18;
F_KL=1-((Direct_Normal_rad./I_tot).^2);     % clearness factor Klucher
modulating function,F_KL
% Area of collector required fo cooling A_co_c and heating A_co_h
% mechanical power and electric power form heat stored
A_co_c=Cooling_load.*1000/nu_thermal.*I_tot.*F_KL;
A_co_h=Heating_load.*1000/nu_thermal.*I_tot.*F_KL;
A_PV=(Electric_load./nu_PV.*I_tot.*F_KL)/3600;
K1=0.5;       % Fraction of power to be stored night cooling and
heating
K2= 0.5;      % Fraction of power to be stored
D_no_sun=3;   % Days without the sun
nu_steamgen=0.42;
Tmedium=12;
PHeat_store=(K1*(Cooling_load.*1000+Heating_load.*1000)+K2*(Cooling_lo
ad+Heating_load)*1000*D_no_sun)/nu_thermal; % Power in Heat storage
PHeat_store_mean=mean(PHeat_store);
VHeat_Tank =PHeat_store*3600*Tmedium/(rho_nf*Cp_nf*(673-393));
% Volumn of heat storage tank
P_thermal_Mech=PHeat_store.*nu_steamgen;
P_thermal_Mech_mean=mean(P_thermal_Mech);
%Computing the electric power of the PV Modules
Beta_PV= 0.065;   % Temperature coefficienct of PV cell
NOCT=47;
T_ref=25;
Ta=20;
C_PV=7; %concentration ratio
nu_opt= 0.7;   %Optical efficeincy
nu_PV=0.18;    % Efficiency of PV cell
A_PV_Mod=1.65;
G=A_PV_Mod.*I_b.*C_PV.*nu_opt;
T_PV_Cell=Ta+((NOCT-20)/800)*I_tot.*1000;
P_PV=G.*nu_PV.*(1+Beta_PV.*(abs(T_PV_Cell-T_ref)));
P_PV_mean=mean(P_PV);
%Computing wind power
v_rated=12;    % rated speed of 15 kW Kingspan wind turbine from
manufacturer technical specification
h_hub=25;      % turbine hub height from the 15 kW Kingspan wind
turbine from manufacturer technical specification
h_ref=10;      % wind speed measurement height
alpha=0.6;     % Hellmann constant
v_cut_in=2.5;
v_cut_out=25;
d_rotor=9;
nu_WT=0.4;
P_rated=15000;  % Turbine rated power 15 kW
v_hub=Wind_speed.*(h_hub/h_ref)^alpha;  % Wind speed at hub height
a=P_rated/(v_rated^3-v_cut_in^3);
b=v_cut_in^3/(v_rated^3-v_cut_in^3);
P_w=a*v_hub.^3-b*P_rated;                % wind turbine available
power
A_wt=pi*d_rotor^2/4;
P_WG=P_w*A_wt*nu_WT;
```


```
P_WG_mean= mean(P_WG);
P_WT_avail=0.5*0.45*1.2*v_hub.^3;
Dia_avg=sqrt(Electric_load.*1000./8760.*P_WT_avail.*pi*0.25);
A_WT_avg=pi*Dia_avg.*Dia_avg./4;
% Computing Fuel cell Power from the enhanced deterministic algorithm
P_FC= 1.2.*Electric_load*1000;
P_FC_mean= mean(P_FC);
% Computing excess Energy for battery charging and charging
Electrolyser
nu_inv=0.75;
P_bat_Elyser=(P_thermal_Mech*0.25+P_PV+P_WG)-
Electric_load.*1000/nu_inv;
P_Gen=(P_thermal_Mech*0.25+P_PV+P_WG);
P_dem=Electric_load.*1000/nu_inv;
P_deli=P_bat_Elyser;
P_Elyser=P_bat_Elyser/2;
P_Elyser_mean=mean(P_Elyser);
LSP=P_bat_Elyser/Electric_load.*1000;
% Computing Hydrogen long term storage for worst case scenario of no
sun
% and wind for 21 days (21X24)504 hours
nu_FC=0.65;
HHV=3.55;
T_long=504;
E_H2_Tank= P_bat_Elyser.*T_long/nu_FC;
E_H2_Tank_mean=mean(E_H2_Tank/T_long);
V_H2_Tank=E_H2_Tank./HHV;
% Cooling and heating rate
Td_cool=28;     %Cooling design temeperature
Td_heat=21;     % Heating design temperature
T_amb=32;       % Ambient temperature
T_min=13;       % Minimum temperature
T_rm=25;
T_max=0.33*T_rm+21.8;
T_ew=T_min+((T_max-T_min)/(Td_cool-Td_heat))*(T_amb-Td_heat);
%Quadratic polynomial correlation coefficient for heating and cooling
%cooling coefficient
k0_c=1;
k1_c=-1.5597e-2;
k2_c=-1.5931e-4;
%heating coefficient
k0_h=1.53;
k1_h=-2.29609e-2;
k2_h=6.8744e-5;
%Maximum coefficient of performance
COP_max_c=4.5;
COP_max_h=5.5;
% computing Heating rate
COP_h=COP_max_h*(k0_h+k1_h*T_ew+k2_h*T_ew^2);
H_rate=Heating_load.*1000*COP_h;
% computing cooling rate
COP_c=COP_max_c*(k0_c+k1_c*T_ew+k2_c*T_ew^2);
C_rate=Cooling_load.*1000*COP_c;
%Battery current
V_bat=48;
I_bat=0.01*P_bat_Elyser./V_bat;
% Battery manufacturer data from datasheets Deep cycle AGM Trojan's
12v
% Type J185-AGM @ C5 5h charging rate is 157Ah, C10 10h charging rate
is
```


```
% 171Ah and C20 200Ah
Cbat_man=200;
T_bat=300.15;      % 27 deg C @ C20 charge rate Trojan
www.trojanbattery.com/reliatagm
delta_c=0.006;
nu_bat=0.8;
sigma=0.002;
SOC_int=0.35;
deltaT=1;
Tshort=10;   %10 hours short term storage
DOD_max=0.4;
nu_inv=0.7;
%Cbat=Cbat_man*(1+delta_c*(T_bat-298.15));
Cbat=Electric_load.*Tshort/V_bat*DOD_max*T_bat*nu_bat;  % Battery
Capacity in Ampere Hour Kaabeche,Belhamel & Ibtiouen model
% State of charge of Short term battery storage
%SOC=abs((SOC_int*(1-
sigma*deltaT/24)+I_bat.*delta*nu_bat/Cbat)*V_bat/1000);
Cbat_kW=Cbat*V_bat;
Cbat_kW_mean=mean(Cbat_kW);
SOC=SOC_int*(1-sigma)+(P_bat_Elyser-Electric_load./nu_inv)*nu_bat;
SOC_per=SOC_int*(1-sigma)+((P_bat_Elyser-
Electric_load./nu_inv)*nu_bat)/Cbat*V_bat/1000;
% State of charge of Long term Hydrogen storage
% Electrolyser current is computed from the electrolyser nominal
voltage
% V_Elyser_Nor for any Pure Energy electrolyser @400VAC
% www.pureenergycentre.com/hydrogen-electrolyser
V_Elyser_Nor=400;
P_Elyser_Nor=30500;                  %30.5 kW
I_Elyser=P_Elyser_Nor/V_Elyser_Nor;

I_Elyser_Nor=P_bat_Elyser./V_Elyser_Nor;
N_Elyser=min(I_Elyser_Nor)/I_Elyser;
% Computing Hydrogen produced by Electrolyser
F=96485.3329;                              %Faradays constant
rho_H2=0.0899;                             %Density of Hydrogen kg/m3
V_Elyser=(I_Elyser_Nor./(2*F))*rho_H2;  % Volume of hydrogen in m3/s
%LPSP2=trapz(Electric_load*1000);
% Computing Hydrogen consumed by fuel cell using Nedstack FCS 10-HP at
% 43-73 VDC at 230A
I_FC_Nor=230;
V_FC_Nor=70;
I_FC=P_FC/V_FC_Nor;
N_FC=max(I_FC)/I_FC_Nor;
% Computing the consumption of hydrogen gas by the fuel cell
mu_H2=0.8;     %Hydrogen Ultilisation factor
R=8.314;
P_atm=101325;
CR_H2=mu_H2.*I_FC/2*F;
V_FC_H2=((CR_H2.*R*273/P_atm)/T_long)/3600;  % Volume of H2 consumed
in m3/s by Fuel cell
%State of charge of long term hydrogen storage
V_MH_int=V_H2_Tank*0.1;
MH_SOC=(10*(V_MH_int+V_Elyser-V_FC_H2)/V_H2_Tank)*100;
% State of charge and discharge of medium term heat storage
T_day=0:0.0278:10;
k_SM=45;
mdot=0.085;
mdot_d=0.077;
```


```
L_vap=250;           % Latent heat of fusion of paraffins
T_m=400;
T_HTF_in=234;
rm=50;
ri=11;
T0_SOC_SM=234;
m_gra=0.5;
Cp_gra=1800;
m_para=1000;
Cp_para=1420;
T0_SOD_SM=195;
%x_qual=((2*pi*k_SM/mdot*L_vap)*(T_m-T_HTF_in)/log(rm/ri))*L;
%x_qual_SOC=1-x_qual;
%Qdot=PHeat_store+L_vap*trapz(T_day,x_qual_SOC);
%T_SOC_SM=T0_SOC_SM+mdot*Qdot/(m_gra*Cp_gra+m_para*Cp_para);
% State of charge of discharge of medium term heat storage
%Qdot_d=PHeat_store-trapz(T_day,x_qual);
%T_SOD_SM=T0_SOD_SM+mdot_d*Qdot_d*L_vap/(m_gra*Cp_gra+m_para*Cp_para);
%Loss of Load probability, a relability model for guranting that the
load
%is met
LOLP=Electric_load*1000/P_bat_Elyser;
%Financial modelling of the HCCHP
% Feed-in-tariff data Ofgen data April 2016-2017
FITth_el=13.61;
FITth_PV=4.53;
FITth_WG=13.89;
Tsell_grid=4.85;
Lp=20;
% Computing present value of Feed-in-Tariff investments
I_FIT=Lp*((P_thermal_Mech*FITth_el/3600)+P_PV*FITth_PV/3600+P_WG*FITth
_WG/3600);
I_sell_grid=Lp*Tsell_grid*(P_bat_Elyser/3600);
% Computing initial capital cost
C_unitPV=0.741;        % Unit capital cost of PV
C_unitWG=0.525;        % Unit capital cost of Wind turbine
C_th_el=2.028;         % Unit capital cost of parabolic trough
C_unitHeat=4.85;       % Selling tariff(Export tariff) p/kWh
C_unitH2=4.85;
C_unitBat=4.85;
N_heat=1;
N_h2=1;
N_bat=1;
C_IC=(A_co_c+A_co_h)/3600000.*C_th_el+A_PV.*C_unitPV+A_WT_avg.*C_unitW
G;   %Capital cost of generation
C_store=10*(N_heat*C_unitHeat*PHeat_store/3600+N_h2*C_unitH2*E_H2_Tank
/3600+N_bat*C_unitBat*Cbat/3600)/1000; % Capital cost of storage
% Computing replacement and maintenance and operation cost
% Computing replacement
kd=0.0025;       % Interest rate 0.25%
f=0.02;          % Inflation rate 2%
Nrep=1:360;
N=20;
C_rep=N_bat*Cbat*C_unitBat*sum((1+f)./(1+kd)).^((N./Nrep)+1);
% maintainance and operation cost
kpv= 0.001; kthel=0.001;kwG=0.003;kbat=0.001;kH2=0.001;kHeat=0.002;
C_OM0=C_IC.*(kpv+kthel+kwG+kbat+kH2+kHeat);
C_M_Op=C_OM0*((1+f)./(kd-f))*(1-((1+f)./(1+kd))).^Lp;
% Computing Levelised Cost of Energy storage
LCOE_Heat=0.208;LCOE_H2=0.039; LCOE_bat=0.067;
```


```
C_LCOE=Lp*P_bat_Elyser/3600*(LCOE_Heat+LCOE_H2+LCOE_bat);
ROI=I_FIT+I_sell_grid-(C_IC+C_LCOE)./(C_IC+C_LCOE);
%computing effective angle of incidence for diffuse, reflective and
beam radiation
theta_d=59.7-0.1388*beta+0.00149*beta.^2;  % effective angle of
diffuse radiation
theta_r=90-0.5788*beta+0.00269*beta.^2;    % effective angle of
reflective radiation
theta_b=acos(CosIn);                      % effective angle of beam
radiation
% Computing the effective Incidence angle modiffier of incidence for
diffuse, reflective and beam radiation

% Receiver model constant

% Copper top receiver constant
mt=0.5;    %Mass of copper top
Ct= 384.4; %Specific heat capacity
h=13.1;    % heat transfer coefficient air through copper
Wt=0.0023;  % Width of the copper plate top cover
rhot= 8960; % Density of copper

u_in=1;     % inlet Velocity m/s
vis=0.0021;  % Viscosity
d_in= 0.022; % internal diamter of copper half tube
rho_nf=3156.5;
Cp_nf=1709.1;
k_nf=0.381;
Re_no=d_in*u_in*rho_nf/vis;    % Reynolds number
Ffac=(0.790*log(Re_no)-1.64)^-2;   % Fanning friction factor
Petukhov's correlation
Pr=Cp_nf*vis/k_nf;                % Prandtl number
hmf=rho_nf/d_in*(Ffac*(Re_no-
1000)*Pr/8)/(1+12.7*(Ffac/8)^0.5*(Pr^0.67)-1)*(1+(d_in./L).^0.67);
%Heat transfer coefficient of metal to fluid
Nus=0.23*Re_no^0.8*Pr^0.2;     % Nusselt number
hf=k_nf*Nus*4/d_in;            % Fluid heat transfer coefficient
NTU=(0.5*(pi*d_in^2/4)/((1/hf)+1))/rho_nf*u_in*(0.5*(pi*d_in^2/4))*Cp_
nf;
epsilon=1-exp(NTU);
% Automate the code in MATLAB Command window as line  39 40 41 and use
the new name as I_totData as name in the from workspace block
Temperature_surData=[t',Temperature_sur];
I_totData=[t',I_tot];
I_bData=[t',I_b];
Electric_loadData=[t',Electric_load*1000];
Heating_loadData=[t',Heating_load];
Cooling_loadData=[t',Cooling_load];
CosInData=[t',CosIn];
P_thermal_MechData=[t',P_thermal_Mech];
P_PVData=[t',P_PV];
P_WGData=[t',P_WG];
```

Design optimisation array code snippet

```
%%
% Generate the runs for a Box-Behnken experiment:
settings = bbdesign(3);
```


```
%%
% Randomize the order of the runs, and display in real-world units.
clear x;
format short g
runorder = randperm(15);    % random permutation of the runs
bounds=[0.8 3; 0.005 4;500 1000]; % min and max values for each factor
x = coded2real(settings,bounds);
disp(sortrows([runorder' x]))
commandwindow

%% Analyze the experimental results
TestResult=randsample(Tri_FanFric,15);
% We have already carried out this experiment, with these results:
output=TestResult;
%output = [837 864 829 856 880 879 872 874 834 833 860 859 874 876
875]';
disp([settings output])
commandwindow

%%
CodedValue=bbdesign(3);
RealValue=zeros(size(CodedValue));
disp({'Run Number','Length','Velocity','BeamRad','TestResult'})
disp(sortrows([runorder' RealValue TestResult]));

for i = 1:size(CodedValue,2) % Convert coded values to real-world
units
    zmax = max(CodedValue(:,i));
    zmin = min(CodedValue(:,i));
    RealValue(:,i) = interp1([zmin zmax],bounds(i,:),CodedValue(:,i));
end
StoreCorr=table(TestResult,Length,Velocity,BeamRad);
%StoreDep=table(PHeat_store,E_H2_Tank,Cbat_kW);

Exp=table(runorder', RealValue(:,1),RealValue(:,2),RealValue(:,3),...
TestResult,'VariableNames',{'RunNumber','L','V','B','TriangularNusselt
'});

%% Response surface
mdl=fitlm(TriangularNuss,'TestResult~Length*Velocity*BeamRad-
Length:Velocity:BeamRad+Length^2+Velocity^2+BeamRad^2');
figure()
h = bar(mdl.Coefficients.Estimate(2:10));
s=regstats(TestResult, CodedValue,'quadratic');
set(h,'facecolor',[0.8 0.8 0.9])
legend('Coefficient')
set(gcf,'units','normalized','position',[0.05 0.4 0.35 0.4])
set(gca,'xticklabel',mdl.CoefficientNames(2:10))
ylabel('Trangular Nusselt')
xlabel('Normalized Coefficient')
title('Quadratic Model Coefficients')
plotSlice(mdl)

%%
% The form of our quadratic model:
%
%    AF = B0 + B1*Distance + B2*Pitch + B3*Clearance +
%         B4*Distance*Pitch + B5*Distance*Clearance +
B6*Pitch*Clearance +
```


```
%         B7*Distance^2 + B8*Pitch^2 + B9*Clearance^2

%%
% Use regstats to estimate and compare the coefficients:
s = regstats(output, settings, 'quadratic');
h = bar(s.beta(2:10)); set(h,'facecolor',[.8 .8 .9]);
legend('Coefficient');
set(gcf,'units','normalized','position',[.05 .4 .7 .4])
set(gca,'xticklabel',{'Length' 'CopperID' 'HTFDia' 'L*C' ...
    'L*H' 'C*H' 'L^2' 'C^2' 'H^2'});
rmse = sqrt(s.mse)

%%
% Use rstool to look at slices of the fitted function, and to
manipulate
% the inputs to get better outputs.
rstool(x,output,'quadratic',0.05,{'Length','Velocity','BeamRad'},
'TestResult')

%%
% Surface plot of response vs. two of the three factors.
ezsurf(@(x,y)x2fx([x,y,-ones(size(x))],'quadratic')*s.beta,[-1 1 -1
1])
title('Triangular Nusselt Number vs. Length and Velocity')
ylabel('Normalized Length')
xlabel('Normalized Velocity')
zlabel('Triangular Nusselt')

%% Find optimal factor values
% Use fmincon from the Optimization ToolboxTM to find the place with
the
% highest air flow.

%% Optimisation
f = @(x) -x2fx(x,'quadratic')*mdl.Coefficients.Estimate;
lb = [-1 -1 -1];
ub = [1 1 1];
x0 = [0 0 0];
[optfactors,fval] = fmincon(f,x0,[],[],[],[],lb,ub,[]);
% Convert the results to a maximization problem and real-world units
maxval = -fval;
maxloc = (optfactors + 1)';
bounds=[0.8 3; 0.005 4;500 1000];
maxloc=bounds(:,1)+maxloc .* ((bounds(:,2) - bounds(:,1))/2);
disp('Optimal Values:')
disp({'Length','Velocity','BeamRad','Triangular Nusselt'})
disp([maxloc' maxval])

% f = @(x) -x2fx(x, 'quadratic')*s.beta;
% lb = [-1 -1 -1]; ub = [1 1 1]; x0 = [0 0 0];
% [optfactors, fval] = fmincon(f,x0,[],[],[],[],lb,ub);
% maxval = -fval;
% maxloc = coded2real(optfactors,bounds)';

%% Addtional pitch angle analysis
% Load results from additional testing and plot them.
TestResult;
figure
```


```
plot(newpitch,newflow)

%% Fit a new model to describe Nuseelt
% Fit a new model that includes additional test data and omits
negligible
% terms from the previous model.
z = [x; ones(11,1), newpitch, ones(11,1)];
zz = [output; [838.378 851.709 863.482 872.536 878.084 878.276 883.833
882.161 880.839 872.447 864.624]'];
mdl = [0 0 0;1 0 0;0 1 0;0 0 1;0 2 0];
rstool(z,zz,mdl)
s = regstats(zz, z, mdl);
rmse = sqrt(s.mse);

%% Use Monte Carlo simulation to study variance in Nusselt
% Generate 10,000 normally distributed random numbers for three
factors
% based on manufacturing tolerance and noise.
Length = normrnd(optfactors(1),0.08,[10000 1]);
Velocity = normrnd(optfactors(2),0.02,[10000 1]);
BeamRad = normrnd(optfactors(3),0.04,[10000 1]);
modelvar = normrnd(0,rmse,[10000 1]);

%%
% Calculate Nusselts number for 10,000 simulated recivers
simfactor=[Length Velocity BeamRad];
%simfactor = coded2real([Length Velocity BeamRad],bounds);
X = x2fx(simfactor,'quadratic');
%X = x2fx(simfactor, mdl);
simflow = X*s.beta + modelvar;
[mufan,sigmareciver] = normfit(simflow);
figure; histfit(simflow); hold on
title(['Mean: ' num2str(mufan) '  ::  ' 'Standard deviation: '
num2str(sigmafan)])

%% Capability analysis of the shapes
% Determine percentage of fans that will be out of spec and find
capability
% indices
S=capability(simflow,[7.71605525 88.7363371]);
%[poutspec, Cp, Cpk] = capable(simflow, [7.71605525 88.7363371]);
commandwindow
```

LQR Control array code snippet

```
%% heating cooling system
% A1=[0.036 -0.036 1.5 0;0 0.036 0 0;17.44 7116.88 34.88 0;0 0 0
0.0003];
% B1=[-1.42 0 1.5 0;0.00025 0 0 0;34.88 0 34.88 0;0 0 0 0];
% C1=[0 0 0 0;0 1 0 0;0 0 1 0;0 0 0 1];
% D1=0;


A1=[0.036 -0.036 1.5;0 0.036 0;17.44 7116.88 34.88];
B1=[-1.42 0 1.5;0.00025 0 0;34.88 0 34.88];
C1=[1 0 0;0 0 1;0 0 1];
D1=0;
```


```
[U1,S1,V1] = svd(A1);
sysHC=ss(A1,B1,C1,D1);
THC=tf(sysHC);
cond(A1);
bode(sysHC)
figure
grid
nyquist(sysHC)
figure
grid
pzmap(sysHC)
figure
sgrid
step(sysHC,0.5)

%% Electrolyser

A2=[-0.0123 0 0 ;0 -0.0123 0 ;-0.0123 0.00615 0.0123];
B2=[0.000337 0 0; 0 0.000170 0;0.000337 0.000170 0.000507];
C2=[1 0 0;0 1 0;0 0 1];
D2=0;
[U2,S2,V2] = svd(A2);
cond(A2);
sysEly=ss(A2,B2,C2,D2);
TEly=tf(sysEly);
bode(sysEly)
figure
nyquist(sysEly)
figure
pzmap(sysEly)
figure
sgrid
step(sysEly)
%% Fuel Cell system
A3=[-3.45 1 0 0;-7.32 0 1 0;-5.74 0 0 0;-0.001 0 0 -0.0017];
B3=[0.144 0 0;2.217 0 0;8.544 0 0;0 0.005 0.0016];
C3=[1 0 0 0;0 0 0 1];
D3=0;
[U3,S3,V3] = svd(A3);
cond(A3);
poles=eig(A3);
rank_of_FCSys=rank(ctrb(A3,B3));
sysFC=ss(A3,B3,C3,D3);
Tfc=tf(sysFC);
bode(sysFC)
figure
nyquist(sysFC)
figure
pzmap(sysFC)
figure
sgrid
step(sysFC)

%% Wind turbine mechanical system
A4=[-48.16 48.16 1; 8.26 -8.26 -1;-2602.89 2602.89 0];
B4=[0.0026 0 0;0 0.00044 0;0 0 0];
C4=[1 0 0; 0 1 0;0 0 0];
D4=0;
```


```
[U4,S4,V4] = svd(A4);
cond(A4); % Condition number
poles=eig(A4);
rank_of_WTmSys=rank(ctrb(A4,B4));
sysWTm=ss(A4,B4,C4,D4);
Twtm=tf(sysWTm);
bode(sysWTm)
figure
nyquist(sysWTm)
figure
pzmap(sysWTm)
sgrid
step(sysWTm)
figure

%% Wind turbine electromechanical and conveter system
A5=[0 1.54e-7 0;-101 -0.77 0;0 0 3.2];
B5=[-101 0 0;0 -101 0;0 0 1];
C5=[1 0 0;0 1 0;0 0 1];
D5=0;
[U5,S5,V5] = svd(A5);
cond(A5);
sysWTe=ss(A5,B5,C5,D5);
Twte=tf(sysWTe); % Transfer function
bode(sysWTe)
figure
nyquist(sysWTe)
figure
step(sysWTe)
figure
pzmap(sysWTe)
sgrid
poles=eig(A5);
rank_of_WTeSys=rank(ctrb(A5,B5));
%% Battery subsystem
A6=[-0.98 0;-4.51 3];
B6=[0.058 0;0.063 3];
C6=[1 0;0 1];
D6=0;
[U6,S6,V6]=svd(A6);
cond(A6); %Condition number
sysBatt=ss(A6,B6,C6,D6);
Tbat=tf(sysBatt); % transfer function of battery subsystem
bode(sysBatt)
figure
nyquist(sysBatt)
figure
step(sysBatt)
figure
pzmap(sysBatt)
sgrid
poles=eig(A6);
rank_of_Batt=rank(ctrb(A6,B6));
```


Appendix B

Datasheets of hydrogen combined cooling heat and power system

The datasheet of the electrolyser is presented as follows:

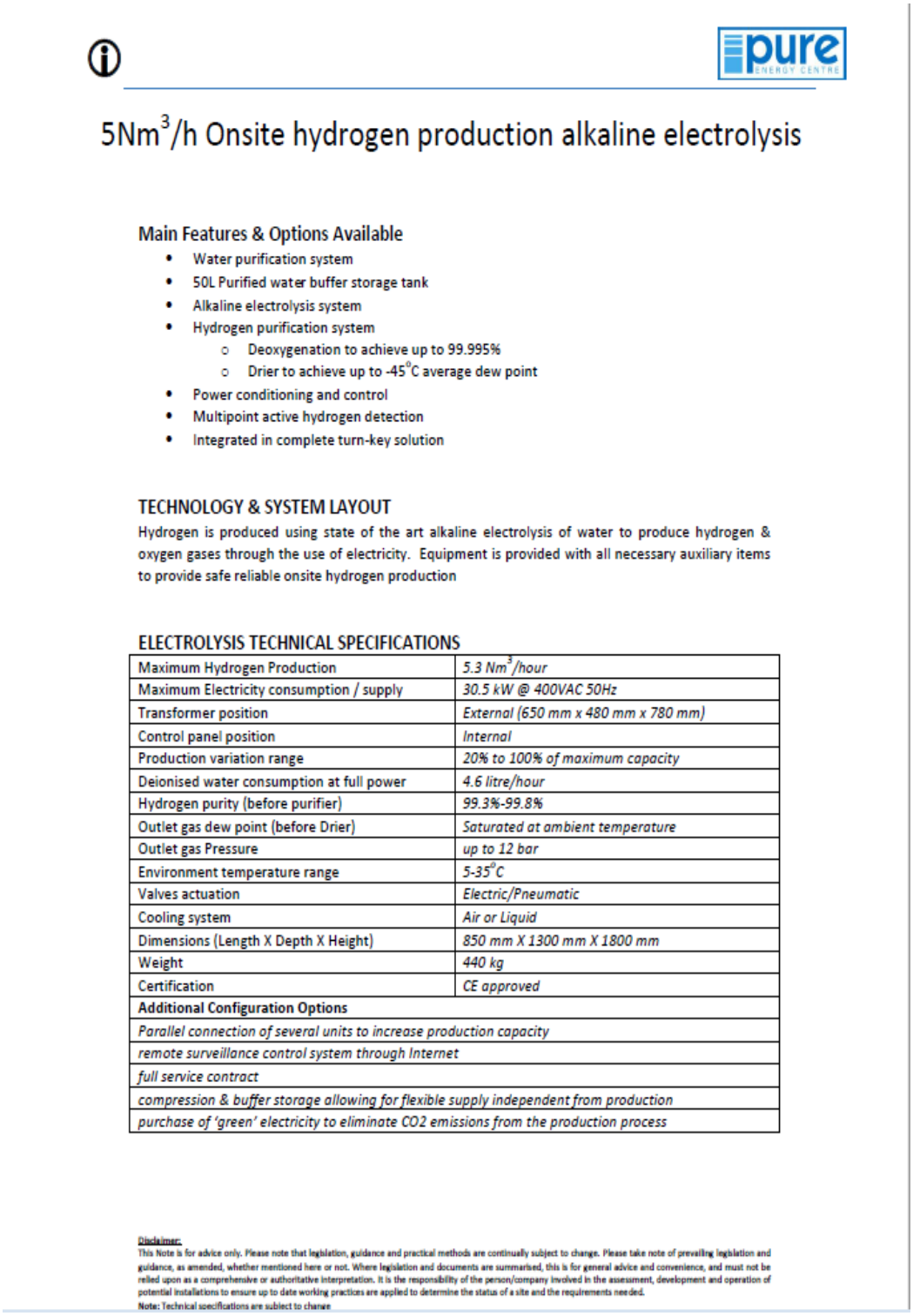

5Nm^3/h Onsite hydrogen production alkaline electrolysis

Main Features & Options Available

- Water purification system
- 50L Purified water buffer storage tank
- Alkaline electrolysis system
- Hydrogen purification system
  - Deoxygenation to achieve up to 99.995%
  - Drier to achieve up to -45^{0}C average dew point
- Power conditioning and control
- Multipoint active hydrogen detection
- Integrated in complete turn-key solution

TECHNOLOGY & SYSTEM LAYOUT

Hydrogen is produced using state of the art alkaline electrolysis of water to produce hydrogen & oxygen gases through the use of electricity. Equipment is provided with all necessary auxiliary items to provide safe reliable onsite hydrogen production

ELECTROLYSIS TECHNICAL SPECIFICATIONS

Maximum Hydrogen Production	*5.3 Nm^3/hour*
Maximum Electricity consumption / supply	*30.5 kW @ 400VAC 50Hz*
Transformer position	*External (650 mm x 480 mm x 780 mm)*
Control panel position	*Internal*
Production variation range	*20% to 100% of maximum capacity*
Deionised water consumption at full power	*4.6 litre/hour*
Hydrogen purity (before purifier)	*99.3%-99.8%*
Outlet gas dew point (before Drier)	*Saturated at ambient temperature*
Outlet gas Pressure	*up to 12 bar*
Environment temperature range	*5-35^{0}C*
Valves actuation	*Electric/Pneumatic*
Cooling system	*Air or Liquid*
Dimensions (Length X Depth X Height)	*850 mm X 1300 mm X 1800 mm*
Weight	*440 kg*
Certification	*CE approved*
Additional Configuration Options	
Parallel connection of several units to increase production capacity	
remote surveillance control system through Internet	
full service contract	
compression & buffer storage allowing for flexible supply independent from production	
purchase of 'green' electricity to eliminate CO2 emissions from the production process	

Disclaimer:
This Note is for advice only. Please note that legislation, guidance and practical methods are continually subject to change. Please take note of prevailing legislation and guidance, as amended, whether mentioned here or not. Where legislation and documents are summarised, this is for general advice and convenience, and must not be relied upon as a comprehensive or authoritative interpretation. It is the responsibility of the person/company involved in the assessment, development and operation of potential installations to ensure up to date working practices are applied to determine the status of a site and the requirements needed.
Note: Technical specifications are subject to change

(Angel Wind Energy, 2010).

Wind turbine

Proven wind turbine data sheet with power curve

Cut In mph (m/s)	5.6 (2.5)
Cut Out mph (m/s)	None
Survival mph (m/s)	156.6 (70)
Rated mph (m/s)	26.9 (12)
Rotor Type	Downwind, Self Regulating
No. of Blades	3
Blade Material	Glassthermoplastic Composite
Rotor Diameter ft (m)	29.5 (9)
Generator Type	Brushless, Direct Drive,Permanent Magnet
Battery charging	48V DC
Grid connect with Windy Boy Inverter	230Vac 50Hz or 240 Vac 60Hz
Direct Heating	240Vac
Rated RPM	150
Annual Output	15,000-30,000 kWh
Head Weight lbs (Kg)	2425 (1100)
Mast Type	Tilt-up, tapered, self-supporting, no guy wires (Taller guyed towers also available on request)
Hub Height ft (m)	49.2 or 82 (15 or 25)
Turbine Foundation ft (m)	12.1x12.1x3.9 or 16.4x16.4x6.6 (3.7x3.7x1.2 or 5x5x2)
Winch Foundation ft (m)	4.9x4.9x3.9 (1.5x1.5x1.2)
Tower Weight ft (m)	3258.4 or 6159.7 (360 or 656)
Mechanical Brake	Yes
Noise @ 11.1mph 5(m/s)	48dBA
Noise @ 44.7mph 20(m/s)	65 dBA
Rotor Thrust (kN)	26

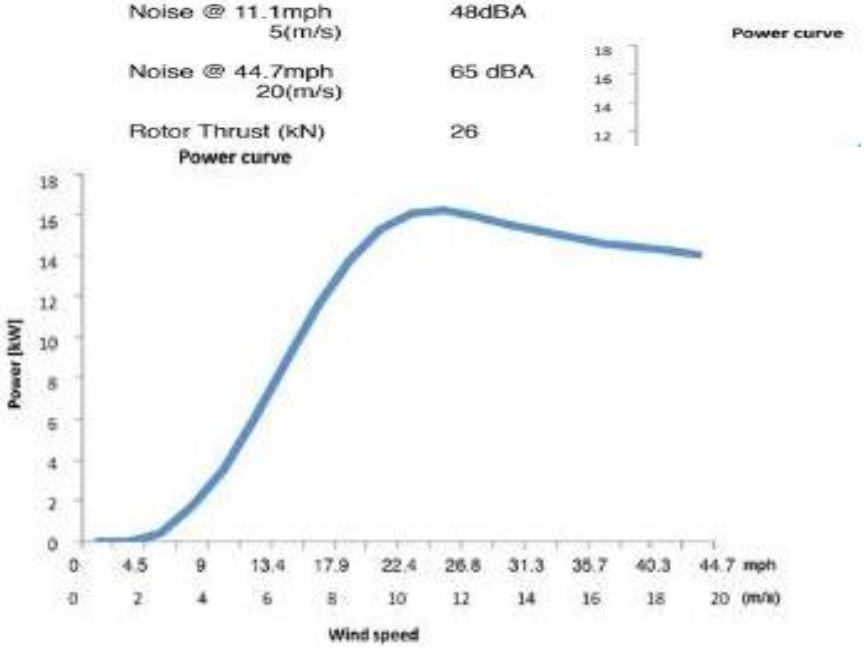

(Angel Wind Energy, 2010).